Development of a Low Background Environment for the Cryogenic Dark Matter Search

a Ph.D. Thesis

by

Angela Jane Da Silva

Department of Physics
The University of British Columbia

April 1996

DEVELOPMENT OF A LOW BACKGROUND ENVIRONMENT FOR THE CRYOGENIC DARK MATTER SEARCH

by

ANGELA JANE DA SILVA

B.A.Sc., The University of British Columbia, 1986
M.A.Sc., The University of British Columbia, 1988

A THESIS SUBMITTED IN PARTIAL FULFILLMENT OF

THE REQUIREMENTS FOR THE DEGREE OF

DOCTOR OF PHILOSOPHY

in

THE FACULTY OF GRADUATE STUDIES

DEPARTMENT OF PHYSICS

We accept this thesis as conforming
to the required standard

THE UNIVERSITY OF BRITISH COLUMBIA

April 1996

©Angela Jane Da Silva, 1996

Abstract

A major problem currently facing astrophysics and cosmology is the question of dark matter. Although there is little doubt about the existence of dark matter, there is considerable uncertainty about the abundance and nature of this matter. One possibility is that dark matter consists of weakly interacting massive particles (WIMPs), such as the lightest stable particle in supersymmetry models.

Direct detection experiments look for nuclear recoils from WIMPs scattering in a detector. The first generation of direct detection experiments were ultimately limited by radioactive backgrounds. The Cryogenic Dark Matter Search (CDMS) is a direct detection experiment based on novel particle detectors operated at millikelvin temperatures that provide intrinsic background rejection. This capability, however, is not 100% effective. Therefore a low background environment is essential to the experiment.

To create such an environment, all possible background sources have been extensively studied both by measuring the background contribution from muons, photons and neutrons and by performing detailed Monte Carlo simulations of the photon and neutron backgrounds. The results of this investigation, as discussed in this thesis, have influenced all aspects of the CDMS experiment.

The initial site for the CDMS experiment is the Stanford Underground Facility. The relatively high muon flux at this site due to its shallow depth was balanced against the convenience of a local site with the unlimited access necessary for operating a complicated cryogenic system and developing new detector technology. The cryostat used to house

the detectors was designed to accommodate the extensive shielding necessary to reduce the ambient backgrounds to acceptable levels and to minimize the amount of radioactive contamination near the detectors. Simulations and measurements of the local backgrounds led to a layered shield design that consists primarily of plastic scintillators to veto muons, lead and copper to attenuate photons and polyethylene to moderate neutrons.

With the background rejection capabilities of the cryogenic detectors and the low background environment created in the Stanford Underground Facility, we expect to extend the current limit on WIMP dark matter by more than an order of magnitude and begin testing models for the lightest supersymmetric particle.

Contents

Abstract ii

Table of Contents vii

List of Tables viii

List of Figures xii

Acknowledgement xiii

1 Introduction 1

1.1 Evidence for Dark Matter 2

1.1.1 Galactic Rotation Curves 3

1.1.2 Clusters of Galaxies 4

1.2 Nature of Dark Matter 6

1.2.1 Standard Cosmology 7

1.2.2 Measurements of Ω 8

1.2.3 The Value of Ω 12

1.2.4 Nucleosynthesis and Ω_b 12

1.2.5 Baryonic Dark Matter 14

1.2.6 Non-Baryonic Dark Matter 15

1.3 Detecting WIMP Dark Matter 18

1.3.1 First Generation Direct Detection Experiments 18
1.3.2 Current Limits 19
1.3.3 The Cryogenic Dark Matter Search 20

2 The CDMS Detectors **22**
2.1 Principle of Operation 23
2.1.1 Phonon Measurement 23
2.1.2 Ionization Measurement 28
2.1.3 Background Rejection Capability 30
2.2 The BLIP Detector 36
2.3 Tower Geometry 37
2.4 Advanced Detectors 38

3 Photon Backgrounds **43**
3.1 Sources of Background Photons 43
3.1.1 Environmental Radioactivity 43
3.1.2 Radiocontaminants in Detectors and Shielding Material 49
3.2 Detector System for Photon Measurements 51
3.3 Shielding Studies 58
3.3.1 Muon-Induced Activities Versus Lead Contamination 60
3.3.2 Lead Quality 66
3.3.3 Effects of Radon 73
3.3.4 Effects of Hydrogen Capture Gamma 74
3.4 Photon Background Simulations 77

4 Neutron Backgrounds **83**
4.1 Sources of Background Neutrons 83
4.1.1 Neutron Production from Natural Radioactivity 83
4.1.2 Neutron Production from Cosmic Ray Muon Interactions 85

4.1.3 Hadronic component of the cosmic rays 88
4.1.4 Summary of neutron sources 88
4.2 Neutron Monte Carlo Program 88
4.3 Detector System for Neutron Measurements 91
4.3.1 Energy Response and Calibration 92
4.3.2 Detector Background 96
4.4 Measured Neutron Backgrounds in the Stanford Underground Facility . . . 97
4.4.1 Effects of Photon Shielding on Neutron Backgrounds 98
4.4.2 Moderating the Muon-Induced Neutron Backgrounds 100
4.5 Simulation of the Neutron Backgrounds in the Stanford Underground Facility 102
4.5.1 Neutron Production in Lead 102
4.5.2 Effects of the Moderator 107
4.5.3 Neutron Production in the Surrounding Rock 108
4.5.4 Estimating Neutron Backgrounds in a Dark Matter Detector 115

5 Low Background Environment 119
5.1 Stanford Underground Facility 119
5.1.1 Muon Measurements 123
5.2 Shield 126
5.2.1 Passive Shield Design 126
5.2.2 Veto System 127
5.2.3 Measured Photon Backgrounds inside the Shield 131
5.3 Cryogenic System 137
5.3.1 Icebox Design 137
5.3.2 Icebox Performance 140
5.3.3 Detector Towers and Striplines 142
5.4 Simulated Neutron Background Event Rates 146
5.5 Simulating Internal Photon Backgrounds 157

6 Analytical Tools for the CDMS Experiment **162**

6.1 Dark Matter Event Rate 162

6.2 Expected Sensitivity 171

7 Future of the CDMS Experiment **175**

7.1 Deep Underground Site 175

7.1.1 Changes to the Experiment 176

7.1.2 Potential Locations 178

7.1.3 Expected Performance at a Deep Site 181

7.2 A Final Word 182

Bibliography **185**

List of Tables

3.1 Dominant photon lines in the uranium and thorium decay chains. 47

3.2 Isotopes ($T_{1/2} > 1$ day) produced by cosmic rays in the atmosphere. 49

3.3 Cosmogenic spallation products in copper at the earth's surface. 51

3.4 Efficiency of the test veto system at the SUF using Stanford lead. 64

3.5 Efficiency of the test veto system at the SUF using Glover lead. 66

3.6 Physics processes implemented by GEANT3. 69

4.1 Neutron production rate in rock from natural radioactivity. 84

4.2 Average number of neutrons emitted after muon capture. 87

4.3 Response of the BF_3 proportional counter to various (α,n) neutron sources. 94

4.4 Counting rate vs wax thickness inside lead shield at the SUF. 111

4.5 Counting rate vs wax thickness at the SUF. 115

5.1 Measured contamination in materials from the tunnel extension. 123

5.2 Measured vertical muon flux in Tunnel A of the SUF. 125

List of Figures

1.1 Constraints on Υ and Ω as a function of scale. 13

1.2 Low energy spectrum measured with a germanium detector. 19

1.3 Current limits set by first generation direct detection experiments. 20

2.1 The combined phonon and ionization measurement circuits. 24

2.2 Circuit for the voltage measurement of the phonon sensor. 27

2.3 Circuit for the AC biasing scheme used for the phonon measurement. . . . 28

2.4 Schematic diagram of the circuit for the charge measurement. 29

2.5 Schematic diagram of the 60 g prototype germanium detector. 31

2.6 Scatter plot of the phonon measurement versus the ionization measurement. 33

2.7 Distribution of the ratio of phonon and ionization electron equivalent energies. 35

2.8 Schematic diagram of 25 elements of a W/Al QET. 40

2.9 Full size detector utilizing W/Al QET phonon sensors. 41

3.1 Background sources for an underground experiment. 44

3.2 Decay chains for the uranium and thorium series. 46

3.3 Cut away diagram of the Ge detector and mounting hardware. 52

3.4 Photon spectrum measured inside a 10-cm-thick lead shield at LBNL. . . . 54

3.5 Low energy portion of the photon spectrum measured at LBNL. 55

3.6 Background spectrum measured inside a 15-cm-thick lead shield at Oroville. 57

3.7 Measured ambient photon spectrum at the Stanford Underground Facility. 58

3.8 Measured photon spectra inside various lead shields at the SUF. 59
3.9 Test veto shield used to study lead quality and veto effectiveness. 61
3.10 Measured photon spectra inside the Stanford lead test veto shield. 62
3.11 Measured photon spectra inside the Glover lead test veto shield. 65
3.12 Photon spectra measured inside a 15-cm-thick lead shield at Oroville. . . . 67
3.13 Shielding configuration used for the Oroville measurements. 68
3.14 Simulation of the energy deposited in a Ge detector from ^{210}Bi decays. . . 71
3.15 Comparison of measured photon spectra with Monte Carlo simulations. . . 73
3.16 Background spectra measured with and without N_2 purge at the SUF. . . . 75
3.17 Background spectra measured with and without polyethylene at the SUF. . 76
3.18 Measured background spectrum inside a polyethylene-filled lead shield. . . 77
3.19 Comparison of measured and simulated background from U decay chain. . 79
3.20 Low energy portion of measured and simulated background (excluding beta decays) from the U decay chain. 80
3.21 Low energy portion of measured and simulated background (including beta decays) from the U decay chain. 81

4.1 Neutron production in rock. 89
4.2 Neutron emission spectra for the various (α,n) neutron sources. 93
4.3 Predicted and simulated energy response function of the BF_3 counter. . . . 95
4.4 Pulse height spectra measured with the BF_3 counter in the SUF. 98
4.5 Measured rate in the BF_3 counter inside various lead shields at the SUF. . 99
4.6 Pulse height spectra measured with the BF_3 counter in the SUF. 100
4.7 Measured counting rate as a function of wax thickness. 101
4.8 Geometry used in the simulations of the neutron background. 104
4.9 Measured and simulated rates in the BF_3 counter at the SUF. 106
4.10 Components of the simulated rate in the BF_3 counter. 109
4.11 Measured and simulated rate in the BF_3 counter vs wax thickness. 110

4.12 Estimate of the spectrum of neutrons emitted from the rock in the SUF. . 113
4.13 Measured and simulated rates in the BF_3 counter vs wax thickness. 114
4.14 Simulated recoil event rate in a Ge detector due to muon-induced neutrons. 117

5.1 Profile of the main underground laboratory space of the SUF. 120
5.2 Plan view of the Stanford Underground Facility. 122
5.3 Schematic diagram of the muon telescope. 124
5.4 Schematic layout of the 13 scintillator paddles of the muon veto shield. . . 129
5.5 Raw counting rate as a function of energy for two scintillator paddles. . . . 130
5.6 Set-up used to measure the photon background in the final shield. 132
5.7 Distribution of delay times between veto events and HPGe events. 134
5.8 Measured HPGe spectra using various delay times. 135
5.9 Photon background inside the final shield with and without active veto. . . 136
5.10 Schematic layout of the dilution refrigerator and the icebox cryostat. . . . 138
5.11 Temperature history of the icebox cans during cooldown 141
5.12 Schematic diagram of the detector tower. 143
5.13 Geometry of the icebox used in the simulations with multiple detectors. . . 147
5.14 Background reduction achieved by rejecting multiple-detector events. . . . 148
5.15 Simulated components of the muon-induced neutron recoil background. . . 149
5.16 Effect of using an inner moderator to reduce the neutron background. . . . 150
5.17 Simulated components of the muon-induced neutron recoil background. . . 151
5.18 Simulated muon-induced neutron recoil background due to lead shields. . . 152
5.19 Simulated lifetime of the muon-induced neutrons. 153
5.20 Geometry used for simulating the neutron background for the CDMS. . . . 155
5.21 Simulated neutron recoil spectra expected for the CDMS Experiment. . . . 156
5.22 Simulated photon background from 1 μg of uranium contamination. 158
5.23 Simulated photon background from 1 μg of thorium contamination. 159
5.24 Simulated photon background spectra in detector 6 and detector 3. 160

6.1 Calculated event rate for WIMPs of various masses scattering from Ge. . . 168
6.2 Annual modulation of the expected WIMP signal. 169
6.3 Calculated event rate for WIMPs scattering in germanium and silicon. . . 170
6.4 Expected sensitivity for the CDMS experiment at the SUF. 174

7.1 Cosmic ray muon flux as a function of depth. 176
7.2 Expected sensitivity for the CDMS experiment at a deep site. 183

Acknowledgement

I would like to take this opportunity to thank Brian Turrell and the members of my Ph.D. committee: B. Bergersen; W. McCutcheon; C. Waltham and N. Weiss; for their direction and encouragement throughout my Ph.D. program. I would also like to thank Bernard Sadoulet, whose guidance and support made this work not only possible but enriching and enjoyable.

Many people have been involved in various aspects of the work discussed in this thesis, and rather than trying to list everyone (and risk inadvertently overlooking someone) I would rather simply like to acknowledge the contribution made by all members of the CDMS collaboration. In addition, I would like to thank everyone in building 29 at Lawrence Berkeley National Laboratory who educated me in the fine art of germanium detector systems and Al Smith for sharing his considerable expertise. Most of what I know about low background counting techniques I have learned from Al. Finally, I would like to thank everyone at the Center for Particle Astrophysics for making this stimulating scientific environment a most pleasant place to work.

Chapter 1

Introduction

Virtually everything that has been learned about the universe has come from studying the electromagnetic radiation emitted throughout it, whether it be visible photons from luminous stars, x-ray photons from hot gas, radio photons from the 21-cm hyperfine transition in neutral atomic hydrogen (H I), microwave photons from the Cosmic Microwave Background (CMB) radiation or any other form of detectable photons. Substantial evidence exists, however, that more than 90% of the mass in the universe is "dark", that is, it neither emits nor absorbs electromagnetic radiation [1]. So far, the existence of this dark matter has been inferred only by its gravitational effects.

This chapter discusses the observational evidence for dark matter and the possible nature of this dark matter. Then, assuming the dark matter consists of weakly interacting massive particles (WIMPs), it discusses a method of detection and the current experimental limits on WIMPs as dark matter set by the first generation of direct detection experiments. Finally, the chapter discusses the Cryogenic Dark Matter Search (CDMS), a second generation experiment aimed at detecting WIMP dark matter.

1.1 Evidence for Dark Matter

The first detection of matter from its gravitational effects occurred in 1844 when Friedrich Wilhelm Bessel [2] observed that Sirius and Procyon exhibited irregularities in their proper motions which he assumed to be caused by each star being in orbit with an invisible companion of mass comparable to its own. The companion of Sirius, called Sirius B, ceased to be invisible on January 31, 1862 when it was seen by Alvan G. Clark [3] using a 47 cm refractor. Procyon B, the companion of Procyon, remained invisible until November 14, 1896 when it was seen by John M. Schaeberle [4] with the 91 cm refractor at the Lick Observatory. Similarly, the existence of Neptune was predicted in advance of its discovery due to its gravitational pull on Uranus. The position of the new planet was calculated by John Couch Adams in 1845 and by Urbain Le Verrier the following year [5]. On September 23, 1846, Neptune was found near the predicted position by astronomers at the Berlin Observatory [6].

Almost a century later, evidence for nonluminous matter on two very different distance scales surfaced almost simultaneously. First, in 1932, Oort [7] analyzed numbers and velocities of stars near the sun and found that the observed total mass of stars down to +13.5 visual absolute magnitudes was only about 40% of the amount of gravitating matter implied by the velocities. He concluded that the remainder of the mass was most probably contained in stars with absolute magnitudes in the next interval of 2 magnitudes beyond +13.5. Then, in 1933, Zwicky [8] reported the first evidence for dark matter beyond the solar neighborhood. By studying the Coma cluster of galaxies, he found that several of the galaxies belonging to the cluster had radial velocities which differed from the mean velocity of the cluster. Using the measured velocity dispersion to estimate the kinetic energy per unit mass of the galaxies and applying the virial theorem, Zwicky was able to determine the total mass of the cluster. He found that the total mass of the cluster was substantially greater than the sum of the masses of the individual galaxies, and therefore concluded that the majority of the mass in the cluster must be in some sort of invisible

or dark matter. Zwicky's initial suggestion of the presence of dark matter remained controversial for many years, and although the nature of this dark matter has yet to be identified, there is growing consensus in today's physics and astronomy communities that indeed it does exists.

1.1.1 Galactic Rotation Curves

Today, the best observational evidence for dark matter comes from studying the rotation curves of spiral galaxies. In most galaxies, the stars lie mainly in a thin disk and travel on nearly circular orbits around the galactic center. The rotation curve is the observed circular speed, v_c, in the plane of the galaxy as a function of r, the radius from the galactic center.

Once the rotation curve has been measured, the gravitational acceleration due to the total mass of the galaxy, $M(r)$, contained within a given radius, r, is the observed centripetal acceleration at that radius, $v_c^2(r)/r$, i.e.,

$$\frac{GM(r)}{r^2} = \frac{v_c^2(r)}{r} \tag{1.1}$$

where G is the gravitational constant.

Optical measurements of several spiral galaxies by Rubin *et al.* [9] have shown that the rotation curves typically show a steep rise in the rotational speed near the center of the galaxy and then relatively constant speeds for radii out to the last measured point. The measured rotation curves also show that the gravitational force generated by the luminous mass in the stars that can be seen is too small to account for the observed rotational speed. Furthermore, the relatively constant speed at large radii implies that the enclosed mass, $M(r)$, increases linearly with increasing radii, even in regions where practically no more stars are observed. Thus these galaxies must contain substantial amounts of dark matter, and most of this dark matter must be located at radii larger than that of the stars since there is no evidence of the Keplerian falloff (i.e., $v_c(r) = (GM/r)^{-1/2} \propto r^{-1/2}$) expected at the outer part of the visible galaxy.

The shapes of these rotation curves suggest that the dark matter is distributed in extended halos that surround the visible stars. A simple empirical model for the halo density is a spherical distribution

$$\rho(r) = \frac{\rho_0}{1 + r^2/r_c^2} \tag{1.2}$$

where the core radius, r_c, and the central density, ρ_0, are fitting parameters. The fits to the rotation curves produced by this model are quite good [11].

It is also often possible to measure the H I rotation curves of galaxies. These measurements have the advantage that H I data are often available well beyond the visible extent of the galaxy. Even in these cases, the H I rotation curve remains flat at large radii providing evidence for an extended dark halo that contributes up to 94% of the total mass of the galaxy [11]. The H I rotation curve of the Milky Way suggests that the dark halo contributes 80% of the total mass in the central 20 kpc of our galaxy [12].

A simple way to parameterize the ratio of dark to luminous matter is the mass-to-light ratio, Υ, which is usually measured in solar units: $\Upsilon_\odot \equiv M_\odot/L_\odot$ where $M_\odot$ is the solar mass and $L_\odot$ is the solar luminosity. The value of Υ depends on the distance, d, to the galaxy, which can be determined from its radial velocity, v, and the Hubble law: $v = H_0 d$, where the Hubble constant, H_0, measures the current expansion rate of the universe (see Section 1.2.1). Despite recent measurements [13], the value of the Hubble constant remains uncertain by a factor of 2. Therefore, H_0 is often written as $H_0 = 100h$ km/s/Mpc where h is between 0.4 and 1. The resulting Υ determined from rotation curves of typical spiral galaxies are found to be at least $30h\Upsilon_\odot$ [14].

1.1.2 Clusters of Galaxies

Galaxies are not distributed uniformly throughout the universe. Instead, they exist in a wide hierarchy of structures. A cluster of galaxies is a gravitationally bound group consisting of hundreds or even thousands of galaxies. A variety of evidence for dark matter has been provided by studying clusters of galaxies.

Velocity Dispersion in Clusters of Galaxies

In a cluster of galaxies, each galaxy oscillates back and forth through the gravitational potential well of the cluster with a finite peculiar velocity, v_p, defined as the difference between the galaxy's actual velocity, v, and its Hubble expansion velocity, $v_H = H_0 d$ (i.e., $v = H_0 d + v_p = v_H + v_p$). Since these systems are believed to be bound and stationary, the dispersion of these peculiar velocities can be related to the depth of the potential well through the virial theorem

$$\langle \text{kinetic energy} \rangle = -\frac{1}{2} \langle \text{potential energy} \rangle \tag{1.3}$$

Observations of the line-of-sight velocities of galaxies as a function of distance from the cluster center lead to velocity dispersions which can be related to the cluster mass and subsequently Υ. For the Coma cluster, velocity dispersions of the order of 1000 km/s have been determined leading to a mass-to-light ratio of $\Upsilon = 360 h \Upsilon_\odot$ [15].

X-Ray Emission from Hot Gas in Clusters of Galaxies

Clusters of galaxies like Coma have strong x-ray emission from hot intracluster gas that sits within the potential well of the cluster at a temperature of the order of 10^8 K. Assuming this gas is in hydrostatic equilibrium in the central part of the cluster, it can be used to probe the potential distribution of the cluster.

Hydrostatic equilibrium implies that

$$\frac{\mathrm{d}p}{\mathrm{d}r} = -\rho \frac{\mathrm{d}U}{\mathrm{d}r} \tag{1.4}$$

where $p(r)$ is the pressure of the gas, $\rho(r)$ is the density of the gas and $U(r)$ is the gravitational potential. Imaging observations and spectral observations can be fitted to models for the temperature and density distributions of the gas. These can then be combined with Equation 1.4 and the ideal gas equation to yield the potential gradient $\mathrm{d}U/\mathrm{d}r$ and hence the mass distribution.

Although this method is limited by the lack of precise measurements of the temperature profile, the results are close to those obtained using the velocity dispersion of the galaxies [16].

Gravitational Lensing by Clusters of Galaxies

New independent evidence for dark matter in clusters has been obtained by studying gravitational lensing of distant background galaxies by foreground clusters. A round object located far behind the massive cluster will appear elliptical after lensing, with its major axis tangential to the mass distribution contours. Tyson *et al.* [17] found that every background galaxy above some critical redshift will be seen as stretched along a circle centered on the lens, creating a coherent set of distortions centered on the foreground cluster. These distortions can then be used to reconstruct the mass distribution, mapping out the dark matter in the cluster [17, 18]. In addition, Broadhurst *et al.* [19] have suggested a new method for determining the projected mass distribution of the galaxy clusters based solely on the gravitational lens amplification of background galaxies by the cluster potential field.

Unlike velocity dispersions of galaxies and x-ray emission methods, gravitational lensing techniques do not rely on the assumption of equilibrium models to determine the mass distribution. Furthermore, since gravitational lensing techniques do not rely on galaxies or gas to act as tracers for the mass, they are not restricted to the central core of the cluster. As a result, the new method promises to provide a detailed map of the dark matter in large structures.

1.2 Nature of Dark Matter

Before beginning the discussion on the nature of dark matter, a few relevant quantities are defined in a brief overview of standard cosmology.

1.2.1 Standard Cosmology

The current standard model of cosmology, known as the hot big bang model, is based on the Friedmann-Robertson-Walker (FRW) cosmological model [20] which describes the expanding universe as homogeneous and isotropic. The success of the hot big bang model has been its ability to describe the observed universe.

The dynamics of the expanding universe are described by the evolution of the scale factor, $R(t)$, which is given by the Friedmann equation

$$\left(\frac{\dot{R}}{R}\right)^2 + \frac{k}{R^2} = \frac{8\pi G}{3}\rho \tag{1.5}$$

where k is the spatial curvature, G is the gravitational constant and ρ is the density.

The most fundamental feature of the standard cosmology is the expansion of the universe. The expansion rate of the universe is determined by the Hubble parameter, H, which is defined as $H \equiv \dot{R}/R$. The Hubble parameter is not constant, and in general, varies as t^{-1}. The Hubble constant, H_0, is the present value of the Hubble parameter.

By replacing $\dot{R}/R$ with H in Equation 1.5 and rearranging terms, the Friedmann equation becomes

$$\frac{k}{H^2R^2} = \frac{\rho}{3H^2/8\pi G} - 1 \tag{1.6}$$

In this form, it is easy to see that the critical density, ρ_c, defined as the density required for a flat universe ($k = 0$) is given by

$$\rho_c \equiv \frac{3H^2}{8\pi G} \tag{1.7}$$

Because the Hubble parameter is a function of time, the critical density is not constant, but changes as the universe expands. The present-day critical density is given by

$$\frac{3H_0^2}{8\pi G} = 1.88h^2 \times 10^{-29}\ \mathrm{g/cm^3} = 2.77h^2 \times 10^{11}\ M_\odot/\mathrm{Mpc^3} \tag{1.8}$$

The density parameter, Ω, is defined as the ratio of the mean density of the universe, $\overline{\rho}$, to the critical density, ρ_c (i.e., $\Omega \equiv \overline{\rho}/\rho_c$). In terms of Ω, the Friedmann equation

simply becomes

$$\frac{k}{H^2R^2} = \Omega - 1 \tag{1.9}$$

The density parameter is the ratio of the absolute value of the gravitational potential energy to the kinetic energy of the Hubble expansion (assuming no cosmological constant). Thus, for $\Omega < 1$, the universe will expand forever, while for $\Omega > 1$, the universe will eventually collapse back on itself. For $\Omega = 1$, the universe has just enough energy to continue to expand until $t = \infty$, with the rate of expansion approaching zero as $t \rightarrow \infty$. Ω also determines the geometry of the universe; if $\Omega > 1$, the universe is closed and the geometry is spheroidal but if $\Omega < 1$, the universe is open and the geometry is hyperboloidal. If $\Omega = 1$, the universe is flat. Thus Ω is a useful measure of the cosmological significance of the dark matter.

1.2.2 Measurements of Ω

Ω from Mass-to-Light Ratios

It is possible to relate the density parameter, Ω, to the mass-to-light ratio, Υ. The mean mass density of the universe is the product of the mean luminosity density, $\overline{\epsilon}$, and the mean mass-to-light ratio, $\overline{\Upsilon}$. Galaxy surveys [21] show that, to within a factor of two, $\overline{\epsilon} = 1.73h \times 10^8\ L_\odot/\mathrm{Mpc}^3$ [22]. Thus, the critical mass-to-light ratio, Υ_c, is given by

$$\Upsilon_c = \rho_c/\overline{\epsilon} = 1600h\Upsilon_\odot \tag{1.10}$$

and

$$\Omega \equiv \overline{\Upsilon}/\Upsilon_c = \overline{\Upsilon}/1600h\Upsilon_\odot \tag{1.11}$$

So, for example, if $\overline{\Upsilon}$ is equal to the mass-to-light ratio of the Coma cluster ($\Upsilon_{Coma} = 360h\Upsilon_\odot$), then Ω is 0.2 and the universe is open. However, it should be noted that this estimate of Υ_{Coma} was obtained using the virial theorem, and the virial theorem is only sensitive to inhomogeneities in the mass distribution. Therefore, this method only provides a lower limit for Ω.

Virgo Infall

The Virgo cluster, located about 20 Mpc away, represents a nearby enhancement in the density of galaxies and therefore an enhancement in the mass density. The presence of this enhanced mass density distorts the local Hubble flow, resulting in peculiar velocities, v_p, given by

$$v_p = H_0 d - v_r \tag{1.12}$$

where $H_0 d$ is the Hubble velocity and v_r is the observed radial velocity. These peculiar velocities are also given by

$$v_p = \text{acceleration} \times \text{time} \tag{1.13}$$

where the acceleration is due to the inhomogeneities in the local mass density and the time depends on Ω. Using Equations 1.12 and 1.13, a value of Ω can be determined. Typically, the Virgo Infall method leads to a value of Ω of the order of 0.2.

Other Dynamical Methods

On distance scales larger than clusters of galaxies, the process of gravitational collapse is just starting and structure is still forming. On these large scales, a complex distribution of galaxies is observed [23] with voids, filaments, bubbles, and large scale coherent velocity flows, not typical of a virialized system. Therefore, it is no longer possible to apply the virial theorem, since these systems are clearly not stationary, and other methods must be used to determine Ω.

Because the time required for the structure to form is sensitive to the underlying averaged density, observations of the large scale distribution of galaxies and the associated velocity flows can be used to estimate Ω. The evolution of these structures is described by linear perturbations to the FRW model. In the linear regime [24], one can consider the observed peculiar velocities as the product of the acceleration due to the density inhomogeneities, and the time of formation (which is related to Ω), or, one can consider the observed inhomogeneities as the product of the rate of variation due to the peculiar

velocities, and the time. Thus, the measured value of the peculiar velocity of the center of mass of the local group (which includes our own galaxy plus its bound companion M31) with respect to the cosmic microwave background can be compared to that expected from the gravitational field due to the inhomogeneous distribution of galaxies, or, the observed density fluctuations can be compared to those predicted by the divergence of the observed velocity field.

The problem with both of these methods is that observations yield fluctuations in the number density of galaxies, not fluctuations in the mass density, and there are numerous indications that the mass distribution differs from the distribution of light. It is generally assumed that fluctuations in the number density of galaxies, $n(\mathbf{x})$, are proportional to fluctuations in the mass density, $\rho(\mathbf{x})$:

$$\delta_n(\mathbf{x}) = b\delta_\rho(\mathbf{x}) \tag{1.14}$$

where $\delta_n(\mathbf{x}) = n(\mathbf{x})/\overline{n} - 1$, $\delta_\rho(\mathbf{x}) = \rho(\mathbf{x})/\overline{\rho} - 1$, and b is the biasing parameter, usually taken to be a constant of the order of 1.

The best available sample for determining the number-density fluctuations, $\delta_n(\mathbf{x})$, is the set of galaxies detected by the Infrared Astronomical Satellite (IRAS) since the IRAS survey is unaffected by dust obscuration, covers almost the whole sky, has well calibrated flux limits, samples to distances beyond 100 Mpc and provides a sufficiently large volume of the universe.

The method of predicting the density fluctuations from the divergence of the velocity field and comparing it to the observed density fluctuations yields the parameter $\lambda \equiv \Omega^{0.6}/b$. Studies of this type typically lead to values of λ in the range 0.6 to 1.2 [25]. Provided that b is not much smaller than unity, this leads to values of Ω between about 0.4 and 1.3.

Geometrical Methods

Because the geometry of the universe depends on Ω, attempts have been made to determine Ω directly by measuring quantities that are sensitive to this geometry. For example, the variation of the apparent luminosity of a standard candle (an object with constant absolute intensity) as a function of redshift will go as $1/r^2$ only in flat space (k=0). Similarly, a change with redshift in the volume element traced by the density of galaxies would be a direct indication of spatial curvature.

The main problem with these geometrical methods is that uncertainties in the evolution of the observed objects usually overwhelm variations due to geometry. Sandage *et al.* [26] attempted to measure the dependence on distance of the apparent luminosity using the brightest galaxy in a cluster as the standard candle. Unfortunately, the galaxy luminosity evolution dominated any geometrical effect. In an attempt to mitigate the evolutionary effects, a new idea has been proposed [27] to use Type Ia supernovae as the standard candle for the luminosity test. The main problem with this approach appears to be the need for a very large amount of telescope time for photometric and spectroscopic measurements.

The volume variation test was first attempted on radio galaxies, counting their number as a function of luminosity, but the radio galaxies evolve too rapidly with redshift. More recent attempts [28] measure the number density of optical galaxies as a function of luminosity, but, again, the results are ambiguous because the luminosities are affected by such things as age and mergers between nearby companions. A better approach to the volume test would be to directly measure the number of galaxies as a function of redshift without relying on the luminosity. This approach was taken by Loh and Spillar [29] but their work has been criticized on many grounds [30] and their result that $\Omega = 0.9^{+0.7}_{-0.5}$ may be affected by large systematic uncertainties. With the operation of the 10-m Keck telescope, a much more reliable determination of the geometry by counting the number of galaxies as a function of redshift should be possible.

1.2.3 The Value of Ω

Although the exact value of Ω has not yet been determined, it is clear that it is close to unity. Since the spatial curvature of a non-flat universe evolves extremely rapidly, it is difficult to understand why our universe is so close to being flat without being exactly flat ($\Omega = 1$). This flatness problem is one of the reasons that many cosmologists favor the inflation hypothesis [31], since it naturally predicts $\Omega = 1$. Inflation also explains why the cosmic microwave background can have basically the same temperature even at points which naively appear causally disconnected. Thus there is a theoretical prejudice for $\Omega = 1$.

Figure 1.1 summarizes the evidence for dark matter discussed in the previous sections. The following general trends are seen in the figure: (i) the dark mass exceeds the luminous mass in virtually all systems of galaxy size or larger; (ii) the ratio of dark to luminous mass generally increases with scale; (iii) on scales larger than about 10 Mpc, the ratio of dark to luminous mass is large enough that the total density could equal or exceed the critical value needed to close the universe.

1.2.4 Nucleosynthesis and Ω_b

Primordial nucleosynthesis provides both the earliest and the most stringent test of the standard cosmology. In 1948, Gamow, Alpher and Herman [32] proposed that all of the elements in the periodic table could be produced in the big bang. It was soon realized, however, that there would be no significant nucleosynthesis beyond ^{7}Li. Since that time, many detailed calculations [33] of the primordial nucleosynthesis of the light elements have been performed. The agreement between the predicted and observed abundances of D, ^{3}He, ^{4}He and ^{7}Li confirms the standard cosmological model and provides a determination [34] of the fraction of critical density contributed by baryons, Ω_b, given by

$$0.009h^{-2} \leq \Omega_b \leq 0.02h^{-2} \tag{1.15}$$

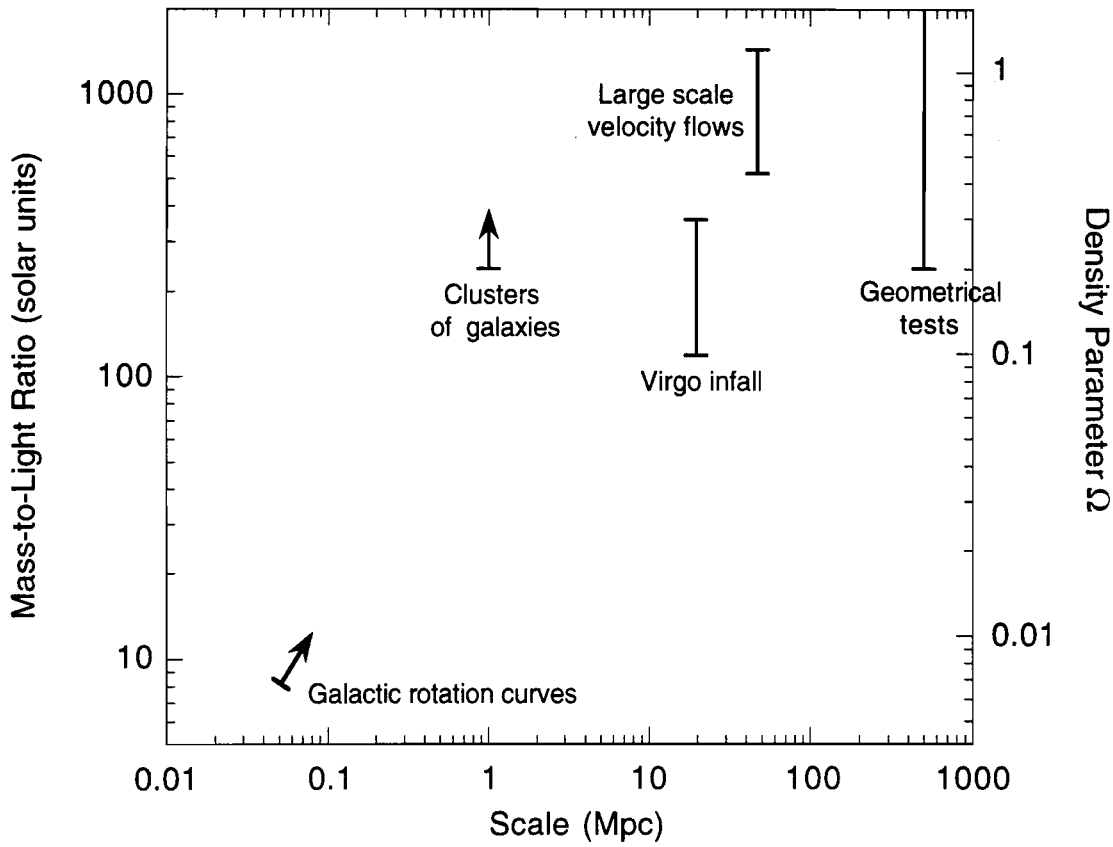

Figure 1.1: Constraints on the mass-to-light ratio, Υ, and the density parameter, Ω, as a function of scale. The relation between Υ and Ω is given by Equation 1.11. The plot assumes the Hubble constant H_0 is 75 km/s/Mpc. The constraint from large scale velocity flows assumes the biasing parameter b is 1. Arrows indicate that only a lower limit has been obtained.

Thus for a generous range for the Hubble constant, $0.4 \leq h \leq 1$, baryons contribute between 1% and 15% of the closure density.

This result has two profound implications. First, since optically luminous matter contributes much less than 1% of the critical density (i.e., $\Omega_{lum} \approx 0.003h^{-1}$ [1]), most baryons must be dark. Second, as discussed earlier in this chapter, there is strong evidence that the average mass density of the universe is considerably greater than 15% of the critical density. If this is indeed the case, then most of the mass density of the universe must be non-baryonic.

1.2.5 Baryonic Dark Matter

The possibilities for baryonic dark matter are somewhat limited as it is difficult to prevent baryons from radiating or absorbing light. For example, clumped hot gas would emit too many x-rays while diffuse hot gas would produce Compton distortions on the cosmic microwave background. Severe limits have been placed on such distortions by COBE observations [35]. Similarly, cold atomic hydrogen gas would have 21 cm emission while molecular hydrogen would lead to an absorption trough in the spectrum of quasars. The absence of this absorption places severe limits the density of neutral hydrogen in intergalactic space [36]. Since dust would absorb light and then re-emit in the infrared, the IRAS survey places severe limits the contribution due to dust.

Instead of being in the form of gas or dust, the baryonic dark matter could be made of condensed objects with masses ranging from that of a large planet to a few $M_\odot$, known collectively as massive compact halo objects (MACHOs) [37], or very massive objects (VMOs) with masses of at least 100 $M_\odot$. MACHOs could be faint stars beyond the detection limit of ground-based observations, brown dwarfs or 'Jupiters' (stars not massive enough to sustain nuclear burning, i.e., $M < 0.08M_\odot$), neutron stars or black holes. Using recent observations with the Hubble Space Telescope, Bahcall *et al.* [38] conclude that faint red stars do not contribute significantly to the mass of our galaxy. Several efforts [39] have

been launched to search for MACHOs using gravitational microlensing [40]. Assuming a simple spherical halo model for our galaxy, like that given by Equation 1.2, with a local dark matter density of $\rho_0 = 0.0079\ M_\odot/\mathrm{pc}^3 = 0.3\ \mathrm{GeV/cm}^3$, early results from the MACHO collaboration [41] suggest that MACHO's may represent 20% of the dark matter in the halo of our galaxy. At a recent meeting of the American Astronomical Society, however, the MACHO collaboration [42] announced that with an additional year of data and improved analyses, they now estimate that MACHO's may represent as much as 50% of the halo dark matter.

1.2.6 Non-Baryonic Dark Matter

Based on the large observed values of Ω, and constraints on the baryon density from primordial nucleosynthesis, there is strong evidence to suggest the existence of non-baryonic dark matter. The most common hypothesis is that this dark matter is made of exotic particles created in the early universe. Two general classes of particles are usually considered: (i) particles produced in thermal equilibrium with the rest of the universe and (ii) particles produced out of thermal equilibrium. For the first class of particles, a distinction is usually made between those particles that were relativistic at the time of freeze out when they decoupled from the rest of the universe, and those particles that were non-relativistic at the time of freeze out.

Axions

The axion [43] is an example of a particle which could have been produced out of equilibrium in the early universe. These particles were originally postulated to solve the problem of CP violation in the strong interactions. The relic abundance of these particles depends totally on the specific model considered. Although there is no guarantee that such particles exist, two experimental searches for axions have been performed [44]. Unfortunately, these first experiments lacked a factor of 1000 in sensitivity for cosmologically

significant axions, but a new experiment currently underway [45] is expected to reach the cosmologically significant region for at least one generic type of axions.

Neutrinos

A light neutrino (i.e., $m_\nu \ll 2$ GeV/c^2) is an example of a particle which could have been produced in thermal equilibrium with the early universe and which was relativistic at the time of freeze out. In this case, the relic mass density is related only to the decoupling temperature and is basically that of the photons in the universe. Therefore, the relic particle density is directly related to its mass, and a neutrino species of 25 eV/c^2 would give Ω of the order of one.

There are currently no good ideas for detecting cosmological neutrinos. There are, however, numerous laboratory experiments underway aimed at measuring the mass of neutrinos through the study of beta decay, neutrinoless double beta decay, and neutrino oscillations.

Weakly Interacting Massive Particles

Weakly Interacting Massive Particles, or WIMPs, are a generic class of particles that were produced in thermal equilibrium with the early universe and were non-relativistic at the time of freeze out. In this case, it can be shown [46] that their present density is a function of their annihilation rate at the time they dropped out of equilibrium (i.e., the freeze out time).

The basic argument is quite simple. In the early universe, the temperature and densities are high enough so that kinetic and chemical equilibrium can be maintained through the annihilation and inverse annihilation reactions between the WIMPs (δ's) and the quarks (q's) and leptons (l's):

$$\delta\bar{\delta} \leftrightarrow q\bar{q} \tag{1.16}$$

$$\delta\bar{\delta} \leftrightarrow l\bar{l} \tag{1.17}$$

As the universe expands and the temperature, T, drops below m_δ, the mass of the WIMP, its equilibrium number density drops exponentially due to the Boltzmann factor, $\exp(-m_\delta/k_B T)$, where k_B is Boltzmann's constant. However, at a certain temperature determined by the annihilation cross-section, the number density of WIMPs becomes too low for annihilation to continue in equilibrium. The number density becomes fixed and the WIMPs "freeze out" with a well determined present-day abundance. If the annihilation rate is much faster than the expansion rate of the universe, and if there is no initial asymmetry between the δ's and the $\bar{\delta}$'s, then all of the WIMPs would disappear and they would not constitute the present dark matter. If, on the other hand, the annihilation rate is too small, the expansion of the universe would quickly dilute the WIMPs to the point where they were unable to find antiparticles to annihilate with and their present abundance would be too large. In order to give the present ratio, Ω_δ, of the average density of WIMPs to the critical density of the universe, the annihilation cross-section for particles with masses in the few GeV/c^2 range is given by [47]

$$\sigma v \sim \frac{10^{-26}}{\Omega_\delta h^2}\ \mathrm{cm}^3/\mathrm{s} \tag{1.18}$$

where h is the Hubble constant in units of 100 km/s/Mpc.

This result is interesting for two reasons. First, for $\Omega_\delta \approx 1$, the annihilation rate has approximately the value expected for weak interactions (hence the name WIMPs), while nowhere in the argument was a particular interaction scale assumed. This may just be a numerical coincidence, but it could also be a hint that physics at the W and Z scale is relevant to the problem of dark matter. Conversely, physics at the W and Z scale naturally leads to particles whose relic density is close to the critical density. The lightest stable particle in supersymmetry models, for example, tends to be in the region of interest for dark matter. Second, the order of magnitude of the interaction rate allows for experimental searches.

1.3 Detecting WIMP Dark Matter

There are two basic experimental methods for searching for WIMPs [48]: (i) direct detection and (ii) indirect detection. In direct detection experiments [49], one looks for the nuclear recoils produced by WIMPs scattering in laboratory detectors. As discussed in Ref. [49], these experiments require detectors with low energy threshold, good energy resolution and excellent background rejection. In indirect detection experiments [50], one looks for the annihilation products presumably produced by WIMPs, such as neutrinos produced by WIMP annihilations in the earth or sun, or high energy gamma rays and antiprotons produced by WIMP annihilations in the galaxy.

1.3.1 First Generation Direct Detection Experiments

The first generation of direct detection experiments used conventional Ge [51] and Si [52] ionization detectors operated at 77 K to look for nuclear recoils produced by WIMPs. As the earth moves through the dark halo of the galaxy, WIMPs are expected to interact elastically with nuclei in the detector producing nuclear recoils. Since the struck atom is usually not ionized after the primary collision, only a small fraction of the recoil energy is transferred into ionization [53]. As a result, the pulse height in an ionization detector from a slow moving nucleus is much smaller than the pulse height due to an electron of the same kinetic energy. By comparing the measured pulse height spectrum with the recoil spectrum expected for a given WIMP model, limits can be placed on the mass and cross-section.

Despite taking extreme care to limit radioactive contamination, the first generation direct detection experiments were eventually limited by radioactive backgrounds. Figure 1.2 shows the low energy portion of the spectrum measured with one of the Oroville Experiment [51, Caldwell *et al.*] germanium detectors. Above the electronics threshold, the measured spectrum is clearly dominated by radioactive backgrounds such as low energy x-ray lines, tritium beta decay and a flat continuum typical of Compton scattering

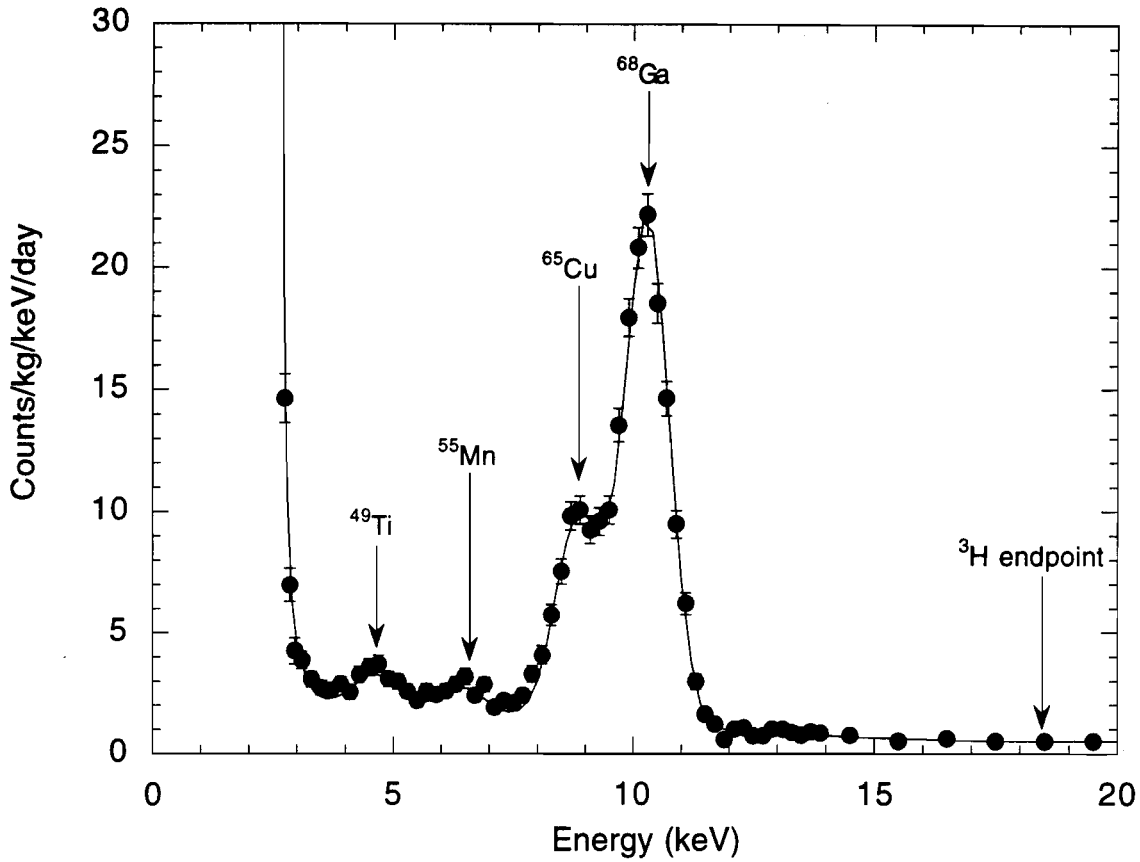

Figure 1.2: Low energy portion of the spectrum measured with one of the Oroville Experiment [51, Caldwell *et al.*] germanium detectors. The points are the measured data. The curve is a fit to the data consisting primarily of a gaussian electronics noise tail, low energy x-ray lines, a tritium beta spectrum and a flat background.

of high energy photons. Despite these backgrounds, the first generation experiments were able to establish limits for WIMPs.

1.3.2 Current Limits

Figure 1.3 shows the low mass region of the current limits for WIMPs. The horizontal axis is the mass of the WIMP and the vertical axis is the total event rate on Ge. The hatched region at the top of the figure is the region that has been excluded by first generation direct detection experiments [54] using Ge ionization detectors. The shaded region at the

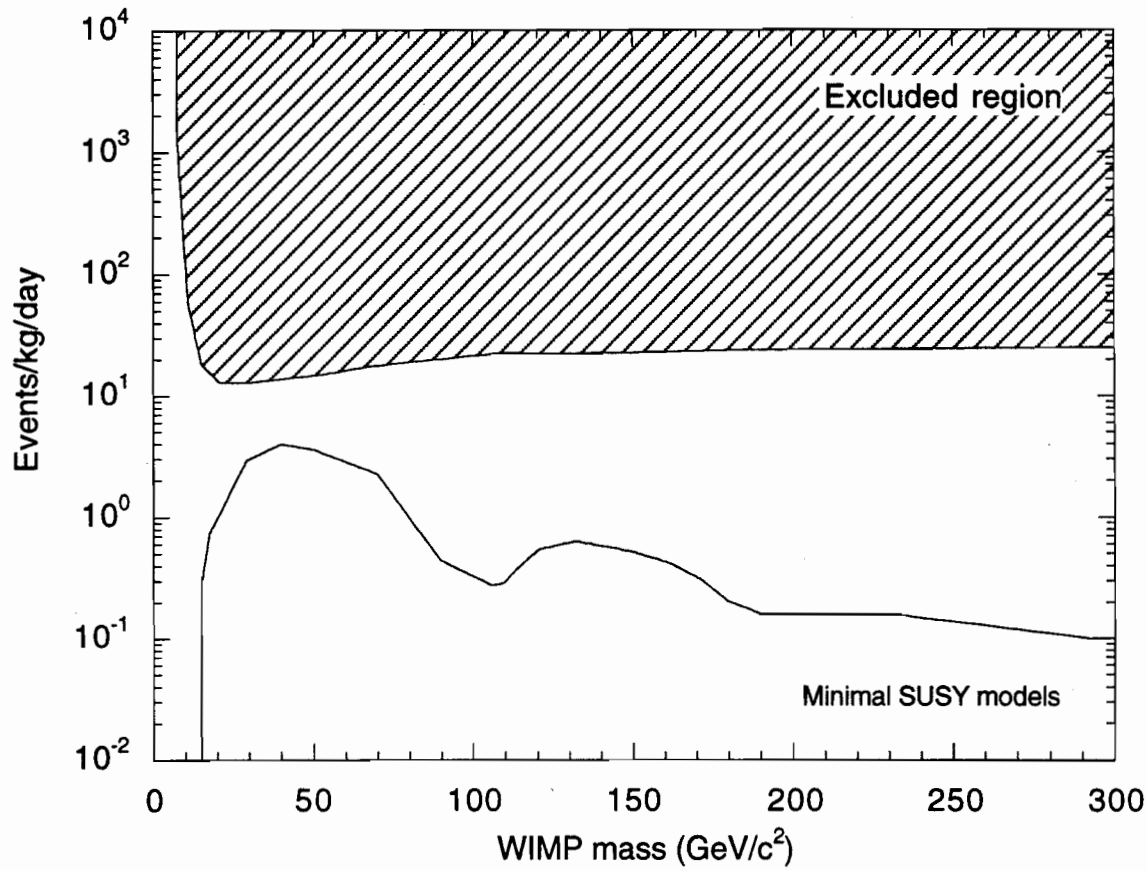

Figure 1.3: Current limits set by first generation direct detection experiments using Ge [51] ionization detectors. The upper hatched region is the region that has been excluded by these experiments [54]. The lower shaded region is the allowed parameter space for various models of the lightest supersymmetric particle [55].

bottom of the figure is the top of the allowed parameter space for various models of the lightest supersymmetric particle [55]. Although the first generation experiments were able to exclude a large region of parameter space, they were not sensitive enough to begin to test theories of the lightest supersymmetric particle.

1.3.3 The Cryogenic Dark Matter Search

As mentioned above, the first generation direct detection experiments were ultimately limited by radioactive backgrounds, such as photons and beta particles, that scatter from

electrons in the detector. In order to increase the sensitivity of these searches, a method of reducing these backgrounds was needed. This requirement led to the emergence of a new generation of experiments.

The Cryogenic Dark Matter Search (CDMS) is one experiment being developed to look for WIMPs. It is based on novel particle detectors operated at millikelvin temperatures that simultaneously measure the ionization and phonon signals produced by interactions in the detectors. Since nuclear recoils of a given phonon energy produce less ionization than electron recoils of the same phonon energy, measurement of both the ionization and phonon signals allows for the discrimination between electron and nuclear recoils. Since WIMPs are expected to scatter from the nuclei, this discrimination capability allows background events from photons and beta particles to be distinguished from WIMP events.

The following chapter discusses the detectors at the center of the CDMS experiment in more detail. Despite the background rejection capability of these detectors, a low background environment is essential for an effective dark matter search. The development of such an environment has been the focus of this thesis work. Chapters 3 and 4 examine the relevant photon and neutron backgrounds respectively, while Chapter 5 examines the issues involved in creating a suitable low background environment for the CDMS experiment. Chapter 6 discusses in more detail the expected dark matter event rate and the expected sensitivity for the CDMS experiment. In conclusion, Chapter 7 discusses the future of the CDMS experiment.

Chapter 2

The CDMS Detectors

As mentioned in the previous chapter, direct detection experiments attempt to detect WIMP interactions in a suitable target material in the laboratory. Detecting these interactions is a difficult task because the energy depositions are expected to be small (a few keV) and the interaction rates are expected to be very low, as low as 0.001 events/kg/day, which is much smaller than the radioactivity occurring in even the purest detector material. As a result, the detectors for this task must have good sensitivity and low internal radioactivity, in addition to active background rejection capabilities.

There has been a great deal of effort in the past several years to develop cryogenic detectors for this formidable task [56]. The motivation behind the cryogenic detector effort has been three-fold. First, cryogenic detectors promise the very low thresholds required to measure the small energy depositions. Second, cryogenic detectors are applicable to a much wider variety of target materials (provided no attempt is made to measure simultaneously ionization or scintillation, in which case the target material is somewhat limited). Third, cryogenic detectors provide active background rejection through the recognition of the nuclear recoils that are expected from WIMP interactions. In general, cryogenic detectors are attractive because they have the potential to provide the maximum amount of information on rare events, information which could be used to identify WIMP inter-

actions and reject background events.

2.1 Principle of Operation

The detector at the heart of the CDMS experiment consists of a disk of single-crystal ultra-pure germanium, which serves as the target for events, maintained at a temperature near 20 mK. When an interaction occurs in the crystal, phonons and electron-hole pairs are generated. By applying a small electric field across the germanium, the ionization yield can be measured. By attaching a thermistor to the germanium, the temperature rise in the crystal due to the interaction can also be measured. With the circuit shown in Figure 2.1, the detectors are capable of measuring simultaneously the amount of ionization and thermal energy produced by particle interactions in the germanium [57, 58]. Since nuclear recoils of a given phonon energy are less ionizing than electron recoils of the same phonon energy, the simultaneous measurement of both the ionization signal and the phonon signal allows for discrimination between electron recoils and nuclear recoils. Distinguishing between these two types of interactions allows for active background rejection since WIMPs are expected to scatter from the nucleus, while radioactive backgrounds, such as photons and beta particles, interact with the electrons.

2.1.1 Phonon Measurement

The total energy deposited in the germanium is measured calorimetrically: the energy deposition in the crystal causes a rise in the bulk crystal temperature given by

$$\delta T = \frac{E}{C} \tag{2.1}$$

where δT is the change in crystal temperature, E is the energy deposited in the crystal, and C is the heat capacity of the crystal. From Equation 2.1 it is clear that the heat capacity of the crystal should be minimized in order to maximize the temperature change for a given energy deposition. The heat capacity of a pure semiconductor is dominated

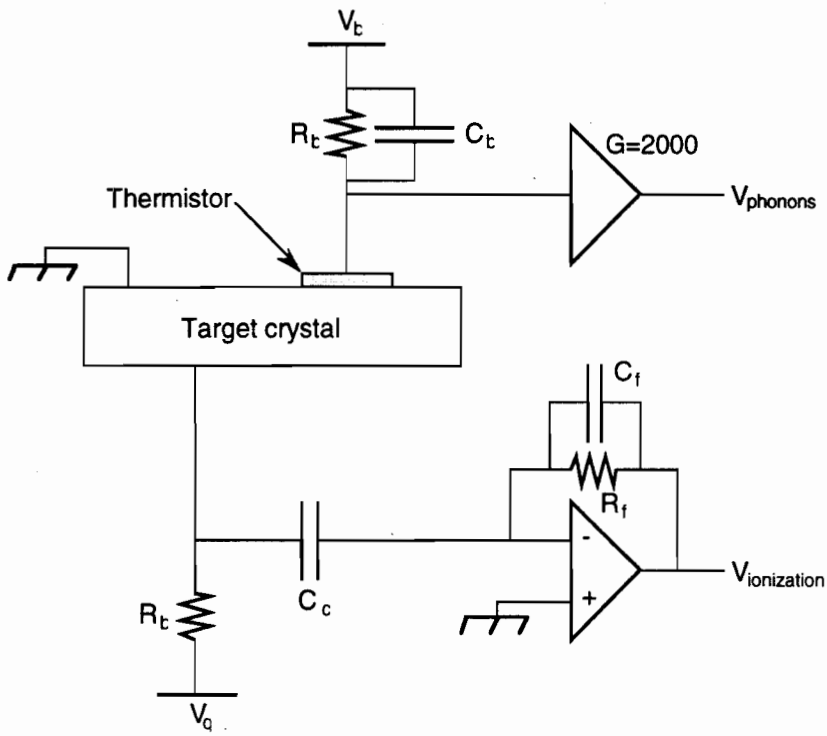

Figure 2.1: Schematic diagram of the combined phonon and ionization measurement circuits connected to the detector.

by the contributions from phonons and at low temperatures, is well approximated by the Debye law:

$$C = 233.8 N k_B \left(\frac{T}{\theta}\right)^3 \tag{2.2}$$

where N is the number of atoms, k_B is Boltzmann's constant and θ is the Debye temperature. For germanium, $\theta = 374$ K, so the heat capacity of a germanium crystal of mass M (in grams) at a temperature T (in Kelvin) is given by

$$C = 5.1 \times 10^{-7} \left(\frac{M}{\mathrm{g}}\right) \left(\frac{T}{\mathrm{K}}\right)^3 \mathrm{J/K} = 3.2 \times 10^{12} \left(\frac{M}{\mathrm{g}}\right) \left(\frac{T}{\mathrm{K}}\right)^3 \mathrm{eV/K} \tag{2.3}$$

It follows from Equations 2.1 and 2.3, that in order for a massive ($\sim$ 100 g) germanium detector to be sensitive to energy depositions of the order of a few keV, it must be operated at millikelvin temperatures. For example, an energy deposition of 5 keV in a 100 g germanium detector operated at 10 mK will result in a temperature change of 15.6 μK, which can be readily measured with a sensitive thermometer.

Neutron transmutation doped (NTD) germanium thermistors [59] are used as the thermal sensors for the phonon measurement. Since the electrical conductivity of highly doped semiconductors at low temperatures is expected to be dominated by variable-range-hopping [60], the zero bias resistance of the NTD Ge thermistor as a function of temperature is given by

$$R(T) = R_0 \exp\left[(\Delta/T)^{1/2}\right] \tag{2.4}$$

where R_0 and Δ are constants which depend on the doping and sample preparation [62] and T is the temperature. As a result, these highly doped NTD Ge thermistors are very sensitive to small temperature changes. At very low temperatures, however, the electrons in the thermistor thermally decouple from the phonons in the thermistor when power is applied to the electron system [61, 62]. In this case, the system comes to a steady state where the electron temperature, T_e, and the phonon temperature, T_φ, are empirically related to the applied power, P, by

$$P = g_{e\varphi}(T_e^\alpha - T_\varphi^\alpha) \tag{2.5}$$

and the parameters $g_{e\varphi}$ and α are determined experimentally. Equation 2.4 remains valid provided that the temperature is taken to be the electron temperature given by Equation 2.5. The behavior of the NTD Ge thermistors used was found to be well described with $\alpha = 6$ [61, 62].

The thermal and electrical properties of the NTD Ge thermistors are strongly affected by mechanical stress. Conventional glue bonding techniques typically lead to high levels of mechanical stress which can make the thermistors unreliable. In order to minimize the level of stress, the NTD Ge thermistors are attached to the germanium crystal using a eutectic bonding technique [62]. This technique is based upon the fact that a mixture of gold and germanium will melt into a liquid phase at a temperature well below the melting temperature of either element alone. A thin layer of gold ($\sim$ 1000 Å) is evaporated onto the optically polished bonding surfaces of the thermistor and the target crystal. In order to enhance the adhesion of the gold to the germanium, a 200 Å thick palladium layer is deposited onto the germanium immediately prior to the gold deposition. The gold contains 2% gallium (by weight) to insure a uniform electrical contact across the bonding area. The gold-coated germanium pieces are then pressed together under vacuum and heated to 380 °C, just above the Au-Ge eutectic temperature ($T_{eu} = 356$ °C) where the Au-Ge alloy becomes liquid. As the sample cools below the eutectic temperature, the Au-Ge mixture solidifies, bonding the two pieces together. The resulting eutectic bonds are shown to be mechanically strong, able to survive low temperatures and thermal cycling, and more transparent to non-thermal phonons than conventional glue bonds [62]. Furthermore, the eutectic bonding process does not change the thermal and electrical properties of the NTD Ge thermistors.

The circuit shown in Figure 2.2 allows for a relatively straightforward voltage measurement of the phonon signal. The resistance of the thermistor changes when its temperature changes. Since the bias resistor, R_b (typically 10 MΩ), is much larger than the resistance of the thermistor, r, the current through the sensor is approximately constant and given by $I = V_b/R_b$ where V_b is the bias voltage. A change in the resistance of the thermistor,

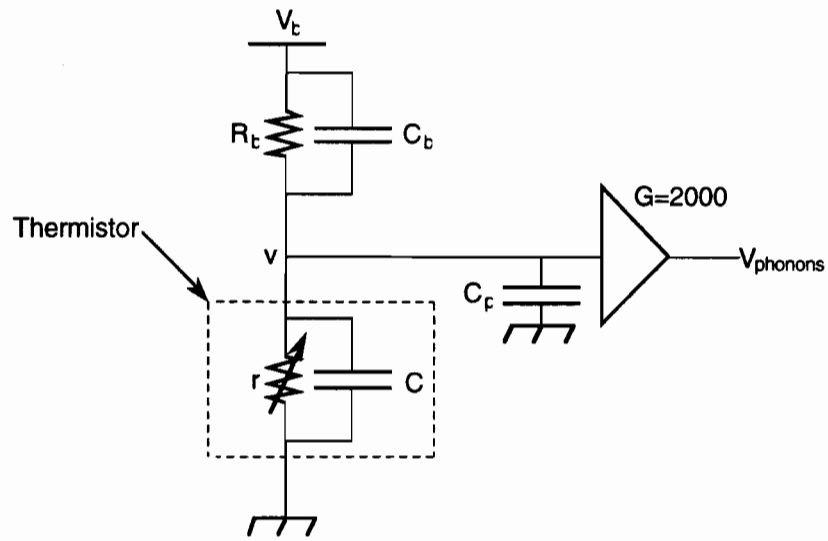

Figure 2.2: Schematic diagram of the circuit for the voltage measurement of the phonon sensor.

δr, due to an event in the crystal is measured as a change in voltage given by $\delta v = I\delta r$. Typical phonon pulses have rise times of the order of 0.5 ms and fall times of the order of 50 ms. Because of the relatively long phonon pulses, low background rates are required to prevent event pile-up.

To avoid microphonics and $1/f$ noise in the phonon measurement, the AC biasing scheme shown in Figure 2.3 is used [63]. The thermistor is biased with a sinusoidal voltage and the signal is mixed with a reference signal of frequency f_0 at the appropriate phase. The mixing process leaves half of the signal at its normal frequency while the other half appears as the amplitude of a signal at $2f_0$. A steep (8 pole Bessel) filter with a cut-off frequency higher than changes of interest in $r(t)$, but well below $2f_0$, is then used to remove the $2f_0$ term. Since the noise signal is not affected by the sinusoidally varying bias, the mixing process effectively separates the noise into a component at $f + f_0$ and a component at $f - f_0$. Thus the noise at low frequencies after mixing is the sum of the noise just above and just below the reference frequency before mixing. By choosing the reference frequency to be outside the range where microphonics noise dominates, this

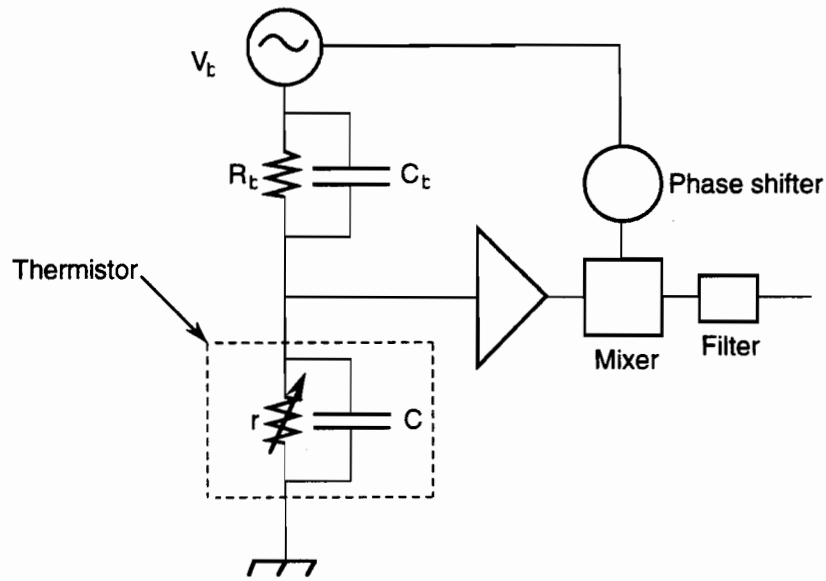

Figure 2.3: Schematic diagram of the AC biasing scheme used for the phonon measurement.

noise can be effectively removed.

2.1.2 Ionization Measurement

The charge measurement is quite different from the phonon measurement. As shown in Figure 2.4, the amplifier acts through a feedback network to keep its input at a virtual ground. This virtual ground acts with the bias V_q on the other side of the detector to create an electric field across the detector. Electrons and holes created by interactions in the detector are drifted by the field to the implanted contacts at the two crystal faces. The bias supplies image charge to the top plane of the detector to hold the top contact at a constant voltage as the charge drifts out and the amplifier supplies image charge to the bottom plane of the detector to maintain the ground voltage. In order to drive this image current through the feedback network, the output of the amplifier has to change, and this change is the signal measured. In this way, the charge, Q, produced by an event in the detector is integrated on the feedback capacitor, C_f, and the voltage at the output

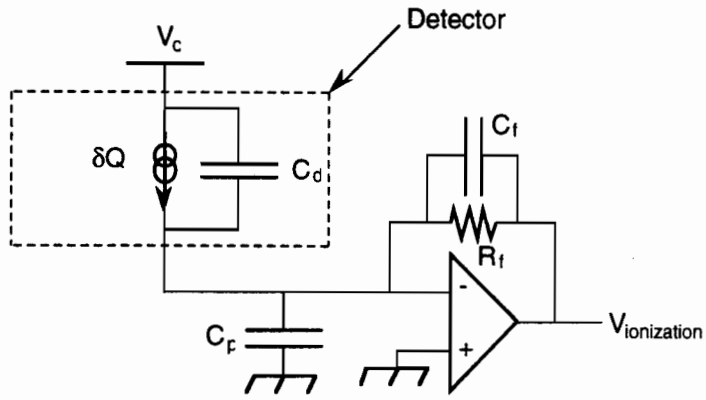

Figure 2.4: Schematic diagram of the circuit for the charge measurement.

as a function of time is given by

$$\delta v(t) = -\frac{Q}{C_f} \exp\left(-\frac{t}{R_f C_f}\right) \tag{2.6}$$

where R_f is the feedback resistance. The rise time of the ionization signal is limited by the amplifier rise time of about 1 μs. The fall time of the pulse is determined by the time constant of the feedback network, $\tau_f = R_f C_f$, which is about 40 μs.

It is inconvenient to combine the phonon and charge measurements on the same device using the exact configurations shown in Figures 2.2 and 2.4. One contact of the detector must serve as the ground (or at least a fixed voltage) for the phonon measurement while at the same time helping to define the bias voltage for the ionization collection. If the ionization is collected on this surface, then changes in the current through the thermistor during an event will also be measured in the charge circuit. To avoid this problem, the two measurements are combined using the circuit shown in Figure 2.1. The ionization amplifier is coupled through a capacitor C_c to the side of the detector that is biased for ionization. Charge flowing to the detector on time scales faster than the roll-off time constant of the bias circuit ($\tau = R_b C_c \approx 5$ ms) passes through C_c to the amplifier circuit and is measured without distortion. Signals slower than this pass across the bias resistor R_b and are not measured.

The simultaneous phonon measurement introduces a further complication for the ionization measurement. To effect complete or near-complete charge collection and avoid trapping or recombination of the charge pairs within the crystal, one would like to use a relatively large bias voltage. However, as N_Q charges are drifted out of the crystal by a bias voltage V, they deposit energy in the form of phonons in the crystal given by

$$E = eN_QV \tag{2.7}$$

where e is the elementary electron charge. For germanium, where one charge pair is produced for every 3 eV of photon energy, the energy deposited by the drifting charge with a 3 V bias would equal the phonon energy from the initial interaction. For much larger bias voltages, the resulting drift heat would dwarf the phonon signal from the initial interaction that one is trying to measure. Therefore, the charge must be collected with a relatively small bias voltage and the total measured phonon energy, E_m, becomes

$$E_m = E_\phi + eN_QV \tag{2.8}$$

where E_ϕ is the phonon energy created by the initial interaction. For the detectors discussed here, the entire recoil energy, E_r, eventually appears as phonons in the detector due to the relaxation of the drifted charges at the ionization contacts [58]; hence $E_\phi = E_r$.

2.1.3 Background Rejection Capability

The electron/nuclear recoil discrimination capability of such a detector has been demonstrated using a 60 g prototype germanium detector [64]. The detector consists of a high purity p-type germanium disk, 3.6 cm in diameter and 1.2 cm thick, with a net dopant concentration of $n_a - n_d \approx 6 \times 10^{11}$ cm^{-3}. The thermal energy is measured with two NTD Ge thermistors attached to the crystal using the eutectic bonding technique described in Section 2.1.1. One of the thermistors is 2.9 mm × 3.0 mm × 1.2 mm and the other is 1.6 mm × 1.6 mm × 0.3 mm. For the ionization measurement, degenerately-doped p$^+$ contact layers are made on the top and bottom faces of the crystal by implanting the

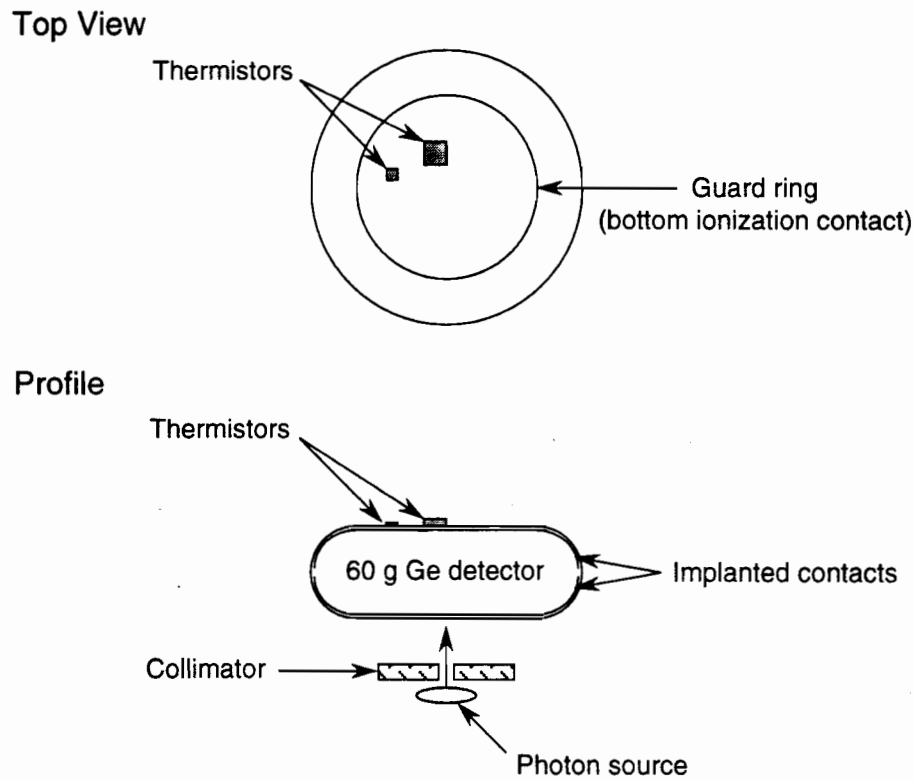

Figure 2.5: Schematic diagram of the 60 g prototype germanium detector along with the collimator and photon source used for the measurements.

p-type germanium with boron ions to a depth of about 2000 Å. In earlier devices [57], the discrimination capability was limited by events near the perimeter of the detector with incomplete charge collection, presumably due to the build-up of charges on the outer surface of the detector that cancel the applied field. To improve the charge collection in the device, the edges of the crystal have been rounded and the implants wrap around the end of the detector, leaving only a small (0.5 mm) gap between the upper and lower contact (see Figure 2.5). A circular break, or guard ring, is made in the lower ionization contact by etching through the implant. The resulting "inner" and "outer" ionization channels provide limited position resolution, i.e., events that occur in the central region of the detector can be distinguished from events that occur near the perimeter of the detector. The total ionization produced by an interaction is given by the sum of the two signals.

The detector is operated in a dilution refrigerator at a temperature near 20 mK and is exposed to 60 keV photons from a collimated ^{241}Am source. The measured FWHM resolution in the phonon signal is 700 ± 35 eV at 60 keV and 495 ± 35 eV on the baseline. The baseline peak is obtained by a template fit to random noise triggers, and is therefore a measure of the electronics noise. The measured FWHM resolution in the ionization signal is 1600 ± 50 eV at 60 keV and 1200 ± 50 eV on the baseline.

The scatter plots of the phonon and ionization measurements shown in Figure 2.6 illustrate the electron/nuclear recoil discrimination capability of the detector. Because the partitioning of energy between phonons and ionization is different for electron recoils and nuclear recoils, the energy measurements are usually defined in terms of "electron equivalent energy", i.e., both measurements are calibrated in terms of the energy of a recoiling electron. So, by definition, a 60 keV photon that is totally absorbed in the crystal has 60 keV of "equivalent ionization energy" and 60 keV of "equivalent phonon energy" while a nucleus recoiling with 60 keV of energy has less than 60 keV of equivalent ionization energy and more than 60 keV of equivalent phonon energy. Thus, in a plot of equivalent phonon energy versus equivalent ionization energy, photon events appear on a

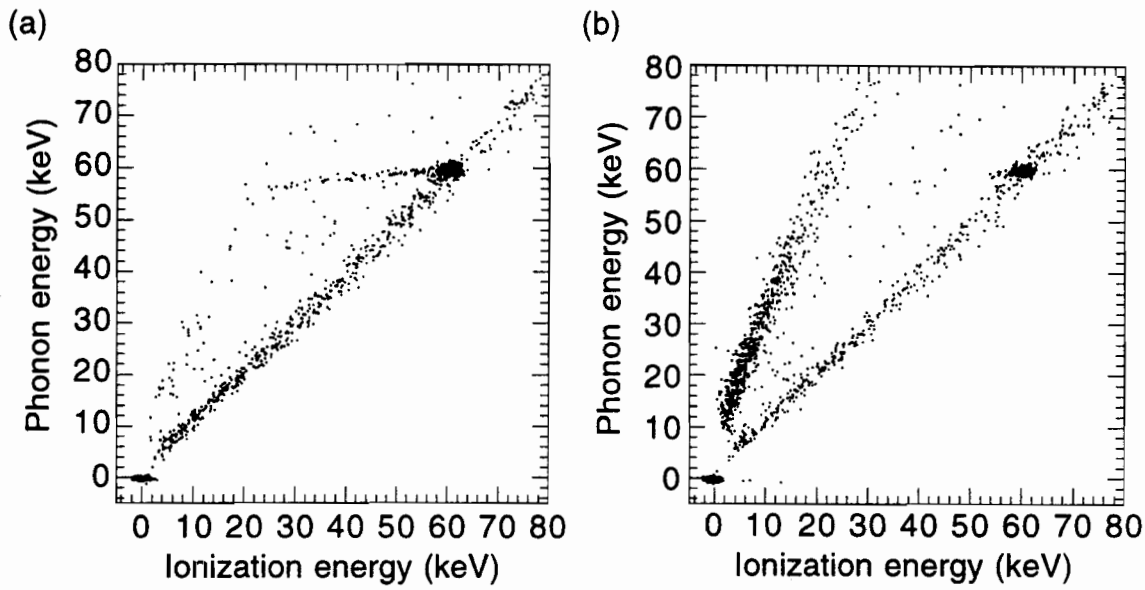

Figure 2.6: Scatter plot of the phonon measurement versus the ionization measurement for the 60 g prototype germanium detector. (a) is obtained with the detector exposed to 60 keV photons from a ^{241}Am source and broad-band background radiation. (b) is obtained with the detector exposed to photons and neutrons from a ^{252}Cf source in addition to the sources used in (a). Both the phonon and the ionization measurements are normalized to electron equivalent energy.

line at a slope of one, while nuclear recoil events appear on a line at a higher slope. The value of the slope is determined by the relative ionization yield

$$R = \frac{N_{Q,n}(E_r)}{N_{Q,e}(E_r)} \tag{2.9}$$

i.e., the ratio of the amount of ionization produced by nuclear recoils, $N_{Q,n}(E_r)$, to the amount of ionization produced by electron recoils, $N_{Q,e}(E_r)$, for a given recoil energy, E_r. The relative ionization yield is not linear at low energies, and in general, must be measured as a function of recoil energy.

Figure 2.6(a) is obtained with the detector exposed to 60 keV photons from a ^{241}Am source and broad-band background radiation. The 60 keV peak is clearly visible and, as expected, most of the events lie along the diagonal since they are mainly electron recoils caused by photon interactions in the crystal. The tail on the 60 keV peak is most likely due to incomplete charge collection for those events which occur in the dead layer a few tens of microns underneath the implanted contacts. Figure 2.6(b) is obtained with the detector exposed to photons and neutrons from a ^{252}Cf source in addition to the sources used in (a). The distribution of less-ionizing nuclear recoils produced by neutron interactions in the crystal is clearly distinguishable from the photon distribution. Comparison of the two figures suggests that there are some background neutrons present even without the ^{252}Cf source. This is not totally unexpected since the experiment was performed in an above ground laboratory with no external neutron shielding. The events that appear between the two distributions are presumably due to incomplete charge collection for photon interactions which occur in the dead layer.

The background rejection efficiency of the detector can be determined from the distribution of the ratio of ionization energy to phonon energy. This distribution is shown in Figure 2.7 for those events in Figure 2.6 with total recoil energies between 10 keV and 30 keV. Since both the phonon and ionization measurements are normalized to electron equivalent energies, the photon events produce a peak at a ratio of 1. The neutrons produce a peak at a ratio of 0.3, which is simply the relative ionization yield. The efficiency

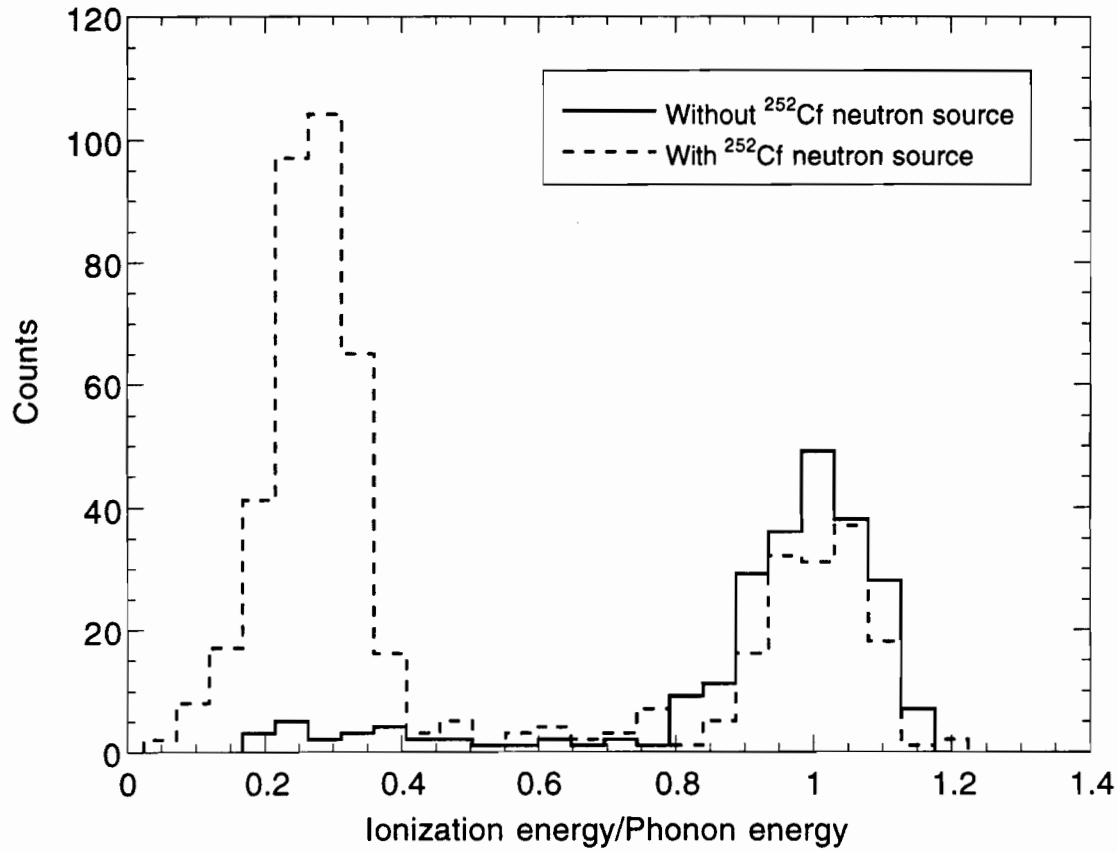

Figure 2.7: Distribution of the ratio of phonon energy to ionization energy for those events in Figure 2.6 with total recoil energies between 10 keV and 30 keV. Photons produce the peak at a ratio of 1 because both the phonon and ionization measurements are normalized to electron equivalent energies. The peak at a ratio of 0.3 is produced by the less-ionizing nuclear recoil events caused by the neutrons.

for rejecting events caused by electron recoils is given by

$$\epsilon = 1 - \frac{N_{nr}}{N_{er}} \tag{2.10}$$

where N_{nr} is the number of events in the nuclear recoil peak without the neutron source and N_{er} is the number of events in the electron recoil peak without the neutron source. In general, the rejection efficiency is a function of energy and it is not linear at low recoil energies.

For the data shown in Figure 2.7, Equation 2.10 gives a rejection efficiency of $\epsilon >$ 93% for events with recoil energies between 10 keV and 30 keV. Because there are some background neutrons present even without the neutron source, only a lower limit on the rejection efficiency can be determined. To determine the true rejection efficiency of the detector, the detector must be shielded from these background neutrons. At higher energies, the rejection efficiency improves to better than 99%. With some optimization, a rejection efficiency of 99% all the way down to threshold should be possible, but this has yet to be demonstrated.

2.2 The BLIP Detector

A larger version of the 60 g prototype germanium detector will be used for the CDMS experiment. The Berkeley Large Ionization and Phonon (BLIP) detector consists of a disk of high purity germanium ($n_a - n_d \approx 6 \times 10^{10}$ cm^{-3}), 6 cm in diameter and 1.2 cm thick. To minimize the production of cosmogenic activity in the detector, the germanium has been stored underground as much as possible. Two NTD Ge thermistors (3.1 mm × 3.1 mm × 2.6 mm) are eutectically bonded to one face of the germanium crystal. Two phonon sensors are used so that events which occur directly in a sensor can be distinguished from events which occur in the target crystal. Degenerately-doped ionization contacts are made on either side of the crystal by implanting boron ions to a depth of about 2000 Å. As with the prototype detector, the edges of the disk are rounded and the implanted

contacts wrap around the end of the detector. "Inner" and "outer" ionization channels are made by etching a guard ring through the bottom ionization contact. The resulting BLIP detector has a mass of 170 g.

2.3 Tower Geometry

Because of the low event rate expected for WIMPs, an efficient search requires a large detector mass. In order to increase the detector mass without making significant changes to the design used for the prototype detector, a multiple detector system will be used. A stack of six BLIP detectors will be mounted in a single modular package, called a "tower", providing an active detector mass of 1 kg. In addition to the detectors, the tower also houses the detector wiring and cold amplifier components. With this modular design, the detector package can be constructed on the bench and tested as a complete assembly before being installed in the experiment. Details of the tower design are discussed in Section 5.3.3.

One of the advantages of the modular design is that it allows for incremental upgrades in the experiment. The search can begin as soon as the first tower of detectors is operational, and as more detectors are produced, additional towers can be constructed and installed. Further detector development can continue in parallel with the experiment and when improved detector technology is developed, towers can be easily replaced with new towers that incorporate the advanced detectors.

Operating multiple detectors also provides some background rejection capabilities. Because of the low interaction cross-section, a WIMP will scatter in only one detector. Background photons and neutrons, however, may interact in multiple detectors. Thus, by rejecting events that occur in multiple detectors, the background rate is reduced while the signal rate is unaffected. Multiple detectors may also help in localizing internal radioactive contamination by comparing the background spectra measured in the individual detectors. Once localized, the source of contamination could be removed thereby reducing the local

background. These background rejection capabilities are discussed further in Sections 5.4 and 5.5.

2.4 Advanced Detectors

The capabilities of the CDMS experiment may be increased through the use of advanced detectors. If more information is available for each event, it may allow for the rejection of additional background events. For example, with position resolution, an interior fiducial volume could be established, eliminating the low energy radioactive background events which may occur in the dead layer of the detector. Position information could also be used to veto multiple-scattering events caused by radioactive backgrounds. Additional information about each event may be provided by detectors that are sensitive to non-equilibrium phonons.

As part of the CDMS collaboration, a group at Stanford University is currently developing detectors sensitive to non-equilibrium phonons that will eventually be used in the CDMS experiment. These devices, called W/Al QET's (quasiparticle-trap-assisted electrothermal feedback transition-edge sensors), use composite superconducting thin-film tungsten and aluminum transition edge sensors deposited on high purity silicon absorbers [65]. When a particle interaction occurs in the silicon, athermal phonons propagate to the surface of the crystal where they are absorbed in the superconducting aluminum film. Since the gap of aluminum ($2\Delta_{\mathrm{Al}} \sim 0.3$ meV) is smaller than the mean athermal phonon energy ($E \sim 2$ meV), incident athermal phonons create quasiparticles in the aluminum film. These quasiparticles diffuse to the tungsten on times that are short compared to the quasiparticle recombination time. Since tungsten has a lower gap than aluminum ($2\Delta_{\mathrm{W}} \sim 0.024$ meV), the quasiparticles become trapped in the tungsten and the energy is rapidly thermalized. This raises the temperature of the tungsten, increasing the resistance of the film and therefore decreasing the current through it. The resulting current pulse, measured with a SQUID array [66] connected in series with the tungsten

film, is approximately 100 ms in duration.

The tungsten film is patterned into 200 parallel line segments. Each line segment consists of a meander pattern 2 μm wide and 800 μm long. Eight superconducting aluminum thin-film phonon collection pads are electrically connected along equal intervals of each tungsten line as illustrated in Figure 2.8. The aluminum phonon collection pads make it possible to cover large surface areas without increasing the sensor heat capacity, allowing for larger absorbers and reducing the phonon collection times. The tungsten lines are stably voltage biased near the center of their resistive transition ($T_c \sim 80$ mK) through Joule self-heating and electrothermal feedback [67]. The substrate is cooled well below T_c. In the extreme electrothermal feedback limit, all the energy from an event that is absorbed by the tungsten is removed by a reduction in Joule heating, and therefore, the energy absorbed by the tungsten is given by the integral of the signal current times the bias voltage with no free parameters.

All aspects of the W/Al QET detectors have been demonstrated [65, 68] in small prototype silicon crystals (0.25 g to 4 g) with up to four W/Al QET sensors. By operating multiple channels and observing the partitioning of energy between the channels, both event position and energy can be determined. The Stanford group has also demonstrated electron/hole collection through high-purity 1-cm-thick silicon crystals as well as electron/nuclear recoil discrimination in silicon using W/Al QETs phonon sensors and Shottky-barrier ionization sensors [69].

Based on this technology, large mass silicon and germanium detectors are being designed for the CDMS experiment. The detectors will be 7.6 cm in diameter and 1 cm thick. This is the largest diameter that can be accommodated by the towers. Silicon detectors of this size will have a mass of 100 g while the germanium detectors will have a mass of 250 g. One tower will be able to house 6 detectors. Each detector will have two ionization channels on one face, and four W/Al QET phonon channels on the opposite face as shown in Figure 2.9. The six channels will provide sub-μsec timing, event localization and electron recoil versus nuclear recoil discrimination. With this information,

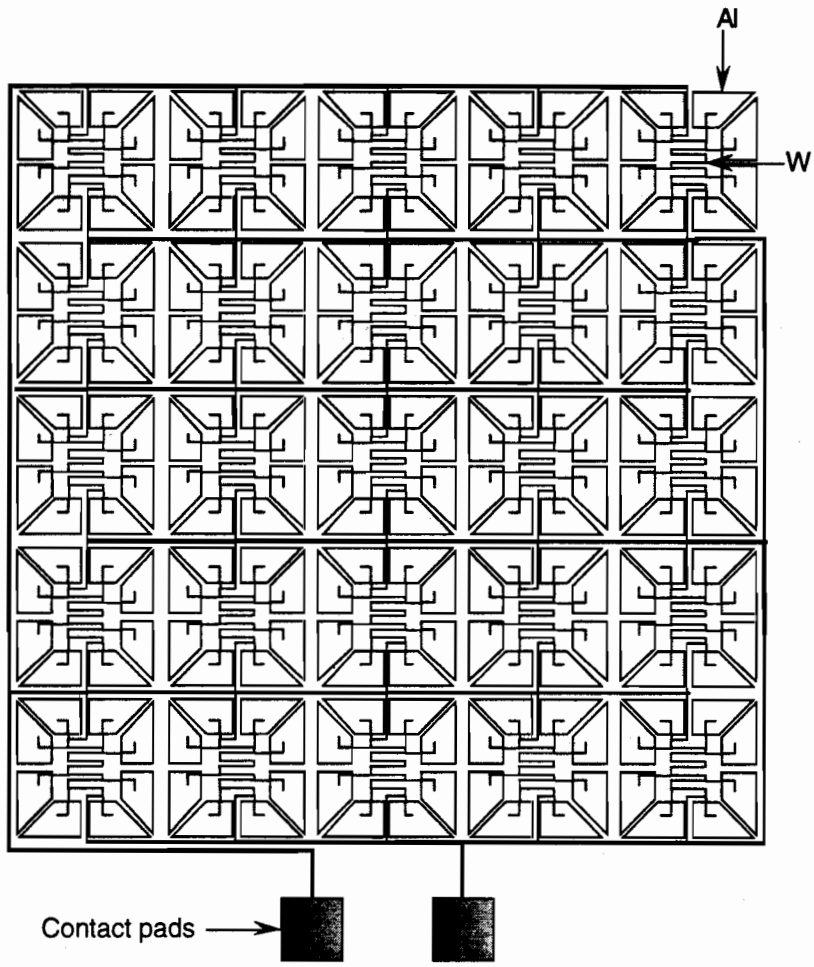

Figure 2.8: Schematic diagram of 25 elements of a W/Al QET. Eight aluminum phonon collection pads (light shaded regions) are electrically connected along equal intervals to each tungsten line. The elements are connected in parallel by aluminum bars connected to aluminum contact pads. Each W/Al QET sensor is made up of 200 such elements.

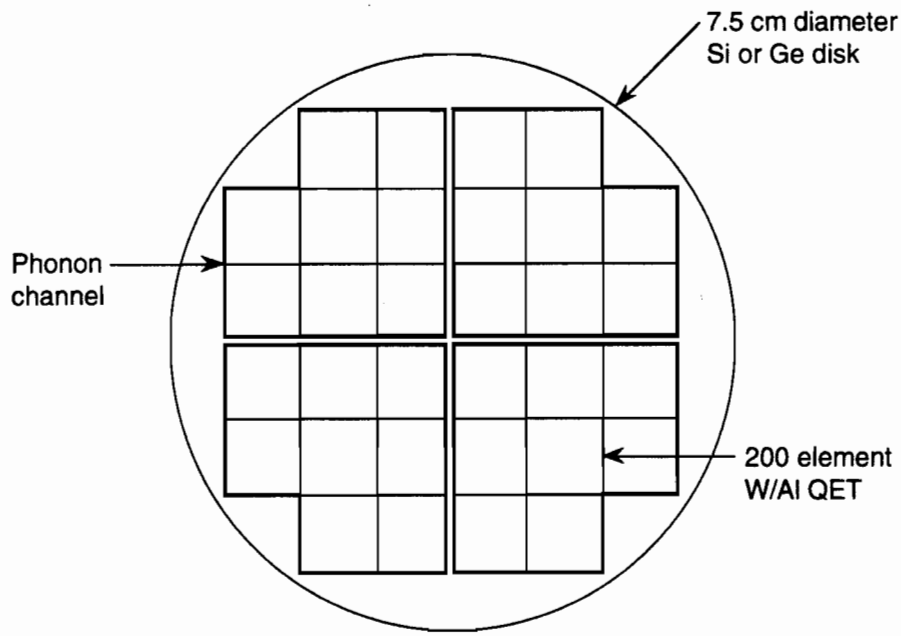

Figure 2.9: Schematic diagram of a full size detector utilizing W/Al QET phonon sensors. The heavy lines delineate the 4 phonon channels, each of which consist of 8 W/Al QET sensors. Each of the W/Al QET sensors consists of 200 parallel elements like those shown in Figure 2.8.

a more sensitive dark matter search should be possible. However, large-scale prototype W/Al QET detectors must be constructed and tested before any improvements can be quantified. Furthermore, since it will be some time before the full-sized W/Al QET detectors are ready for operation, the CDMS experiment will begin with the BLIP detectors. Therefore, throughout the remainder of this thesis, discussions pertaining to the CDMS detectors generally refer to the BLIP detectors.

Chapter 3

Photon Backgrounds

Before an effective effort toward creating a low background environment can be made, a thorough understanding of the background sources is necessary. Many of the possible background sources are illustrated schematically in Figure 3.1. In this chapter, the photon backgrounds are examined in detail. Neutron backgrounds are examined in the following chapter.

3.1 Sources of Background Photons

The sources of background photons can be divided into two broad categories: environmental radioactivity; and radiocontaminants in the detector and shielding materials. In both categories, cosmic rays can contribute to photon backgrounds. These sources of background photons are discussed in detail in the following sections.

3.1.1 Environmental Radioactivity

Radionuclides in our environment are either primordial, cosmogenic or man-made. The main source of gamma radiation stems from the uranium and thorium series and from the decay of ^{40}K. Figure 3.2 shows the decay chains for the uranium and thorium series. After

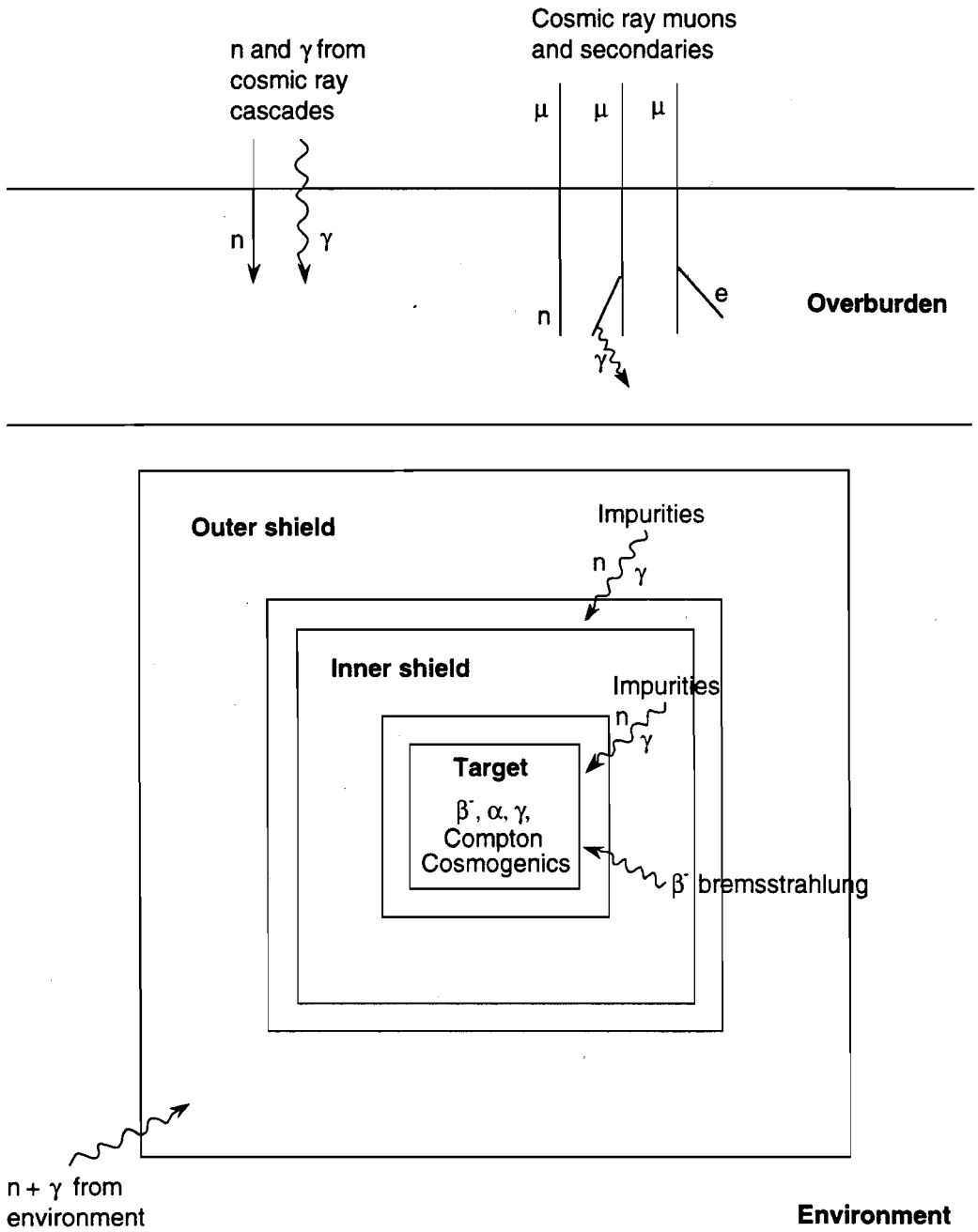

Figure 3.1: Background sources for an underground experiment.

a series of alpha and beta decays, the chains terminate at the stable lead isotopes ^{206}Pb and ^{208}Pb respectively. Secular equilibrium occurs when the parent has an extremely long half-life so that the daughter builds up to an equilibrium amount and then decays at effectively a constant rate. In the uranium and thorium series, the entire chain reaches secular equilibrium when all the elements in the chain are in secular equilibrium. In this case, each of the descendants has built up to an equilibrium amount and they all decay at the rate set by the original parent. Table 3.1 lists the dominant gamma rays emitted in the uranium and thorium chains. The intensity of each line refers to the absolute number of gamma rays emitted per 100 disintegrations of the parent isotope. When the chain is in secular equilibrium, the activities of all daughter nuclides are equal to the activity of their respective parents, so the listed intensities for each isotope refers to 100 disintegrations of the nuclide at the start of the chain (^{238}U and ^{232}Th respectively).

The other dominant source of primordial gamma radiation is potassium. Natural potassium contains 0.0117% ^{40}K, which decays via beta-decay (89.3%) and electron capture (10.67%). The electron capture is accompanied by the emission of a 1460.832 keV γ-ray.

The level of contamination of radionuclides is typically given as either concentration by weight, such as 10^{-9} gU/g or ppb U, or in units of Bq/kg. The conversion factors for the primordial nuclides are given below:

$$1 \text{ Bq } ^{238}\text{U/kg} = 81 \times 10^{-9} \text{ gU/g (81 ppb U)}$$
$$1 \text{ Bq } ^{232}\text{Th/kg} = 246 \times 10^{-9} \text{ gTh/g (246 ppb Th)}$$
$$1 \text{ Bq } ^{40}\text{K/kg} = 32.3 \times 10^{-6} \text{ gK/g (32.3 ppm K)}.$$

The uranium and thorium concentration found in rock varies substantially, depending on composition. Feige [71] takes as representative of the earth's crust [72], a uranium and thorium concentration of 37 Bq/kg and 45 Bq/kg respectively, while Florkowski *et al.* [73] give typical values of 62 Bq/kg (U) and 45 Bq/kg (Th) for granite, 12 Bq/kg (U) and 4 Bq/kg (Th) for limestone and sandstone, and 3 Bq/kg (U) and 8 Bq/kg (Th) for salt.

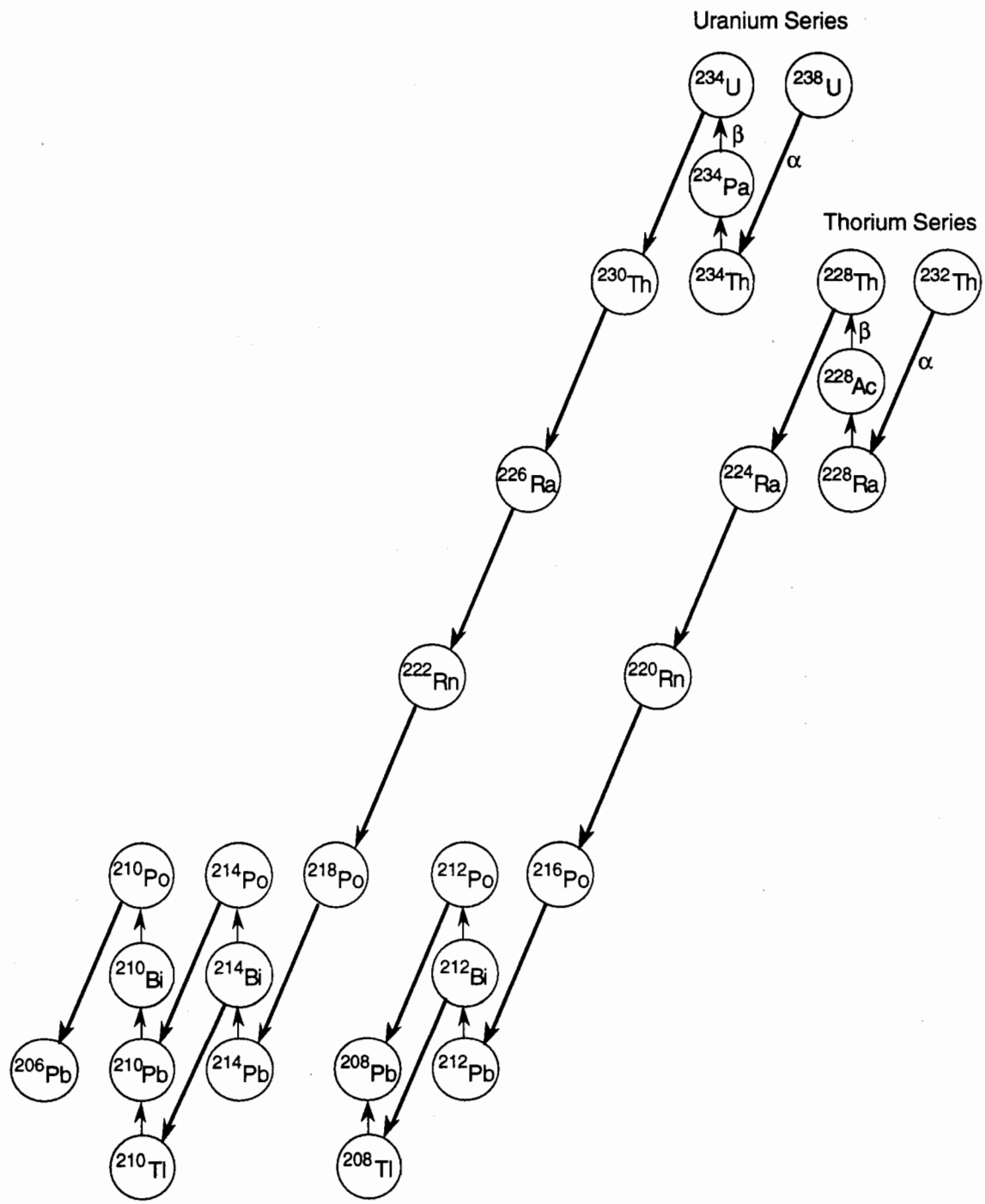

Figure 3.2: Decay chains for the uranium and thorium series. Alpha decays are indicated by diagonal lines and beta decays are shown as short vertical lines. The chains terminate at the stable lead isotopes ^{206}Pb and ^{208}Pb respectively.

Table 3.1: Dominant photon lines (intensity > 1%) in the uranium and thorium decay chains. Data taken from [70].

Uranium Chain			Thorium Chain		
Nuclide	Energy (keV)	Intensity (%)	Nuclide	Energy (keV)	Intensity (%)
^{234}Th	63.288	3.8	^{228}Th	84.26	1.21
	92.35	2.72	^{228}Ac	89.955	3.4
	92.78	2.69		93.35	5.6
^{226}Ra	186.11	3.28		99.55	1.3
^{214}Pb	53.172	1.10		105.362	2.0
	74.814	6.52		129.03	2.9
	77.107	11.0		209.39	4.1
	87.19	3.88		270.26	3.8
	90.128	1.15		328.07	3.5
	241.92	7.46		338.42	12.4
	295.091	19.2		409.62	2.2
	351.87	37.1		463.10	4.6
	785.827	1.09		562.65	1.01
^{214}Bi	609.311	46.1		755.28	1.32
	665.442	1.56		772.28	1.09
	768.35	4.88		794.79	4.6
	806.155	1.23		835.60	1.71
	934.039	3.16		911.16	29.0
	1120.273	15.0		964.64	5.8
	1155.183	1.69		968.97	17.4
	1238.107	5.92		1459.19	1.06
	1280.952	1.47		1496.0	1.05
	1377.659	4.02		1588.23	3.6
	1401.48	1.39		1630.47	1.95
	1407.97	2.48	^{224}Ra	240.76	3.9
	1509.23	2.19	^{212}Pb	74.814	10.5
	1661.258	1.15		77.107	17.7
	1729.58	3.05		87.19	6.27
	1764.49	15.9		90.128	1.86
	1847.41	2.12		238.578	43.6
	2118.53	1.21		300.034	3.34
	2204.09	4.99	^{212}Bi	727.25	6.65
	2447.68	1.55		785.51	1.107
^{210}Pb	46.52	4.05		1620.66	1.51
			^{208}Tl	72.808	2.14
				74.969	3.6
				84.789	1.27
				277.28	6.8
				510.606	21.6
				583.022	86.0
				763.06	1.64
				860.30	12.0
				2614.35	99.79

In most geological formations, the uranium and thorium decay chains are rarely in secular equilibrium since some nuclides in the chain are subject to migration. Radon, for example, an intermediate member of both chains, is a gas which can escape from the solid matrix. In this way about 6.2×10^8 atoms ^{222}Rn/m^2/d [74] are released into the atmosphere from the earth's land surface. This makes ^{222}Rn by far the strongest source of airborne radioactivity, present in dwellings and laboratories at a level of about 40 Bq/m^3 on the average [75]. Although the ^{222}Rn itself dies out quickly ($T_{1/2} = 3.82$ days), it feeds into the long-lived ^{210}Pb ($T_{1/2} = 22$ years).

^{220}Rn from the Th-chain is also present in air, but usually at a much lower level because of its shorter half-life (55.6 s compared to 3.82 d). In addition, the concentration of ^{220}Rn decreases strongly with distance from the emanating walls because of the small diffusion length possible during the short lifetime. Furthermore, the entire ^{220}Rn family dies out within a half-life of 11 hours.

Relatively simple steps can be taken to prevent natural radon and its progeny from contributing to the background. Sealing the detector cavity and supplying a slight over-pressure of radon-free gas (such as old compressed air or nitrogen boil-off from a liquid nitrogen reservoir) can expel trapped radon and prevent it from leaking in through cracks or small openings.

A secondary source of environmental radioactivity comes from radionuclides in the atmosphere produced by cosmic rays. Table 3.2 lists those radioactive isotopes produced by cosmic rays in the atmosphere with half-lives longer than one day [76]. The atmospheric target nuclei primarily responsible for the production of these isotopes is shown in column 3 of Table 3.2. Since the abundance of argon in the atmosphere is small compared to nitrogen and oxygen, the first four isotopes in Table 3.2 are the most important. Furthermore, since the atmospheric abundance of Ne, Kr and Xe is several orders of magnitude smaller than that of Ar, no isotopes produced from these rare gases are included in this table.

In addition, nuclear weapons testing has added major quantities of ^{3}H and ^{14}C as

Table 3.2: Isotopes ($T_{1/2} > 1$ day) produced by cosmic rays in the atmosphere.

Isotope	Half-life	Main Target Nuclide(s)
^{3}H	12.3 y	N, O
^{7}Be	53 d	N, O
^{10}Be	2.5×10^6 y	N, O
^{14}C	5730 y	N, O
^{22}Na	2.6 y	Ar
^{26}Al	7.4×10^5 y	Ar
^{32}Si	50 y	Ar
^{32}P	14.3 d	Ar
^{33}P	25 d	Ar
^{35}S	87 d	Ar
^{36}Cl	3.1×10^5 y	Ar
^{37}Ar	35 d	Ar
^{39}Ar	270 y	Ar
^{81}Kr	2.1×10^5 y	Ar

well as adding other man-made radionuclides to the environment such as ^{137}Cs and ^{90}Sr. The levels of these man-made radionuclides have also been increased by events such as the Chernobyl accident, where substantial amounts of ^{137}Cs were released into the atmosphere. In some cases, this so-called nuclear fallout can become a significant source of background.

3.1.2 Radiocontaminants in Detectors and Shielding Material

A substantial source of photon backgrounds is due to the presence of both primordial and man-made radionuclides in the components of the detector system and the shielding material. Because of the prevalence of primordial radionuclides in ores and other raw materials, many manufactured products contain uranium, thorium and potassium contamination at some level. In addition, certain materials contain substantial levels of other radionuclides such as iron and steel, which often contain high levels of ^{60}Co.

Ordinary, commercially-available lead bricks typically contain high levels of ^{210}Pb because of the high concentration of uranium found in the lead ore. During the smelting and

refining process, the uranium is removed from the ore, but the ^{210}Pb daughter is chemically inseparable and hence remains in the brick. The long-lived ^{210}Pb ($T_{1/2} = 22.3$ years), decays into ^{210}Bi which subsequently decays into ^{210}Po. The end-point of the ^{210}Bi beta-decay is 1.1615 MeV. At these energies, the beta-particle interacts with the high-Z lead and produces substantial amounts of external bremsstrahlung radiation as well as lead x-rays. The internal bremsstrahlung which accompanies the beta-decay also provides continuous-energy photons ranging from 0 up to the beta-particle endpoint, although the intensity of this radiation is less than 0.5% of the beta emission. Thus the ^{210}Bi beta-decay leads to high background rates, particularly at low energies. This background can be reduced by using an appropriate shielding material inside the lead [77], but care must be taken to ensure that this material does not introduce significant levels of other background sources. One possible choice is to use lead that contains very low levels of ^{210}Pb. Such lead is available in the form of ancient lead, where the ^{210}Pb has had sufficient time to decay away, or in the form of commercial lead produced from selected ores with extremely low concentrations of uranium.

Unlike lead, high purity copper is relatively easily obtainable because of the production process; copper is routinely purified after smelting by electrolytic dissolution and redeposition in solution, separating the copper from practically all radioactive contaminants. The concentrations of the primordial nuclides typically found [78] in copper (grade 101) are $< 8.3 \times 10^{-4}$ Bq ^{214}Bi/kg (< 0.07 ppb U), $< 5.0 \times 10^{-4}$ Bq ^{208}Tl/kg (< 0.12 ppb Th) and $< 8.3 \times 10^{-3}$ Bq ^{40}K/kg (< 0.27 ppm K). Unfortunately, many radioactive contaminants are produced in copper via cosmic ray spallation. Table 3.3 lists the equilibrium concentrations of selected cosmogenic spallation products in copper at the earth's surface [78]. These radionuclides are produced primarily by energetic cosmic ray neutrons. The level of these contaminants can be minimized by storing the material underground where the hadronic component of the cosmic rays has been substantially reduced [79].

In addition to generating radiocontaminants in the detector and shielding materials directly, cosmic rays can also lead to secondary sources of photons. For example, neutrons

Table 3.3: Equilibrium concentrations of selected cosmogenic spallation products in copper at the earth's surface. Data taken from [78].

Radionuclide	Equilibrium Activity (Bq/kg)
^{54}Mn	3.33×10^{-4}
^{59}Fe	6.67×10^{-5}
^{56}Co	1.00×10^{-4}
^{57}Co	$< 3.3 \times 10^{-5}$
^{58}Co	8.33×10^{-4}
^{60}Co	1.67×10^{-4}

that are produced by cosmic ray interactions and then captured by hydrogen will become a source of 2223 keV photons.

3.2 Detector System for Photon Measurements

In order to study the photon background at the Stanford Underground Facility, a high purity germanium (HPGe) detector operated at 77 K inside a custom cryostat was constructed. The main constraints of the cryostat design were to minimize the mass of material near the detector and to use only those materials which had low levels of radioactive contamination. The 160 cm^3 (850 g) p-type co-axial detector, 5.5 cm in diameter and 7.0 cm long, was originally used as part of the LBNL/UCSB ^{76}Ge double beta decay experiment [80]. As shown in Figure 3.3, the detector is mounted on an aluminum base via a silicon cylinder and a small insulating boron nitride ring. A low-Z material was desired for the mount so that it would not shadow the detector from external photons, and although aluminum typically contains high levels of uranium and thorium contamination, the sample utilized had relatively low levels of contamination. A bevel on the germanium detector mates with a similar bevel on the silicon cylinder to center the detector. The outside surface of the germanium detector is metallized with 1000 Å of aluminum to reduce

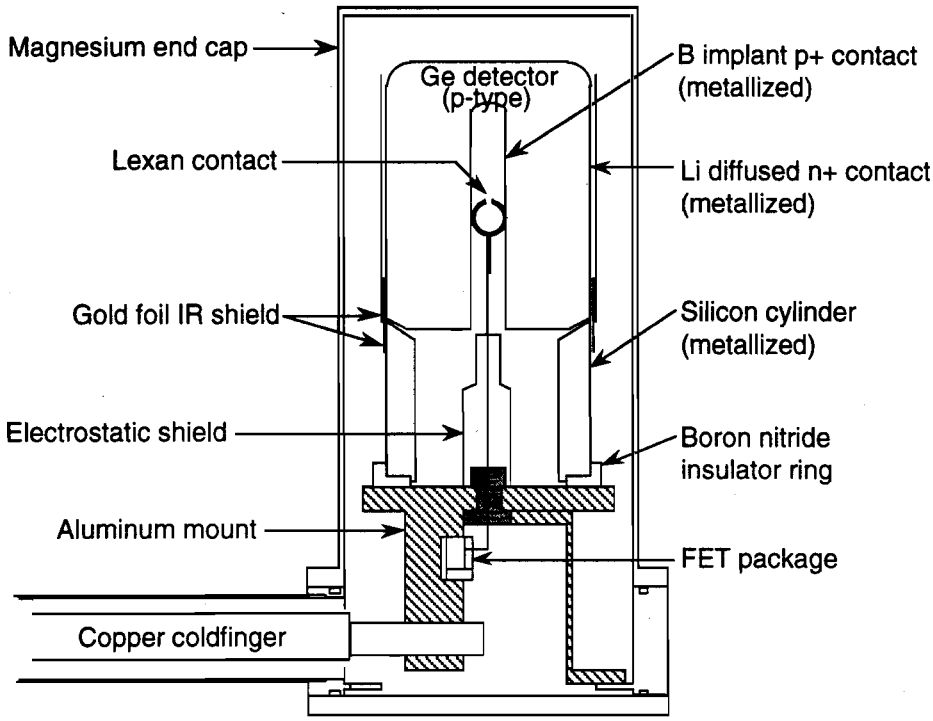

Figure 3.3: Cut away diagram of the Ge detector and mounting hardware.

IR absorption from the warm walls of the cryostat. The silicon cylinder is also metallized in order to reduce its emissivity and hence diminish liquid nitrogen usage. The sides of the detector have also been wrapped with 25-μm-thick gold foils (IR shield) to further shield the detector from IR radiation. To increase thermal contact, 12 gold foil tabs were inserted at the interface between the germanium detector and the silicon cylinder and indium foil o-rings were placed on either side of the boron nitride ring. Although the indium was known to contain a small amount of radioactivity, its use in other similar detector systems demonstrated that its contribution to the detector background would be less that 0.1 counts/keV/day. The aluminum mount is connected to the 7.5 l liquid nitrogen bath via a copper cold finger. The end cap of the detector system is constructed of thin wall (1.27 mm thick) magnesium to minimize attenuation of the external photons to be measured.

A small metallized lexan spring connected to a nickel wire provides the contact be-

tween the metallized p^+ inner contact of the detector and the FET which, together with the feedback resistor and capacitor, constitutes the front-end elements of the electronic preamplifier (FET package) located near the detector on the aluminum mount. The positive detector bias is applied to the outside surface of the detector through the silicon cylinder. A grounded copper cylinder (electrostatic shield) surrounds the signal lead in order to reduce microphonics that could be caused by movement of this wire with respect to the silicon cylinder which is at high voltage. All leads run along the cold finger to vacuum feedthrough connectors mounted on a collar near the nitrogen dewar. The preamplifier and high-voltage filter box are attached to this collar, as is the ion pump used to maintain the vacuum inside the cryostat.

The detector, which has a depletion voltage of +1000 V, was operated with a bias voltage of +1200 V. A commercially available Tennelec TC247 amplifier was used to amplify the signal from the preamplifier. The linearity of the system was checked on the bench using an ^{241}Am source (60 keV line) and a ^{60}Co source (1173 keV and 1333 keV lines). The resolution of the detector was found to be 2.1 keV FWHM at 1173 keV and 2.2 keV FWHM at 1333 keV. These values are typical for a germanium detector of this size. To complete the spectrometer system, a data acquisition system based on an IBM PC computer used in conjunction with an internal 4000 channel ADC card and MAESTRO^{TM}, a multichannel analyzer emulator manufactured by EG&G Ortec, was used.

To evaluate the system further, measurements with external shielding were required. To this end, the detector was taken to the Low Background Counting Facility at the Lawrence Berkeley National Laboratory and surrounded by a 10-cm-thick lead shield. This facility is located underground at a depth of 4 m.w.e. (4 meters of water equivalent), i.e., the shielding provided by this site is equivalent to the shielding that would be provided by 4 m of water. The gain of the amplifier was adjusted so that the photon spectrum could be measured up to several MeV with a threshold of 30 keV. The measured spectrum is shown in Figure 3.4. The residual background can be attributed to the following

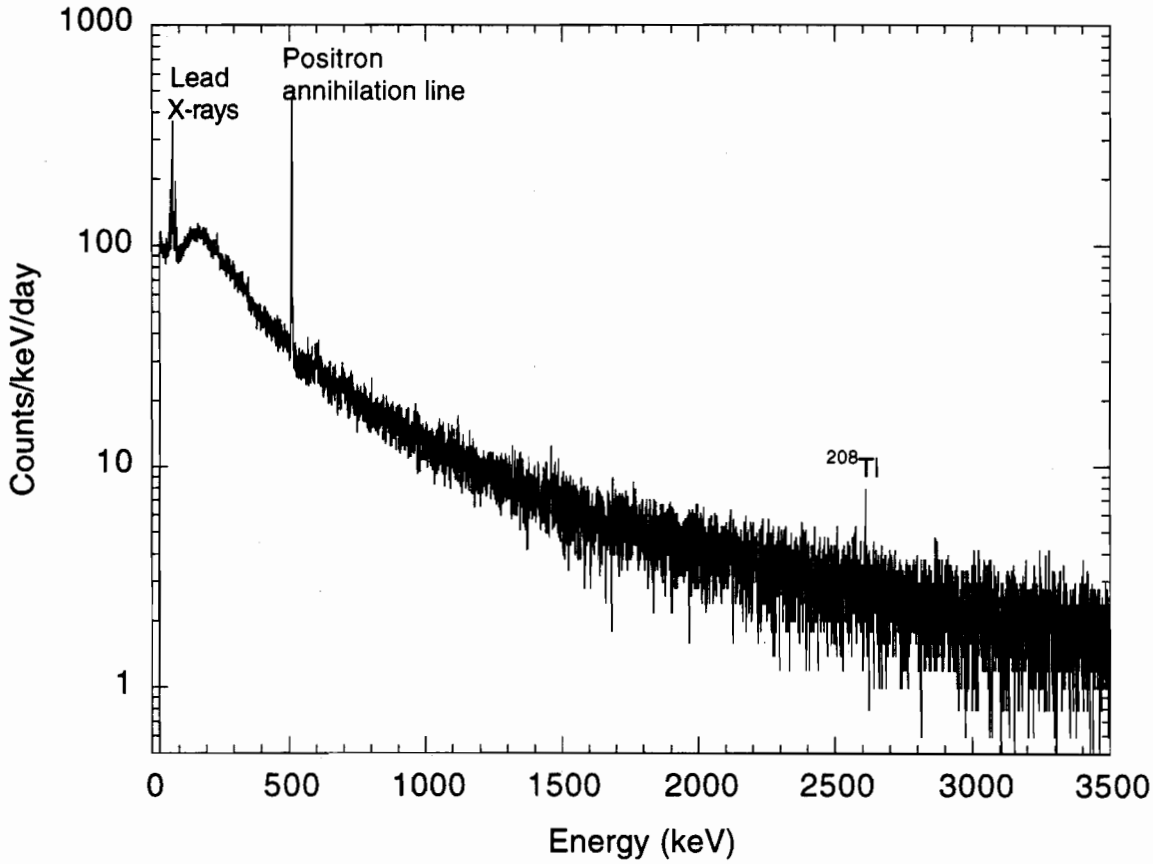

Figure 3.4: Photon spectrum measured inside a 10-cm-thick lead shield at the Low Background Counting Facility at the Lawrence Berkeley National Laboratory.

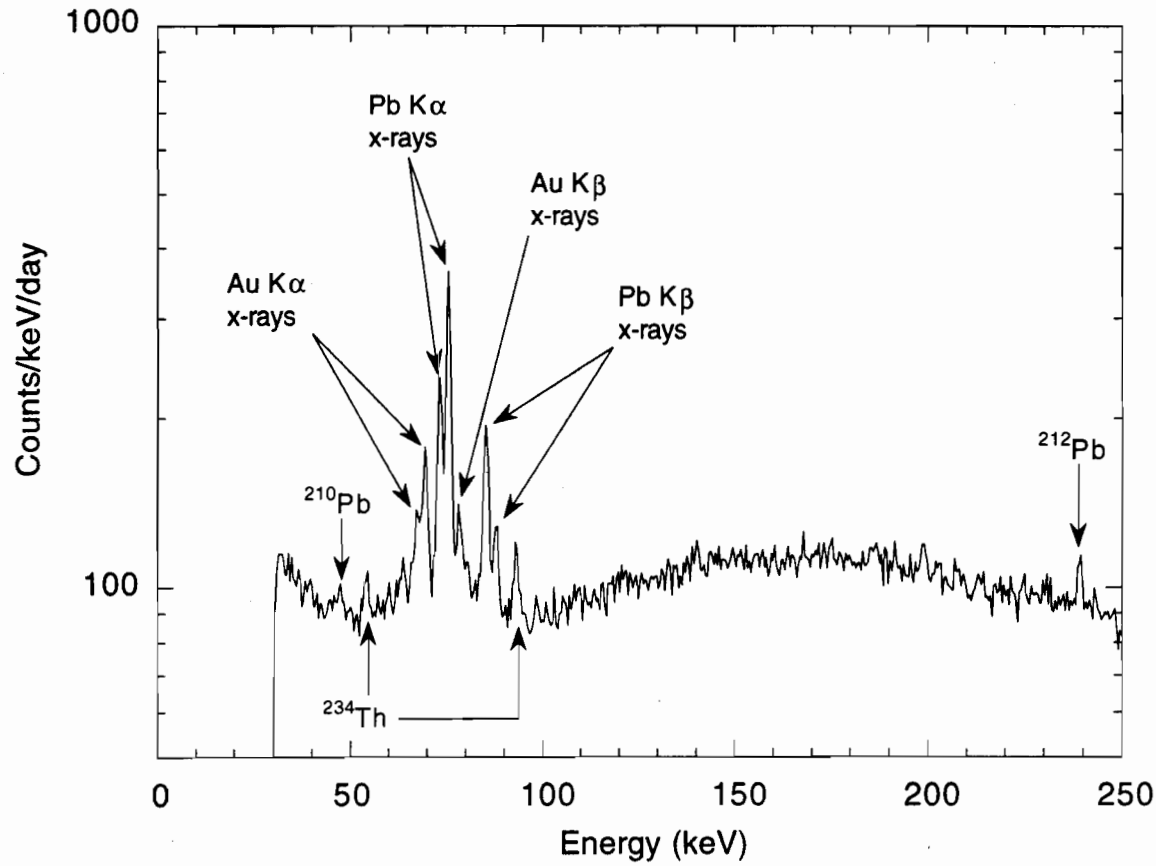

Figure 3.5: Low energy portion of the photon spectrum measured inside a 10-cm-thick lead shield at the Low Background Counting Facility at the Lawrence Berkeley National Laboratory.

components: incompletely shielded external gamma rays; intrinsic contamination of the detector, cryostat and shielding materials; ^{222}Rn and its daughters trapped in the cavities of the shield; cosmic ray induced radiation in the detector and shield.

The ^{208}Tl line at 2614 keV and the lead Kα_1 x-ray line at 75 keV demonstrate the linearity of the system over the entire spectrum. The most prominent feature in the spectrum is the positron annihilation peak at 511 keV. Figure 3.5 reveals several other features that are present in the low energy portion of the measured spectrum. Lead fluorescence lines appear at 75.0 keV (Kα_1), 72.8 keV (Kα_2), 84.9 keV (Kβ_1), 87.3 keV (Kβ_2), and 84.5 keV (Kβ_3) although the Kβ_3 line is unresolved from the Kβ_1 line. The

gold foil IR shield that surrounds the detector leads to the gold fluorescence lines that appear at 68.8 keV ($K\alpha_1$), 67.0 keV ($K\alpha_2$), 78.0 keV ($K\beta_1$), 80.1 keV ($K\beta_2$), and 77.6 keV ($K\beta_3$) and again the $K\beta_3$ line is unresolved from the $K\beta_1$ line.

The lines at 63 keV and 93 keV are from the decay of ^{234}Th while the line at 46.5 keV is from the decay of ^{210}Pb. Both of these isotopes are part of the ^{238}U-chain. The line at 239 keV, however, is from the decay of ^{212}Pb, a daughter in the ^{232}Th-chain. Although care was taken to minimize the amount of radioactivity in the detector system, some contamination was inevitable. However, with this single measurement, it is impossible to determine whether the source of the observed contamination is internal, external or both. The source of internal contamination is most likely the aluminum mount, with some of the contamination, particularly the ^{210}Pb, possibly coming from the small amount of solder used to connect the leads to the FET package. Any external contamination would have to be in the lead shielding.

In an attempt to determine the level of internal contamination, the spectrometer system was taken to the powerhouse of the Oroville Dam, a site in Northern California with an overburden of 600 m.w.e. At this depth, the cosmic ray muon flux is reduced by 3 orders of magnitude. The detector was surrounded by a 15-cm-thick lead shield. To protect the detector from radiocontaminants in the lead, the inner walls of the shield were lined with a thin layer of ultra low activity lead [81] approximately 1 cm thick. The resulting spectrum is shown in Figure 3.6. The persistence of the ^{210}Pb, ^{212}Pb and ^{234}Th lines with the inner shield lining confirms that there is internal contamination since this thickness of lead is more than sufficient to attenuate external photons of these energies. Furthermore, with the reduced background level, several other lines appear, most noticeably ^{226}Ra at 186.11 keV and ^{214}Pb at 295.09 keV and 351.87 keV (uranium daughters), and ^{228}Ac at 338.42 keV (thorium daughter). This measured spectrum represents an upper limit on the internal background of the detector system.

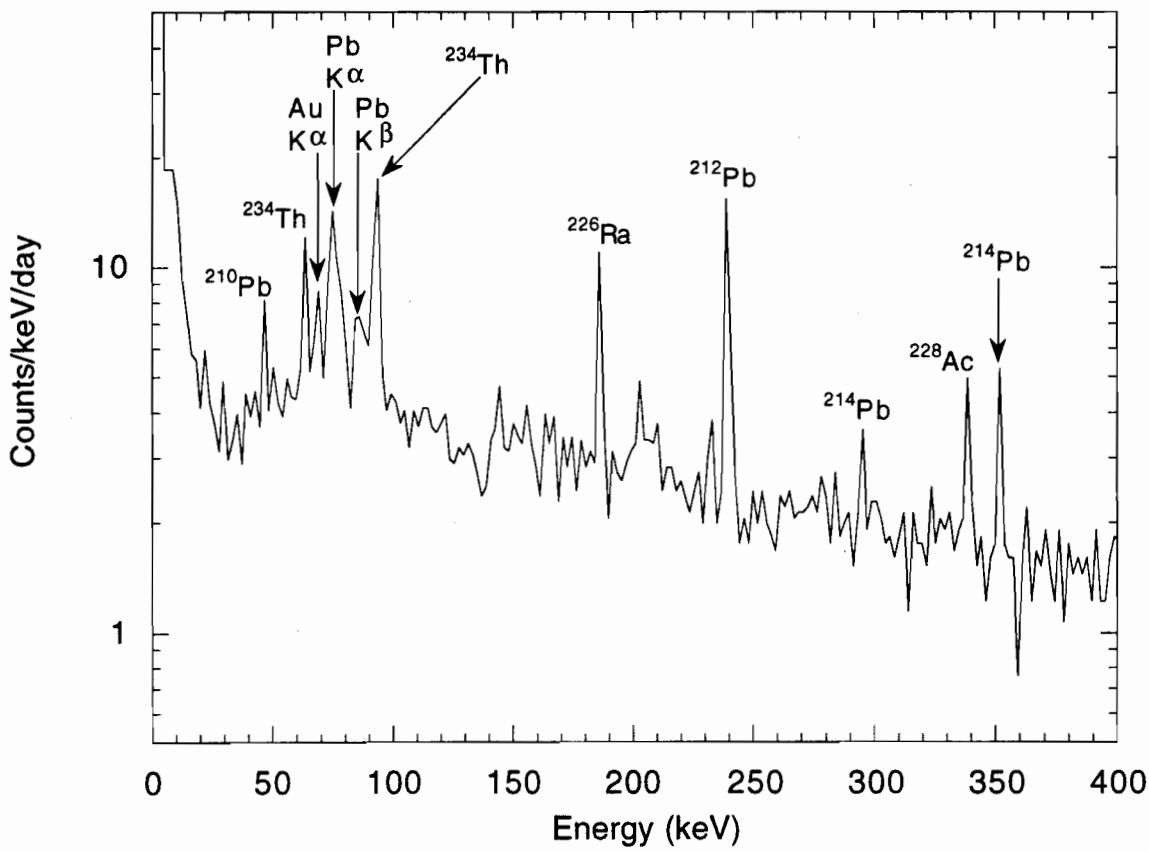

Figure 3.6: Background spectrum measured inside a 15-cm-thick lead shield at Oroville. The inner walls of the shield are lined with a thin layer (approximately 1 cm thick) of ultra low activity lead. The steep rise in the spectrum at low energies is due to electronics noise.

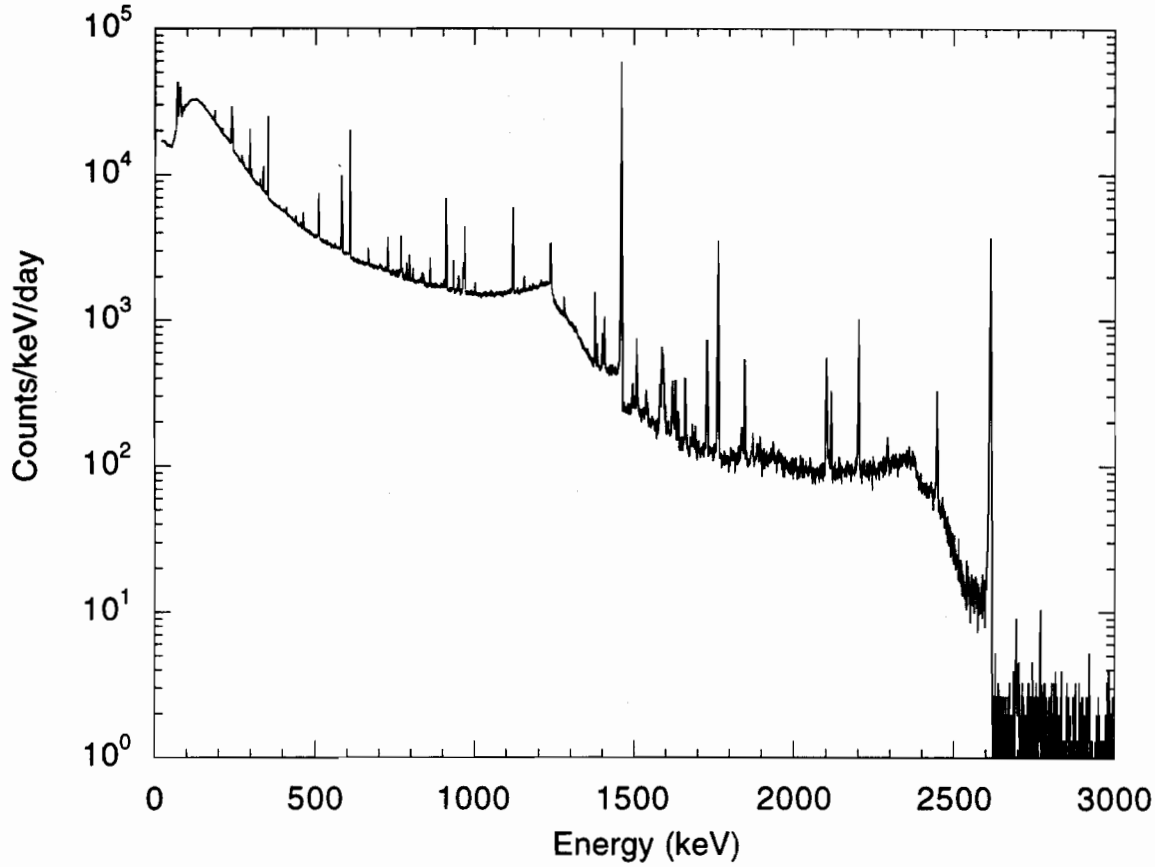

Figure 3.7: Measured ambient photon spectrum at the Stanford Underground Facility.

3.3 Shielding Studies

The HPGe spectrometer was used to measure the photon background in the Stanford Underground Facility and to examine the effectiveness of various shielding configurations. Figure 3.7 shows the ambient photon spectrum measured in the Stanford Underground Facility with no shielding. As expected, the counting rate is very high and the characteristic lines from the U-chain and Th-chain are all present. Other dominant features that appear are the lead x-rays around 75 keV and 85 keV, the positron annihilation line at 511 keV and the ^{40}K line at 1461 keV, as well as the Compton edges at 1243 keV (from the ^{40}K line) and 2382 keV (from the ^{208}Tl line at 2614 keV). The counts above the 2614 keV line are due mainly to cosmic ray interactions such as muons passing through

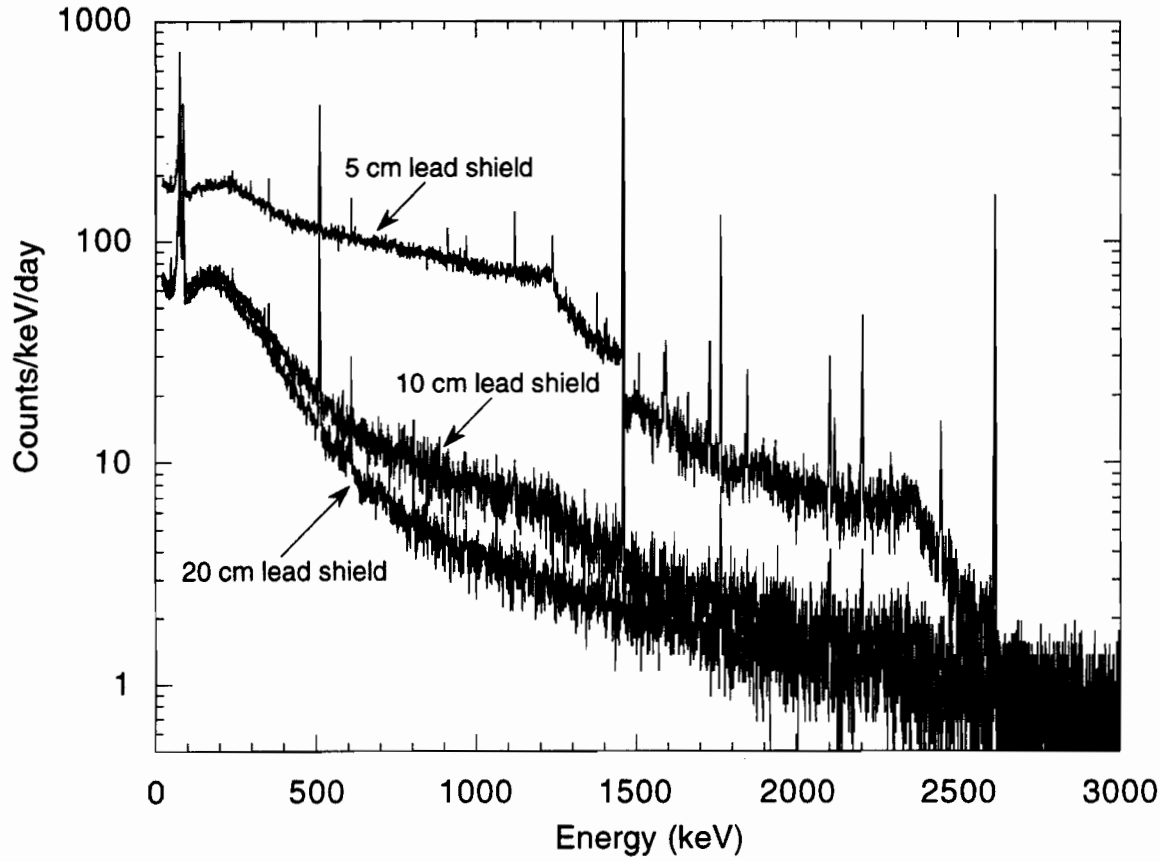

Figure 3.8: Measured photon spectra inside lead shields of various thicknesses at the Stanford Underground Facility.

the detector.

The next step was to shield the detector with various thicknesses of lead to determine what thickness would provide adequate shielding. The lead used for these measurements was provided by Stanford University [82] and hence it is referred to as Stanford lead. The radio-purity of this lead was unknown prior to its use.

Figure 3.8 shows the measured photon spectra inside lead shields of various thicknesses. The first 5 cm of lead reduces the measured photon continuum by more than two orders of magnitude at energies below 200 keV. At higher energies, the continuum is reduced by a factor of ten. With 10 cm of lead, there is a further reduction by almost another order of magnitude at higher energies, but the reduction below a few hundred keV is only a factor

of two. This suggests that part of the low energy continuum is due to the lead itself, either from natural radioactivity in the lead or from cosmogenically induced activities. Increasing the lead thickness to 20 cm reduces the high energy peaks, such as ^{40}K and ^{208}Tl, and the Compton edges associated with these peaks, but it has little effect on the low energy continuum. This along with the appearance of the line at 46.5 keV suggests that the Stanford lead may contain a substantial amount of ^{210}Pb contamination.

3.3.1 Muon-Induced Activities Versus Lead Contamination

In order to separate the muon-induced activities from radioactive contamination in the lead, a new test shield with a muon veto was constructed (see Figure 3.9). The shield was designed so that the inner 5 cm of lead could be changed easily, allowing the radio-purity of the lead to be examined. The muon veto consisted of a 6-sided cube of 1.3-cm-thick plastic scintillator panels surrounding the lead. Each scintillator panel was connected to two photomultiplier tubes and the signals from the two tubes were taken in coincidence to eliminate dark current. A "hit" in any face of the veto box resulted in a 100 μs TTL signal being fed into the ADC card and used as an anticoincidence signal. That is, for 100 μs following a hit in any of the scintillator panels, no signal from the Ge detector was recorded. With a veto rate of approximately 400 s^{-1}, this leads to a dead time of about 4%.

Figure 3.10 shows the spectra measured inside the test veto shield with and without the veto system active. For both measurements, all of the lead used was Stanford lead. Without the veto, the average background level between 20 keV and 40 keV was 63.3 $\pm$ 0.8 counts/keV/day and the 46.5 keV line from ^{210}Pb was clearly visible. The average background level between 100 keV and 200 keV was 62.1 $\pm$ 0.4 counts/keV/day. Also visible was a line at 662 keV, presumably due to ^{137}Cs (nuclear fallout) on the surface of some of the lead bricks. Using this lead, the veto is really only effective at higher energies. With the veto active, the average continuum level between 100 keV and 200 keV only

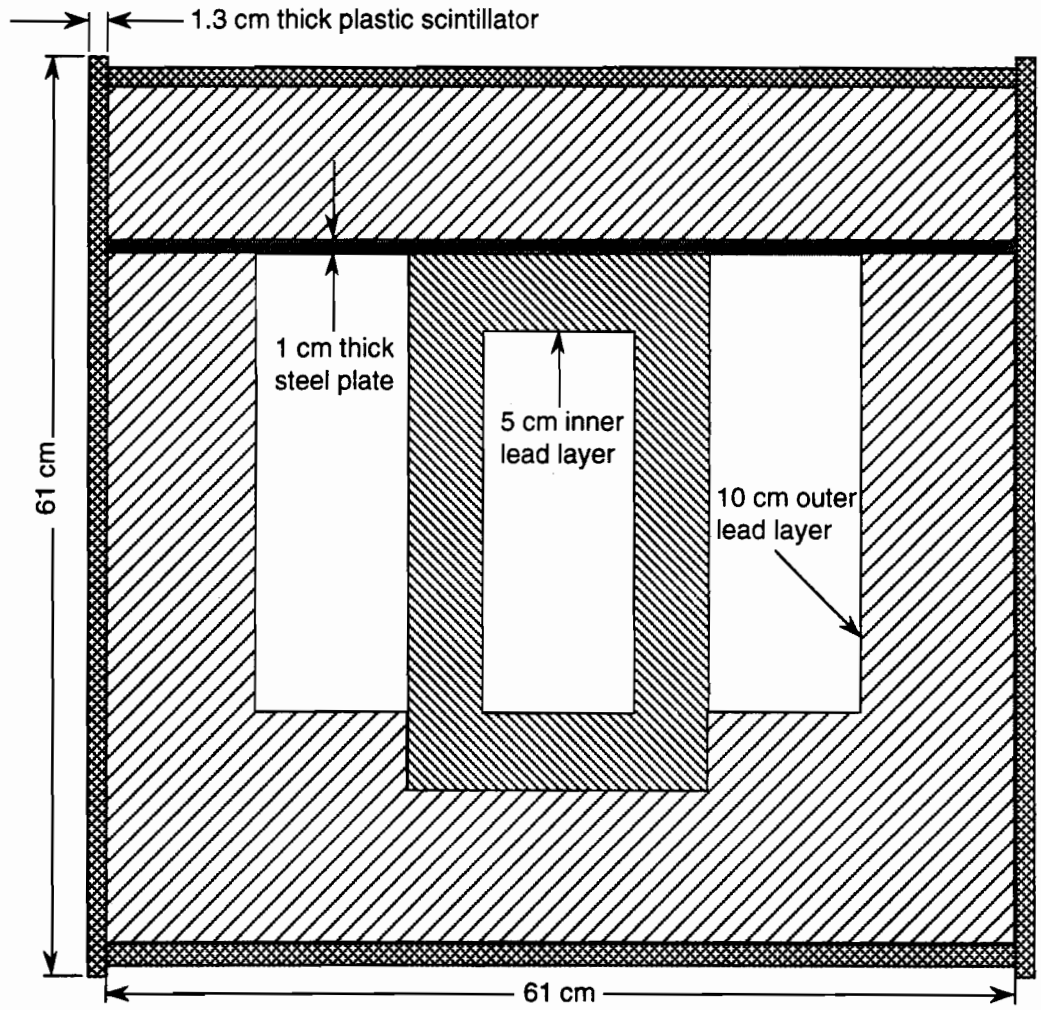

Figure 3.9: Structure of the test veto shield used to study lead quality and veto effectiveness in the Stanford Underground Facility.

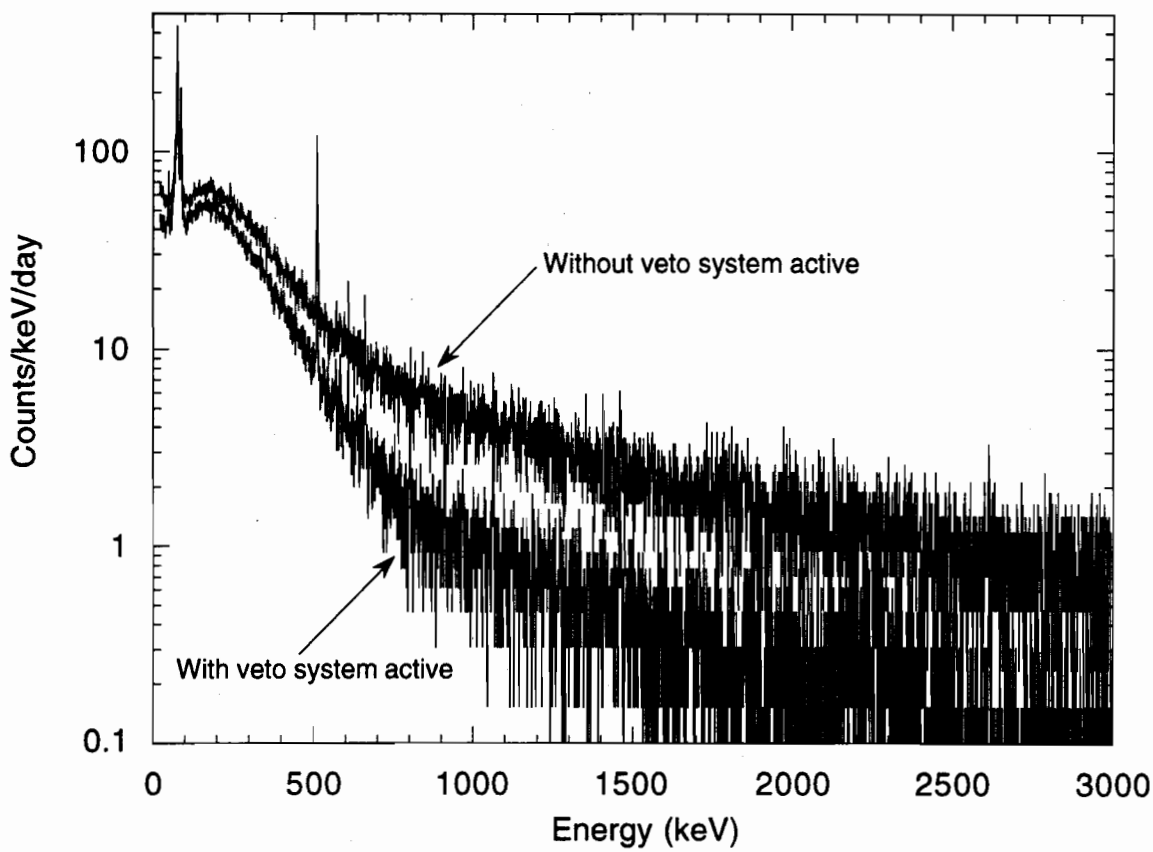

Figure 3.10: Measured photon spectra inside the test veto shield at the Stanford Underground Facility. Upper curve is without the veto system active. Lower curve is with the veto system active. In both cases, only Stanford lead was used.

drops to 50.3 ± 0.3 counts/keV/day while the average continuum in the range 20 keV to 40 keV drops to 45.1 ± 0.5 counts/keV/day. The difference in the background level of the two spectra is a measure of the muon-induced contribution to the background. In the range 100 keV to 200 keV, this contribution amounts to 11.8 ± 0.7 counts/keV/day. The small reduction in the background level at low energies with the veto active is an indication that the low energy background may be dominated by events due to radioactive contamination in the Stanford lead, such as ^{210}Pb, rather than muon-induced activities. To rule out possible surface contamination of the bricks, the inner lead layer was removed and each brick was cleaned with an electric wire brush and washed in water before being replaced inside the shield. The resulting spectrum was virtually identical to the previous measurement with one exception; the 662 keV line was no longer present in the "washed lead" spectrum. This is consistent with the assumption that this line was due to surface contamination of ^{137}Cs.

It is possible that the small reduction in the vetoed spectrum is due to a poorly operating veto system. To rule out this possibility, the efficiency of the veto system can be estimated by looking at the reduction of the 511 keV positron annihilation line or the reduction of the high energy continuum above the 2614 keV line. The 511 keV line can be used because the dominant source of this line is the annihilation of the electron-positron pairs that are produced in the air showers created when the primary cosmic rays interact in the atmosphere. The high energy continuum above the 2614 keV line can be used because 2614 keV is the highest energy gamma ray from natural radioactivity. As illustrated in Table 3.4, both methods give an estimated efficiency of 88%. The main source of inefficiency is the large gap in the scintillator coverage created on the side where the detector system penetrates the shield. This scintillator panel was raised above the level of the coldfinger penetration into the shield, leaving approximately 20 cm along the bottom of this side of the lead shield uncovered with scintillator.

The inner lead layer was replaced with Glover lead [83], commercially available lead that, although not marketed as a low activity material, was believed to be relatively low

Table 3.4: Estimate of the efficiency of the veto system for the test veto shield at the Stanford Underground Facility. Measurements were made using Stanford lead as the inner lead shield.

Region	Without Veto (counts/day)	With Veto (counts/day)	Ratio	Estimated Efficiency
511 keV line	318 ± 8	38 ± 2	8.4 ± 0.7	88%
2700-2800 keV	93 ± 4	12 ± 1	8 ± 1	88%
2900-3000 keV	90 ± 4	10 ± 1	9 ± 1	89%

in ^{210}Pb contamination. With no veto (see Figure 3.11), the average background level between 100 keV and 200 keV is 28.4 ± 0.1 counts/keV/day, a factor of two lower than with the Stanford lead. In addition, the 46.5 keV ^{210}Pb line, although still present, is much reduced. With the veto active, the average background level between 100 keV and 200 keV is reduced to 15.8 ± 0.1 counts/keV/day. As before, the difference in the background level of the two spectra is a measure of the muon-induced contribution to the background, which, in this case, amounts to 12.6 ± 0.2 counts/keV/day in the range 100 keV to 200 keV. This is consistent with the value obtained with the Stanford lead as one might expect since the muon-induced component of the background should not depend on the radio-purity of the lead. At energies above 800 keV, the vetoed and unvetoed spectra with the Glover lead are indistinguishable from the vetoed and unvetoed spectra with the Stanford lead. This suggests that at higher energies, the background is not dominated by radioactive contaminants in the lead. The veto efficiency was estimated as before and was found to be approximately 85% (see Table 3.5).

With the reduced background levels obtained with the Glover lead, additional lines become easily recognizable in the measured spectra. The more dominant of these lines are from ^{226}Ra (186 keV), ^{214}Pb (242 keV, 295 keV, 352 keV), ^{208}Tl (583 keV) and ^{214}Bi (609 keV, 1120 keV, 1764 keV). The latter three isotopes are all radon daughters and their appearance signifies the presence of trapped radon gas inside the shield.

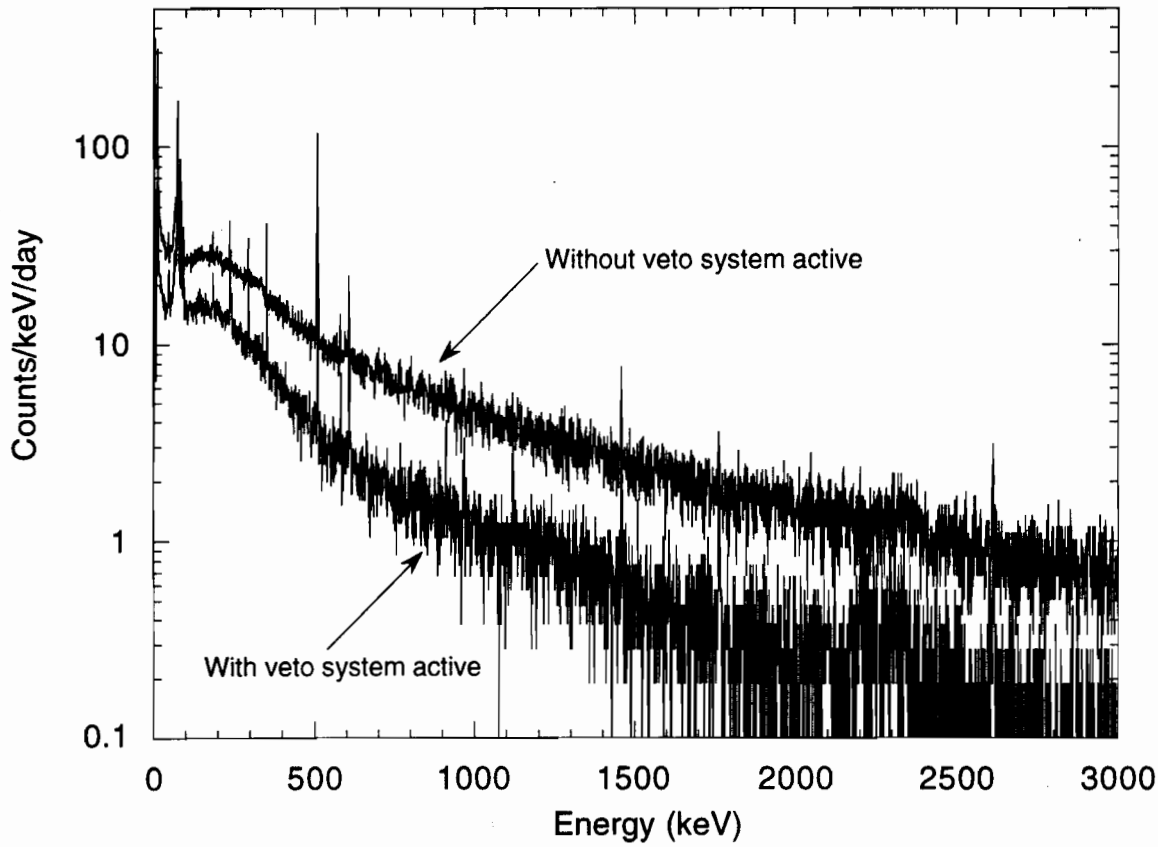

Figure 3.11: Measured photon spectra inside the test veto shield at the Stanford Underground Facility. Upper curve is without the veto system active. Lower curve is with the veto system active. In both cases, Glover lead was used for the inner 5 cm of the lead shield.

Table 3.5: Estimate of the efficiency of the veto system for the test veto shield at the Stanford Underground Facility. Measurements were made using Glover lead as the inner lead shield.

Region	Without Veto (counts/day)	With Veto (counts/day)	Ratio	Estimated Efficiency
511 keV line	347 ± 5	56 ± 2	6.2 ± 0.3	84%
2700-2800 keV	83 ± 2	12 ± 1	6.8 ± 0.7	86%
2900-3000 keV	73 ± 2	11 ± 1	6.6 ± 0.8	85%

3.3.2 Lead Quality

In an effort to determine the level of ^{210}Pb contamination in the Glover lead, a series of measurements was performed at a depth of 600 m.w.e. in the powerhouse of the Oroville Dam [77]. The detector was surrounded by a 15-cm-thick lead shield, with Glover lead used for the inner 5 cm. The outer 10 cm of the lead shield was made of low activity lead borrowed from the LBNL/UCSB ^{76}Ge double beta decay experiment [80]. For the first measurement, no additional shielding was used. For the second measurement, the inside of the lead was lined with a thin shield of OFHC (oxygen free high conductivity) copper (1 cm thick on the sides, 1.6 cm thick on the top and bottom). For the final measurement, the sides of the inner copper shield were replaced by a thin shield of the ultra low activity Nantes lead [81] (approximately 1 cm thick). The three measured spectra are shown in Figure 3.12 while the shielding configuration used for the third measurement is illustrated in Figure 3.13.

The shape of the the spectrum obtained with no liner is typical of what is observed inside contemporary lead shields; a background spectrum dominated by lead x-rays and bremsstrahlung radiation from ^{210}Bi decay. The copper liner greatly reduces the lead x-rays, as well as reducing the continuum level below 400 keV by a factor of about 2, but it does not change the shape of the measured spectrum. This thickness of copper is not sufficient to attenuate the bremsstrahlung radiation. The Nantes lead liner, however,

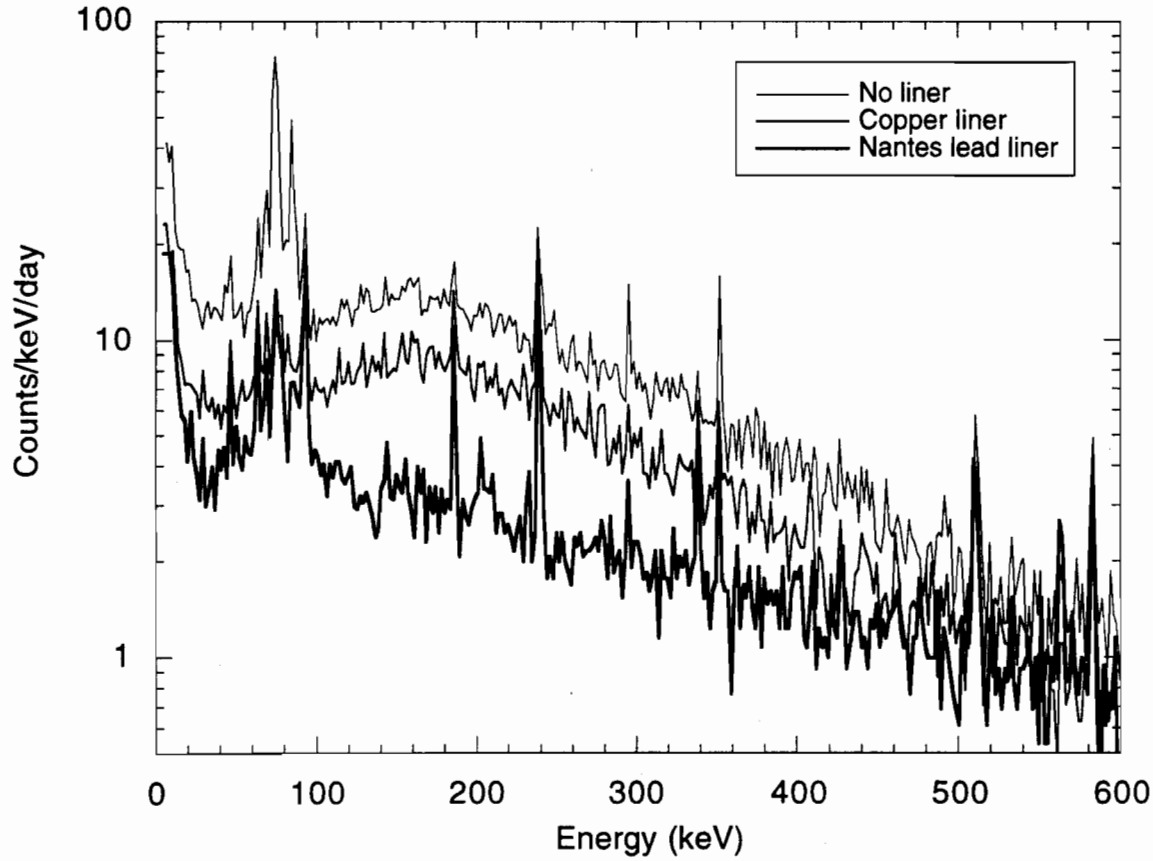

Figure 3.12: Photon spectra measured inside a 15-cm-thick lead shield at Oroville. For the upper curve (No liner), no additional shielding was used. For the middle curve (Copper liner), the inside of the lead shield was lined with a thin layer of OFHC copper. For the lower curve (Nantes lead liner), the inside of the lead shield was lined with a thin layer of ultra low activity lead.

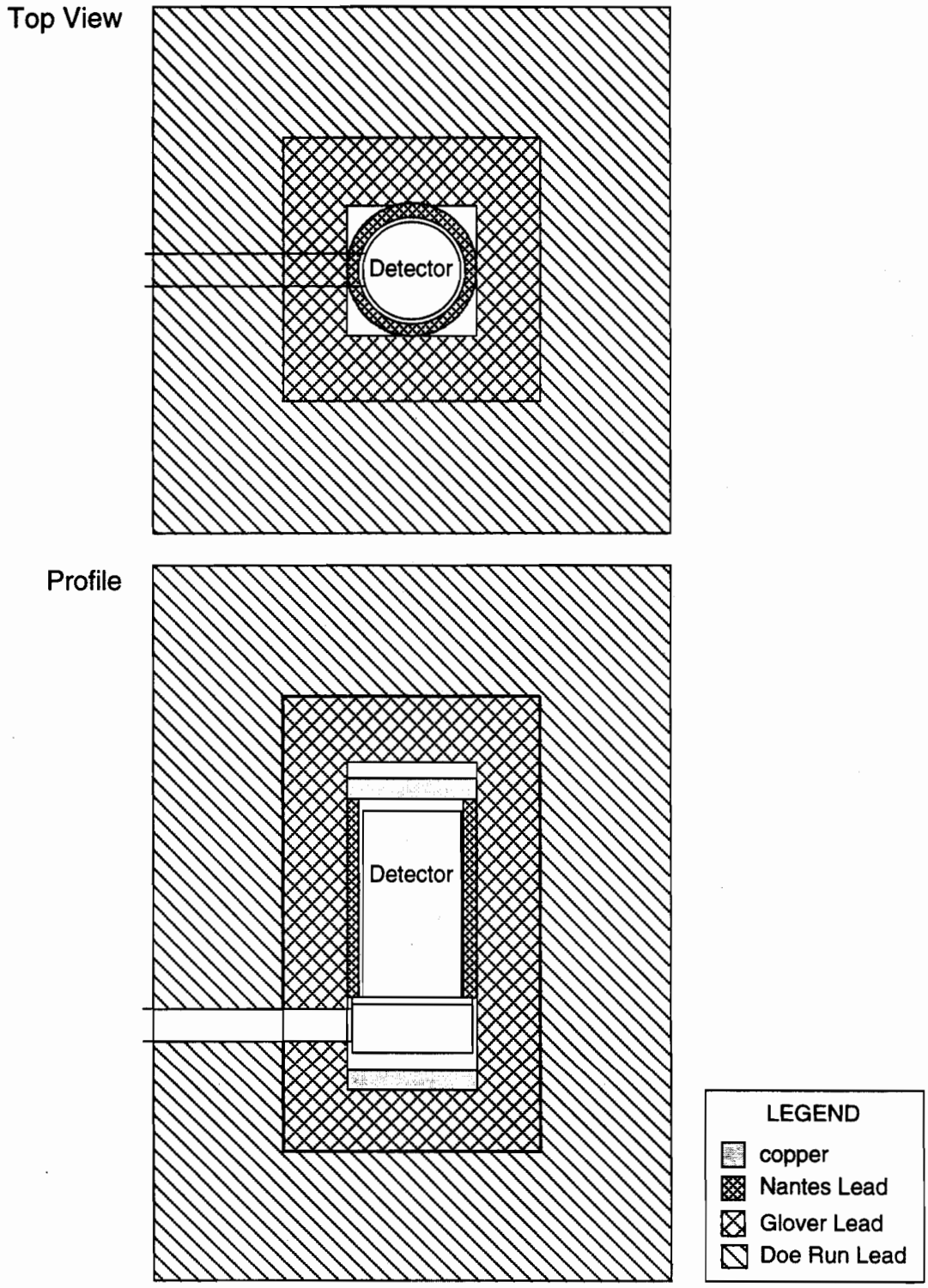

Figure 3.13: Shielding configuration used to obtain the curve labeled "Nantes lead liner" in Figure 3.12.

Table 3.6: Physics processes implemented by GEANT3.

Tracking Particle	Process
Photon	(e^+,e^-) pair conversion
	Compton scattering
	Photo-electric effect
	Photo-fission of heavy elements
	Rayleigh scattering
e^+,e^-	Multiple scattering
	Ionization and delta-ray production
	Bremsstrahlung
	Annihilation of positron
μ^+, μ^-	Decay in flight
	Multiple scattering
	Ionization and delta-ray production
	Bremsstrahlung
	Direct (e^+,e^-) pair production
	Nuclear interactions
Hadrons	Decay in flight
	Multiple scattering
	Ionization and delta-ray production
	Hadronic interactions

does effectively shield the detector from the contamination in the outer lead as illustrated by the further reduction and change in shape of the background continuum below several hundred keV. Above 500 keV there are no significant differences among the three measured spectra.

These measurements were then simulated using GEANT3 [84], a detector simulation program developed at CERN for high-energy physics experiments. GEANT3 allows the user to track particles through a user-defined experimental set-up. The experimental set-up is represented by a structure of geometrical volumes composed of various materials. The materials can be basic elements or compound mixtures. While tracking the particles through the experimental set-up, GEANT3 takes into account the particle interactions with matter. Table 3.6 summarizes the various processes implemented in GEANT3.

In these simulations, the HPGe detector was simply modeled as 1 kg of germanium, with a 1-mm-thick dead layer (i.e., any energy deposition that occurred in the outer 1 mm of the germanium was not included in the spectrum). No details of the cryostat were included in the simulation, but the actual dimensions of all shielding materials were used. The copper and the Nantes lead were assumed to be radioactively clean materials. The outer lead was assumed to contain ^{210}Bi contamination (from ^{210}Pb decay). Since 1 cm of high-purity lead provided adequate shielding from the external lead contamination, it was only necessary to consider ^{210}Bi decays in the inner region of the external shield. Thus, electrons were generated uniformly throughout the inner 2 cm of the outer lead with an isotropic initial direction and with an energy distribution given by a beta decay spectrum with an endpoint of 1.16 MeV [85].

Figure 3.14 shows the total energy deposited in the simulated detector for 15,000,000 ^{210}Bi decays for each of the three shielding configurations: no liner; copper liner; and Nantes lead liner. The simulations show the same general trends as the measurements. With no liner, the typical ^{210}Bi bremsstrahlung shape is apparent. The large peak which appears in the region of 50 keV to 100 keV is due to the decreased photon cross-section just below the lead K-edge; no lead fluorescence x-rays are generated in the simulations. With the copper liner, the general shape of the spectrum is unchanged, but the continuum level is reduced by the expected factor of about 2. The low energy peak is no longer present since photons of this energy are attenuated by the inner copper shield. With the Nantes lead liner, only a small, relatively flat background remains.

As discussed previously, the detector cryostat used for these measurements contains a small quantity of ^{210}Pb contamination in addition to small amounts of U and Th contamination. If the Nantes lead itself is not a significant source of background, and if the 1-cm-thick Nantes lead liner along with the 1.6-cm-thick copper used for the top and bottom of this liner is sufficient to completely block the background due to the outer lead, then the measured spectrum obtained with the Nantes lead liner represents the background due to contamination in the detector and its cryostat, as well as any other

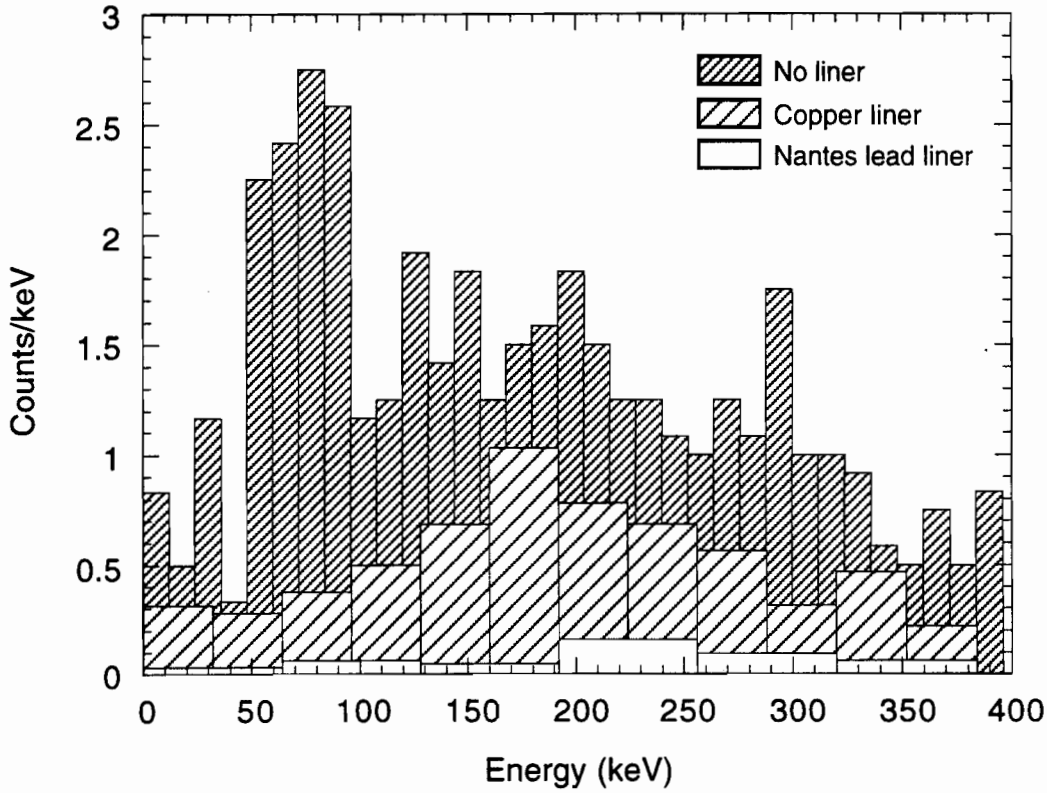

Figure 3.14: Monte Carlo simulation of the energy deposited in a Ge detector from ^{210}Bi decays in the outer lead shield for the same three shielding configurations used in the measurements shown in Figure 3.12.

backgrounds that penetrate through the 15 cm of outer lead. The simulation with the Nantes lead liner shows that this liner does not completely block the background from the outer lead, but it does reduce it substantially. Therefore, an estimate of the contribution to the background due to contamination in the Glover lead with no liner and with the copper liner can be made by subtracting the measured spectrum obtained with the Nantes lead liner from the measured spectra obtained with and without the copper liner. This can then be compared to the simulations with no liner and with the copper liner to determine the level of contamination in the Glover lead.

In the measured spectrum with the Nantes lead liner subtracted from the measured spectrum with the copper liner, there were 1029 counts/day in the 850 g detector in the region of 100 keV to 400 keV. In the simulation with the copper liner, there were 172 counts in this energy range in the 1 kg detector after 15,000,000 simulated decays. Requiring these two counting rates to be the same gives the equivalent time for the simulation as 0.142 days. To estimate the decay rate per unit mass, the mass of the lead in which there were (simulated) decays (i.e., the mass of the inner 2 cm of the Glover lead shield) is also necessary. This is given by

$$8\left[(14.7)(7.08)^2\text{cm}^3 - (12.7)(5.08)^2\text{cm}^3\right]\left[0.01135\ \text{kg/cm}^3\right] = 37.15\ \text{kg} \tag{3.1}$$

Finally, an estimate for the activity of ^{210}Bi, and hence, assuming equilibrium, the activity of ^{210}Pb in the Glover lead is given by

$$\frac{(15,000,000\ \text{decays})}{(37.15\ \text{kg})(0.142\ \text{days})}\left(\frac{1\ \text{day}}{86400\ \text{seconds}}\right) = 33 \pm 3\ \text{Bq/kg} \tag{3.2}$$

Similarly, for the case with no liner, there were 2086 counts/day between 100 keV and 400 keV in the background subtracted spectrum measured with the 850 g detector while in the simulation there were 363 counts in the same energy range in the 1 kg detector after 15,000,000 simulated decays. This leads to a simulation time of 0.148 days and a ^{210}Pb activity of 32 ± 2 Bq/kg in the Glover lead, which is compatible with the above result.

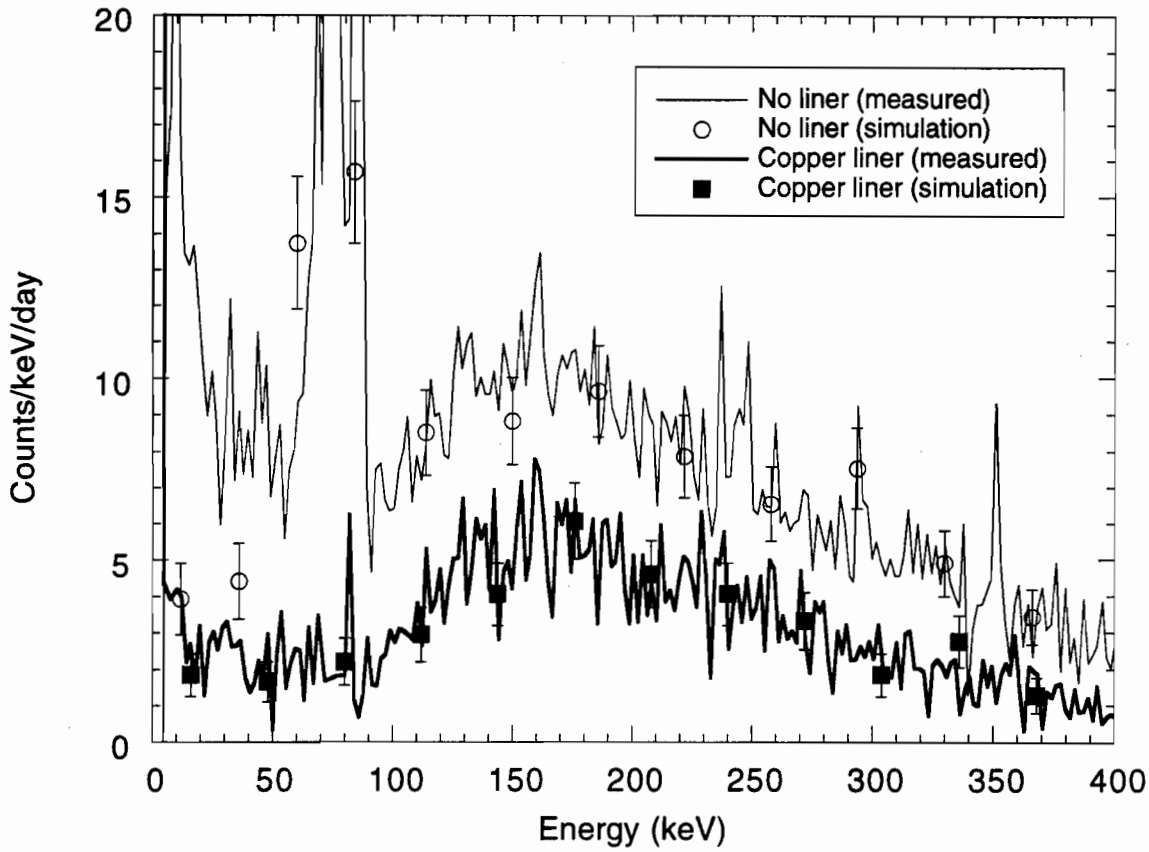

Figure 3.15: Comparison of background-subtracted measured photon spectra with Monte Carlo simulations. (See text for details of the background subtraction).

Using the equivalent simulation time obtained above to scale the simulated spectra, Figure 3.15 shows the excellent agreement between the simulations and measurements for energies above 100 keV. Because the simulation does not generate any lead fluorescence lines, the peak between 50 keV and 90 keV is only qualitatively reproduced in the no liner configuration.

3.3.3 Effects of Radon

All the measurements discussed so far were made inside relatively small-cavity shields. For the dark matter experiment, however, a large-cavity shield is necessary to accommo-

date neutron shielding inside the lead. This can lead to additional photon backgrounds because radon gas collects inside the shield and subsequently decays. This effect is clearly demonstrated in Figure 3.16.

The HPGe detector was placed inside a 15-cm-thick lead shield. The inner 5 cm of the shield was constructed using Glover lead, while the remainder of the shield was constructed with Stanford lead. The volume of space inside the lead shield was approximately 1.4 m^3. The upper spectrum in Figure 3.16 was then measured. The lower spectrum in Figure 3.16 was obtained when the cavity was continuously flushed with boil-off nitrogen gas from a liquid nitrogen dewar. The increased background level and the prominence of the ^{214}Pb (242 keV, 295 keV, 352 keV) and ^{214}Bi (609 keV, 768 keV, 934 keV) lines observed in the upper spectrum, along with the lack of the corresponding ^{226}Ra line at 186 keV, indicate the presence of radon gas inside the shield cavity. This background is effectively removed when the radon gas is prevented from collecting in the cavity as illustrated by the lower curve in Figure 3.16. The background level obtained with the nitrogen purge is the same as the background level obtained in the small cavity shield (see Figure 3.11, curve without veto system active).

3.3.4 Effects of Hydrogen Capture Gamma

The neutron shielding required for the dark matter experiment can also lead to additional photon backgrounds, particularly at low energies. This effect is illustrated in Figure 3.17. The upper curve in this figure was obtained by filling the inside of the large-cavity shield discussed in the previous section with polyethylene. The polyethylene was screened for radio-impurities before it was used and no significant level of contamination was found. The lower spectrum was obtained with the shield empty. In both cases, a nitrogen purge was used to minimize radon gas contamination.

With the polyethylene installed, the low-energy background level increased by almost a factor of 5. The lack of any prominent photon peaks (aside from the positron annihilation

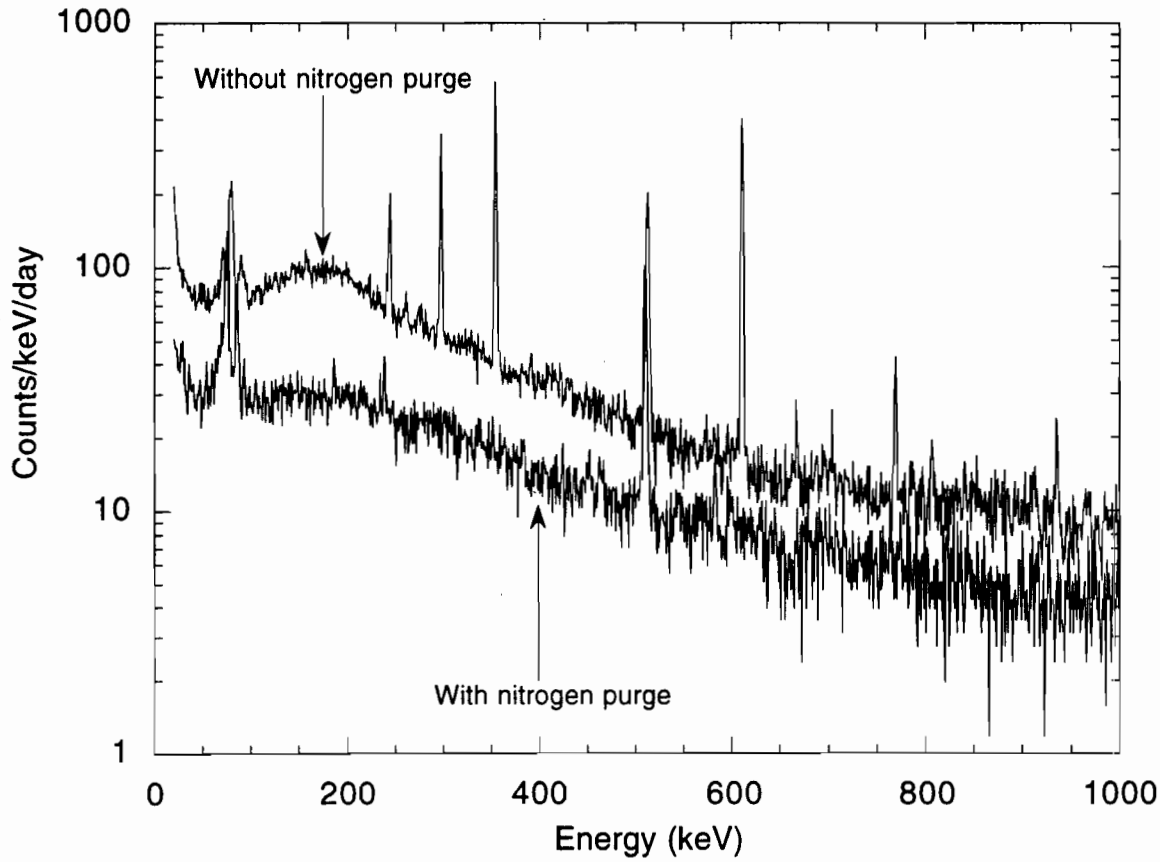

Figure 3.16: Background spectra measured inside a 15-cm-thick lead shield at the Stanford Underground Facility. To obtain the lower curve, the shield cavity was flushed with boil-off gas from a liquid nitrogen reservoir to expel radon. For the upper curve, no nitrogen purge was used. The increased background and prominent ^{214}Pb and ^{214}Bi lines indicate the presence of radon gas inside the shield cavity.

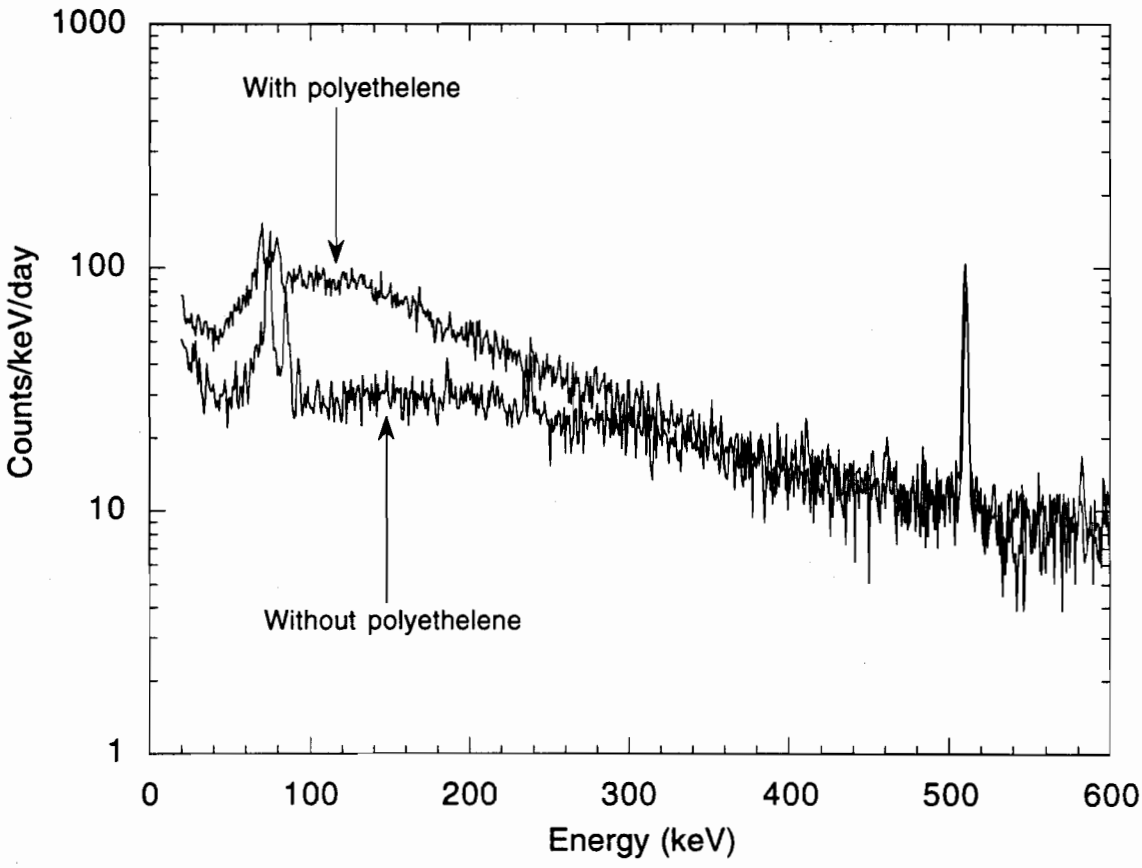

Figure 3.17: Background spectra measured inside a 15-cm-thick lead shield at the Stanford Underground Facility with and without the shield cavity filled with polyethylene.

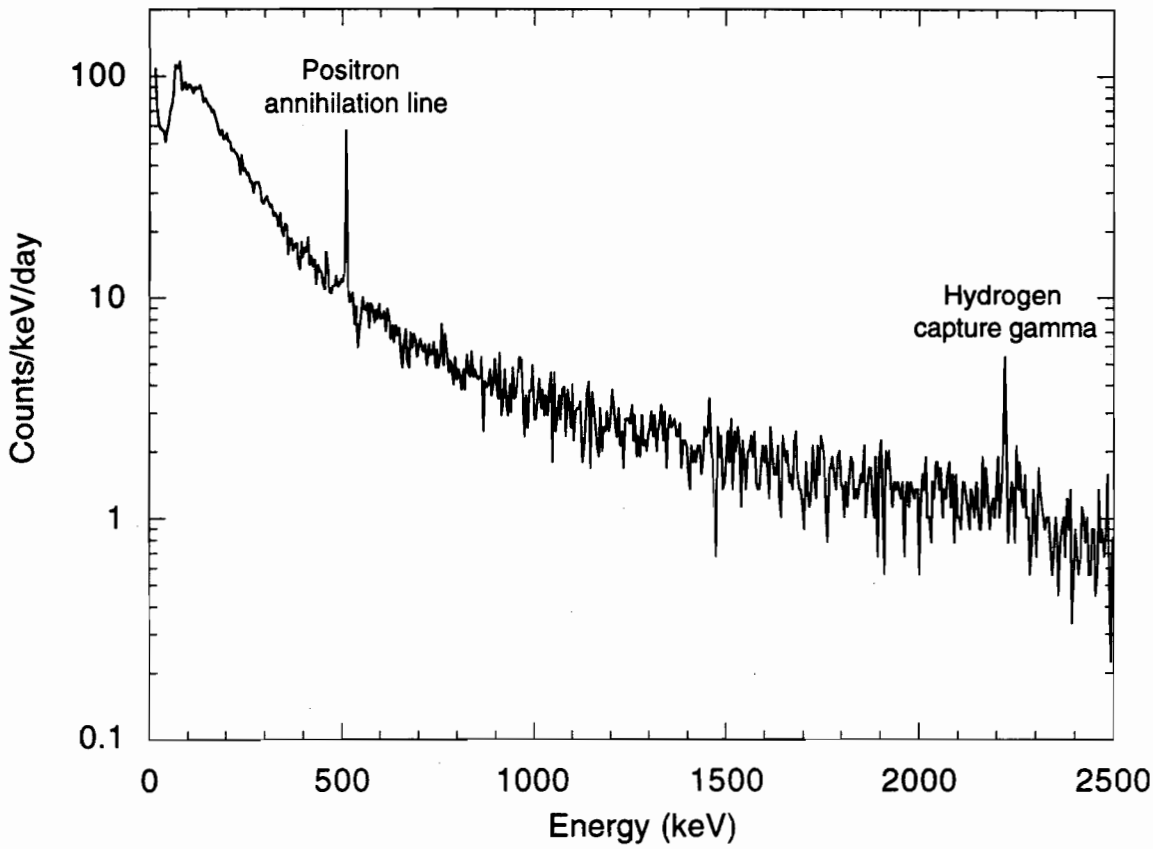

Figure 3.18: Measured background spectrum inside a 15-cm-thick lead shield filled with polyethylene. The line observed at 2223 keV is due to the capture gamma emitted when neutrons are captured by hydrogen in the polyethylene.

line at 511 keV) is consistent with the polyethylene being relatively free of radio-impurities. The increased background is due to the 2223 keV photons that are emitted when neutrons are captured by hydrogen in the polyethylene. This capture gamma line is easily seen in Figure 3.18.

3.4 Photon Background Simulations

Since the majority of photon backgrounds originate from the uranium and thorium decay chains, a method for determining these backgrounds is desirable. In order to use GEANT3

to simulate these backgrounds, appropriate event generation is necessary. The full decay chains are rather complicated, but reasonable approximations can be made to simplify the process. First, the chain is assumed to be in secular equilibrium. This determines the relative intensities of the photon emission from each daughter. Every photon line with an intensity of at least 0.1% is included in the event generation. Secondly, correlations between decays are not accounted for; photons are simply generated according to their relative intensities. Finally, alpha and beta decays within the chains are not included. Because the range of alpha particles is extremely short, alpha decays are not expected to contribute to the background unless the contamination is contained within the detector itself. Similarly, the range of beta particles is quite small so that external beta decays are not expected to contribute much to the background. However, high energy beta decays can lead to substantial bremsstrahlung which may have to be accounted for.

Two energy calibration runs were performed while the HPGe detector was in Oroville using a uranium ore sample as the calibration source. This sample of natural uranium provided the entire uranium chain in secular equilibrium. The measured spectrum is shown in the upper part of Figure 3.19. This measurement was then simulated using GEANT3 with the event generation described above. For the purposes of these simulations, the HPGe detector was modeled as a 900 g germanium cylinder with a 1-mm-thick dead layer on the outer surface and a 1 cm diameter, 5-cm-long hole in the center of the cylinder. The only part of the cryostat to be included in the simulation was the 0.127-cm-thick magnesium endcap surrounding the germanium. The actual dimensions of all shielding materials were used. Detector resolution was included in the simulation to make the simulation easier to compare to the measurements. The result of the simulation is shown in the lower part of Figure 3.19. The agreement between the measurement and the simulation at first sight is quite remarkable.

Closer inspection of the low energy portion of the spectra, however, shows that the simulated rate underestimates the measured rate for energies below 400 keV (see Figure 3.20). This results from neglecting the beta decays in the uranium chain in the simulation. By

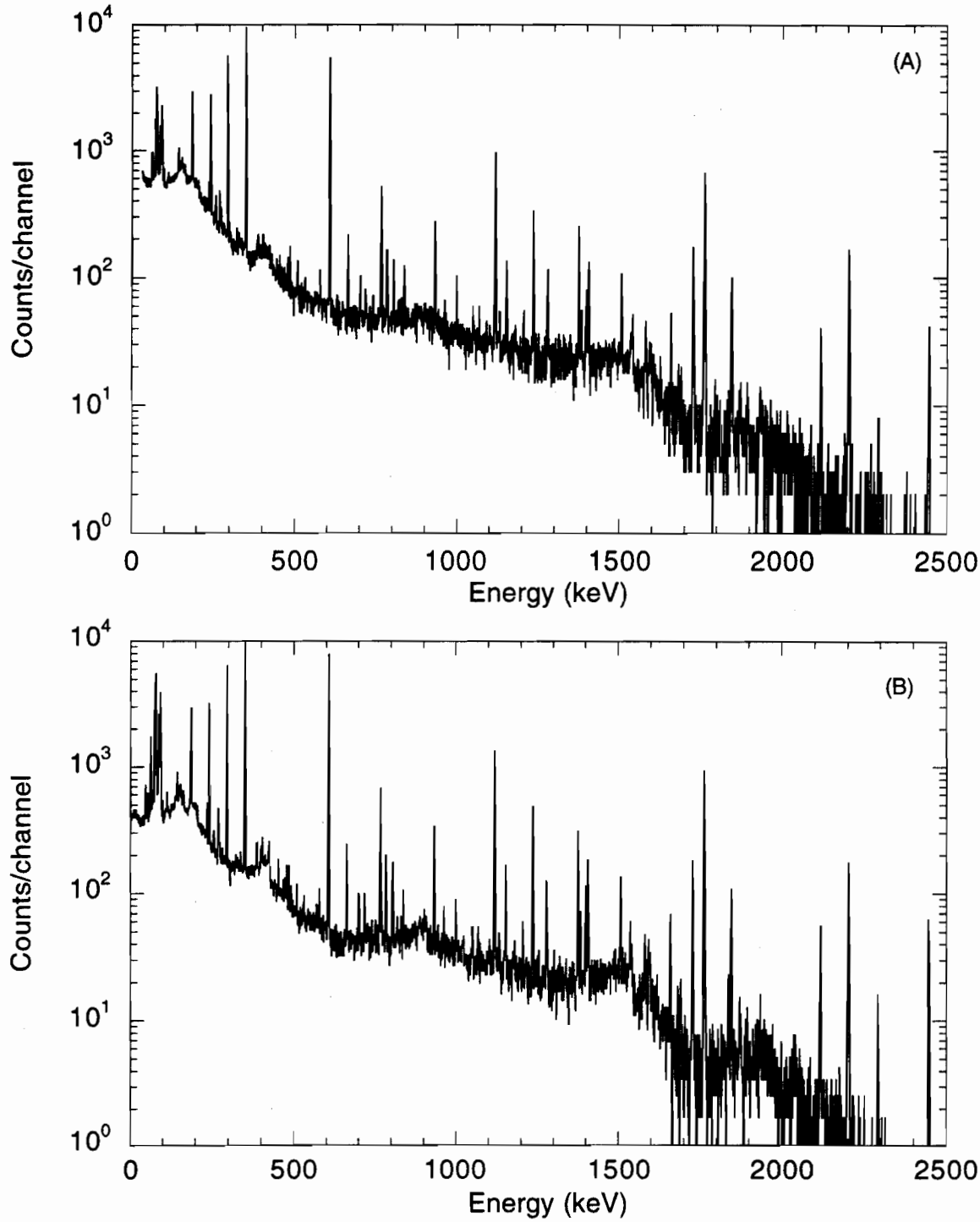

Figure 3.19: (A) Background spectrum from a natural uranium ore sample measured with a HPGe detector. (B) Simulation of the background due to the photon lines in the uranium decay chain.

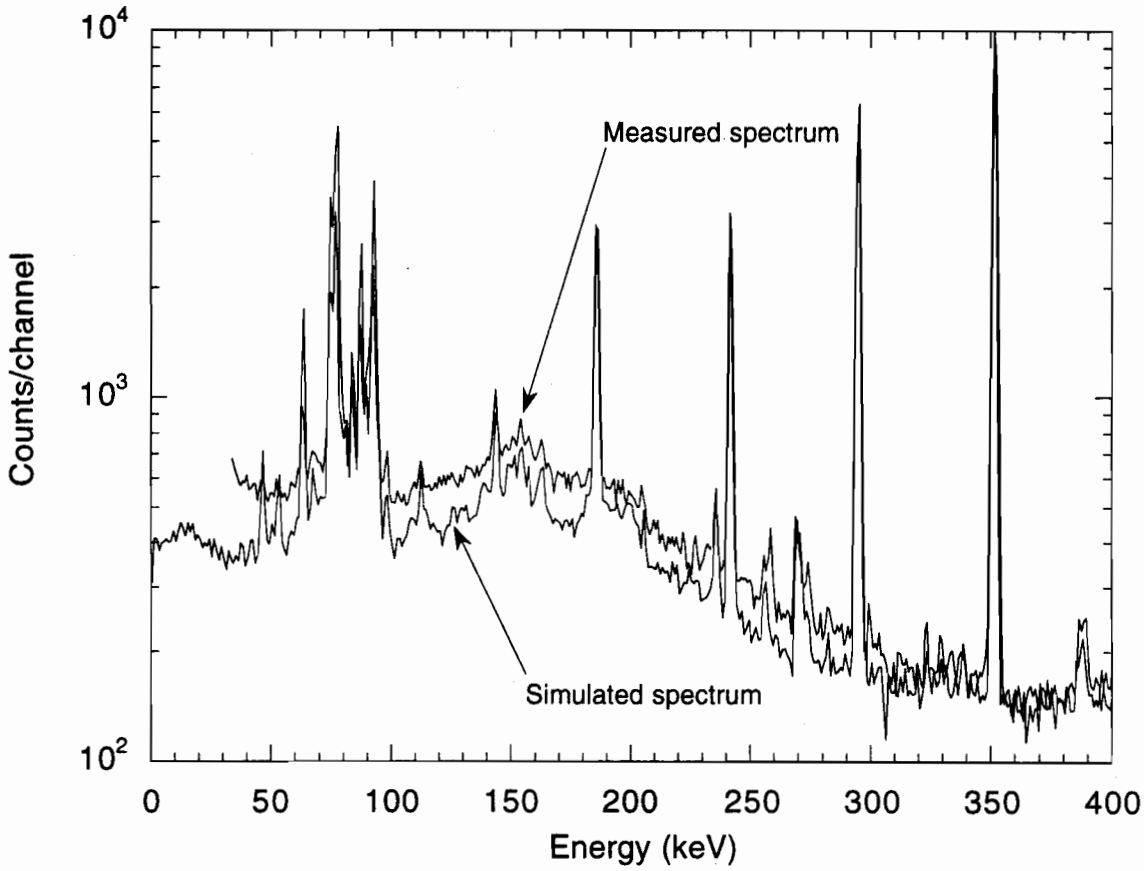

Figure 3.20: Comparison of the low energy portion of the measured spectrum from a natural uranium ore sample and the simulated spectrum obtained from the photon lines in the uranium decay chain.

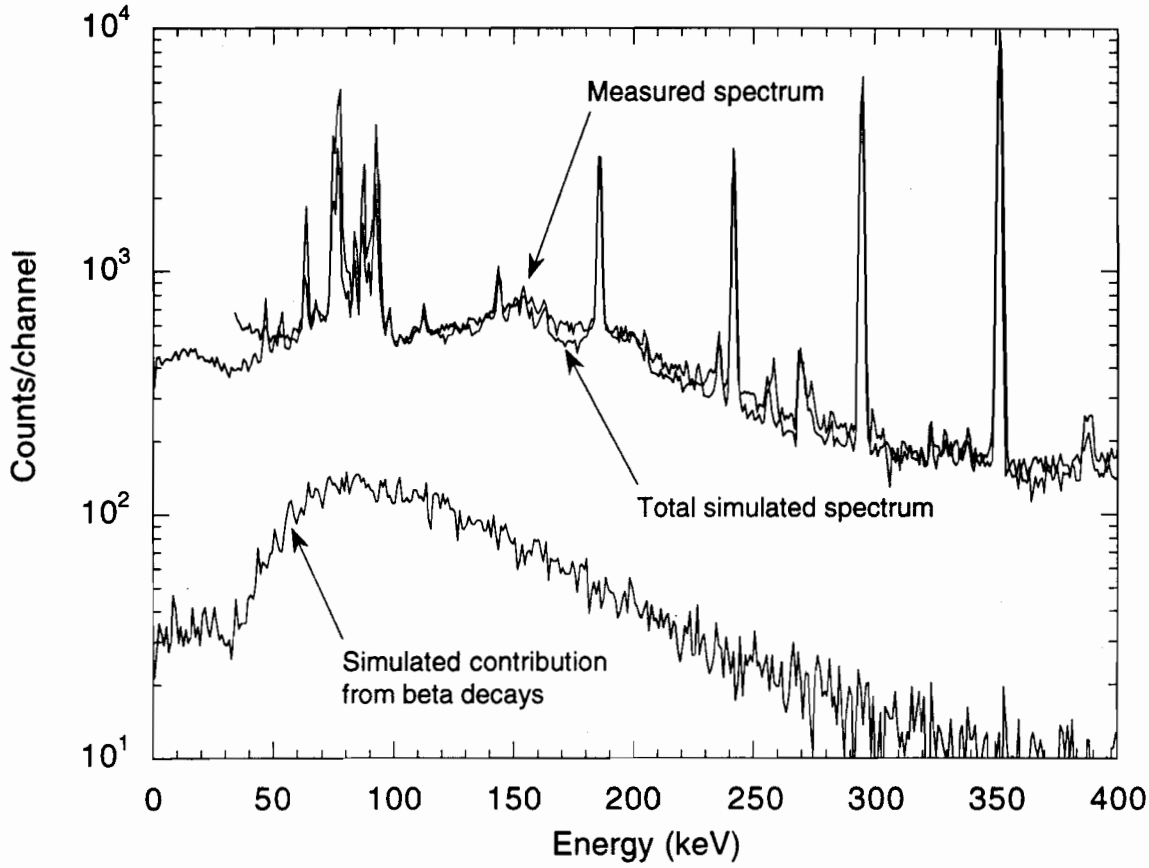

Figure 3.21: Comparison of the low energy portion of the measured spectrum from a natural uranium ore sample and the simulated spectrum obtained when including both the photon lines and the beta decays in the uranium decay chain. Also shown is the contribution to the simulated background from the beta decays alone.

including the beta decays, the simulated spectrum becomes almost indistinguishable from the measured spectrum (see Figure 3.21).

The excellent agreement between the simulation and the energy calibration run of the HPGe detector confirms that GEANT3 can be used successfully to predict the backgrounds from uranium contamination. In a similar manner, backgrounds from thorium contamination can also be determined. Furthermore, the simulations show that including only the photon lines from the decay chains is nearly sufficient to reproduce the background. This can greatly reduce the computation time for the simulations. This powerful

simulation tool will be discussed further in Section 5.5.

Chapter 4

Neutron Backgrounds

4.1 Sources of Background Neutrons

There are four main sources of neutrons: (α, n) reactions; fission; cosmic ray muon interactions; the hadronic component of the cosmic rays. The first two sources are often collectively referred to as neutrons from natural radioactivity. Different sources dominate the background at different depths. At shallow depths, the hadronic component of the cosmic rays dominates the neutron flux while at great depths the neutron flux is dominated by natural radioactivity. Cosmic ray muon interactions are the dominant source of neutrons at intermediate depths. Each of these sources will be discussed in detail in the following sections.

4.1.1 Neutron Production from Natural Radioactivity

All geological formations contain some level of uranium and thorium. These primordial nuclides can lead to neutron production through (α, n) reactions and spontaneous fission. The number of neutrons produced depends mainly on the concentration of uranium and thorium in the rock. Table 4.1 summarizes the neutrons production rate from natural radioactivity in several types of rock.

Table 4.1: Neutron production rate in rock from natural radioactivity. Data taken from [73].

	Contamination		Neutron Production (n/g/y)		
Type of Rock	U (ppm)	Th (ppm)	U (α, n)	Th (α, n)	fission
granite	5	11	7.85	7.755	2.33
limestone	1	1	0.64	0.285	0.467
sandstone	1	1	0.837	0.38	0.467
granite A	1.32	7.79	2.24	5.92	0.62
granite B	6.25	4.59	10.62	3.49	2.92
granite C	1.83	4.38	3.11	3.33	0.85
salt I	0.30	2.06	1.60	4.77	0.14
salt II	0.13	1.80	4.17	0.69	0.06

Neutron Production from (α, n) Reactions

The α-particles originate from decays in the uranium and thorium chains. The highest energy α-particle occurring in these chains is only 8.78 MeV (from the decay of ^{212}Po in the thorium chain), which is below the threshold energy for the (α, n) reaction in ^{16}O, ^{28}Si and ^{40}Ca which make up about 79% of the earth's crust by weight [73]. Thus the α-particles react mainly with elements such as Al, Na and less abundant isotopes of oxygen, magnesium and silicon to produce neutrons with energies of a few MeV. The actual neutron production rate depends on the type of rock present, and it varies from about 2 neutrons/g/y in sandstone to about 16 neutrons/g/y in granite. For sites deeper than $\sim$ 100 m.w.e. this is the dominant process contributing to the underground neutron flux.

Neutron Production from Spontaneous Fission

The uranium and thorium present in the rock also undergo spontaneous fission with the following half lives:

$$^{238}\mathrm{U} : \mathrm{T}_{1/2\ fission} = 1.01 \times 10^{16}\ \mathrm{y}$$

$$^{235}\mathrm{U} : \mathrm{T}_{1/2\ fission} = 1.8 \times 10^{17}\ \mathrm{y}$$

$$^{232}\mathrm{Th} : \mathrm{T}_{1/2\ fission} = 5 \times 10^{19}\ \mathrm{y}$$

The rate of neutrons emitted from 1 kg of natural U by spontaneous fission has been estimated by several authors and the average value quoted in [73] is 16 neutrons/kg/s. Thus a U concentration in rock of 1 ppm corresponds to a production rate of 0.5 neutrons/g/y. The longer fission half-life of ^{232}Th generally makes neutron production from ^{232}Th fission negligible compared to spontaneous fission of natural uranium.

4.1.2 Neutron Production from Cosmic Ray Muon Interactions

The cosmic ray muon flux has two components: a fast, high-energy component and a slow, low-energy component. Miyake [86] gives the following empirical formulae for the integral and differential muon intensities at the earth's surface as a function of zenith angle, θ:

$$I(>\mathrm{E}) = \frac{174}{5\mathrm{E}\cos\theta + 400}(5\mathrm{E} + 10\sec\theta)^{-1.57}\frac{\mathrm{E}+15}{\mathrm{E}+10+5\sec\theta} \tag{4.1}$$

$$I(\mathrm{E})\mathrm{dE} = \frac{372}{\mathrm{E}\cos\theta + 80}(5\mathrm{E} + 10\sec\theta)^{-2.57}\frac{\mathrm{E}+15}{\mathrm{E}+15\sec\theta} \tag{4.2}$$

These formulae agree with most experimental observations within 10%. Both components of the cosmic ray muon flux contribute to neutron production. Slow negative muons can be captured to produce neutrons via $\mu^- + \mathrm{p} \rightarrow \mathrm{n} + \nu_\mu$. Fast muons can produce neutrons as a result of photonuclear reactions (γ, n) or photofission (γ, Xn) from both the real and virtual photons associated with the muons. All three of these processes are expected to contribute to the neutron production at the Stanford Underground Facility.

Neutron Production from μ^- Capture

Negative muons slowing down in matter can be captured in the Coulomb field of a nucleus and occupy a Bohr orbital. The muon cascades rapidly ($\sim 10^{-11}$ s) down to the 1s level from which it either decays via

$$\mu^- \rightarrow \mathrm{e}^- + \bar{\nu}_e + \nu_\mu \tag{4.3}$$

or is captured by a proton of the nucleus via

$$\mu^- + \mathrm{p} \rightarrow \mathrm{n} + \nu_\mu \tag{4.4}$$

releasing a neutron. The neutron emission after capture occurs as either direct emission or evaporation. Direct emission refers to the neutrons produced which succeed in leaking out of the nucleus without interacting. The percentage of direct neutrons emitted decreases with increasing mass number, with the fraction of direct neutrons estimated to be (20±2)% in calcium and $(12 \pm 2)\%$ in lead [88]. These neutrons typically have fairly high energies, from a few MeV to up to 40-50 MeV, with a high energy spectrum given by [88]

$$\mathrm{dN(E)} \sim \exp(-\mathrm{E}/\mathrm{E}_0)\mathrm{dE} \tag{4.5}$$

where E is the energy of the emitted neutron and E_0 is the high-energy decay constant. Experimentally, E_0 is found to be of the order of 8 MeV and the general trend is for E_0 to decrease slightly with increasing mass number [88].

The majority of neutrons emitted after capture, however, are evaporation neutrons. In this case, the excitation energy from the neutrons is shared with the other nucleons, forming a compound nucleus in an excited state. The nucleus relaxes by boiling off mainly low-energy neutrons. The energy of these neutrons follows an evaporation-type spectrum

$$\mathrm{dN(E)} \sim (\mathrm{E}/1\ \mathrm{MeV})^{5/11} \exp(-\mathrm{E}/\theta)\mathrm{dE} \tag{4.6}$$

where again, E is the energy of the emitted neutron and θ is the nuclear temperature. Typically, θ is of the order of 1 MeV and is found to decrease slightly with increasing mass number. The neutron multiplicities have been measured by MacDonald et al. [89] and are shown in Table 4.2.

The neutron production rate from μ^- capture can be calculated as

$$\mathrm{P} = \frac{\mathrm{dI}_\mu}{\mathrm{d}h} \frac{\mu^-}{\mu^+ + \mu^-} f_c f_n \tag{4.7}$$

where $\frac{\mathrm{dI}_\mu}{\mathrm{d}h}$ is the muon stopping rate at a depth h which can be determined from the well known experimental intensity-depth relation for muons [86], $\frac{\mu^-}{\mu^+ + \mu^-}$ is the fraction

Table 4.2: Average number of neutrons emitted after muon capture. Data taken from [89].

Element	Average Multiplicity
Al	1.26 ± 0.06
Si	0.86 ± 0.07
Ca	0.75 ± 0.03
Fe	1.13 ± 0.04
Ag	1.62 ± 0.06
I	1.44 ± 0.06
Au	1.66 ± 0.04
Pb	1.71 ± 0.07

of negatively charged muons which can be determined from the measured muon charge ratio [90], f_c is the fraction of the stopped muons which are captured by a proton [91] (the rest of the muons decay) and f_n is the neutron multiplicity discussed above.

Neutron Production from Fast Muon Interactions

Fast muons produce neutrons as a result of interactions of the electromagnetic field of the muons with nuclei, or as a result of photonuclear interactions of real photons contained in showers produced by δ electrons, bremsstrahlung of muons and pair production [92]. In a detailed analysis, Gorshkov and Zyabkin [93] have carefully calculated the fast-muon production of neutrons in lead, cadmium, iron and aluminum at depths up to 1000 m.w.e. and their values are in rather good agreement with experimental values. In a more phenomenological approach, Pritychenko [94] has developed a linear approximation for estimating the photonuclear production at depths of 0 to 100 m.w.e. for elements from carbon to uranium. For this range, the production rate can be estimated by

$$\mathrm{P} = 6.02\mathrm{I}_\mu(h)\mathrm{A}^{0.8}(h+40) \times 10^{-8} \ \text{ neutrons/g/s} \tag{4.8}$$

where $\mathrm{I}_\mu(h)$ is the total muon intensity at a depth h (in m.w.e.) and A is the atomic number of the target element. This simple approximation agrees with the Gorshkov and Zyabkin calculation at about the 10% level.

4.1.3 Hadronic component of the cosmic rays

At very shallow depths, the hadronic component of the cosmic rays is the main source of neutrons. However, this source quickly loses its dominance. At a depth of 5 m.w.e., the contribution to the neutron flux from the hadronic component of the cosmic rays is reduced by a factor of ten. At a depth of 10 m.w.e., the contribution has been reduced by three orders of magnitude [76].

4.1.4 Summary of neutron sources

Figure 4.1 shows the relative importance of various neutron sources as a function of depth. At very shallow depths, below $\sim$ 5 m.w.e., the nucleonic component of the cosmic rays dominates. At intermediate depths, neutron production is dominated by cosmic ray muon interactions. At depths greater than $\sim$ 100 m.w.e., the neutron production rate becomes dominated by the natural radioactivity present in the rock. The curve shown in Figure 4.1 is an average value for non-granitic rock.

4.2 Neutron Monte Carlo Program

In order to interpret the experimental data and to predict detector response, a neutron simulation program was needed. GEANT3 [84], coupled with GHEISHA7 [95], a hadronic shower development program used to generate hadronic interactions, was used as a starting point for the neutron Monte Carlo program. The hadronic interactions implemented in GHEISHA7 include elastic scattering, inelastic incoherent scattering, nuclear fission with inelastic scattering and neutron capture by nuclei. Simulating a given process involves two main steps: evaluate the probability of the process occurring by sampling the total cross-section; generate the final state after the interaction by sampling the differential cross-section. If these interactions result in new particles being generated, these particles are stored and they themselves are then tracked once tracking of the original particle has

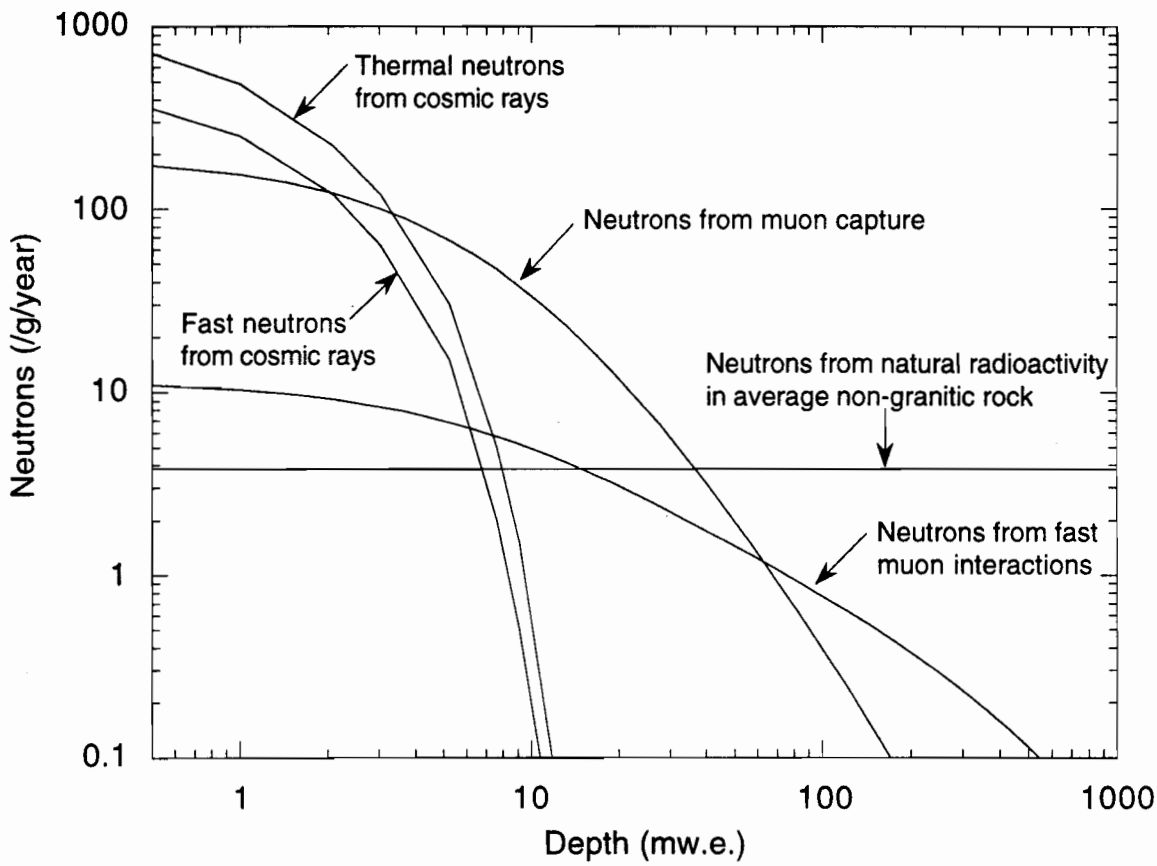

Figure 4.1: Neutron production in rock. Hadronic component of cosmic rays taken from [76]. Neutrons from natural radioactivity taken from [73]. Neutrons from μ^- capture estimated using Equation 4.7. Neutrons from fast muon interactions estimated using Equation 4.8.

been completed.

While GEANT3/GHEISHA7 considers the dominant processes which can occur over a wide range of energies, there are some limitations for neutron tracking, particularly at energies below 1 MeV. In order to use GEANT3/GHEISHA7 for low energy neutrons, two major modifications to the program were required. Firstly, GEANT3/GHEISHA7 had to be modified so that the program would continue to track neutrons below the low-energy cut-off. Along with some other relatively minor changes, this required the addition of cross-section data for low-energy neutrons. Scattering cross-sections were tabulated at 17 energies (from 0.01 eV to 1 MeV) for 15 elements (H, B, C, N, F, Cu, Ge, Pb, O, Si, Al, Fe, Cd, He and Li). Linear interpolation was done between energy bins and resonances in the scattering cross-sections were not included in any detail. The capture cross-sections for these elements were tabulated at 0.025 eV and a simple inverse-velocity fall-off in the cross-section was assumed. This modification was made so that data for additional elements could be easily added as necessary. The inelastic scattering cross-section below 1 MeV was assumed to be zero. For energies above 1 MeV, the original GHEISHA7 cross-section data were used.

Secondly, the tracking routines in GEANT3/GHEISHA7 contained poor approximations for low-energy scattering, and no facility at all for thermal scattering. The routines were modified so that neutrons with energies between 1 MeV and 50 MeV undergo coherent elastic scattering (with the associated forward peaked distribution), while neutrons below 1 MeV are scattered isotropically in the center of mass until their energy drops below 5 kT (where k is Boltzmann's constant and T is the temperature of the scattering material). At this point, a routine for thermal scattering was included. The energy of the scattered neutron is approximated by a thermal Boltzmann distribution [96] (independent of its incident energy) and the scattering is assumed to be isotropic in the center of mass frame.

A further modification was necessary in order to use the simulation program to predict detector response; in addition to tracking the neutrons through the experimental set-up,

it is also necessary to keep track of the nuclear recoils that they produce in the detector. Unfortunately, GEANT3, which was designed to simulate the propagation of elementary particles through some experimental set-up, does not keep track of recoiling nuclei (except for very light nuclei, such as deuterons, tritons and alpha particles, which the program treats as elementary particles). Therefore, some additions to the program were needed in order to provide information about the recoiling nuclei.

The program provides the energy and momentum of the initial particle, prior to scattering, as well as the energy and momentum of the scattered particle (both in the lab frame). It also provides a routine to determine the angle, ψ, that the particle was scattered through (again, in the lab frame). Using this information, along with the mass of the scattered particle, m_1, and the mass of the recoiling nucleus, m_2, the ratio of the kinetic energy of the scattered particle in the lab frame, T_1, to its initial kinetic energy in the lab frame, T_0, can be calculated according to [97]

$$\frac{T_1}{T_0} = \frac{m_1^2}{(m_1+m_2)^2}\left[\cos\psi \pm \sqrt{\left(\frac{m_2}{m_1}\right)^2 - \sin^2\psi}\right]^2 \tag{4.9}$$

where the plus sign for the radical is to be taken unless $m_1 > m_2$, in which case the result is double-valued. Since we are concerned with neutrons scattering from detector nuclei, $m_1 < m_2$ and the result is single-valued. The kinetic energy of the recoiling particle in the lab frame, T_2, can then be determined from

$$\frac{T_2}{T_0} = 1 - \frac{T_1}{T_0} \tag{4.10}$$

Once calculated, the energy of the recoiling nucleus can be returned to the user.

4.3 Detector System for Neutron Measurements

The neutron measurements discussed in this chapter were made using a BF_3 proportional counter. In this type of detector, based on the $^{10}B(n,\alpha)$ reaction, the BF_3 gas acts both as the target for converting slow neutrons into directly detectable secondary particles

as well as a proportional gas. The counter used for the measurements consisted of a stainless steel tube, 5.1 cm in diameter, with an active length of 22.9 cm. This tube contains BF_3 gas, enriched to 96% in ^{10}B, at a pressure of 600 torr. It is surrounded by a 6.4-cm-thick paraffin moderator and a cadmium jacket. The entire system is then enclosed in an aluminum case. Because of the large capture cross-section of cadmium for thermal neutrons, the jacket absorbs incident thermal neutrons before they can interact in the BF_3. High energy neutrons are moderated in the paraffin before being captured on the ^{10}B. With the proportional counter operated in this configuration, it provides a reasonably flat response for neutrons with energies between 10 keV and 20 MeV [98].

4.3.1 Energy Response and Calibration

The relatively flat energy response of this detector was demonstrated by calibrating the detector with a variety of (α,n) neutron sources. Four different sources were used for this purpose: ^{238}PuLi, ^{238}PuF, ^{238}PuB and ^{239}PuBe. The average energy of the neutrons emitted from each source ranged from 0.5 MeV to 4.2 MeV. The emission from the three lower-energy sources (PuLi, PuF and PuB) is narrow band, with the majority of the emission falling within 0.5 MeV to 1.5 MeV of the mean energy. The PuBe source, however, is broad band, with significant emission between 1 MeV and 8 MeV and with some emission continuing up to 11 MeV [99] (see Figure 4.2).

For each of these calibrations, the detector and the neutron source were elevated 140 cm above the thick concrete floor, and the source was placed 100 cm away from the detector. In this configuration, the increase in flux seen by the detector due to neutrons scattering from the floor had been previously determined by the Health Physics Group at LBNL [100]. The unit flux response of the detector, defined as the observed counting rate for an incident flux of one fast neutron per cm^2 per second, was determined for each of the four sources and the results are shown in column three of Table 4.3. For the three higher energy sources, the unit flux response was found to be independent of the source,

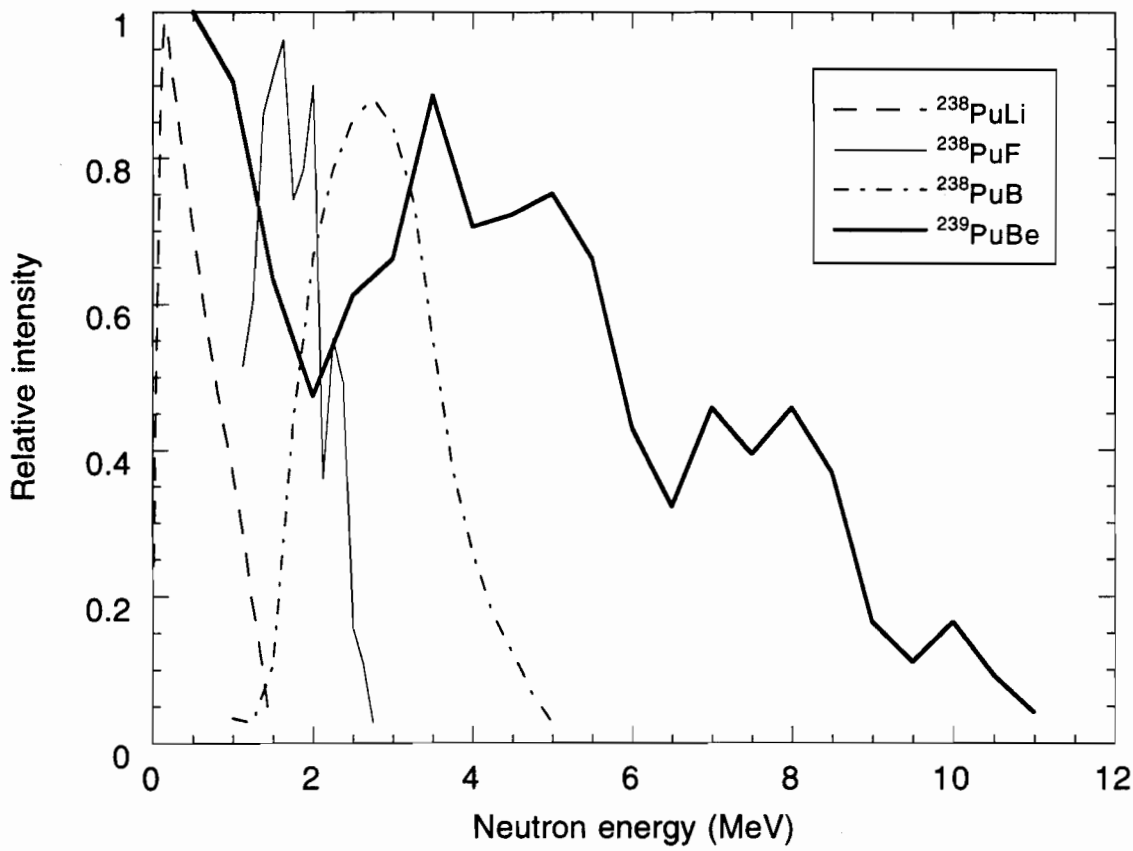

Figure 4.2: Neutron emission spectra for the various (α,n) neutron sources used to calibrate the BF_3 proportional counter. Data taken from [99].

Table 4.3: Unit flux response of the BF_3 proportional counter to various (α,n) neutron sources as measured and as determined by the neutron simulation program.

Neutron Source	Mean Neutron Energy (MeV)	Unit Flux Response Measured (counts/s)	Unit Flux Response Simulated (counts/s)
PuLi	0.53	28.7 ± 0.2	25.5 ± 0.8
PuF	1.75	24.2 ± 0.2	33.5 ± 1.0
PuB	2.84	23.7 ± 0.2	29.0 ± 0.8
PuBe	4.23	24.2 ± 0.2	24.7 ± 0.8

and hence, independent of the energy. For the lowest energy source, the measured unit flux response was only slightly higher. Since there is only a very small dependence on energy, the unit flux response can be averaged to give 25 counts/s.

In order to check the neutron Monte Carlo program discussed in Section 4.2, the program was used to simulate these calibrations. First, mono-energetic neutrons were used as input for the simulation, in an attempt to reproduce the predicted energy response function [98] of the BF_3 counter. As shown in Figure 4.3, the simulated response as a function of energy agrees quite well with the predicted response function over most of the energy range. The simulation, however, does give a somewhat elevated response rate in the energy range of 1.5 MeV to 4 MeV. This is presumably due to several broad scattering resonances for carbon in this energy range that are not accurately accounted for in GEANT3. Furthermore, the simulations show that the energy response remains relatively constant for energies down to 1 keV, but it begins to fall at lower energies..

Next, appropriate energy spectra for the various (α,n) neutron sources were used as input for the simulation in order to reproduce the calibration measurements themselves. The unit flux responses determined by the simulation for the various neutron sources are shown in column four of Table 4.3. As expected, the simulated unit flux response for the PuF source and the PuB source are somewhat higher than the measured values since much of the neutron emission from these sources is in the energy range where the

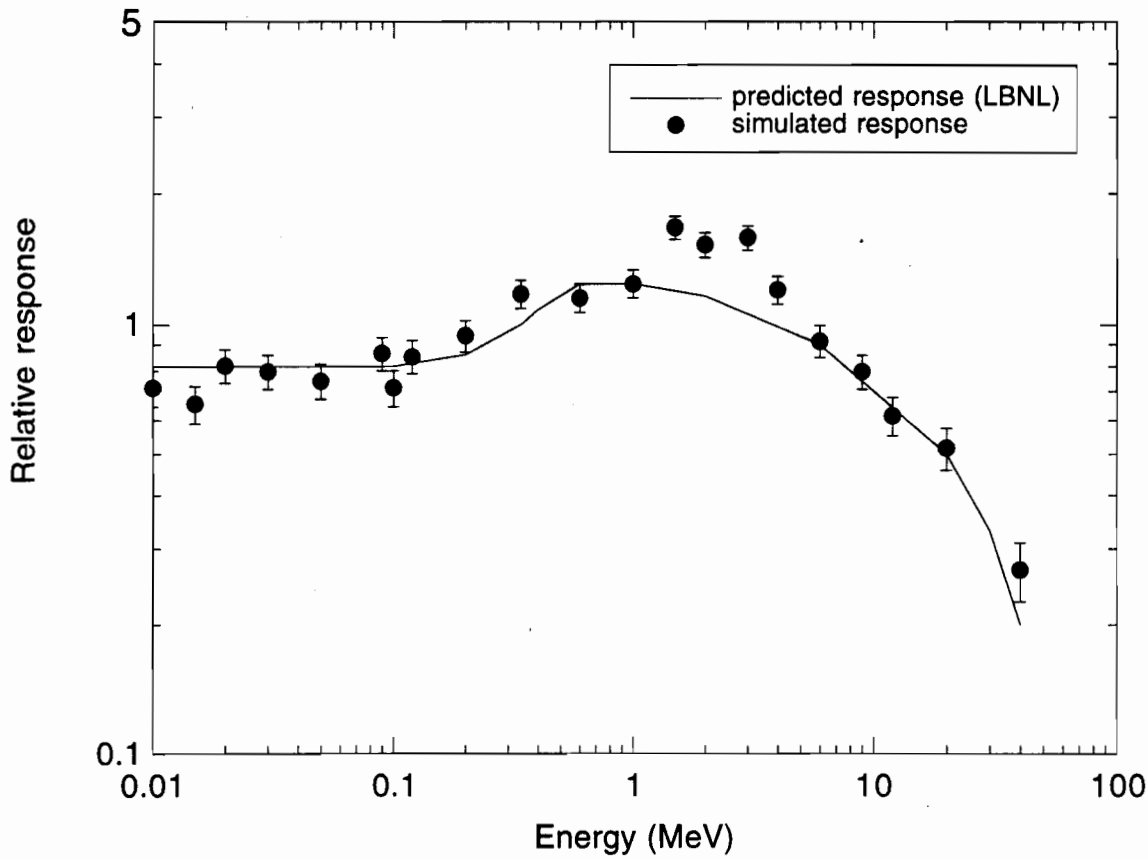

Figure 4.3: Predicted [98] energy response function of the BF_3 counter compared to the energy response of the counter simulated with the neutron Monte Carlo program.

simulation gives an elevated response. On the other hand, the agreement between the measured and simulated response for the PuBe source, which has the broadest energy emission, is excellent.

At this point, it should be noted that the unit flux response that has been determined both experimentally and with the neutron simulation program, is for neutrons from a point source directed towards the side of the counter. If the counter is immersed in an isotropic sea of neutrons, the unit flux response of the detector will be somewhat lower because some of the neutrons will be incident on the ends of the counter. In this case, the isotropic flux is defined as the number of neutrons crossing a sphere with unit cross-sectional area per unit time. The Monte Carlo program must be used to determine the unit flux response of the detector in this configuration. In the simulation, a uniform isotropic neutron flux is generated around the counter and the response is observed. As before, the response is relatively energy independent, and an average response of (19.6 ± 0.5) counts/s is obtained for an isotropic flux of 1 neutron/cm^2/s.

4.3.2 Detector Background

When using the BF_3 counter to measure small neutron fluxes, it is important to account for both types of detector background: counts due predominantly to alpha-particles emitted from radioactive contaminants within the BF_3 tube and counts due to neutrons which have been produced by muon interactions within the detector. These two types of backgrounds are referred to as alpha background and muon-induced background respectively.

The level of alpha background can be determined by measuring the counting rate obtained at a deep site with the bare BF_3 tube surrounded with a suitable material to absorb the local thermal neutrons, or by looking at the level of the flat portion of the measured spectrum above the neutron peak. Both methods were used to determine the level of this background in the BF_3 counter. The bare tube was taken to Oroville, where it was surrounded with 5 cm of boric acid to shield the detector from external thermal

neutrons, and the resulting counting rate was measured. Then the counter was taken to the Stanford Underground Facility, surrounded by 40 cm of wax to reduce the external neutron flux incident on the detector, and the counting rate above the neutron peak was measured. Based on these two measurements, the contribution of alpha background was found to be (20 ± 1) counts/day. Since the level of this detector background is well determined experimentally, it can be subtracted from all subsequent measurements made with this detector.

The level of muon-induced background cannot be measured directly. Its contribution, however, can be determined by using the neutron Monte Carlo program discussed in Section 4.2. Details of this simulation are discussed later in this chapter. Since the contribution due to muon-induced background cannot be measured, this background was not subtracted from any of the subsequent measurements. However, its contribution was included in all simulations of BF_3 measurements made in the Stanford Underground Facility.

4.4 Measured Neutron Backgrounds in the Stanford Underground Facility

Using the BF_3 counter, the ambient flux of neutrons with energies above a few hundred eV was measured in the Stanford Underground Facility and found to be $(8.1 \pm 0.6) \times 10^{-5}$ neutrons/cm^2/s. This is almost two orders of magnitude higher than the flux of neutrons, with energies between 1 keV and 25 MeV, measured at a deep underground site [101]. The main reason for the huge difference in the measured neutron backgrounds at these two sites is the neutron production at the shallower site due to cosmic ray muon interactions.

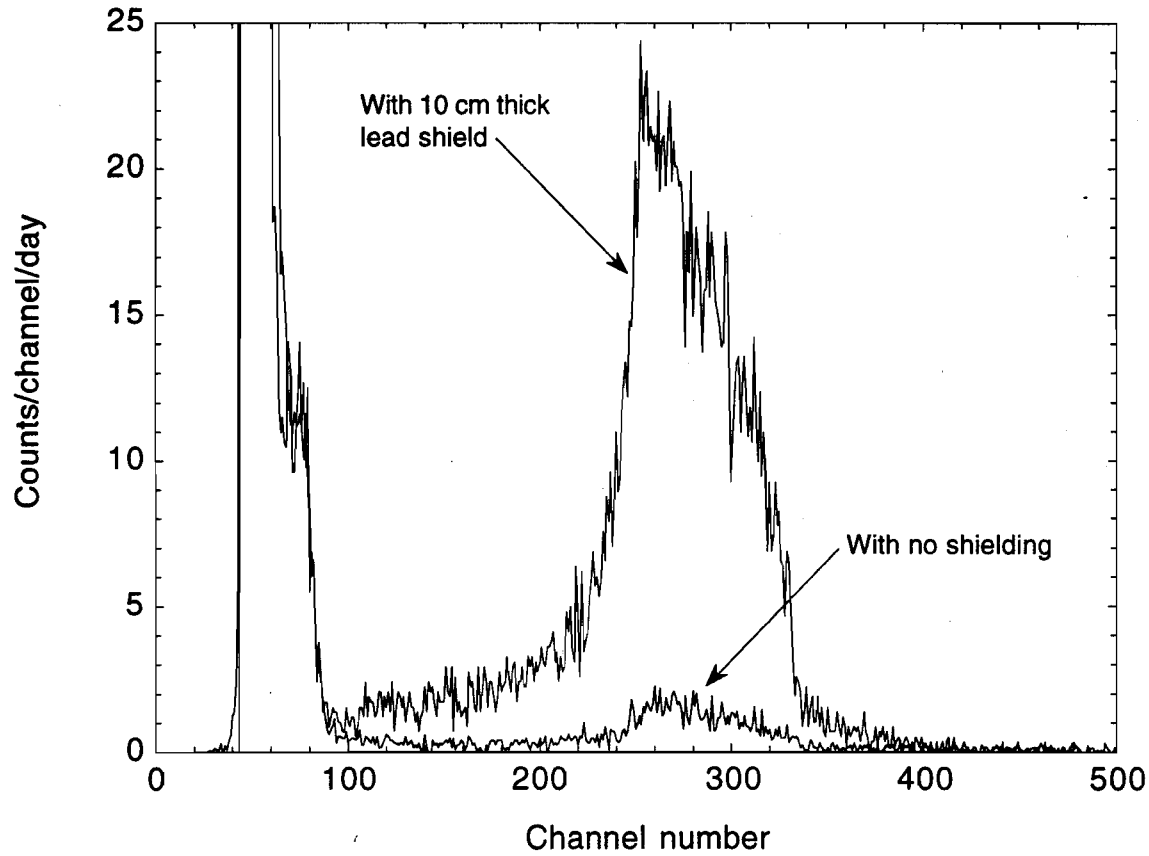

Figure 4.4: Pulse height spectra measured with the BF_3 counter in the Stanford Underground Facility. To obtain the upper curve, the BF_3 counter was surrounded by a 10-cm-thick lead shield. To obtain the lower curve, no shielding was used. (The low amplitude events are due to γ-interactions and electronics noise).

4.4.1 Effects of Photon Shielding on Neutron Backgrounds

As discussed previously, the ambient photon flux must be reduced in order to reach the background levels necessary for a dark matter search. The reduction of the external photon flux is accomplished by surrounding the detector with a lead shield. At the shallow depth of the Stanford Underground Facility, however, this lead shield becomes a neutron source due to the muon-induced interactions in the lead. This effect is clearly demonstrated in Figure 4.4 which shows the spectra measured with the BF_3 counter in the Stanford Underground Facility with and without a 10-cm-thick lead shield. Without

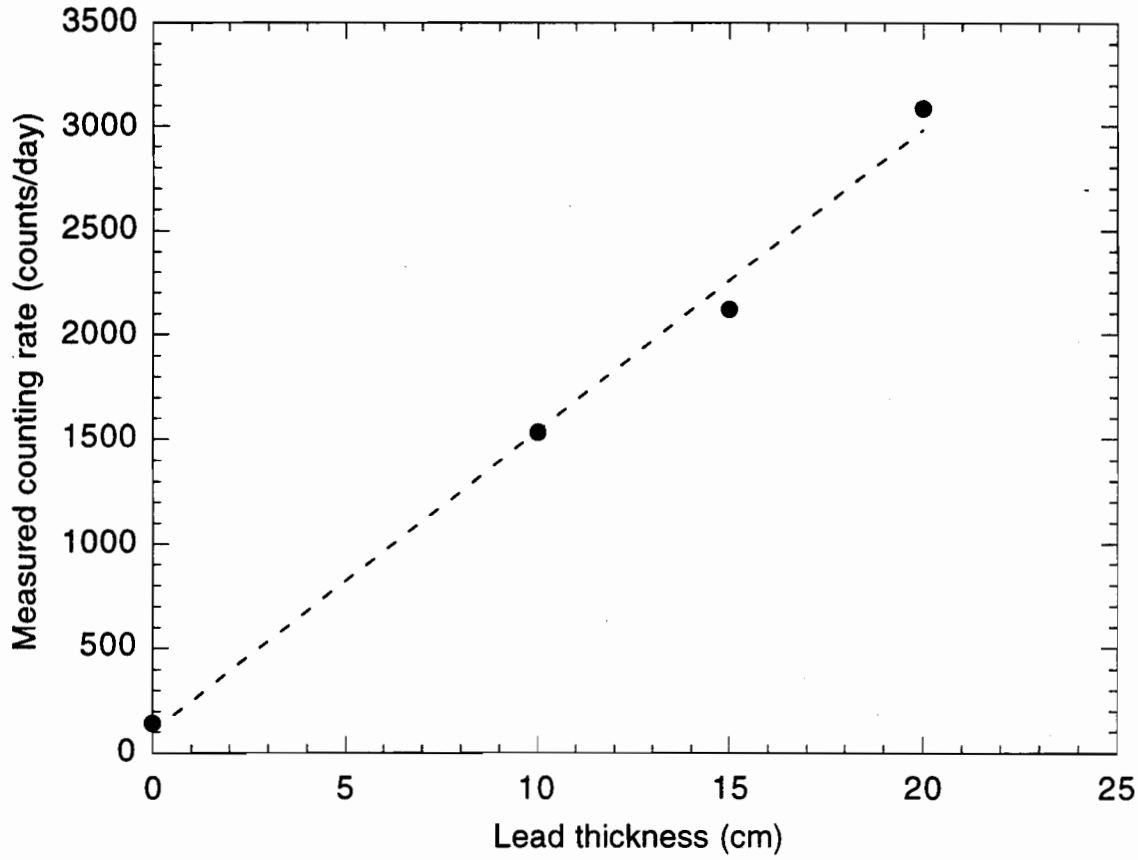

Figure 4.5: Measured counting rate in the BF_3 counter inside small lead shields of various thickness in the Stanford Underground Facility. Error bars are smaller than the size of the data points. Dashed line is a linear fit to the data.

the lead shield, the measured counting rate is (143 ± 5) counts/day, while with the lead shield, the measured counting rate is (1783 ± 19) counts/day. The increase in the neutron flux by more than a factor of ten is due to the neutrons produced in the lead by cosmic ray muon interactions.

In an effort to determine the neutron production rate in lead at this particular depth, a series of measurements was made with the BF_3 counter surrounded by small, rectangular shields of various thicknesses. Figure 4.5 shows the measured count rate as a function of lead shield thickness. As expected, the measured counting rate increases linearly with lead thickness.

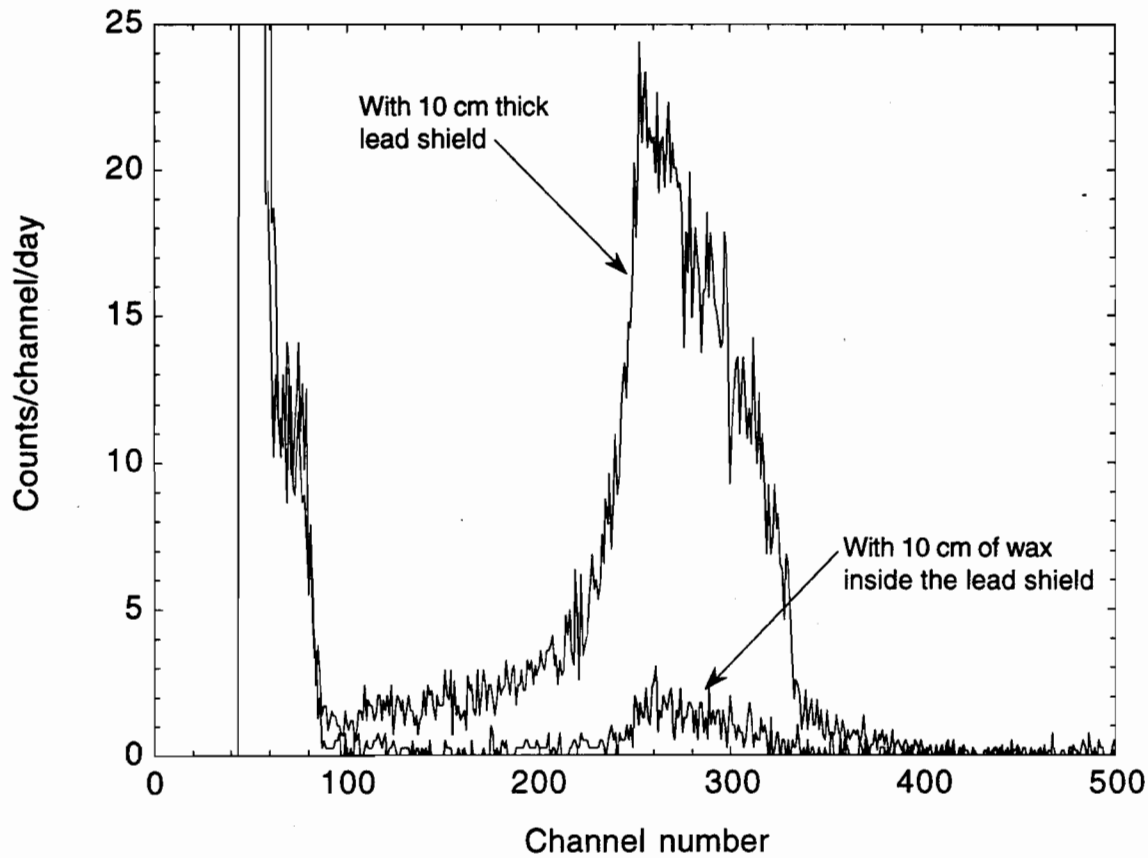

Figure 4.6: Pulse height spectra measured with the BF_3 counter in the Stanford Underground Facility. To obtain the upper curve, the BF_3 counter was surrounded by a 10-cm-thick lead shield. To obtain the lower curve, a 10-cm-thick wax shield was placed between the detector and the outer lead shield.

4.4.2 Moderating the Muon-Induced Neutron Backgrounds

To reduce the neutron flux to acceptable levels, a suitable material can be placed inside the lead shield to moderate and capture the muon-induced neutrons produced in the lead. As illustrated in Figure 4.6, by placing a 10-cm-thick wax shield between the BF_3 counter and the outer lead shield, the measured counting rate is reduced to (128 ± 7) counts/day, slightly lower than the rate obtained without the lead shield.

To study this effect further, a series of measurements was performed inside a large, 10-cm-thick lead shield in the Stanford Underground Facility. The outer dimensions of

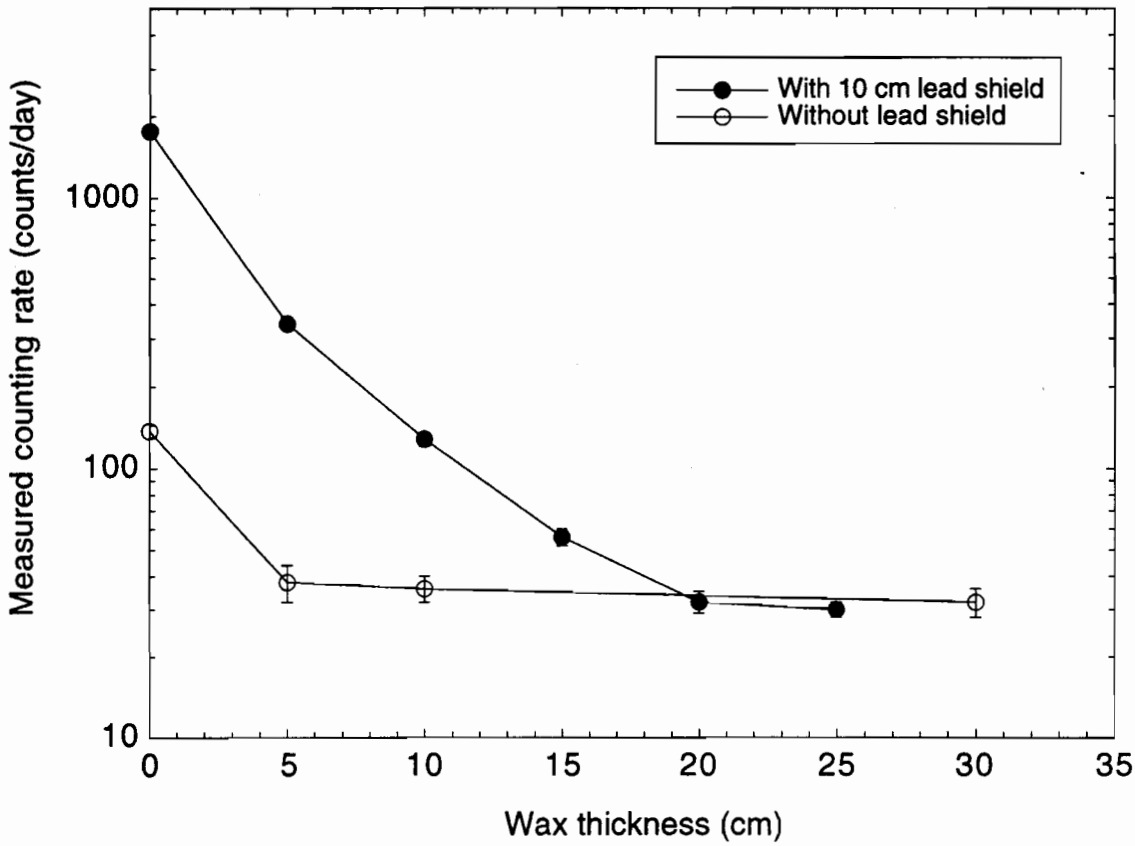

Figure 4.7: Measured counting rate in the BF_3 counter in the Stanford Underground Facility as a function of the wax thickness surrounding the counter. To obtain the filled circles, a 10-cm-thick lead shield was placed around the wax shield and the counter. To obtain the open circles, no lead shielding was used.

the lead shield were approximately 132 cm × 132 cm × 142 cm. The BF_3 counter was surrounded by various thickness of wax and placed inside the lead shield. The resulting counting rates as a function of wax thickness are presented in Figure 4.7. Also presented in this figure is the counting rate obtained with the BF_3 counter surrounded by various thickness of wax without the lead shield in place. In both cases, the measured neutron flux decreases as the thickness of the wax begins to increase. Eventually, however, the measured neutron flux stops decreasing and becomes relatively constant. Furthermore, the limiting value that is reached is the same with or without the lead shield. This limit

is reached because the cosmic ray muons are also producing neutrons in the wax and the BF_3 counter itself (see the earlier discussion on detector background).

4.5 Simulation of the Neutron Backgrounds in the Stanford Underground Facility

In order to understand the neutron backgrounds in the Stanford Underground Facility and to test the validity of the neutron simulation program, the background measurements described in the previous sections were simulated with the neutron Monte Carlo program discussed in Section 4.2. Along with the simulation program, models for the neutron production at the Stanford Underground Facility were necessary. Neutrons produced by cosmic ray muon interactions are the main source of neutrons at this site. These neutrons can be produced by both the slow component of the cosmic rays (μ^- capture) and the fast component of the cosmic rays (photonuclear reactions) as discussed in detail in Section 4.1.2.

4.5.1 Neutron Production in Lead

As demonstrated by the measurements made in the Stanford Underground Facility, the lead shielding is the dominant source of neutrons. Cocconi and Cocconi Tongiorgi [87] have reported that at 20 m.w.e., only about half of the neutrons produced in lead by cosmic ray muon interactions are from muon capture. The remainder are produced via fast muon interactions. In constructing the model for the neutron production in the lead to be used in the simulation, however, the energy spectrum of the neutrons emitted following μ^- capture was used for all of the emitted neutrons.

As discussed in Section 4.1.2, the spectrum of neutrons emitted following μ^- capture consists of two components: an evaporation component and a direct component. The majority of the neutrons emitted following μ^- capture in lead are evaporation neutrons

which, for energies below 4.5 MeV, follow the evaporation spectrum given by Equation 4.6 with a nuclear temperature $\theta = (1.22 \pm 0.06)$ MeV [102]. The direct neutrons are emitted at higher energies, and for energies above 4.5 MeV, they follow the exponential spectrum given by Equation 4.5. The high-energy decay constant for lead has been measured by Schröder *et al.* [102] as $E_0 = (9.0 \pm 1.2)$ MeV. They also report that approximately 10% of the emitted neutrons have energies above 4.5 MeV. Combining this information and normalizing leads to the following model for the spectrum of neutrons emitted from the lead used in the simulations:

$$dN(E) = \begin{cases} 0.812(E/1\ \text{MeV})^{5/11} \exp(-E/1.22\ \text{MeV})dE & \text{for } E < 4.5\ \text{MeV} \\ 0.018 \exp(-E/9.0\ \text{MeV})dE & \text{for } E > 4.5\ \text{MeV} \end{cases} \tag{4.11}$$

With this model for the input neutron spectrum, the measurements inside the small lead shields of various thicknesses could be simulated with the neutron Monte Carlo program. The geometry of the set-up used in the simulations is illustrated in Figure 4.8. The BF_3 counter is modeled as a tube of BF_3 gas, 30 cm long and 5 cm in diameter. The density of the gas is taken as 0.0021 g/cm^3 and it is assumed to be enriched to 100% ^{10}B. The paraffin surrounding the gas is simply modeled as CH_2 with a density of 0.935 g/cm^3. The cadmium surrounding the paraffin is assumed to be 0.08 cm thick, and it does not cover the ends of the counter. A count is recorded in the simulation if a neutron is captured in the BF_3 tube.

The lead shield thicknesses of 10 cm, 15 cm and 20 cm used were the same as in the measurements. The neutrons were generated uniformly throughout the lead shield, with a random, isotropic initial direction and an energy distribution according to the spectrum constructed above. The simulation was normalized so that the simulated counting rate obtained with the 10-cm-thick lead shield was equal to the measured counting rate obtained with the same lead shield. This normalization determines the neutron production rate in the lead at this depth:

$$\frac{\text{simulation captures}}{\text{neutron triggers}} \times \frac{\text{neutron production}}{\text{kg} \cdot \text{day}} \times \text{mass of shield} = \frac{\text{measured counts}}{\text{day}} \tag{4.12}$$

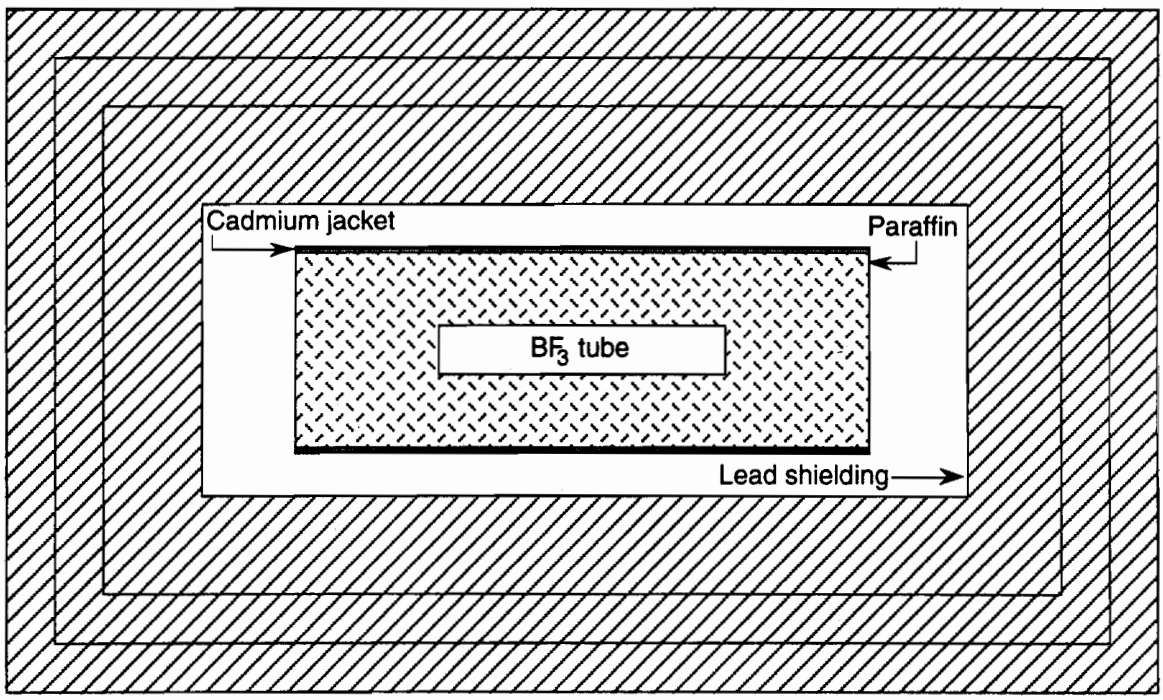

Figure 4.8: Geometry of the set-up used in the simulations of the neutron background inside various lead shields in the Stanford Underground Facility. Lead shield thicknesses of 10 cm, 15 cm and 20 cm are shown.

For the 10-cm-thick lead shield simulation, there were 1794 captures after 500,000 neutron triggers and the total mass of the lead shield was 1737.9 kg. According to the above formula, this leads to a neutron production rate of (243 ± 9) neutrons/kg/day in lead at this depth. With this production rate determined, there are no longer any free parameters for the 15-cm-thick shield and the 20-cm-thick shield simulations. Nevertheless, as illustrated in Figure 4.9, the agreement between the simulations and measurements is excellent. This production rate can be compared to the values of 200 neutrons/kg/day reported by Cocconi and Cocconi Tongiorgi[87] and 233 neutrons/kg/day predicted by Gorshkov and Zyabkin[93] for the cosmic ray induced neutron production rate in lead at 20 m.w.e. It is not unexpected that the rate determined here is slightly higher than these values, since the depth of the Stanford Underground Facility is only 16 m.w.e.

Using this production rate, the measurement made inside the large 10-cm-thick lead shield was also simulated. In this case, however, there seemed to be a large discrepancy between the simulation and the measurement; the simulation predicted a counting rate of (2673 ± 117) counts/day while the measured rate was only (1769 ± 16) counts/day. The reason for this apparent discrepancy was that the simulation did not include the 1.3-cm-thick plywood box that lined the inside walls of the large lead shield. The plywood was used only to provide structural support for the shield and it was not expected to effect the background significantly. Lining the inside of the small 10-cm-thick lead shield with 1.3 cm of plywood and re-measuring the background demonstrated that this amount of plywood was sufficient to moderate and capture some of the neutrons produced in the lead, reducing the measured counting rate from (1534 ± 17) counts/day without the plywood to (1383 ± 20) counts/day with the plywood. Thus it was necessary to include the plywood in the simulation. The exact chemical composition of the wood used was unknown, but there is no important difference in elementary chemical composition among woods [103]. For the simulations, the wood was taken to be composed of 49% carbon, 6% hydrogen, 44% oxygen and 1% nitrogen by weight, with a density of 0.7 g/cm^3. With the plywood included, the simulated counting rate became (1359 ± 35) counts/day which agrees well

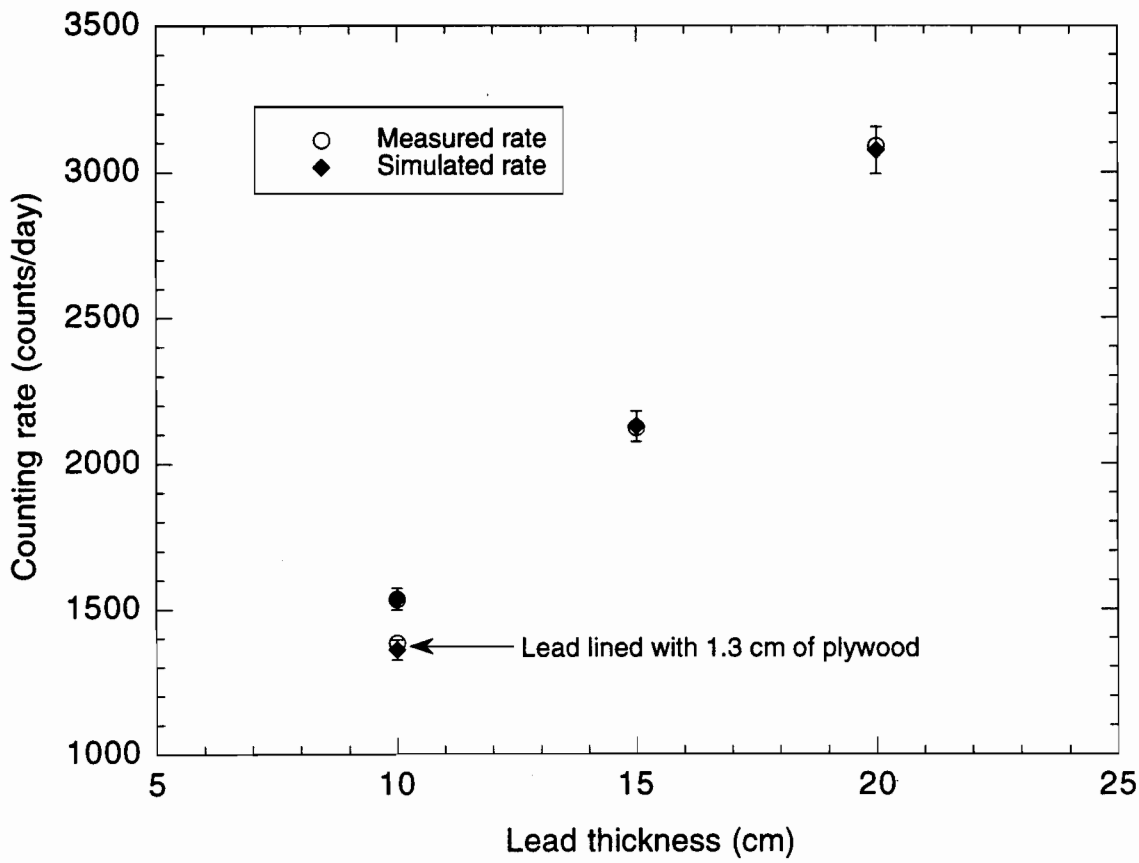

Figure 4.9: Comparison of the measured counting rate and the simulated counting rate in the BF_3 counter inside small lead shields of various thickness in the Stanford Underground Facility. Errors in the measured points (open circles) are smaller than the size of the data points. Statistical errors in the simulated points (filled diamonds) are indicated with error bars. To obtain the lower points with the 10-cm-thick lead shield, the inside of the shield was lined with 1.3 cm of plywood. The plywood moderates and captures some of the neutrons produced in the lead thereby reducing the counting rate.

with the measurement (see Figure 4.9). Including the plywood in the simulation with the large lead shield reduces the simulated rate to (1925 ± 72) counts/day which is much closer to the measured rate.

4.5.2 Effects of the Moderator

To simulate the measurements in which wax was used to moderate the neutron flux from the lead, the muon-induced neutron production in the wax itself must also be considered. In order to account for the neutrons emitted from the wax, a model for the energy spectrum of these neutrons is necessary. Since the percentage of high-energy neutrons emitted following μ^- capture increases with decreasing mass number [88], the relative number of high energy neutrons emitted from the wax, which is primarily carbon by weight, should be greater than the relative number of high energy neutrons emitted from the lead. Of the neutrons emitted after μ^- capture in carbon, 38% will follow an evaporation spectrum with a nuclear temperature of $\theta = 1.01$ MeV and 62% will be direct and follow an exponential distribution with a high energy decay constant $E_0 \sim 7.5$ MeV. Combining this information and normalizing leads to the following model for the spectrum of neutrons emitted from the wax used in the simulations:

$$dN(E) = \begin{cases} 0.577(E/1\ \text{MeV})^{5/11} \exp(-E/1.01\ \text{MeV})dE & \text{for } E < 2\ \text{MeV} \\ 0.105 \exp(-E/7.5\ \text{MeV})dE & \text{for } E > 2\ \text{MeV} \end{cases} \tag{4.13}$$

Unfortunately, the production rate of neutrons in wax at this depth cannot be measured in the same manner as it was for the lead because other sources dominate the neutron flux. As discussed in Section 4.1.2, however, the production rate can be calculated. Pritychenko [94] has estimated the production rate of neutrons in wax at this depth to be 11 neutrons/kg/day. This value has been used in the simulations.

As mentioned in Section 4.3.2, it is also necessary to account for the muon-induced background in the BF_3 counter. This background cannot be measured directly, but can be estimated with the neutron simulation program. To accomplish this, the counter was

considered to be composed of 4 parts: the inner stainless steel tube which holds the gas; the pre-amplifier package at one end of the tube; the moderator surrounding the tube; and the outer case, consisting of the aluminum jacket and the cadmium sheet. For the metal parts, a neutron production rate of 100 neutrons/kg/day with the lead emission spectrum was used. For the moderator, a production rate of 11 neutrons/kg/day with the wax emission spectrum was used. This leads to a simulated rate of (17 ± 1) count/day due to muon-induced background in the detector.

With all the necessary pieces in place, the measurements made inside the large, 10-cm-thick lead shield in the Stanford Underground Facility can be simulated. Figure 4.10 and Table 4.4 show the components of the simulated counting rate in the BF_3 counter as a function of the wax thickness surrounding the counter inside the lead shield. With a thin layer of moderator, the counting rate is dominated by the neutron production in the lead. When the moderator becomes thicker than 20 cm the counting rate becomes dominated by the muon-induced neutron production in the counter itself. Furthermore, at this moderator thickness, the contribution to the counting rate from neutron production in the moderator has levelled off. Thus, the contribution to the neutron background from muon-induced neutron production in the moderator cannot be reduced by further increasing the thickness of the moderator. Figure 4.11 compares the total simulated counting rate to the measured counting rate in the same configuration. The agreement between the simulations and the measurements is quite good, provided that the muon-induced background in the counter is taken into account.

4.5.3 Neutron Production in the Surrounding Rock

To simulate the measurements in which no lead shielding was used, a model for the ambient neutron flux in the Stanford Underground Facility was required. Constructing this model is more difficult because there are three sources of neutrons which must be considered: neutrons from natural radioactivity; neutrons produced by cosmic ray muon

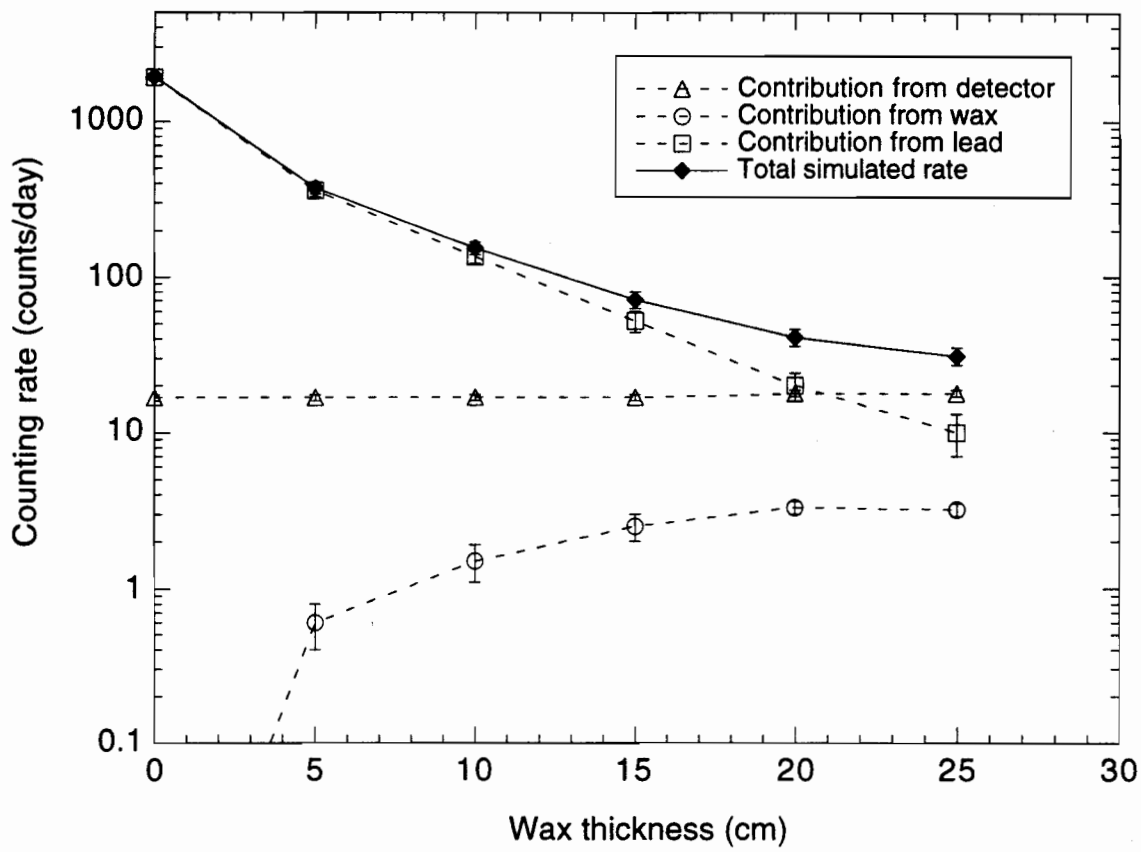

Figure 4.10: Components of the simulated counting rate in the BF_3 counter in the Stanford Underground Facility as a function of the wax thickness surrounding the counter inside a 10-cm-thick lead shield. In the simulations, neutrons are produced by cosmic ray muon interactions in the detector, the wax surrounding the detector and the lead shield. Neutrons from the surrounding environment are not included in these simulations because environmental neutrons are negligible compared to the neutrons produced in the lead shield.

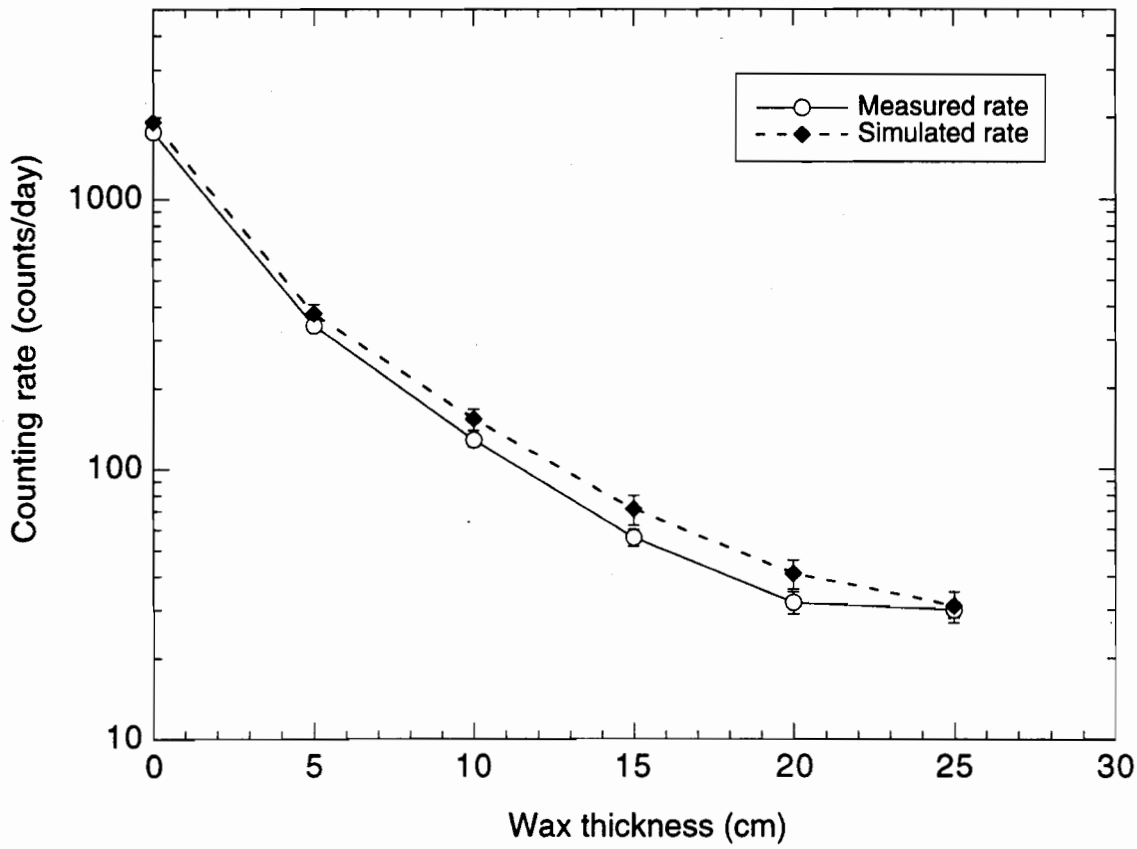

Figure 4.11: Comparison of the measured counting rate and the simulated counting rate in the BF_3 counter in the Stanford Underground Facility as a function of the wax thickness surrounding the counter inside a 10-cm-thick lead shield.

Table 4.4: Comparison of the simulated and measured counting rate in the BF_3 counter inside a 10-cm-thick lead shield in the Stanford Underground Facility as a function of the wax thickness surrounding the detector. For the simulations, the total rate is broken down into components due to muon-induced neutron production in the detector, the wax and the lead shielding.

	Components of Simulated Counting Rate				
Wax Thickness (cm)	Detector Neutrons (counts/day)	Wax Neutrons (counts/day)	Lead Neutrons (counts/day)	Simulated Rate (counts/day)	Measured Rate (counts/day)
0	16.7 ± 0.8	0 ± 0	1908 ± 71	1925 ± 72	1769 ± 16
5	16.7 ± 0.8	0.6 ± 0.2	358 ± 31	375 ± 32	339 ± 11
10	16.7 ± 0.8	1.5 ± 0.4	135 ± 13	153 ± 14	128 ± 7
15	16.7 ± 0.8	2.5 ± 0.5	52 ± 8	71 ± 9	56 ± 4
20	17.8 ± 0.9	3.3 ± 0.3	20 ± 4	41 ± 5	32 ± 3
25	17.8 ± 0.9	3.2 ± 0.2	10 ± 3	31 ± 4	30 ± 2

interactions; and neutrons present in the hadronic component of the cosmic rays.

The neutron production rate due to natural radioactivity depends on the concentration of U and Th present in the rock. Furthermore, the neutron flux that is present also depends on the neutron attenuation properties of the rock itself. Since the exact composition of the surrounding rock was unknown, typical values given by Florkowski *et al.* [73] were used: 30 neutrons/kg/day from (α, n) reactions and 4.1 neutrons/kg/day from ^{238}U fission. The spectra of neutrons from fission and (α, n) reactions in thick targets fall off rapidly above 2 MeV [104] and have similar shapes. Therefore, neutrons from both of these processes were characterized by a fission spectrum of the form [105]:

$$dN(E) \sim (E/1\ \mathrm{MeV})^{1/2} \exp(-E/1.29\ \mathrm{MeV})dE \tag{4.14}$$

where E is the energy of the emitted neutron.

The spectrum of the neutrons emitted as a result of muon interactions is constructed in a manner similar to that which was used for the lead and the wax, using results for elements commonly found in geological formations, or elements with atomic numbers similar to commonly found elements. Sundelin [106] gives the high energy decay constant

for silicon as $E_0 \sim 7$ MeV while Singer [88] gives the nuclear temperature for sulphur as $\theta \sim 1.7$ MeV. Singer also reports that 16.2% of the emitted neutrons have energies above 11.5 MeV while 28.7% of the emitted neutrons have energies above 7.73 MeV. This leads to a spectrum of the form:

$$dN(E) = \begin{cases} 0.38(E/1\ \text{MeV})^{5/11} \exp(-E/1.7\ \text{MeV})dE & \text{for } E < 4.5\ \text{MeV} \\ 0.10 \exp(-E/7.0\ \text{MeV})dE & \text{for } E > 4.5\ \text{MeV} \end{cases} \tag{4.15}$$

Florkowski *et al.* [73] estimate the neutron production rate in the rock by muon interactions at a depth of 17 m.w.e. as 41 neutrons/kg/day.

Neutrons from hadron cascades contribute only to the fast neutron flux. At this depth, the major contributions to the neutron flux above 10 MeV are from muon interactions and hadron cascades, and the neutron yield from cascades is approximately one half of the neutron yield (at all energies) from muon interactions [107]. Thus, a production rate of 19 neutrons/kg/day for neutrons from the cascade is considered. For energies between 10 MeV and 50 MeV, the spectrum of neutrons in the cascade falls off as $\sim E^{-1/2}$. At higher energies, it falls more rapidly [104].

Combining these three components results in an estimate of the neutrons produced (or present) in the surrounding rock at the Stanford Underground Facility. The total spectrum is shown in Figure 4.12, along with the relative contributions from the individual components. This spectrum is used in the simulations of the measurements made in the Stanford Underground Facility without any lead shielding.

Figure 4.13 compares the measured counting rate to the simulated counting rate in the BF_3 counter in the Stanford Underground Facility as a function of the wax thickness surrounding the counter. The relative contributions to the simulated counting rate are shown in Table 4.5. In this case, the agreement between the simulations and the measurements is not quite as good, but the general trends of the measurements are reproduced. The discrepancies are most likely due to the inaccuracies involved in estimating the neutron emission spectrum from the surrounding rock and in describing the material through

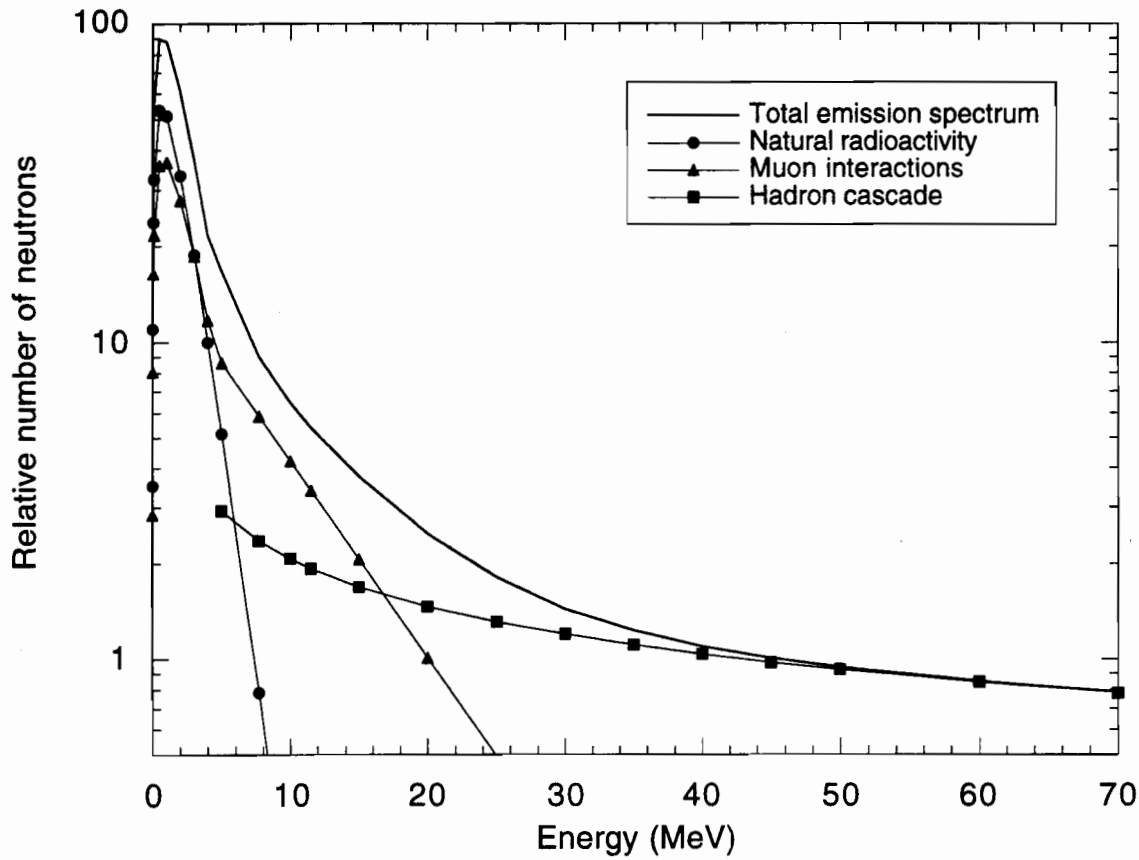

Figure 4.12: Estimate of the spectrum of neutrons emitted from the surrounding rock in the Stanford Underground Facility used in the simulations shown in Figure 4.13. The total emission spectrum is the sum of neutrons from natural radioactivity, neutrons from cosmic ray muon interactions and neutrons in the hadronic component of the cosmic rays.

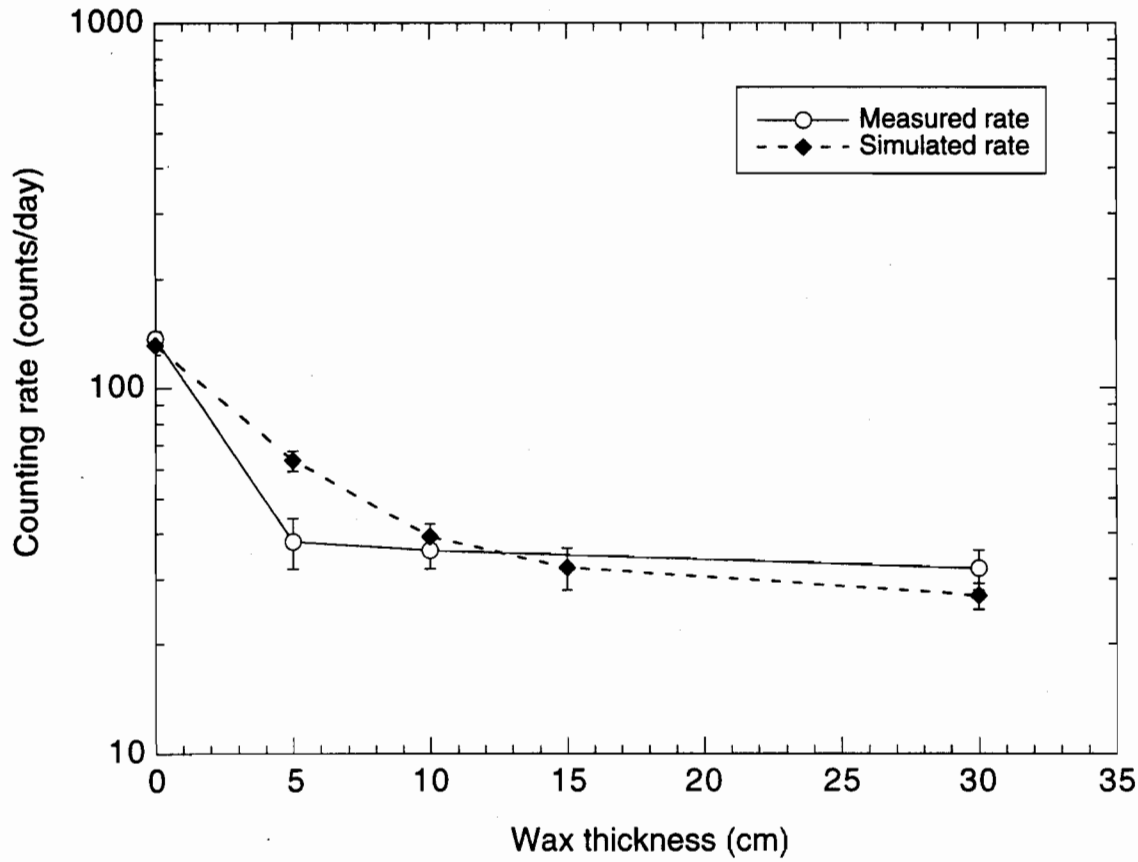

Figure 4.13: Comparison of the measured counting rate and the simulated counting rate in the BF_3 counter in the Stanford Underground Facility as a function of the wax thickness surrounding the counter.

Table 4.5: Comparison of the simulated and measured counting rate in the BF_3 counter in the Stanford Underground Facility as a function of the wax thickness surrounding the detector. For the simulations, the total rate is broken down into components due to muon-induced neutron production in the detector, the wax and the surrounding rock.

	Components of Simulated Counting Rate				
Wax Thickness (cm)	Detector Neutrons (counts/day)	Wax Neutrons (counts/day)	Rock Neutrons (counts/day)	Simulated Rate (counts/day)	Measured Rate (counts/day)
0	16.7 ± 0.8	0 ± 0	115 ± 6	132 ± 7	137 ± 7
5	16.7 ± 0.8	0.6 ± 0.2	47 ± 4	64 ± 5	38 ± 6
10	16.7 ± 0.8	1.5 ± 0.4	21 ± 3	39 ± 4	36 ± 4
15	16.7 ± 0.8	2.5 ± 0.5	13 ± 3	32 ± 4	
30	17.8 ± 0.9	3.2 ± 0.2	6 ± 1	27 ± 2	32 ± 4

which these neutrons propagate. However, as demonstrated by both the measurements and the simulations, the lead shielding is by far the dominant source of neutrons. Thus accurate simulations involving the rock neutrons are not necessary.

4.5.4 Estimating Neutron Backgrounds in a Dark Matter Detector

Both the simulations and the measurements made in the Stanford Underground Facility demonstrate the huge increase in the neutron flux caused by the presence of high-Z materials. This increased neutron flux is a result of cosmic ray muon interactions in these materials. However, the simulations and measurements also show that this increased neutron flux can be effectively reduced by the appropriate use of moderators. Furthermore, the excellent agreement obtained between the simulations and the measurements that were made with various shielding configurations demonstrate the validity of both the neutron simulation program and the models of the neutron production from cosmic ray muon interactions at this site. Thus, the neutron Monte Carlo program can be used, with some confidence, to investigate the expected event rate in the dark matter detector due

to the neutron backgrounds at the Stanford Underground Facility.

To obtain a first estimate of the level of this background, the experimental set-up for the dark matter search is simply modeled as a 1 kg germanium cylinder enclosed in a copper can, which represents the cryostat required to house the real detectors, surrounded by 25 cm of polyethylene and 15 cm of lead. Neutrons are generated uniformly throughout the polyethylene and the lead using the production rates and emission spectra discussed in the previous sections. The resulting spectrum of nuclear recoils that these neutrons produce in the germanium is one component of the muon-induced neutron background at the Stanford Underground Facility. This simulation shows that this amount of polyethylene is sufficient to attenuate the event rate in the germanium detector due to muon-induced neutrons produced in the outer shield to an acceptable level.

The copper cans of the cryostat represent a significant mass of material inside the polyethylene shielding. Therefore, the muon-induced neutron production in the copper cans must also be considered. In order to include this contribution in the simulation, the neutron production rate in copper at this depth was estimated to be 100 neutrons/kg/day and the emission spectrum was assumed to be the same as for the lead. The upper curve in Figure 4.14 shows the resulting simulated background spectrum of nuclear recoils in a germanium detector due to the muon-induced neutrons produced in the copper cans of the cryostat at the Stanford Underground Facility. This simulation shows that these neutrons produce a non-negligible event rate in the detector; the background event rate is of the order of 5 recoils/kg/keV/day for recoil energies above a few keV. This background can be reduced by surrounding the germanium detector with moderator inside of the copper. With 10 cm of polyethylene surrounding the germanium, a background event rate of the order of 1 recoil/kg/keV/day can be achieved for recoil energies above a few keV. The two lower curves in Figure 4.14 illustrate the reduction in this background that can be obtained by surrounding the germanium detector with an inner moderator of 5 cm of polyethylene and 10 cm of polyethylene.

These simulations using simple geometry demonstrate that with sufficient polyethylene

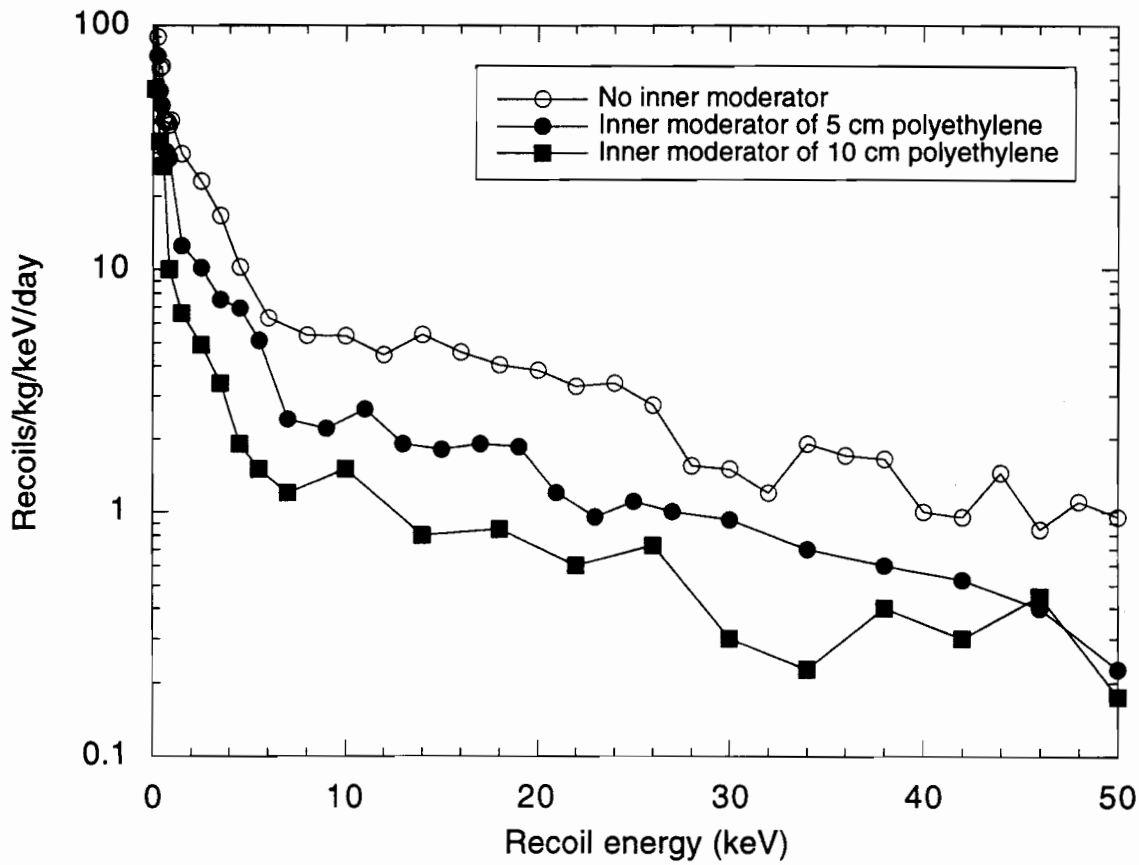

Figure 4.14: Simulated recoil event rate in a germanium detector, with and without inner moderator, due to neutrons produced in the copper cryostat by cosmic ray muons at the Stanford Underground Facility. For the upper curve, no moderator was used inside the copper. For the middle curve, the germanium was surrounded by 5 cm of polyethylene. For the lower curve, the germanium was surrounded by 10 cm of polyethylene.

inside the lead shield, the dominant source of neutron background will be from the muon-induced neutrons in the copper cryostat. This means that an inner moderator within the cryostat will be necessary in order to reduce this background to an acceptable level. Furthermore, these simulations demonstrate the need to minimize the mass of passive material inside of the cryostat since this material becomes a neutron source. Simulations using more detailed geometries will be discussed in Section 5.4.

Chapter 5

Low Background Environment

Because of the extremely low event rate expected for a dark matter search, it is essential to create a low background environment in which the detectors can operate. This Chapter discusses the issues involved in creating such an environment for the CDMS experiment.

5.1 Stanford Underground Facility

An underground site is needed to reduce the cosmic ray background. The complexities of operating cryogenic detectors, however, mandate a site that is conveniently located and provides unlimited access. These requirements led to the Stanford Underground Facility, a shallow-depth site located near the physics department on the Stanford University campus. The main underground laboratory space was built as an extension of tunnel A, an existing (unused) beam dump in End Station III of the Hansen Experimental Physics Laboratory (HEPL). The original tunnel was 9.5 m long, 2 m high and 2 m wide. The tunnel was extended by 18 m, with the last 15 m of the new portion of the tunnel being 3.6 m high and 3.6 m wide. A profile of the tunnel is illustrated in Figure 5.1. The overburden at the end of the tunnel extension is about 10.6 m of dirt or, equivalently, about 16 meters of water. The overburden has been determined from the measured muon

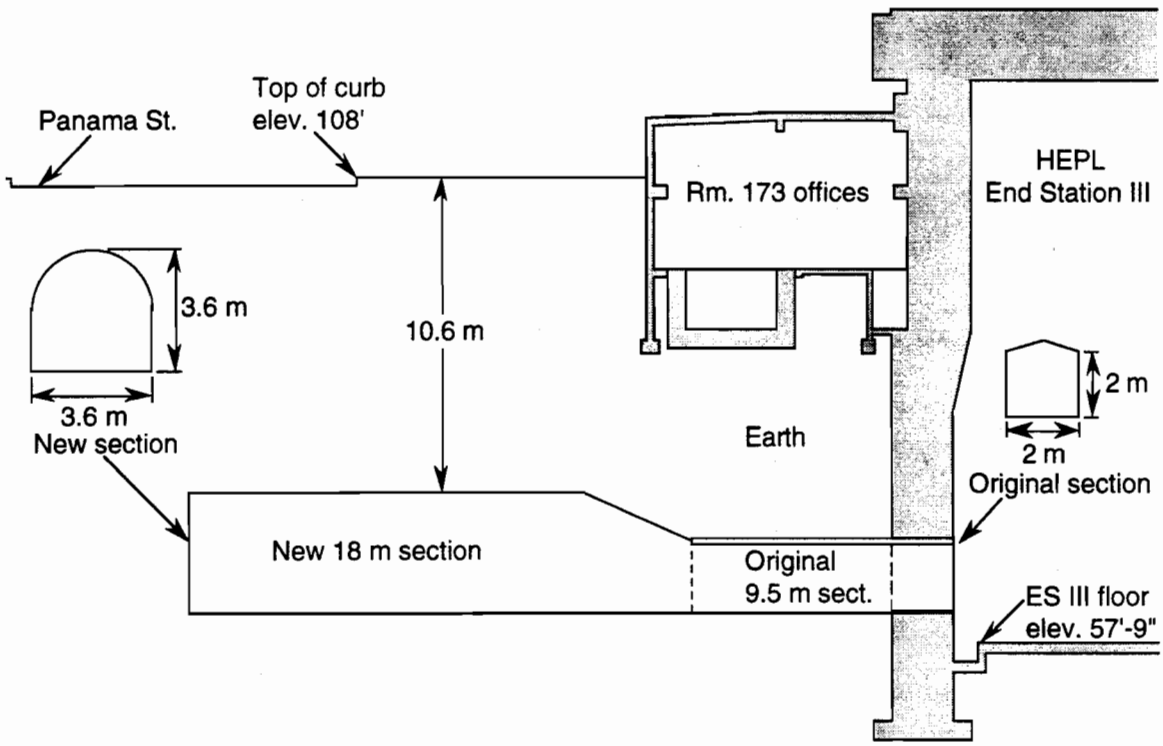

Figure 5.1: Profile of the main underground laboratory space of the Stanford Underground Facility.

flux inside the tunnel as described in the following section. Figure 5.2 shows a plan view of the Stanford Underground Facility. In addition to the main experimental tunnel, there are two other pre-existing tunnels (tunnels B and C) located adjacent to the new tunnel. Tunnels B and C are roughly the same size as tunnel A before the extension. These three tunnels, together with the loading platform which spans the entrances of all of the tunnels, constitute the Stanford Underground Facility.

During construction of the tunnel extension, samples of excavated material, as well as construction materials, were measured [108] for radioactive contamination. The level of uranium, thorium and potassium contamination found in these materials is given in Table 5.1. The level of radioactivity in the excavated material is typical of most geological formations. So as not to increase the ambient photon background in the tunnel extension, the level of radioactivity in construction materials should be no greater than the activity of the surrounding rock. The level of radioactivity in the sand and gravel used for the shotcrete that covered the walls of the tunnel was lower than the activity in the surrounding rock. The cement contained somewhat higher levels of uranium contamination, but since the proportion of cement in the shotcrete mixture is small and the layer of shotcrete is fairly thin, this level of radioactivity was not considered prohibitive. The walls were sealed using a masonry waterproofing material and finally painted to reduce dust. Photon measurements made in the tunnel before and after the extension demonstrated that the ambient photon background was not significantly changed by the construction.

The CDMS detectors are housed in a cryostat, called the icebox (see Section 5.3.1), located in tunnel A. The tunnel has been fully equipped with lighting, electricity and ventilation, as well as the plumbing required to operate the dilution refrigerator. All electrical conduits are broken before entering the main laboratory space at the end of the tunnel to minimize electrical noise. The ventilation system draws in fresh air from outside and pumps it in from the closed end of the tunnel to minimize the build-up of radon gas near the experiment. The air is also filtered to remove dust particles which may contain small quantities of radioactivity. The various pumps that are required to operate

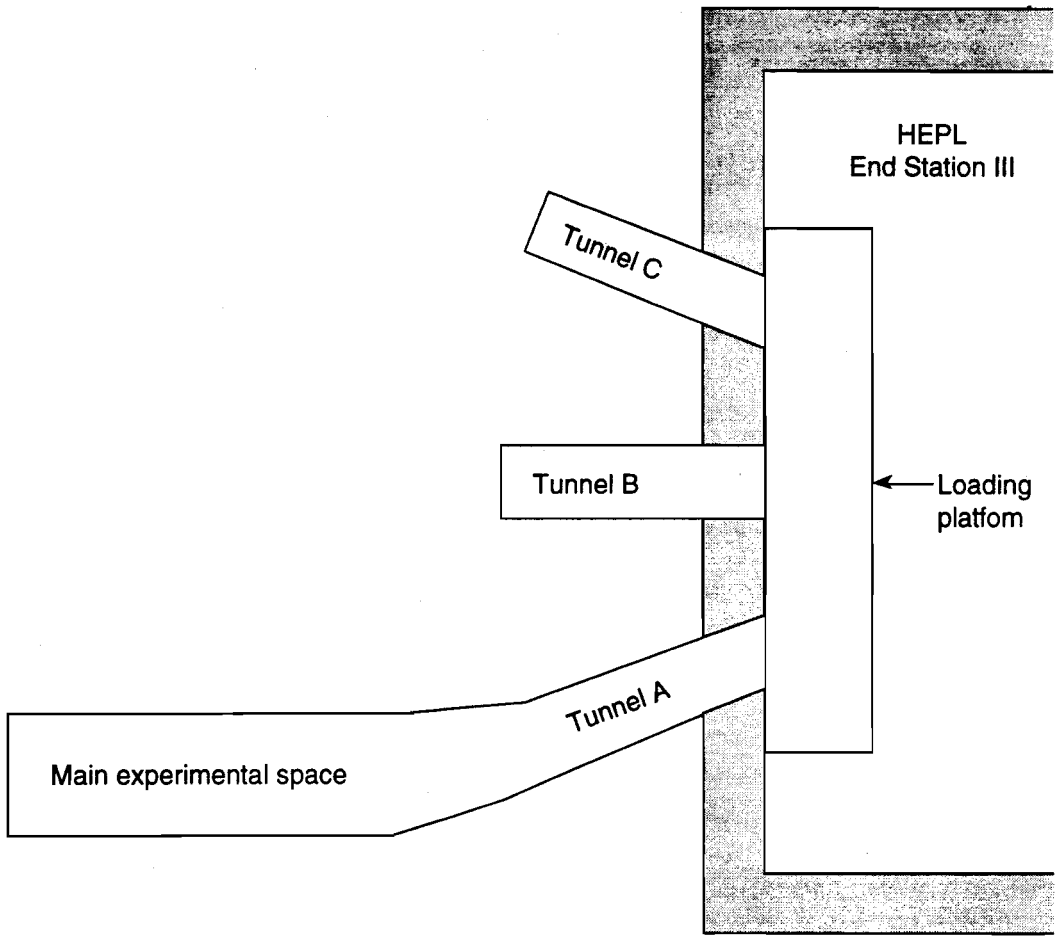

Figure 5.2: Plan view of the Stanford Underground Facility.

Table 5.1: Measured levels of primordial contamination in materials from the tunnel extension at the Stanford Underground Facility. The sand, gravel and cement were mixed to form the shotcrete that was sprayed on the walls of the tunnel.

Sample	Uranium (ppm)	Thorium (ppm)	Potassium (%)
excavated material	2.38 ± 0.04	7.82 ± 0.12	1.80 ± 0.01
sand	0.77 ± 0.01	2.18 ± 0.03	1.04 ± 0.002
gravel	1.16 ± 0.03	2.73 ± 0.07	0.54 ± 0.005
cement	6.90 ± 0.04	2.91 ± 0.06	0.238 ± 0.005

the dilution refrigerator are located in tunnel B in order to isolate the experiment from this particularly noisy equipment. Tunnel C is used mainly to store materials that will be used near the detectors since underground storage reduces cosmogenic activation of the material.

5.1.1 Muon Measurements

The muon rate in the Stanford Underground Facility was measured using a telescope consisting of two plastic scintillating paddles approximately 59 cm $\times$ 15 cm $\times$ 2.5 cm thick separated by 100 cm. Each scintillator was connected to a photomultiplier tube via a light guide.

A schematic diagram of the muon telescope is shown in Figure 5.3. The solid angle seen by the lower paddle, C_1, looking at the upper paddle, C_2, is estimated [109] to be $\Delta\Omega \simeq 0.079$ sr. Multiplying by the area of C_2 gives the geometrical factor for the telescope: $A\Delta\Omega \simeq 73$ cm^{2}sr. The telescope was constructed so that it could be operated at five zenith angles: $\theta = 0°$; 22.5°; 45°; 67.5° or 90°.

The counting rate in each of the scintillators was recorded as was the coincidence rate. For small zenith angles, the coincidence rate corresponds to the muon rate. For larger zenith angles the coincidence rate is somewhat higher than the muon rate because of the

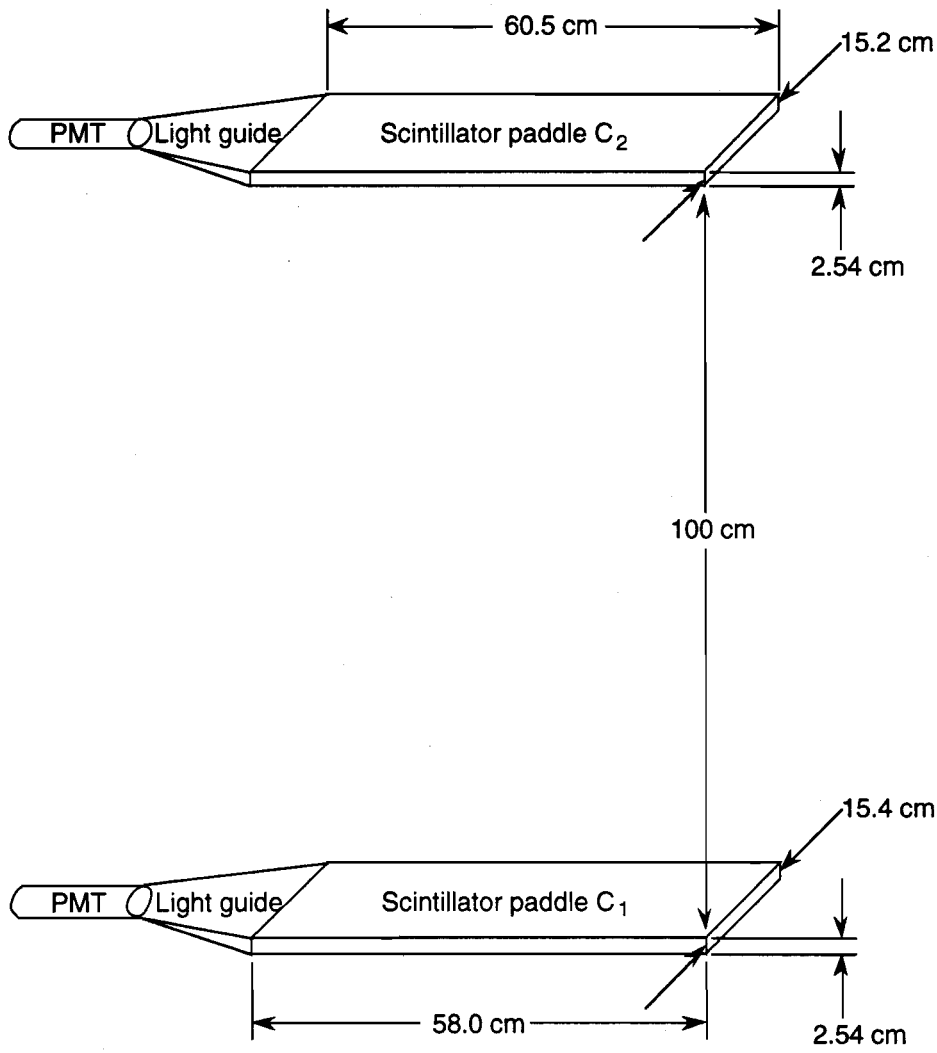

Figure 5.3: Schematic diagram of the muon telescope.

Table 5.2: Measured vertical muon flux in Tunnel A of the Stanford Underground Facility.

Location	Coincidence Rate (s^{-1})	Vertical Muon Flux ($m^{-2}s^{-1}sr^{-1}$)
End of tunnel A before extension	0.257 ± 0.001	35.2 ± 0.2
Same position - after extension	0.253 ± 0.002	34.7 ± 0.3
End of extended tunnel A	0.213 ± 0.001	29.2 ± 0.2

added contribution to the coincidence rate due to showers. It is difficult to determine quantitatively the contribution due to showers for large zenith angles. Using the geometrical factor of the telescope, the measured muon rate can be converted into a muon flux. The measured counting rate and corresponding muon flux in various locations in tunnel A are recorded in Table 5.2

Once the muon flux has been measured, it can be used to determined the overburden using the empirical formula for the muon flux intensity as a function of the vertical depth (for flat topology) given by Miyake [86]:

$$\Phi(x) = \frac{174.0}{(x+400)}(x+10)^{-1.53}\exp(-8\times 10^{-4}x) \tag{5.1}$$

where x is the vertical depth in m.w.e. and $\Phi(x)$ is the vertical muon flux in $cm^{-2}s^{-1}sr^{-1}$. Based on the measurements in Table 5.2, the overburden of the main experimental space at the Stanford Underground Facility is 16 ± 1 m.w.e., while the overburden in the entrance tunnel is only 12 ± 1 m.w.e. The smaller overburden in the entrance tunnel is due to the overhead offices shown in Figure 5.1.

The dependence of the muon flux on zenith angle θ is given by

$$\Phi(x,\theta) = \Phi(x)\cos^n(\theta) \tag{5.2}$$

where $n \simeq 2$ for vertical depths up to $\sim$ 500 m.w.e. [110]. Using this expression for the zenith angle dependence, and assuming no dependence on the azimuthal angle, J_1, the integrated muon flux per unit horizontal area is simply given by

$$J_1 \equiv \int_{\theta\leq\frac{\pi}{2}} j(\theta,\phi)\cos\theta d\Omega = \frac{\pi}{2}j(\theta=0) \tag{5.3}$$

where $j(\theta, \phi)$ is the muon flux as a function of zenith and azimuthal angles. Using the measured vertical muon flux of 29.2 muons/m^2/s/sr at the end of the tunnel extension, this leads to an integrated muon flux of 45.8 muons/m^2/s. J_1 can also be determined by numerically integrating in muon fluxes measured at various zenith angles. This method gives an integrated muon flux of 44.4 muons/m^2/s. This is only a factor of 4 lower than the sea-level value [111] of 180 muons/m^2/s.

5.2 Shield

In order to reach the background levels required for a dark matter search, the ambient photon flux incident on the detectors must be reduced. This can be accomplished by surrounding the experiment with an appropriate amount of high-Z material that is relatively free of radioactive impurities. Unfortunately, due to the limited overburden at the Stanford Underground Facility, the cosmic ray muon flux remains relatively high. Therefore, a muon veto is necessary and additional shielding material is required to minimize secondary activities induced by the muons.

5.2.1 Passive Shield Design

Based on the measurements discussed in Chapter 3, a 15-cm-thick lead shield was constructed. To allow access to the inside of the shield, the lid was split into two pieces that are mounted on wheels that run on a track attached to the side walls of the shield. Because they are required to support the weight of the lid, the thickness of the side walls was increased to 20 cm. The outer dimensions of the lead are 142.2 cm$\times$142.2 cm$\times$157.5 cm high.

The base and the walls of the shield were constructed with standard-sized (5 cm $\times$ 10 cm $\times$ 15 cm) lead bricks stacked in a labyrinth to avoid cracks penetrating through the entire thickness of the shield. Glover lead was used for the inner 5 cm of the shield because of its relatively low ^{210}Pb activity. Stanford lead was used for the outer 10 cm of the shield.

For the lid, interlocking sections were cast out of Glover lead. For structural support, the inner walls of the lead shield were lined with 1-cm-thick copper plates. The radio-purity of the copper was tested [112] and no measurable levels of primordial contamination was found.

As discussed in Chapter 4, this large mass of lead at such a shallow depth becomes a significant neutron source. To mitigate this effect, the space surrounding the icebox inside of the shield is filled with polyethylene. The total thickness of the polyethylene is approximately 20 cm on the sides, 25 cm on the ends and 28 cm on the top and bottom. (The thickness on the sides is less because the thickness of the lead side walls was increased at the expense of the moderator due to the limited space inside the tunnel). Before being placed inside the shield, the radio-purity of the polyethylene was measured [112]. The level of the uranium series in the polyethylene was found to be (980 ± 170) ppt. Upper limits on the level of the thorium series and natural potassium were found to be respectively 650 ppt Th and 250 ppb K.

The final component of the passive shield was included to shield the experimental space from magnetic fields, rather than radioactivity. A thin shield of Carpenter Hipernom Alloy [113] was placed directly around the icebox, and long sleeves of this material were placed around the cold stem and the electronics stem. As with all the other shielding materials, the Hipernom alloy was checked for radio-purity before being used. A measurable level of (2.7 ± 0.4) ppb of the uranium series was found, while only upper limits of 3 ppb Th and 0.7 ppm K were placed on the level of the thorium series and natural potassium.

5.2.2 Veto System

The relatively high muon flux at the Stanford Underground Facility necessitates the use of a muon veto system. Time correlations between signals in the muon veto system and events in the CDMS detectors may be simultaneous, prompt, delayed or late, depending

on the characteristic times of the physical processes involved. Muons which strike both the veto and a CDMS detector will produce simultaneous events. Muons that hit the veto and then stop in or near the shield without striking a detector will subsequently decay (with a mean lifetime of 2.2 μs), and the electron daughter or later gammas may hit a detector. Neutrons that are generated by muons interactions in the shield will be moderated in the polyethylene and may subsequently hit a CDMS detector. Or, the neutrons may be captured (on a timescale of the order of 100 μs), thereby producing gammas that may hit a detector. Finally, long-lived excited states may be produced by muons or their secondaries, and correlated events in the veto and the CDMS detectors may result that are widely separated in time.

The muon veto system consists of 13 veto counters made of 4-cm-thick NE110 plastic scintillators and 26 Burle 8575 and 8850 photomultiplier tubes. Figure 5.4 shows a schematic layout of the 13 veto counters along with the positions of the 26 photomultiplier tubes. Most of the photomultiplier tubes are coupled to the scintillators with acrylic waveshifter bars (Bicron BC482_A), except for the 4 bottom panels, where the photomultiplier tubes are coupled using conventional light guides. The photomultiplier tubes are attached to the plastic using Epotek 301-B glue which is transparent to the blue emission spectrum of the scintillator. To increase the light collection, at least 2 photomultiplier tubes are attached to each scintillator paddle (except for the 4 small bottom counters where one photomultiplier tube per paddle is sufficient). To improve the separation between the muon peak and the gamma continuum, the signals from each photomultiplier tube on a given scintillator are summed (see Figure 5.5).

The photomultiplier bases, which were made in the electronics shop of the University of California at Santa Barbara, are significantly shorter than commercially available bases. This eases the installation in the confined space of the Stanford Underground Facility. Because the bases contain low precision resistors, each base has been permanently assigned to a particular photomultiplier tube. The bases are surrounded by removable Mu metal magnetic shields made by Conetics.

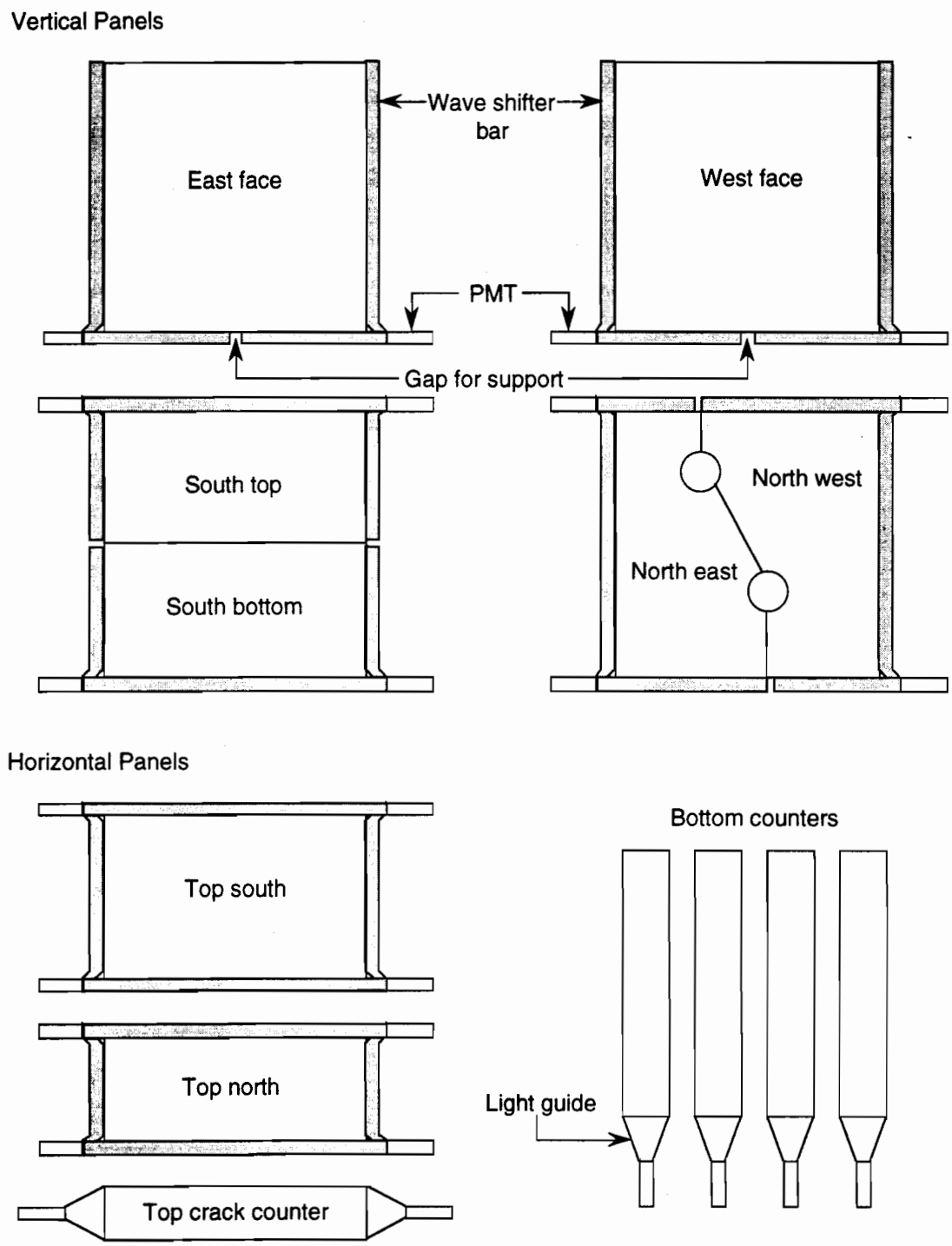

Figure 5.4: Schematic layout of the 13 scintillator paddles of the muon veto shield.

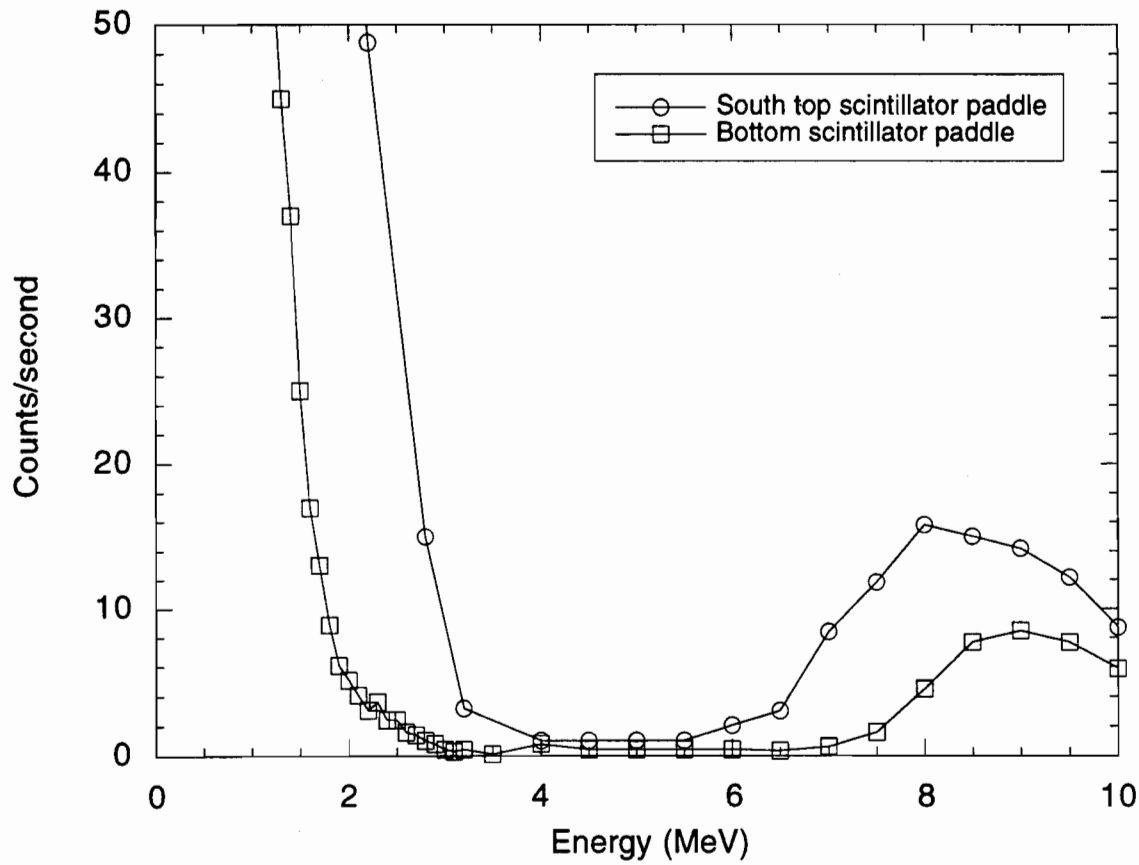

Figure 5.5: Raw counting rate as a function of energy for two of the scintillator paddles of the muon veto. The plateau between 4 MeV and 6 MeV demonstrates the good separation that is obtained between the low energy gamma events and the high energy muon events. To obtain this separation in the South top scintillator, the signals from the two photomultiplier tubes must be summed.

The photomultiplier tubes are powered by a single LeCroy HV4032A high voltage power supply which has 32 separately programmable negative high voltage channels. This device continuously measures the voltage to correct for drift and will shut down individual channels if it discovers a serious problem. Using a ^{232}Th source, the photomultiplier tube voltages were individually adjusted to help achieve uniform response over the entire paddle area. The resulting voltages ranged from about -1500 V to -1800 V.

5.2.3 Measured Photon Backgrounds inside the Shield

Before installing the cryogenic system, the performance of the final experimental shield was evaluated using the HPGe detector discussed in Chapter 3. For these measurements, the coldfinger of the HPGe detector system penetrated the final experimental shield through the opening designed for the electronic stem of the icebox. (Details of the cryogenic system are described later in this chapter). Although this hole is cut at an angle of 20°, the diameter of the hole is large enough to allow the coldfinger to remain perpendicular to the shield wall, leaving enough room for the plastic scintillator paddles of the veto shield to be installed with the detector in place (see Figure 5.6). In this configuration, the HPGe detector sits just inside the copper wall on the inside of the lead. With the detector in place, the space in the shield wall around the coldfinger was filled with thin lead sheets. Although a small crack remained around the coldfinger, there was no direct line of sight to the detector.

The interior of the shield was filled to 95% of its capacity with polyethylene leaving a small cavity surrounding the HPGe detector. The inside of this cavity was lined with 1.27-cm-thick high purity copper plates. The only other item inside the shield was the copper stand which is used to support the icebox when it is in place. During these measurements, no nitrogen purge was used.

To ensure good separation between gamma events and muon events in the scintillators, the signals from each of the photomultiplier tubes on a given scintillator paddle were

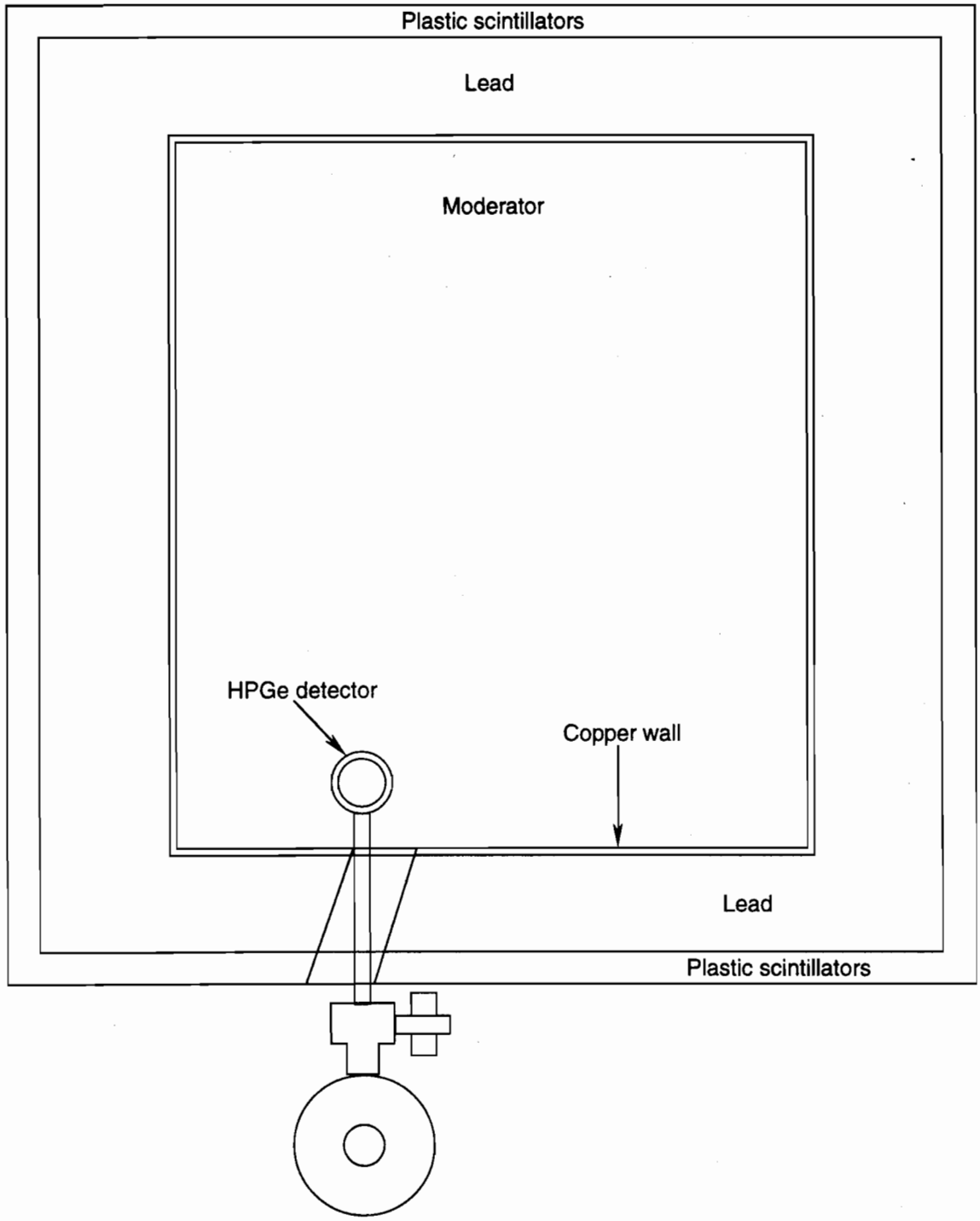

Figure 5.6: Set-up used to measure the photon background in the final shield at the Stanford Underground Facility.

summed. For each paddle, a threshold was then set so that the rate of gamma events was approximately 0.0016 $\gamma/\mathrm{cm}^2/\mathrm{s}$. With these thresholds set, the overall trigger rate in the scintillators was approximately 600 s^{-1}.

To investigate the time correlations between hits in the scintillators and events in the HPGe detector, the electronics were set-up so that a signal in any of the scintillator paddles would start a clock and a subsequent signal in the HPGe detector would stop the clock (100 μs after the signal in the HPGe detector). Thus, for each event in the HPGe detector, both the energy of the event and the time since the last scintillator hit, or "delay time", were recorded. Figure 5.7 shows the typical distribution of delay times that was obtained. Three distinct time scales are apparent in the data. Immediately following the coincidence peak, there is a sharp fall-off with a mean time of ~ 2 μs which corresponds to the mean lifetime of the muons. Following this, there is a fall-off with a ~ 150 μs timescale which corresponds to those events in the HPGe detector produced by muon-induced neutrons, particularly gamma emission following neutron capture. Finally, there is the long time constant of ~ 2000 μs which corresponds to the accidental rate. Events which occur with negative delay times are events in which there was a second veto hit in the 100 μs between the hit in the HPGe detector and the stop signal.

The shapes of the measured spectra will also depend on the physical processes involved. This effect is illustrated in Figure 5.8. The upper spectrum consists of those events which are nearly coincident in the veto and the HPGe detector (delay times less than 3 μs). Because this class of events includes muons which pass through both the veto and the HPGe detector, there is a substantial high energy continuum that continues well past 2.6 MeV (the highest energy, naturally occurring gamma line). Also, the positron annihilation line is a prominent feature in this spectrum. The lower spectrum in Figure 5.8 consists of those events with delay times between 4 μs and 200 μs. In this case, the event rate is much lower and the shape of the spectrum is somewhat different; the positron annihilation line is no longer a dominant feature and there is very little high energy continuum above 2.6 MeV. Also, the 2.2 MeV gamma line produced by neutrons being

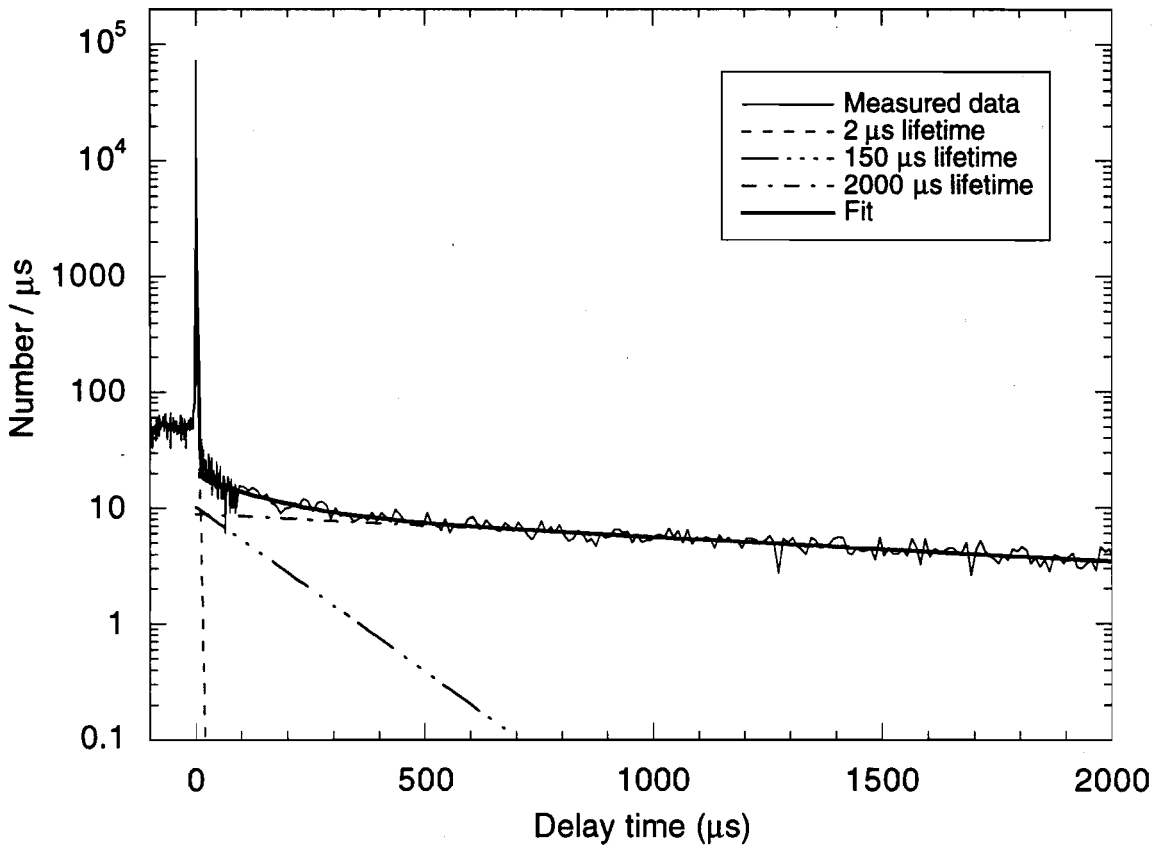

Figure 5.7: Distribution of delay times between events in the scintillators and events in the HPGe detector. The fit to the data consists of three exponential components: a 2 μs time constant, corresponding to the lifetime of the stopping muons; a 150 μs time constant corresponding to the capture time of the neutrons; and a 2000 μs time constant corresponding to the accidental rate. Events which occur with negative delay times are events in which there was a second veto hit in the 100 μs between the hit in the HPGe detector and the stop signal.

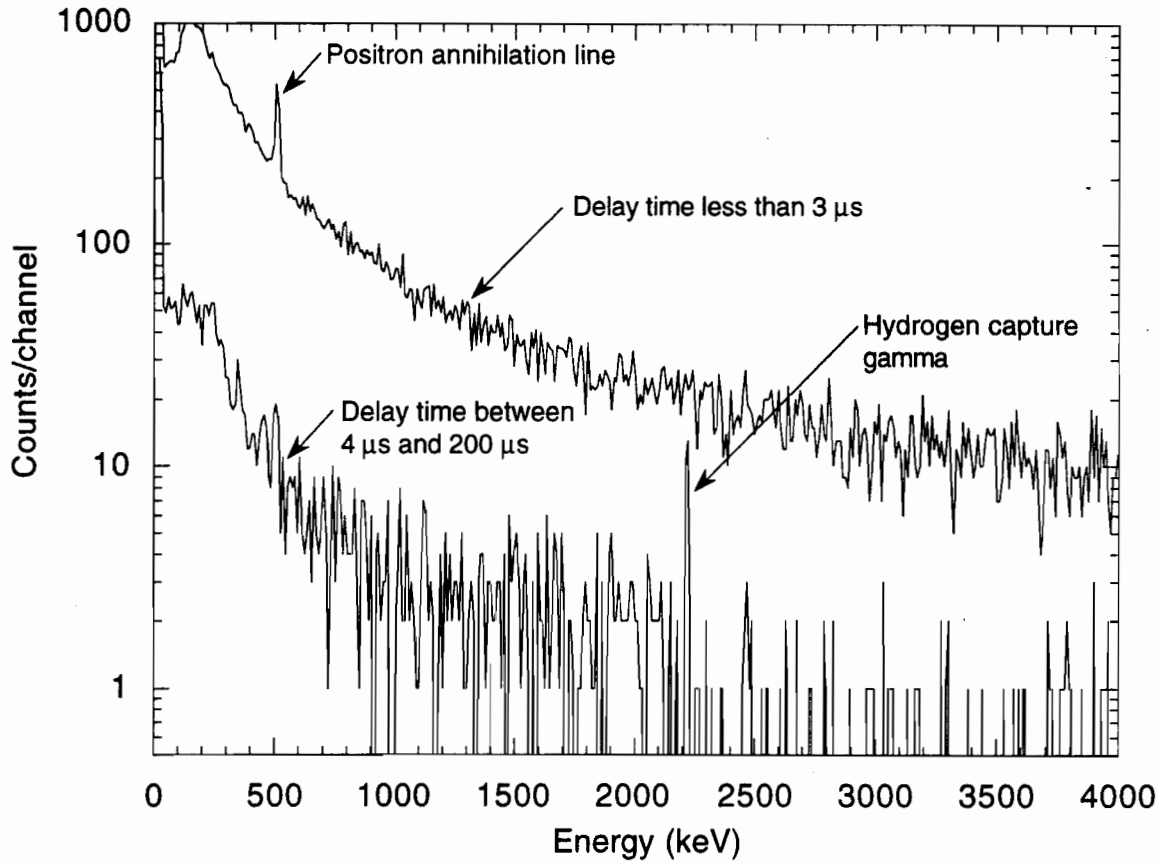

Figure 5.8: Measured HPGe spectra with delay times less than 3 μs and between 4 μs and 200 μs. Events in the upper spectrum are due mainly to coincident events. The positron annihilation line is the most dominant feature and there is a strong continuum of high energy events. The hydrogen capture gamma at 2.2 MeV can be seen in the lower spectrum.

captured by hydrogen is clearly visible in this spectrum.

Figure 5.9 shows the measured photon background inside the final shield at the Stanford Underground Facility both with and without the active veto. The lower curve was obtained by rejecting all events in the HPGe detector which occurred within 200 μs of a signal in the scintillators. Making the veto time much longer than 200 μs only leads to greater deadtime. It does not substantially decrease the background.

By comparing the total number of high energy events above 6 MeV in the vetoed and un-vetoed spectra, the efficiency of detecting a muon in the veto for those muons which

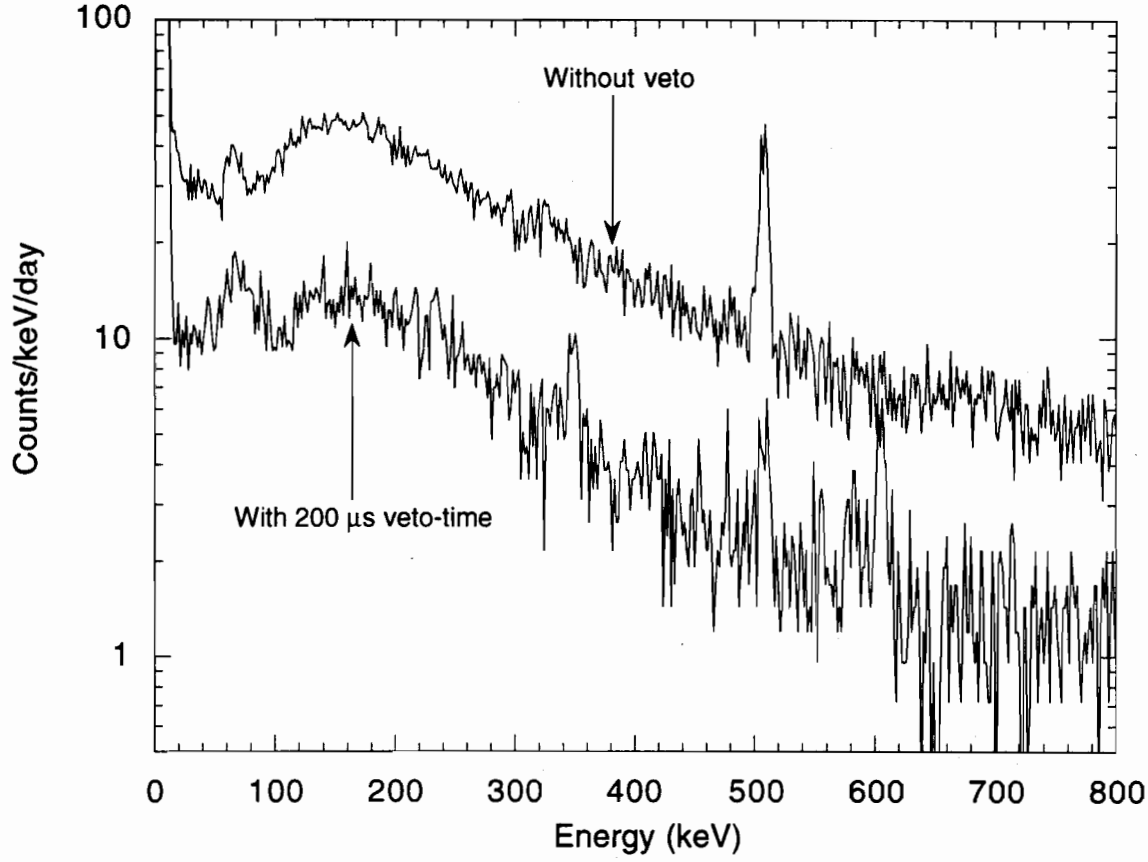

Figure 5.9: Photon background inside the final shield at the Stanford Underground facility measured with the HPGe detector with and without an active veto.

interact in the HPGe detector can be determined. This efficiency was found to be 99.8% for a relatively wide range of scintillator paddle thresholds. The relative insensitivity of the efficiency on the threshold indicates that there is good separation between the muon and gamma distributions, and therefore thresholds can be set high in the gamma distribution. Comparing the ratio of the integrated rates at lower energies gives a measure of the correlated veto-HPGe events. This ratio is also relatively insensitive to the scintillator thresholds indicating that gammas do not produce many correlated events.

5.3 Cryogenic System

The cryogenic system [114] was designed to accommodate the extensive shielding necessary to reduce the ambient backgrounds to acceptable levels and to minimize the amount of radioactive contamination near the detectors. This was accomplished by separating the cooling system (dilution refrigerator) from the cold experimental volume (icebox) and using only pre-screened, radioactively clean construction material for the icebox. To accommodate the multiple detectors necessary to have sufficient active detector mass and the large number of signal wires this leads to, modular detector packages (towers) and high density multi-conductor signal cables (striplines) were developed.

5.3.1 Icebox Design

As shown in Figure 5.10, the cryogenic system consists of a commercially available Oxford 400S dilution refrigerator with horizontal side access connected to a set of nested copper cans, called the icebox. The dilution refrigerator has a liquid nitrogen bath but no cryogenic liquids below the level of the mixing chamber. When operated by itself, the dilution refrigerator has a base temperature under 5 mK. Each of the nested cans in the icebox corresponds to a thermal stage in the dilution refrigerator. Thus there is an outer vacuum can (OVC), liquid nitrogen (LN) can, liquid helium (LHe) can, still (ST) can,

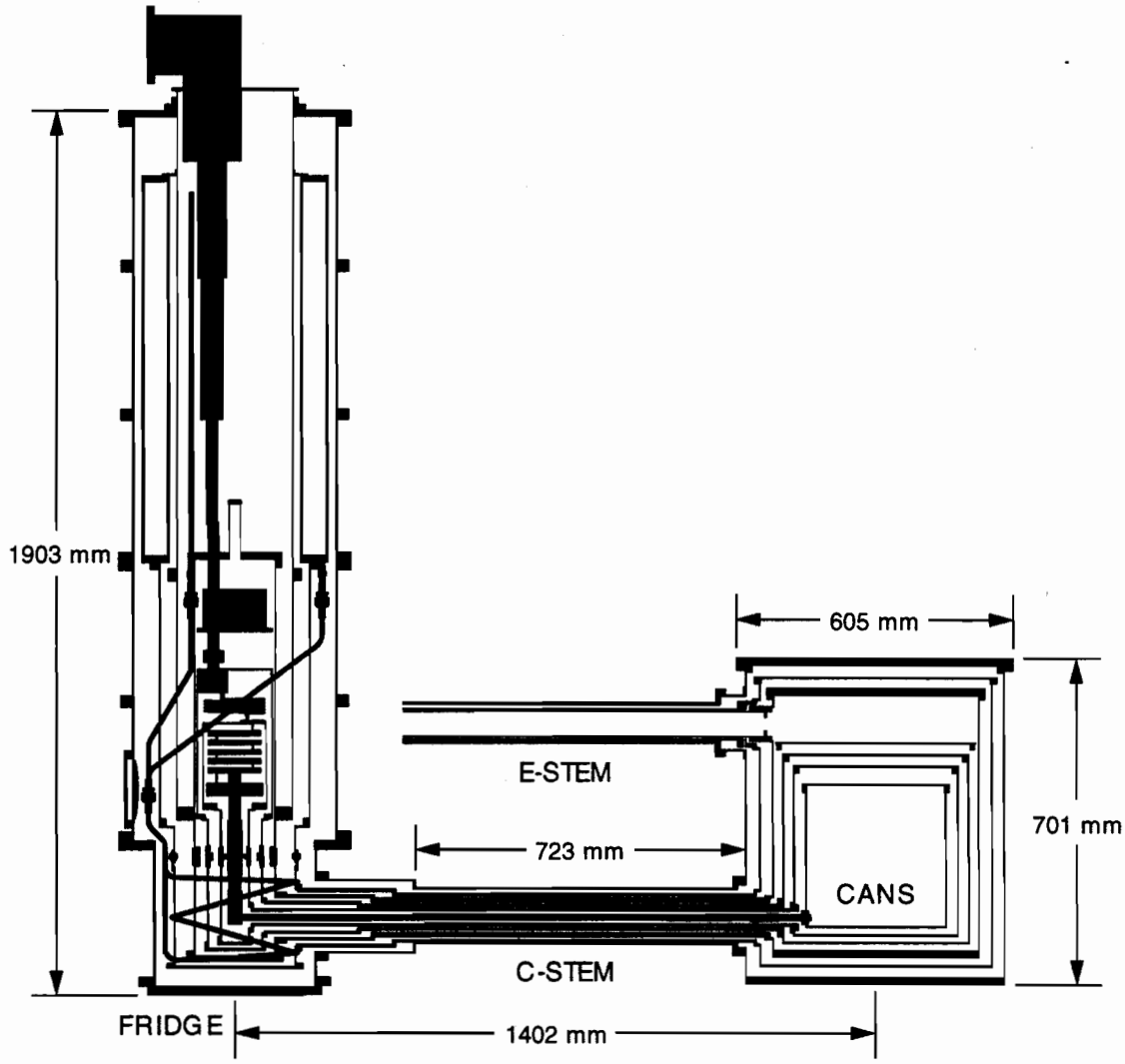

Figure 5.10: Schematic layout of the dilution refrigerator and the icebox cryostat. The vertical section at the left is the dilution refrigerator. The set of nested cans at the right is the icebox. The icebox cans are cooled via conduction along the set of lower stems (c-stem) which connect each can to the corresponding temperature stage in the refrigerator. The set of upper stems (e-stem) house the electrical wiring for the detectors.

cold plate (CP) can and mixing chamber (MC) can with nominal temperatures of 300 K, 77 K, 4.2 K, 600 mK, 50 mK and 5 mK respectively. The icebox is connected to the dilution refrigerator via a copper coldfinger and a set of concentric copper tubes, collectively referred to as the cold stem or c-stem. Each stem connects one can to the corresponding thermal stage in the refrigerator, with the copper coldfinger connecting the innermost can directly to the mixing chamber. The icebox itself contains no cryogenic liquid; all cooling power is generated in the refrigerator and the icebox is cooled via conduction along the c-stem.

A second set of stems penetrates the three outermost cans near the top of the icebox. This set of stems, referred to as the electronics stem or e-stem, houses the electrical wiring for the detectors. To provide better access to the e-stem, it is rotated by an angle of 20° with respect to the c-stem.

The innermost can is 30 cm in diameter and 30 cm high providing approximately 21 l of experimental space at base temperature. Access to this space is obtained by removing the lid at the top of every can.

In order to minimize the radioactive contamination near the detectors, the icebox was constructed almost entirely from OFHC copper, pre-screened for radioactivity. Electron beam welds were used to make all seams. A supply of relatively clean brass was used to fabricate all the screws necessary to put the cryostat together. Vacuum seals were made using copper foil gaskets with rounded nose sealing flanges. The cans are not rigidly connected to each other but rather each can is hung by a pair of kevlar loops from the next warmer can, with the ultimate support coming from the room temperature outer vacuum can (OVC). This non-rigid design accommodates the thermal contractions that occur during the cooldown, allowing the cans to move toward the refrigerator as the c-stem contracts.

5.3.2 Icebox Performance

The entire cryogenic system (dilution refrigerator and icebox) was first assembled and tested in a laboratory on the campus of the University of California at Berkeley. The first cooldown required a total of one week to cool the icebox from room temperature to below 10 mK. While the system was cold, a series of cooling power tests was performed by applying heat to each of the cans while monitoring the temperature. The applied powers were representative of the heat loads expected for a fully instrumented compliment of detectors. In all cases, the icebox performed within the parameters predicted with the thermal model used extensively in the design of the icebox. Ultimately, the inside of the icebox reached a temperature of 7.7 ± 0.07 mK, as measured with a ^{60}Co nuclear orientation thermometer mounted at the top of the MC can.

After this very successful first cooldown, the system was disassembled, packed and shipped to the Stanford Underground Facility. While the system was dismantled, all monitoring sensors and wiring connectors inside the icebox and stems were replaced using clean solder [115] and housing-less connectors to reduce the radioactive contamination inside the shield. In addition, each part was cleaned with alcohol in a clean room and double wrapped in plastic before being taken into the tunnel in an effort to reduce the amount of potentially radioactive dust introduced into the experimental area. During assembly, the outer plastic bag was removed just before the part was passed through the plastic curtain that defines the HEPA (high efficiency particulate) filtered region of the tunnel surrounding the shield. The inner plastic bag was removed inside the HEPA filtered air region.

With the icebox reassembled inside the Stanford Underground Facility, the system was cooled for the second time. Figure 5.11 shows the temperature history of the inner five cans. Liquid nitrogen was transferred into the helium and nitrogen baths for the first 13 hours of the run. To facilitate the cooling of the inner regions of the refrigerator and the icebox, the inner vacuum space was filled with helium exchange gas. The baths were

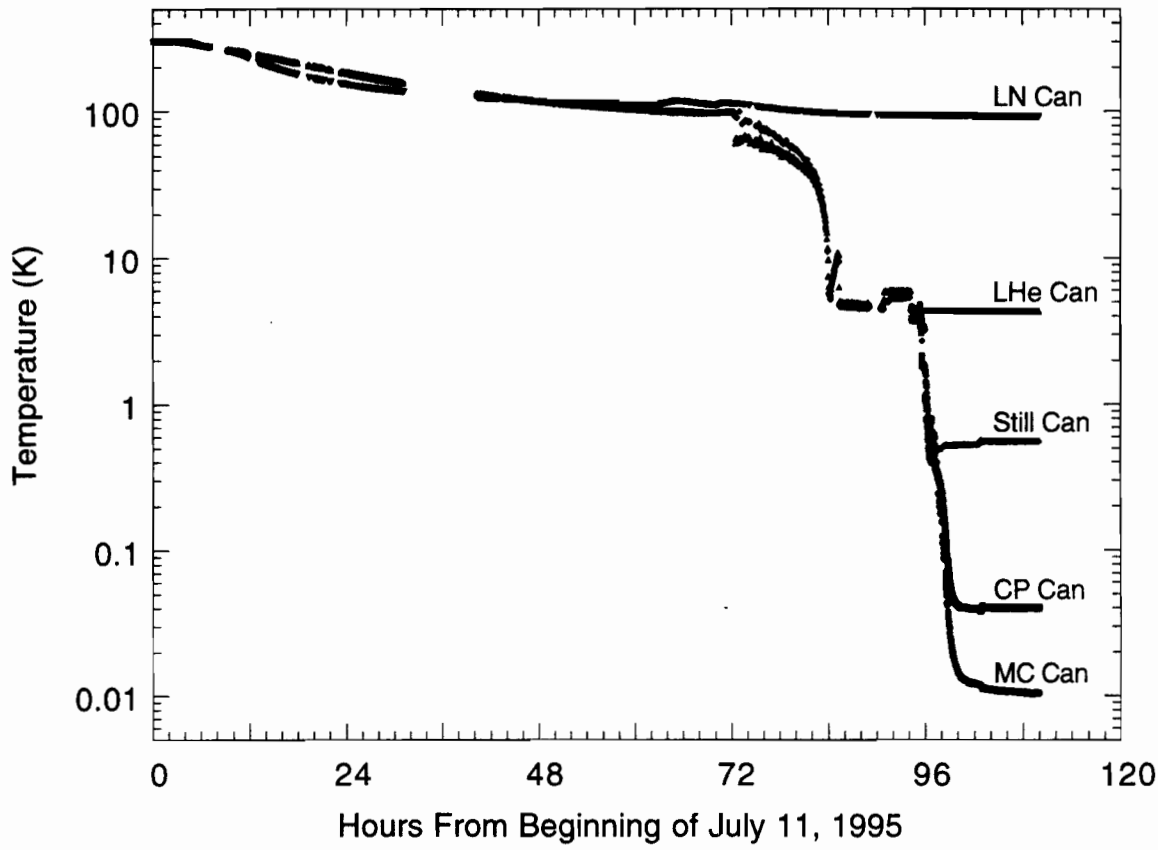

Figure 5.11: Temperature history of the icebox cans during the first cooldown of the icebox after installation of the system in the Stanford Underground Facility.

then topped off for the next two days while the temperature of the system cooled to under 100 K. A total of 500 l of liquid nitrogen was required to reach this point in the cooldown. With the system at 100 K, the slow transfer of liquid helium began. This transfer took a total of $13\frac{1}{2}$ hours and 300 l of liquid helium to fill the 36 l bath. The helium exchange gas was pumped out of the inner vacuum space for $8\frac{1}{2}$ hours before performing the necessary leak checks. After completing the test procedures, 2 hours were required to condense the mixture and begin circulation. Within $1\frac{1}{2}$ hours of establishing circulation, the MC can was under 100 mK. Within 6 hours, it was under 12 mK. In only $4\frac{1}{4}$ days, the MC can cooled from 300 K to less than 10 mK. Over the next two weeks, the circulation rate was optimized and the MC can ultimately reached a temperature of 5.51 ± 0.05 mK.

Once the icebox is cold, the helium consumption averages 29 l per day, requiring liquid helium transfers to the 36 l helium reservoir every 24 hours. The nitrogen consumption eventually settles down to an average of 40 l per day, requiring liquid nitrogen transfers to the 60 l nitrogen reservoir every 36 hours.

5.3.3 Detector Towers and Striplines

The detector tower illustrated in Figure 5.12 is a modular package used to house all the hardware necessary to interface the external modular wiring (striplines) to the cold amplifier components, as well as the wiring down to the detectors and the detectors themselves. With this modular design, the detector package can be constructed on the bench and tested as a complete assembly before being installed in the icebox.

The tower is supported from the top of the mixing chamber can. The detectors are suspended below the support while the cold amplifier components (FETs), wiring and heatsinks are mounted above the support.

In plan view, the towers are hexagonal with a diameter (defined as the distance between a pair of parallel faces) of 9.6 cm. This size allows detectors of up to 7.6 cm in diameter to be mounted in the towers. The hexagonal shape offers several advantages. First,

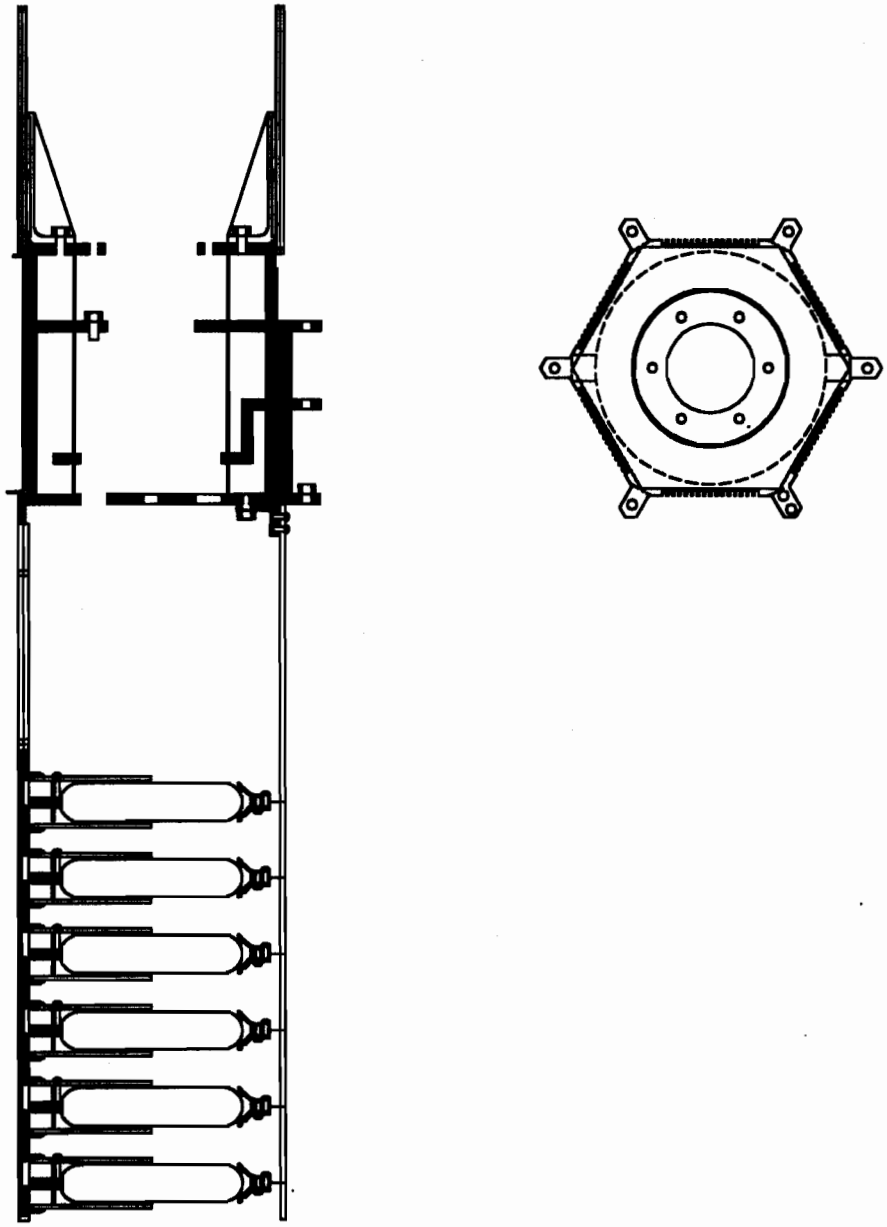

Figure 5.12: Schematic diagram of the detector tower. The side view is presented at the left and the top view is presented at the right. In the side view, two FET cards are shown mounted above the LHe floor and a stack of 6 BLIP detectors are shown mounted below the MC floor.

multiple towers can be close packed in the icebox, allowing for up to 7 towers provided no inner moderator is necessary (i.e., at a deep site where muon-induced neutrons are no longer a major background source). Secondly, the sides of the hexagon provide a flat surface on which to mount the wiring and heatsinking from the LHe stage down to the detectors. Each side can accommodate 16 wires, which is sufficient to operate one of the BLIP detectors described in Section 2.2 (with two phonon and two ionization channels) so a single tower can house six detectors. Finally, the corners provide 6 tabs which can be used in pairs to connect the tower to the various temperature stages without limiting access to the layer below.

The bulk of the tower is the section between the LHe stage and the MC stage. This section consists of copper "floors" which fit into the lids of each temperature stage can below (LHe, ST, CP and MC). These floors are thermally anchored via high conductivity copper wires and mechanical support between floors is provided by graphite tubes (chosen to minimize thermal conduction between the various temperature stages). The main function of this section of the tower is to support the cold components of the amplifier and to heatsink the detector wiring.

The FET card is mounted on the top of the LHe floor. The card provides the connector for the stripline as well as containing the FET for the amplifier. The card is made from multilayer kapton with copper traces. Since the FETs are operated around 110 K (to minimize FET noise), they are mounted on a 127 μm kapton window to reduce thermal conduction. Care must be taken in shielding the FETs to prevent IR radiation from the hot FETs heating the detectors. In addition, evaporated platinum traces are used on the window to minimize thermal conduction from the FETs down the traces. The window also supports a heater and a thermometer so that the temperature of the FETs can be monitored and controlled.

The detector wiring from the LHe stage down to the MC stage is rather unconventional. Each wire runs inside a channel in a copper plate that runs down along the side of the floors. The copper channel acts like a coaxial shield, preventing crosstalk between signal

wires. Since there is no insulator between the signal wire and the shield, only vacuum, these assemblies are referred to as vacuum coax assemblies. Small gaps in the shield wall between floors prevent heat flow from one temperature stage to the next. The signal wires are soldered to heat sinks at either end (LHe and MC floor) and at the ST floor using low activity solder [115].

The detectors are supported below the MC floor using a light weight truss. It is important to minimize the mass of passive material near the detectors because it acts as both a neutron source as a result of muon interactions, as well as a low-energy photon source as a result of Compton scattering. The wiring for a given detector is brought down along one side of the tower from the MC floor to the detector mount using a continuous channel 16-wire vacuum coax assembly since both ends are at the same temperature.

The wiring from the LHe floor to room temperature consists of striplines, high density multi-conductor shielded flat cable fabricated using flexible circuit technology [116]. Each stripline contains 50 traces on a flexible circuit that is 2.9 m long and 2.34 cm wide over most of its length. Each of the 50 traces is 127 μm wide and runs between grid pads used for 50-pin connectors. The traces are patterned in 19-μm-thick ($\frac{1}{2}$ oz. per square foot) copper. On either side of the trace layer there is a set of dielectric layers, 150 μm thick, consisting of 66% to 80% kapton and the remainder acrylic adhesive. Each dielectric layer has a ground plane, either 0.6 μm or 1.0 μm thick. The difference in composition and ground plane thickness is due to manufacturing constraints. Finally, each ground plane has a 51-μm-thick kapton cover layer for protection. The high wiring density achieved with the stripline is necessary to keep the diameter of the electronics stem, which carries all of the striplines from LHe to room temperature, relatively small, thereby minimizing the size of the shield penetration. The modular nature of the stripline also facilitates installation of the 96 wires required for each full tower of detectors.

5.4 Simulated Neutron Background Event Rates

The neutron Monte Carlo program discussed in Chapter 4 was used to simulate various effects relevant to the CDMS experiment. For these simulations, a detailed geometry of the final experimental shield was used, and each of the icebox cans was modeled as a separate can of the appropriate dimensions. (Details such as flanges were not included). Neither the cold stem nor the electronics stem were included in the simulation geometry. The set-up of the detectors themselves, and the moderator inside the lowest temperature can (referred to as "inner moderator"), varied from simulation to simulation.

For the series of simulations discussed in this section, the detectors were modeled as a stack of six germanium disks, with each disk 5 cm in diameter and 1 cm thick, and with a 1 cm gap between adjacent disks (see Figure 5.13). The stack of detectors was located at the center of the 5 mK can, which allows for 11 cm of inner moderator radially and 9 cm of inner moderator above and below the stack of detectors.

As discussed in Section 4.5, the dominant source of neutron recoils will be due to those neutrons produced by cosmic ray interactions in the copper cans of the cryostat. Using the neutron emission spectrum and production rate discussed in Section 4.5, this neutron source was used as the input for many of the simulations. In all cases, the muon-induced neutrons were generated uniformly throughout the copper cryostat. To begin with, no inner moderator was used in the simulations.

An advantage of having multiple detectors is demonstrated in Figure 5.14. By rejecting those events which scatter in more than one detector, the background recoil rate is reduced. Since WIMPs will scatter in only one detector, rejecting events in multiple detectors will not reduce the signal rate.

Although the muon-induced neutrons in the copper cans of the cryostat are the dominant source of nuclear recoils, they are not the only source. Figure 5.15 shows the contribution to the background recoil spectrum due to muon-induced neutrons produced in the copper cryostat, the outer lead shield and the outer polyethylene. In all cases,

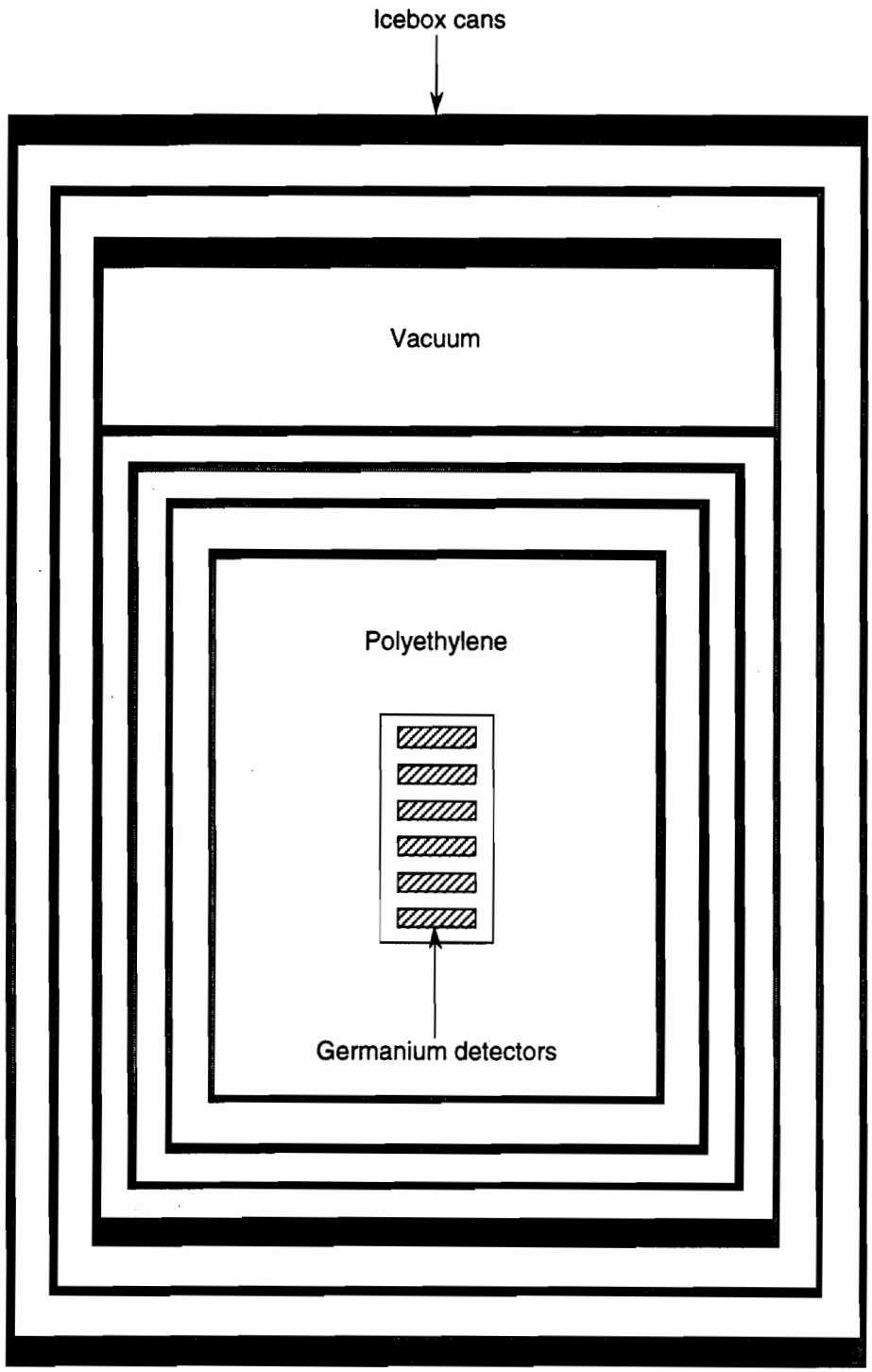

Figure 5.13: Detailed geometry of the icebox cans as used in the simulations with multiple detectors.

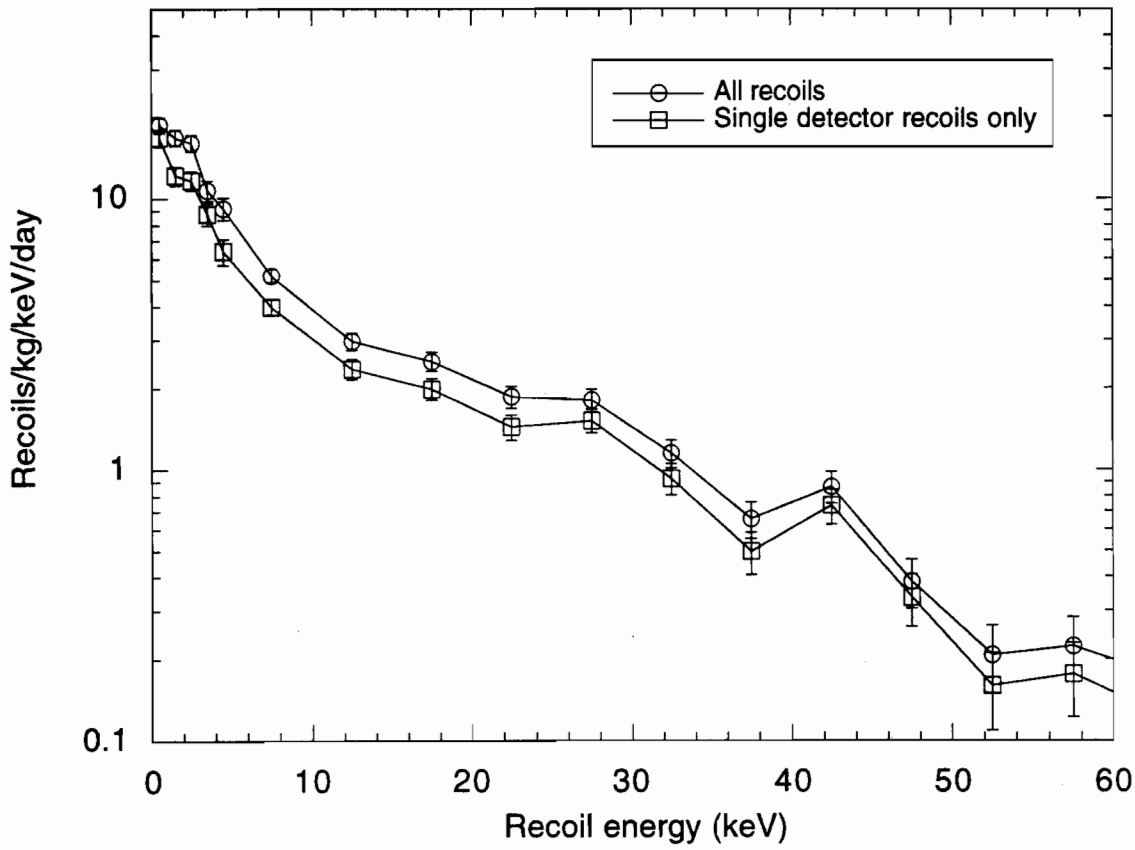

Figure 5.14: Reduction in background achieved by rejecting nuclear recoils which occur in multiple detectors. The upper curve is the simulated recoil spectrum from muon-induced neutrons in the copper cans of the icebox. The lower spectrum is obtained by rejecting those events which scatter in more than one detector.

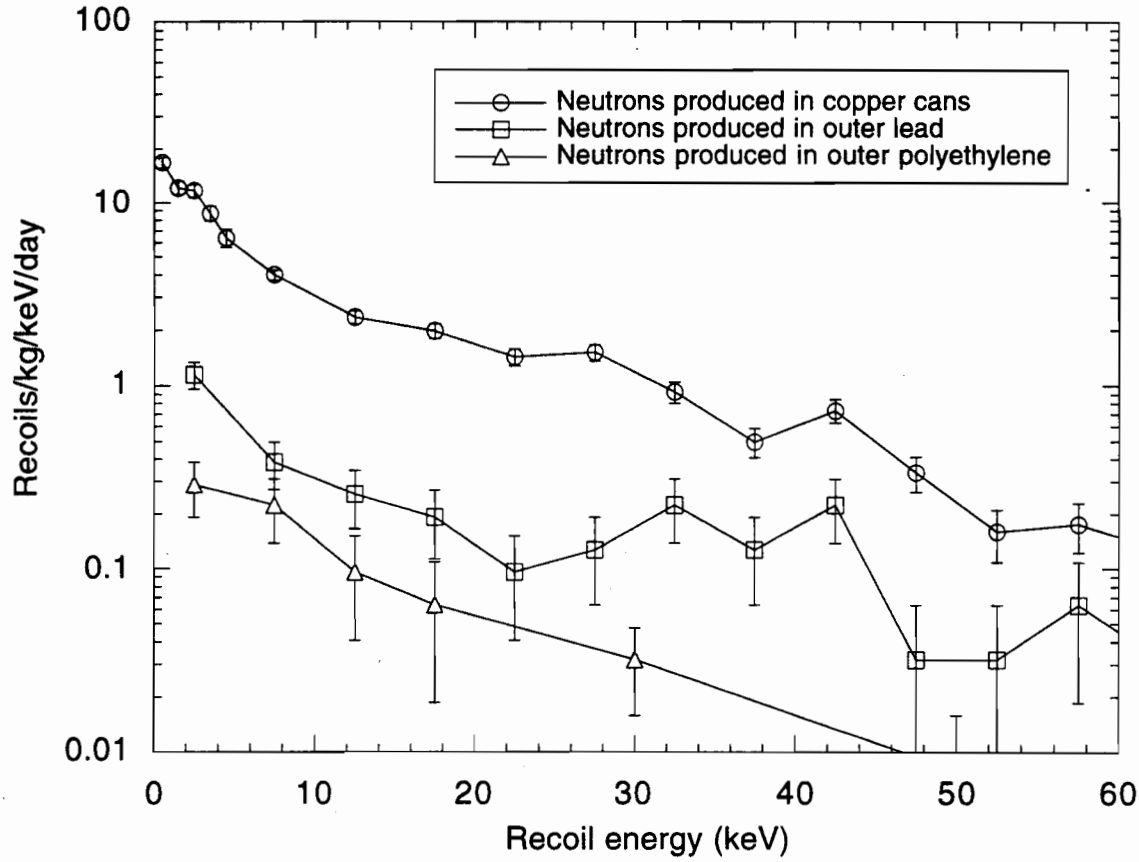

Figure 5.15: Simulated contribution to the neutron recoil background from muon-induced neutrons produced in the copper cans of the cryostat, the outer lead shield and the outer polyethylene. In all cases, only those recoils that occur in single detectors are recorded. No inner moderator was included in these simulations.

the neutrons were generated uniformly throughout each material using the neutron emission spectra and production rates discussed in Section 4.5. For these simulations, no inner moderator was used and only those recoils that occurred in single detectors were recorded.

As first demonstrated in Section 4.5.4, these background recoils rates can be effectively reduced by using an inner moderator. Figure 5.16 shows the effect of using an inner moderator of polyethylene to reduce the neutron background. The upper curve is the simulated recoil spectrum due to the muon-induced neutrons produced in the copper cans of the icebox. By filling the inside of the 5 mK can with polyethylene (as illustrated in

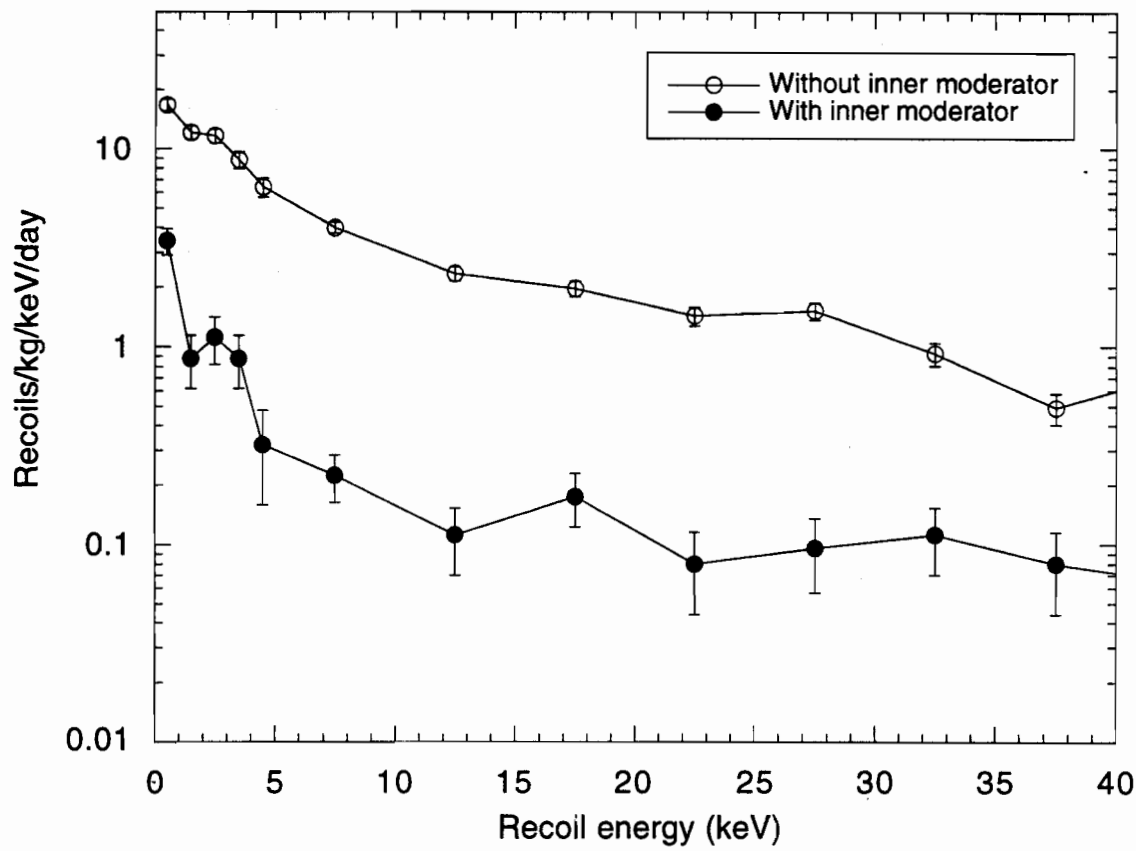

Figure 5.16: Effect of using an inner moderator to reduce the neutron background. The upper curve is the simulated recoil spectrum from muon-induced neutrons in the copper cans of the icebox. The lower spectrum is obtained by filling the inside of the inner icebox can with polyethylene as illustrated in Figure 5.13. In both cases, only those recoils that occur in single detectors are recorded.

Figure 5.13), the recoil spectrum is reduced by an order of magnitude.

With the inner moderator included, the recoil background from the neutrons produced in the copper becomes comparable to the recoil background from the neutrons produced in the outer lead shield as illustrated in Figure 5.17.

If the photon background rate inside the icebox is unacceptably high, it may become necessary to provide additional photon shielding inside the icebox. To be effective, this shielding material must be high-Z, to provide sufficient photon attenuation, and relatively free of internal radioactive contamination. For example, the low activity Nantes lead

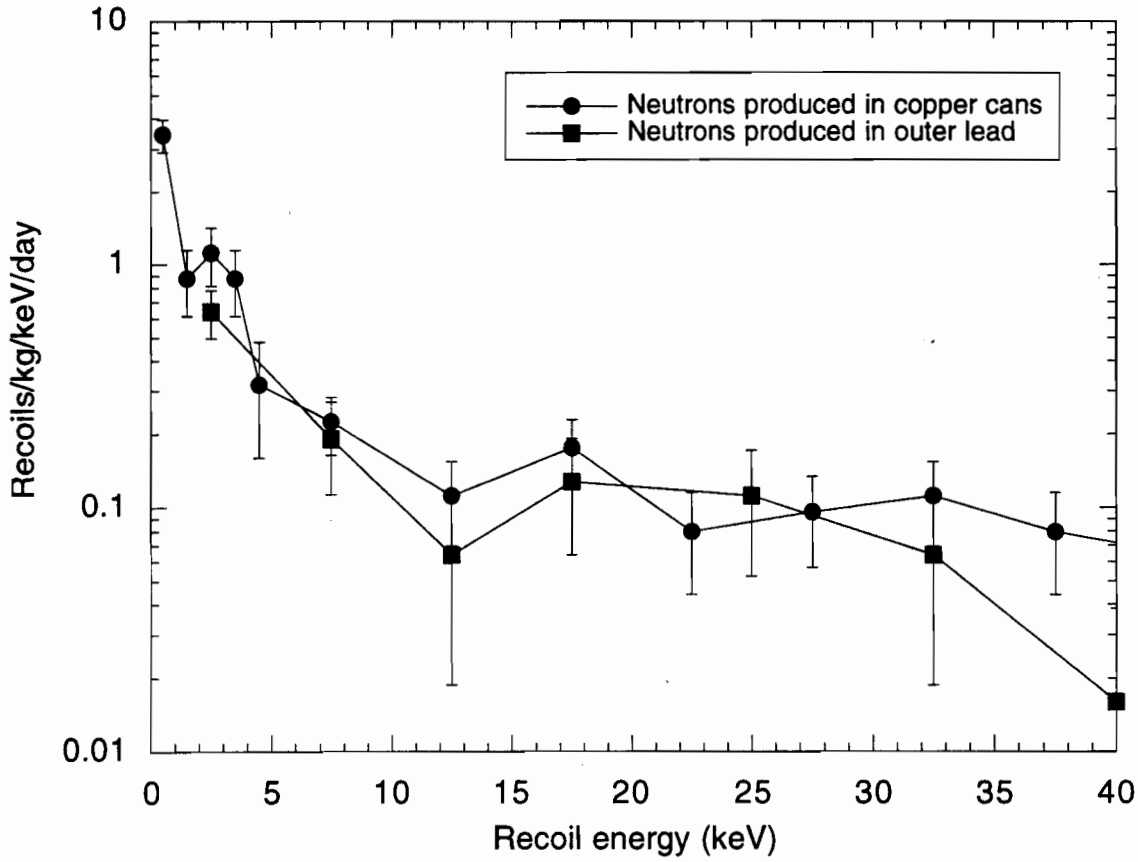

Figure 5.17: Simulated contribution to the neutron recoil background from muon-induced neutrons produced in the copper cans of the cryostat and the outer lead shield with the 5 mK can filled with polyethylene as shown in Figure 5.13. In both cases, only those recoils that occur in single detectors are recorded.

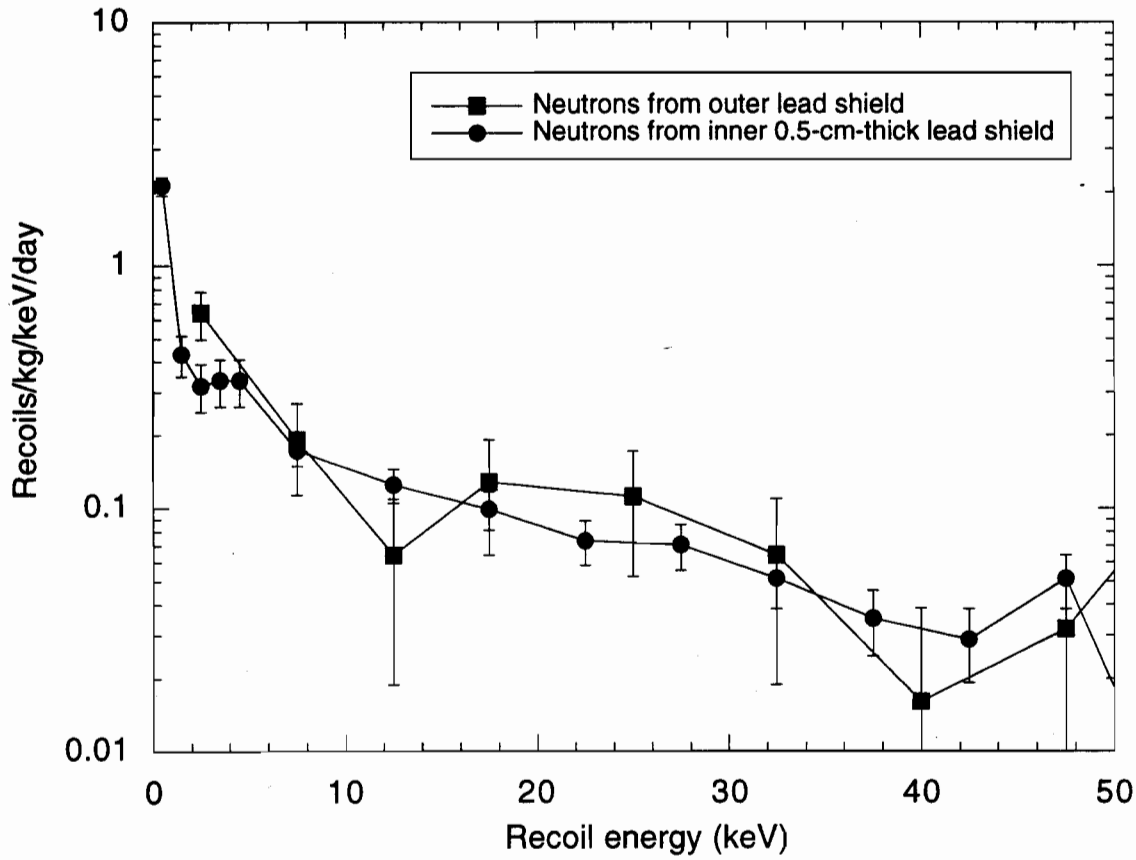

Figure 5.18: Comparison of the simulated neutron recoil background due to muon-induced neutrons produced in the outer lead shield and in a 0.5-cm-thick lead shield just outside the inner-most icebox can. In both case, the inner icebox can is filled with polyethylene as illustrated in Figure 5.13.

may be a suitable material for internal icebox shielding. Unfortunately, such a photon shield would become a neutron source, and thus the reduction in the photon background would have to be balanced against the increase in the neutron background. As shown in Figure 5.18, the neutron recoil background due to muon-induced neutrons produced in a 0.5-cm-thick lead shield just outside the inner-most icebox can is comparable to the neutron recoil background due to the muon-induced neutrons produced in the outer lead shield, with inner moderator being used in both cases.

The reduction in the neutron recoil background that can be achieved by using the

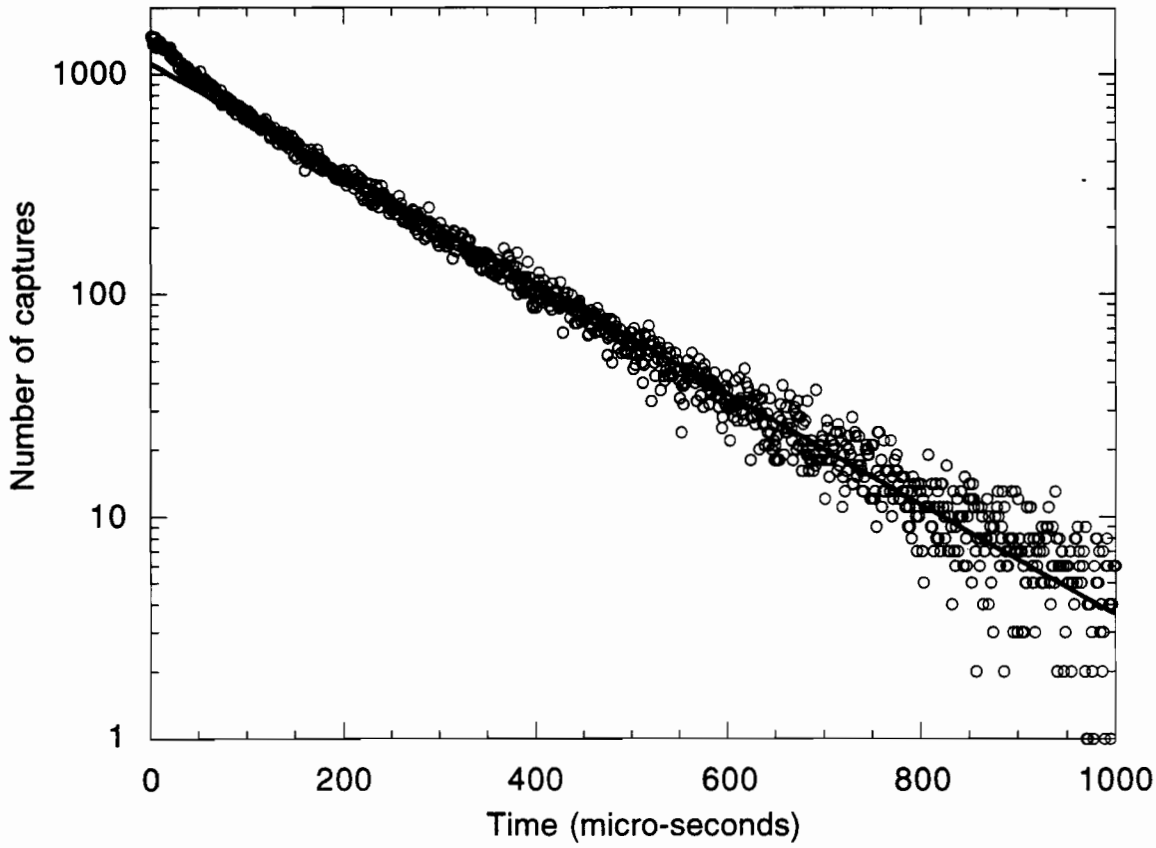

Figure 5.19: Simulated lifetime of the neutrons produced by muon interactions in the copper cans of the cryostat. Points show the number of neutrons captured as a function of the time since they were produced. The curve is an exponential fit to the data with a mean lifetime of $\tau = 175$ μs.

muon veto has not been included in any of these simulations. Although most of the neutrons that are produced by muon interactions are prompt, relatively long veto times may be necessary because these neutrons scatter many times before being sufficiently moderated or captured. Figure 5.19 illustrates the long capture lifetime of the neutrons produced in the copper cans; the average time for these neutrons to be captured is 175 μs. Therefore, veto times of the order of a few hundred microseconds may be required. At this relatively shallow site, where the total muon rate in the veto is of the order of a few hundred per second, this can lead to substantial, although manageable, deadtime.

As discussed in Section 5.2.3, the efficiency for identifying a muon event in the detector with a muon event in the veto was found to be 99.8%. What is important here is the efficiency of identifying a neutron event in the detector with a muon event in the veto. This efficiency could not be measured with the HPGe detector because the neutron events could not be identified in the background of photon events. With the electron/nuclear recoil discrimination capability of the BLIP detectors and the identification of neutrons through multiple scattering events, it should be possible to measure this efficiency which is expected to be at least 95%. Thus, the use of the muon veto should reduce the background recoil rates simulated with the neutron Monte Carlo program by at least a factor of 20, bringing the background rate to a level where a dark matter search is feasible.

To obtain an estimate of the expected neutron background recoil rate for the CDMS experiment, a somewhat more realistic description of the inner-can geometry was used for the final series of simulations. The inner-most icebox can was filled with a cylinder of polyethylene with three cylindrical holes cut out of it to allow for the towers (see Figure 5.20). In this geometry, the radial thickness of the inner moderator is only 5 cm in some places, but there is a full 9 cm of moderator at the top and the bottom of the can. Since the icebox will be run with only one tower installed initially, these simulations were run with one tower instrumented with a stack of six detectors, with each detector modeled as a germanium disk 6 cm in diameter and 1.3 cm thick. The separation between adjacent detectors was taken to be 0.7 cm. With these dimensions, each detector weighs 196 g, giving a total detector mass of just under 1.2 kg. Figure 5.21 shows the simulated neutron recoil spectra expected due to muon-induced neutrons produced in the copper cans of the cryostat and in the outer lead shield. In both cases, only those recoils that occur in a single detector are recorded in the spectra. And, as before, these spectra are the recoil rates obtained without using the muon veto.

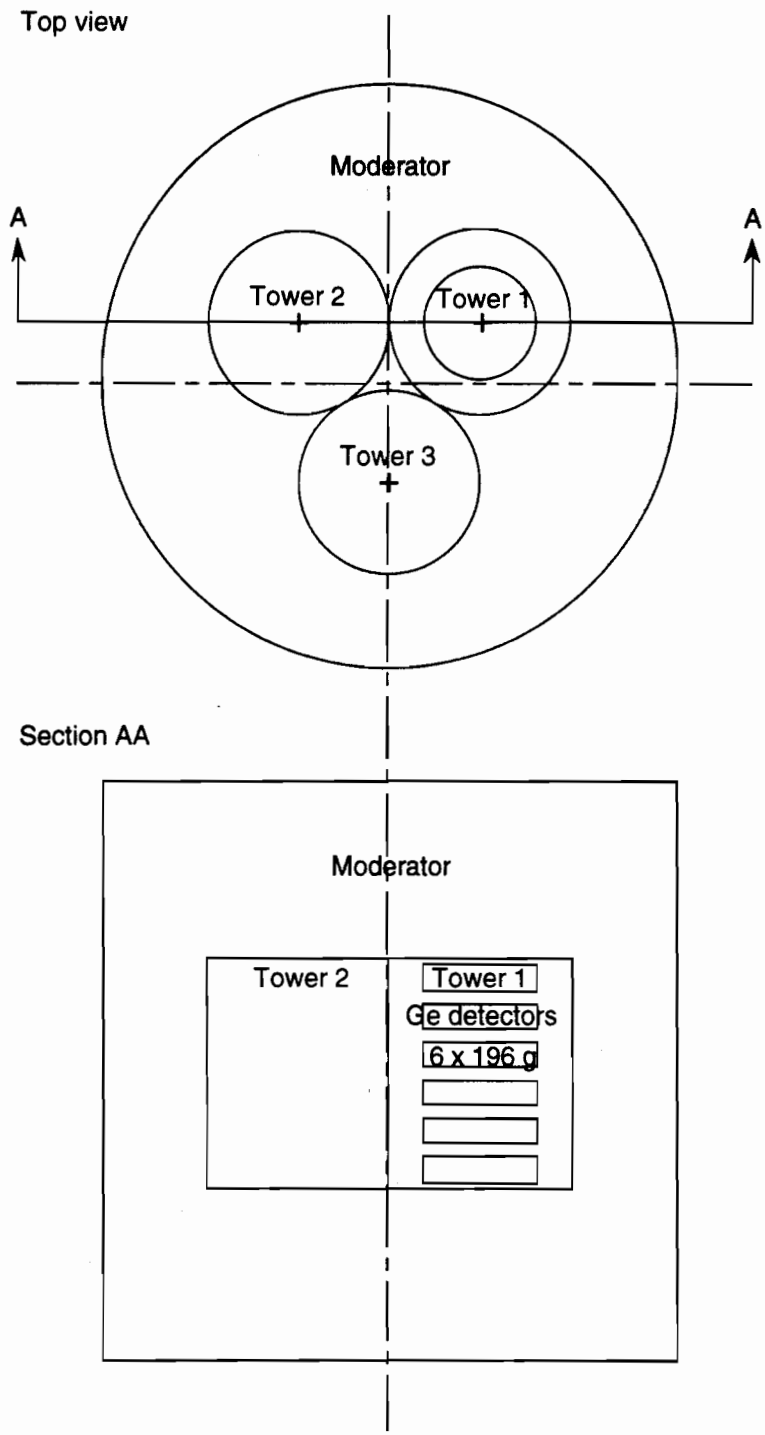

Figure 5.20: Geometry used in the simulations to estimate the expected neutron background rates for the CDMS Experiment.

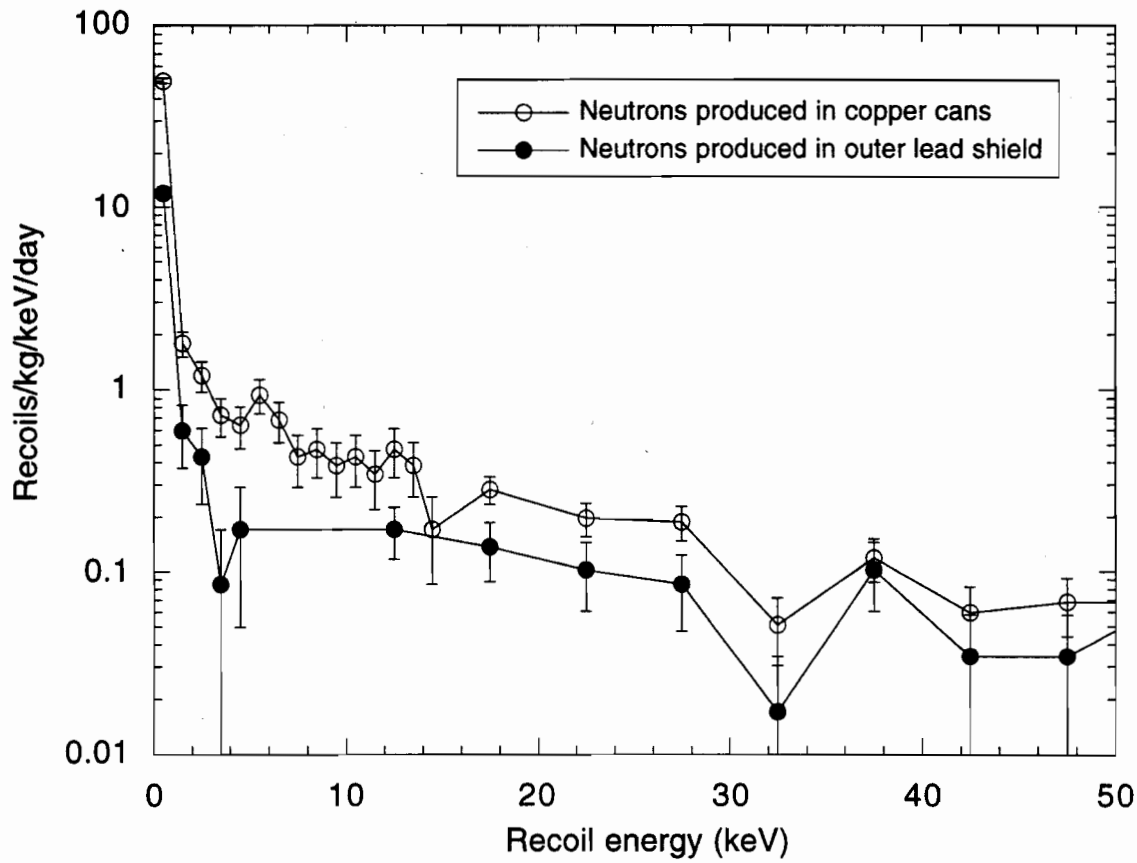

Figure 5.21: Simulated neutron recoil spectra expected for the CDMS Experiment due to muon-induced neutrons in the copper cans of the icebox and the outer lead shield. An inner moderator of polyethylene is assumed as shown in Figure 5.20. In both cases, only those recoils that occur in a single detector are recorded in the spectra.

5.5 Simulating Internal Photon Backgrounds

Using the geometry of the icebox cans illustrated in Figure 5.13 and the detector geometry shown in Figure 5.20, along with the event generation described in Section 3.4, GEANT3 was used to study the expected photon backgrounds from uranium and thorium contamination inside the icebox. To limit the amount of computational time necessary, only the gamma lines in the decay chains were considered. As demonstrated in Section 3.4, the beta decays in the uranium chain contributed little to the overall background rate. These simulations further demonstrate the advantage of having multiple detectors.

Figure 5.22 shows the simulated photon background from 1 μg of uranium contamination located in the center of the stack of six detectors. In the upper curve, all events are recorded in the spectrum. If a single photon interacts in one detector more than once, the signal appears as one event at the energy equal to the sum of the energies of the individual interactions. If a single photon interacts in more than one detector, the signal appears as one event in each detector involved at the energy equal to the total energy deposited in that detector. To obtain the lower curve, only those events which occur in a single detector are recorded. Since WIMPs will only interact in one detector, anything which interacts in more than one detector must be background and can therefore be rejected. As expected, this rejection technique does not reduce the photopeaks, but the continuum level is reduced by a factor of 2. Figure 5.23 shows the same two spectra for 1 μg of thorium contamination in the same position (i.e., the center of the detector stack).

Multiple detectors may also be able to help in localizing internal contamination by examining the background spectra measured in individual detectors. Figure 5.24 shows the simulated background spectra measured in detector 6, the bottom detector, and detector 3, the third detector from the top, for uranium contamination located just below detector 6. As expected, the background level in detector 6 is much higher than the background level in detector 3. This, however, is not the only difference in the two spectra. The low energy lines do not appear in the detector 3 spectrum and the shape of the

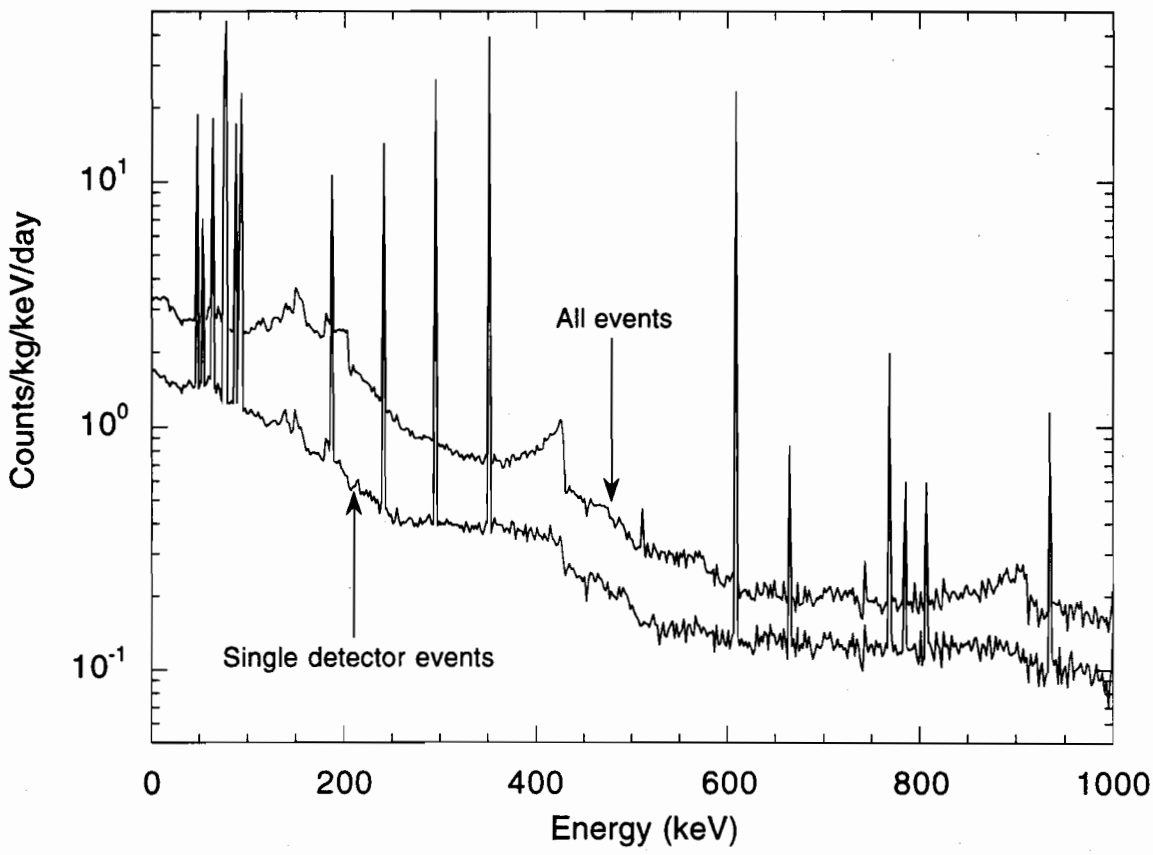

Figure 5.22: Simulated photon background from 1 μg of uranium contamination located at the center of the detector stack. For the upper curve, all events are recorded in the spectrum. For the lower curve, only those events which occur in a single detector are recorded in the spectrum.

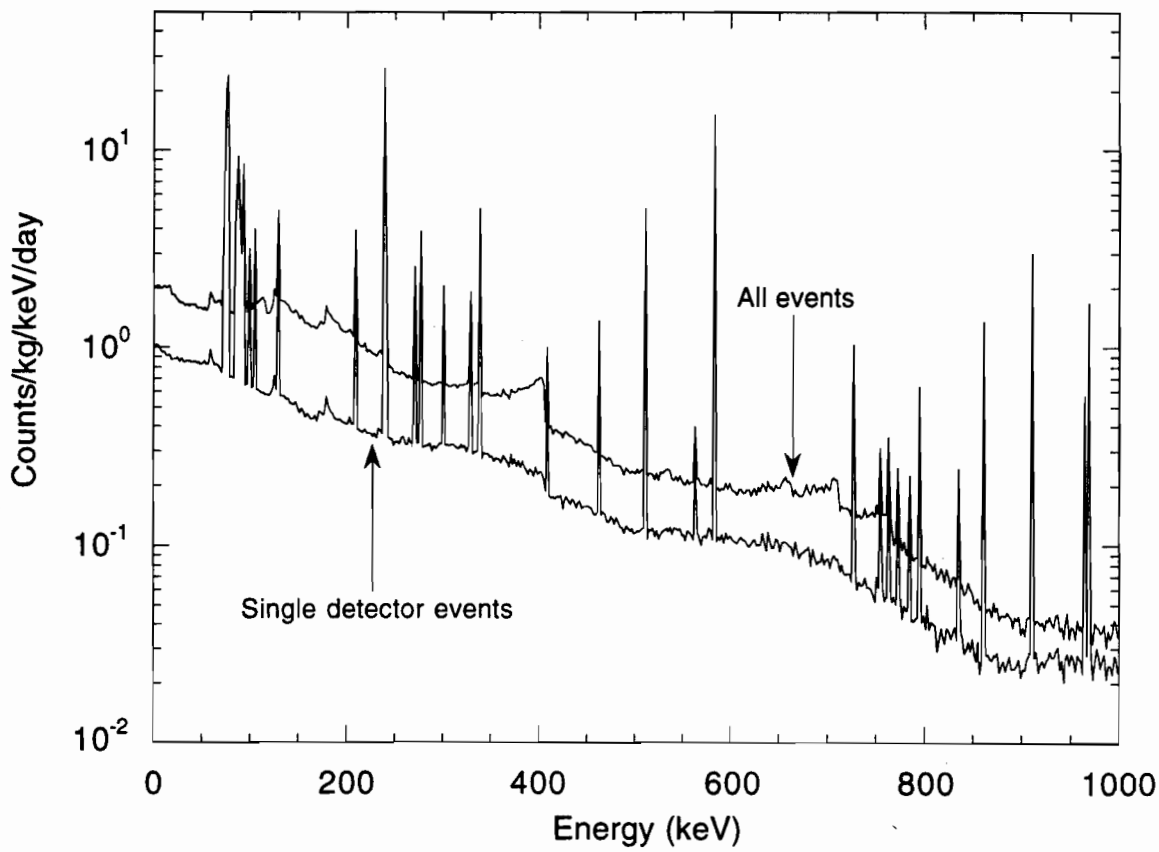

Figure 5.23: Simulated photon background from 1 μg of thorium contamination located at the center of the detector stack. For the upper curve, all events are recorded in the spectrum. For the lower curve, only those events which occur in a single detector are recorded in the spectrum.

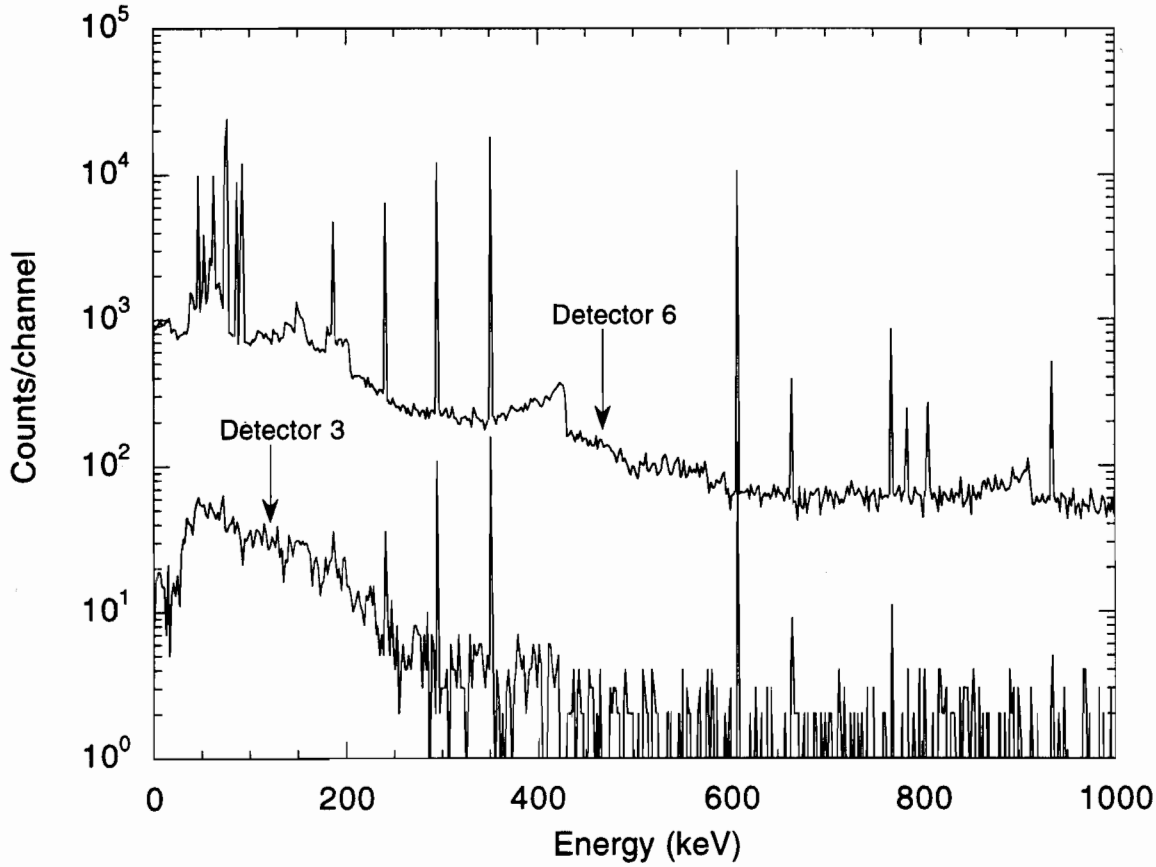

Figure 5.24: Simulated photon background spectra in detector 6 (bottom detector) and detector 3 (third detector from the top) from uranium contamination located just below detector 6.

low energy continuum is quite different from that in the detector 6 spectrum. Also, only the most dominant lines in the uranium chain are apparent in the detector 3 spectrum. Thus by comparing the spectra measured in the different detectors, it may be possible to localize internal contamination which could help in identifying the source of the radioactivity. Once identified, it may be possible to remove the unwanted contamination thereby reducing the local background.

Chapter 6

Analytical Tools for the CDMS Experiment

6.1 Dark Matter Event Rate

As discussed in Section 1.3, direct detection experiments look for the nuclear recoils produced by WIMPs scattering in laboratory detectors. The expected rate of these interactions can be calculated as follows [117].

The rate of interactions in a detector depends upon ρ_0, the density of WIMPs near the earth, and $f(v)$, the velocity distribution of WIMPs in the galactic halo near the earth. The galactic halo is commonly modeled as a cored spherical isothermal halo [118] with the density given by

$$\rho(r) = \rho_0 \frac{a^2 + r_0^2}{a^2 + r^2} \tag{6.1}$$

where r is the radius from the galactic center, r_0 is the distance from the sun to the galactic center ($r_0 \approx 8.5$ kpc), a is the core radius of the halo and $\rho_0 = \rho(r_0)$ is the local halo density. With this density distribution, the velocity distribution of the WIMPs must be close to Maxwellian in order to maintain a self-consistent, steady-state density model. Therefore, the local velocity distribution of the WIMPs is usually taken to be Maxwellian,

i.e.,

$$f(v)d^3v = \frac{1}{\pi^{3/2}v_0^3}\exp(-v^2/v_0^2)d^3v \tag{6.2}$$

where v_0 is the rotation speed at large radii and the mean-squared velocity is given by $\langle v^2 \rangle = \frac{3}{2}v_0^2$. The values of the parameters a and ρ_0 are determined by fitting to the galactic rotation curve. Jungman *et al.* adopt values of $a = 6.4$ kpc, $\rho_0 = 0.3$ GeV/cm^3 and $v_0 = 220$ km/s, but because of the uncertainty in the measured rotation curve and the uncertainty in the contribution of the disk to the rotation curve, the uncertainty in the local halo density is at least a factor of two.

Direct detection experiments measure the number of events per kilogram of detector material per day as a function of energy deposited, Q. Qualitatively, this event rate is simply given by

$$R \approx \frac{n\sigma\langle v \rangle}{m_N} \tag{6.3}$$

where n in the WIMP number density (given by the local mass density, ρ_0, divided by m_δ, the mass of the WIMP), σ is the elastic-scattering cross-section, $\langle v \rangle$ is the average speed of the WIMP relative to the target, and the detector mass is divided by the target nucleus mass, m_N, to get the number of target nuclei.

To be more accurate, one should take into account that the WIMPs move in the halo with velocities determined by $f(v)$, the differential cross-section depends upon $f(v)$ through a form factor $F(Q)$, and detectors have an energy threshold, E_T, below which they are insensitive to WIMP-nuclear recoils. Furthermore, the earth moves through the galactic halo and this motion should also be taken into account via $f(v)$.

In general, the differential rate per unit detector mass can be written

$$dR = \frac{\rho_0}{m_\delta m_N} v f(v) \frac{d\sigma}{d|\vec{q}|^2} d|\vec{q}|^2 dv \tag{6.4}$$

where $|\vec{q}|$ is the absolute value of the momentum transfer and $\frac{d\sigma}{d|\vec{q}|^2}$ is the differential cross-section. The differential cross-section can be written as

$$\frac{d\sigma}{d|\vec{q}|^2} = G_F^2 \frac{C}{v^2} F(|\vec{q}|) = \frac{\sigma_0}{4m_r^2 v^2} F(|\vec{q}|) \tag{6.5}$$

where G_F is the Fermi constant (1.1664×10^{-5} GeV^{-2}), C is a dimensionless number that carries all the particle physics model information, F is the form factor normalized so $F(0) = 1$ and m_r is the reduced mass (given by $m_r = m_N m_\delta/(m_N + m_\delta)$. The form factor accounts for the loss of coherence when the momentum transfer is small compared to the size of the nucleus. For non-zero momentum transfer, the form factor is simply the Fourier transform of the nucleon density. For convenience, σ_0 is defined as the "standard" total cross-section at zero momentum transfer:

$$\sigma_0 = \int_0^{4m_r^2 v^2} \frac{d\sigma(q=0)}{d|\vec{q}|^2} d|\vec{q}|^2 = 4G_F^2 m_r^2 C \tag{6.6}$$

but it is not really the total cross-section since it does not include the form factor suppression.

The momentum transferred is given by

$$|\vec{q}|^2 = 2m_r^2 v^2 (1 - \cos\theta^*) \tag{6.7}$$

where m_r is the reduced mass and θ^* is the scattering angle in the center-of-momentum frame. Thus, the energy deposited in the detector (i.e., the energy transferred to the nucleus), is given by

$$Q = \frac{|\vec{q}|^2}{2m_N} = \frac{m_r^2 v^2}{m_N}(1 - \cos\theta^*) \tag{6.8}$$

To find the total rate, dR must be integrated over all possible incoming velocities and over deposited energies between E_T and $Q_{max} = 2m_r^2 v^2/m_N$. Using Equations 6.4, 6.5 and 6.8, one obtains

$$\frac{dR}{dQ} = \frac{\sigma_0 \rho_0}{2m_\delta m_r^2} F(Q) \int_{v_{min}}^{\infty} \frac{f(v)}{v} dv \tag{6.9}$$

where

$$v_{min} = \left(\frac{Q m_N}{2m_r^2}\right)^{1/2} \tag{6.10}$$

and $F(Q)$ is the form factor discussed below. By using the energy transfer, Q, all of the dependence on the WIMP velocity has been put into one integral. The total rate of events

per kilogram per day is found from

$$R = \int_{E_T}^{\infty} \frac{dR}{dQ} dQ \tag{6.11}$$

The scalar cross-section for WIMPs scattering from a nucleus of mass m_N can be written [119]

$$\sigma_0 = \frac{4m_\delta^2 m_N^2}{\pi(m_\delta + m_N)^2} \left(\frac{f_p}{m_n}\right) \tag{6.12}$$

where $m_n \simeq 0.94$ GeV/c^2 is the nucleon mass and f_p is the WIMP-nucleon coupling. In this way, all the information about the specific supersymmetric particle model is contained in f_p. For models in which the lightest supersymmetric particle is the dark matter, the cross-section on germanium is typically less than 4×10^{-36} cm^2 [117].

The most commonly used form factor for scalar interactions is the exponential form factor, first used in this context by Freese *et al.* [120]:

$$F(Q) = \exp(-Q/Q_0) \tag{6.13}$$

where Q is the energy transferred from the WIMP to the nucleus and Q_0 is the nuclear "coherence energy" given by

$$Q_0 = \frac{2\hbar^2}{3m_N R_0^2} \tag{6.14}$$

for the radius of the nucleus, R_0, given by

$$R_0 = \left[0.3 + 0.91\left(\frac{m_N}{\text{GeV}}\right)^{1/3}\right] \times 10^{-13} \text{ cm} \tag{6.15}$$

The exponential form factor implies that the radial density profile of the nucleus has a gaussian form. A more accurate form factor can be obtained [121] by writing the density in the form

$$\rho(\mathbf{r}) = \int \rho_0(\mathbf{r}')\rho_1(\mathbf{r} - \mathbf{r}')d^3r' \tag{6.16}$$

where ρ_0 is a constant inside a sphere of radius $R_1 = (R^2 - 5s^2)^{1/2}$ (with $R \simeq 1.2A^{1/3}$ fm and $s \simeq 1$ fm) and $\rho_1(\mathbf{r}) = \exp[-\frac{1}{2}(r/s)]$. In this case, the Fourier transform of the density becomes

$$F(Q) = \frac{3j_1(qR_1)}{qR_1} \exp\left[-\frac{1}{2}(qs)^2\right] \tag{6.17}$$

where $q = \sqrt{2m_N Q}$ is the momentum transferred and j_1 is a spherical Bessel function. For most practical purposes the exponential form factor of Equation 6.13 is adequate and is much easier to manipulate analytically. In both cases, the form-factor dependence of dR/dQ is small at small Q, but becomes appreciable for larger recoil energies.

For axial-vector (spin) interactions, the full momentum dependence of the form factor must be calculated from detailed nuclear models. Then, to get the total rate, the rates from both spin and scalar interactions must be added together. However, since scalar interactions often dominate the elastic scattering cross-section, the scalar form factor can be used if detailed nuclear calculations for the spin interaction are not available.

Consider now the simple Maxwellian halo with the velocity distribution given by

$$f(v')d^3v' = \frac{1}{\pi^{3/2}v_0^3}\exp(-v'^2/v_0^2)d^3v' \tag{6.18}$$

Ignoring the motion of the sun and the earth, integration over angles leads to the one-dimensional distribution

$$f'(v')dv' = \frac{4(v')^2}{v_0^3\sqrt{\pi}}\exp(-v'^2/v_0^2)dv' \tag{6.19}$$

and

$$\int_{v_{min}}^{\infty} f'(v')dv' = \frac{2}{\sqrt{\pi}v_0}\exp(-v_{min}^2/v_0^2) \tag{6.20}$$

where v_{min} is given in Equation 6.10. For light WIMPs where $F(Q) \approx 1$, the differential event rate becomes

$$\frac{dR}{dQ} = \frac{\sigma_0\rho_0}{\sqrt{\pi}v_0 m_\delta m_\tau^2}\exp\left(-\frac{Qm_N}{2m_\tau^2 v_0^2}\right) \tag{6.21}$$

and the total integrated rate is

$$R = \frac{\sigma_0\rho_0}{m_\delta m_N}\frac{2}{\sqrt{\pi}}v_0\exp\left(-\frac{E_T m_N}{2m_\tau^2 v_0^2}\right) \tag{6.22}$$

With $E_T = 0$, this is precisely the simple result given in Equation 6.3 since $\langle v\rangle = \frac{2}{\sqrt{\pi}}v_0$ for the velocity distribution of Equation 6.19.

However, one needs to take into account the motion of the sun and the earth. This increases the total rate and gives rise to a yearly modulation in the event rate which may

provide a method of identifying a WIMP signal [122, 120]. To account for this motion, one subtracts the velocity of the earth, v_e, from v' in Equation 6.18 to get the velocity of the WIMP, v, in the reference frame of the earth. That is,

$$\vec{v'} = \vec{v} + \vec{v_e} \tag{6.23}$$

$$v'^2 = v^2 + v_e^2 + 2vv_e \cos\chi \tag{6.24}$$

where χ is the angle between the WIMP velocity in the earth frame and the direction of the earth's motion. As a function of time, v_e changes as the earth's motion comes into and out of alignment with the sun's motion through the halo. This causes a yearly modulation in the event rate which peaks around June 2nd each year [122, 123]. The velocity of the earth can be written as [120]

$$v_e = v_0 \left[1.05 + 0.07 \cos\left(\frac{2\pi(t - t_p)}{1 \text{ year}}\right)\right] \tag{6.25}$$

where t_p = June 2nd $\pm$ 1.3 days. Changing variables, using $\frac{d^3v'}{d^3v} = \frac{v'^2}{v^2}\frac{\cos\theta}{\cos\chi}$ and integrating over angles, one obtains [120]

$$f(v)dv = \frac{vdv}{v_e v_0 \sqrt{\pi}} \left[\exp\left(-\frac{(v - v_e)^2}{v_0^2}\right) - \exp\left(-\frac{(v + v_e)^2}{v_0^2}\right)\right] \tag{6.26}$$

Then

$$\int_{v_{min}}^{\infty} f(v)dv = \frac{1}{2v_e}\left[\text{erf}\left(\frac{v_{min} + v_e}{v_0}\right) - \text{erf}\left(\frac{v_{min} - v_e}{v_0}\right)\right] \tag{6.27}$$

and Equation 6.9 becomes

$$\frac{dR}{dQ} = \frac{\sigma_0 \rho_0}{4 v_e m_\delta m_r^2} F(Q) \left[\text{erf}\left(\frac{v_{min} + v_e}{v_0}\right) - \text{erf}\left(\frac{v_{min} - v_e}{v_0}\right)\right] \tag{6.28}$$

Equation 6.28 is a very general expression for the differential event rate expected for WIMP dark matter which can be compared directly to the measured differential energy spectrum from a direct detection experiment.

Figure 6.1 shows the calculated event rate on germanium for a variety of WIMP masses using Equation 6.28 with the exponential form factor given in Equation 6.13.

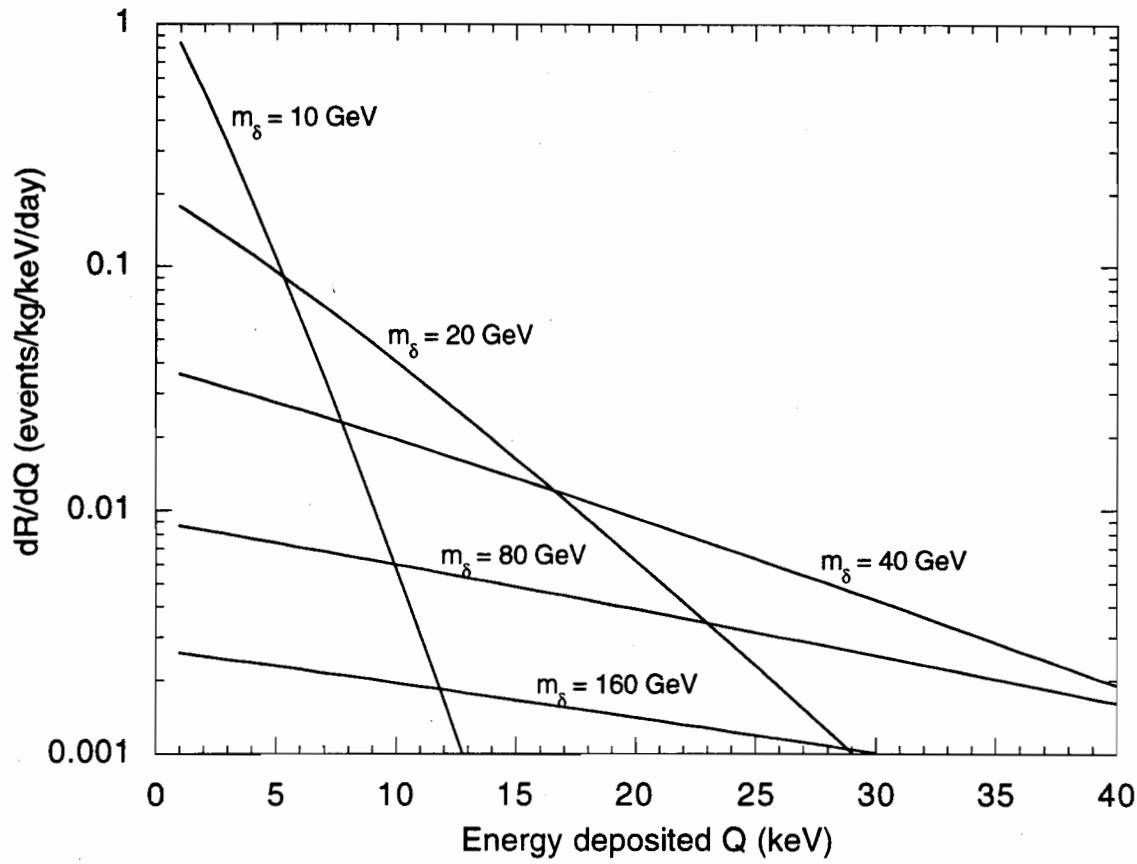

Figure 6.1: Calculated event rate for WIMPs of various masses scattering from germanium. An arbitrary cross-section of $\sigma_0 = 4 \times 10^{-36}$ cm^2 was used, along with standard values of $v_0 = 220$ km/s and $v_e = 231$ km/s. The exponential form factor given in Equation 6.13 was assumed.

An arbitrary cross-section of $\sigma_0 = 4 \times 10^{-36}$ cm^2 was used, and despite this relatively high WIMP cross-section, the expected event rate is orders of magnitude lower than the measured gamma-ray background shown in Figure 1.2.

The annual modulation of the WIMP signal is illustrated in Figure 6.2 which shows the expected event rate for 40 GeV WIMPs scattering in germanium in June and December calculated using Equation 6.28 with v_e given by Equation 6.25. As before, the exponential form factor and an arbitrary cross-section of $\sigma_0 = 4 \times 10^{-36}$ cm^2 were used. Observation of such a modulation in a measured spectrum would be a strong indication of a WIMP

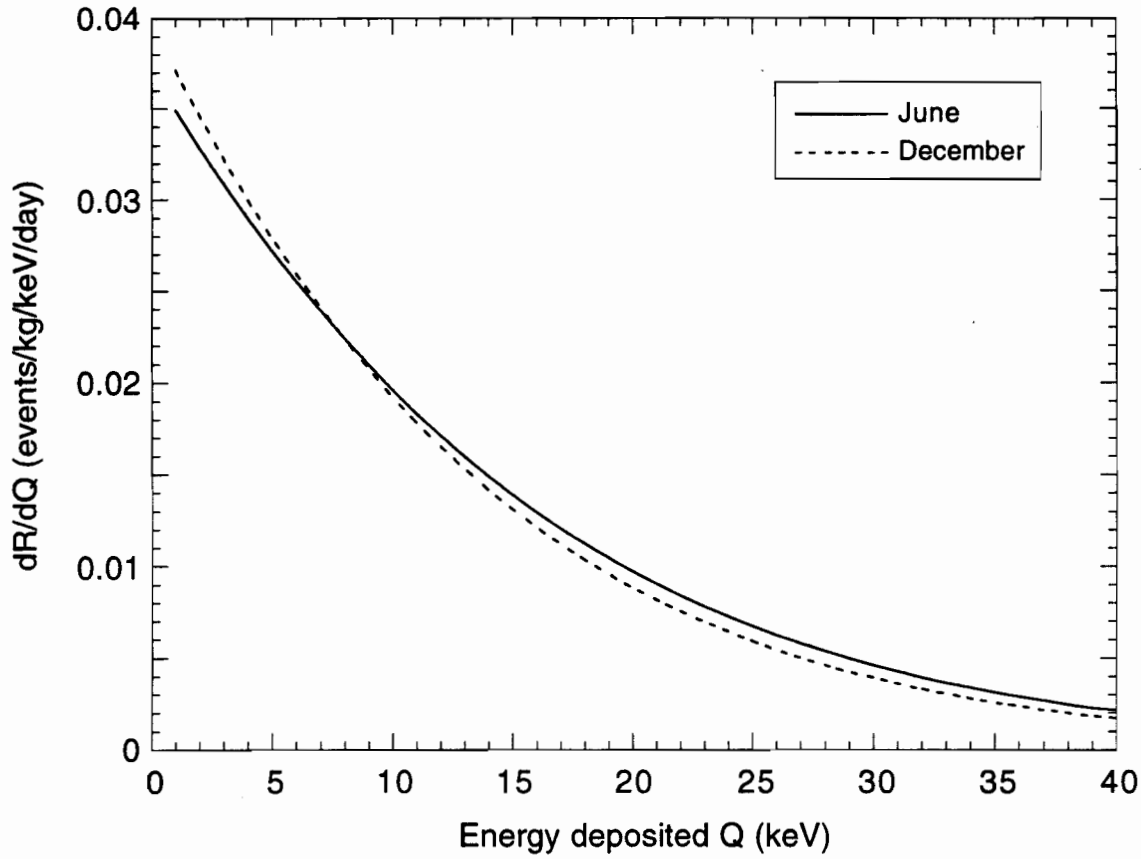

Figure 6.2: Annual modulation of the expected WIMP signal in a germanium detector. The exponential form factor and an arbitrary cross-section of $\sigma_0 = 4 \times 10^{-36}$ cm^2 were used along with $v_0 = 220$ km/s and v_e given by Equation 6.25.

signal.

Another way a WIMP signal may be identified is to look for the recoil spectra in more than one target material. For example, Figure 6.3 shows the expected event rates for 20 GeV and 80 GeV WIMPs scattering in germanium and silicon.

Finally, Equation 6.28 can be integrated over Q, from the detector threshold energy, E_T, to infinity to give the total integrated event rate. In many cases, a numerical integration is easiest, but for the exponential form of $F(Q)$ given in Equation 6.13, the total integrated rate can be given analytically by

$$R_{exp} = \frac{\sigma_0 \rho_0}{\sqrt{\pi} m_\delta m_N} \frac{v_0^2}{v_e b} \left[e^{-E_T/E_0} \mathcal{F}(A_-, A_+) - \frac{\mathcal{F}(\tilde{A}_-, \tilde{A}_+)}{(1+b)^{1/2}} \exp\left(-\frac{b}{1+b} \frac{v_e^2}{v_0^2} \right) \right] \tag{6.29}$$

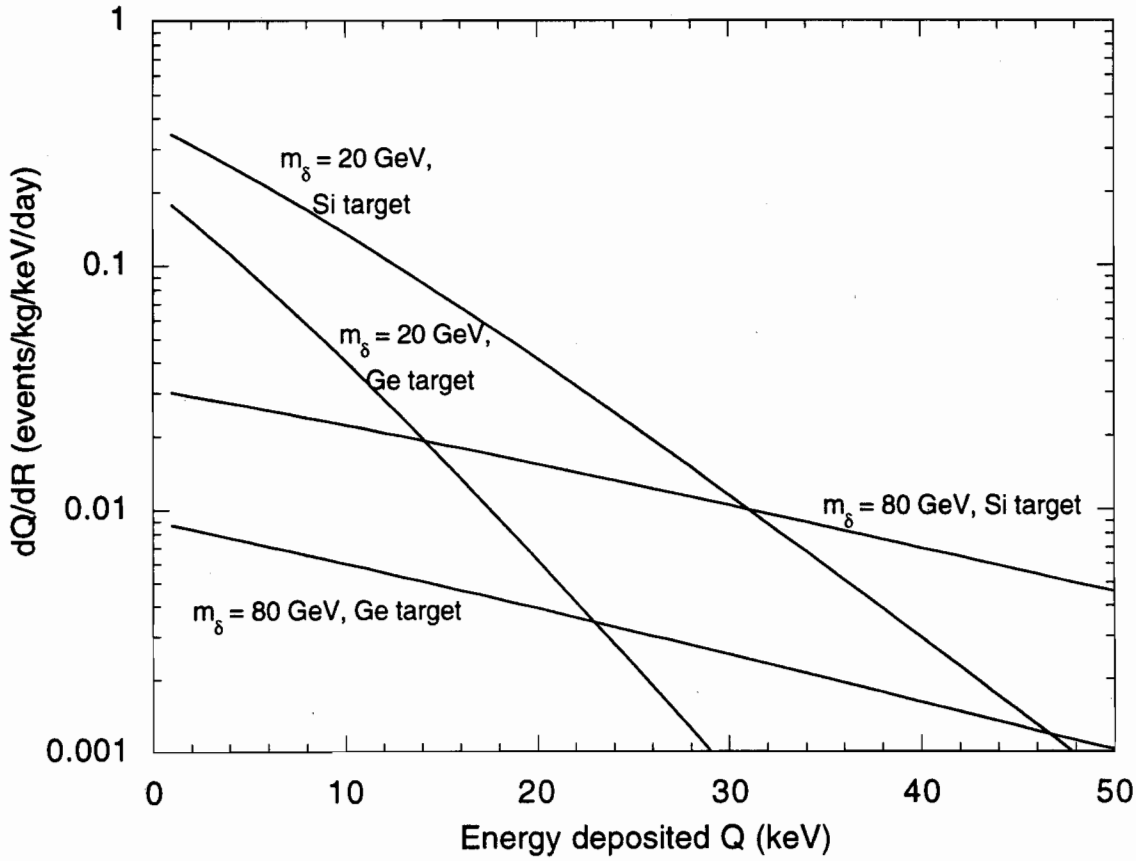

Figure 6.3: Calculated event rate for WIMPs of various masses scattering in germanium and silicon. An arbitrary cross-section of $\sigma_0 = 4 \times 10^{-36}$ cm^2 was used, along with standard values of $v_0 = 220$ km/s and $v_e = 231$ km/s. The exponential form factor given in Equation 6.13 was assumed.

where

$$\begin{aligned}
\mathcal{F}(x_1, x_2) &= \frac{\sqrt{\pi}}{2}[\mathrm{erf}(x_2) - \mathrm{erf}(x_1)] \\
A_{\pm} &= A_T \pm (v_e/v_0) \\
A_T^2 &= m_N E_T (2m_r^2 v_0^2)^{-1} \\
\tilde{A}_{\pm} &= (1+b)^{-1/2}[A_T(1+b) \pm (v_e/v_0)] \\
b &= 2v_0^2 m_r^2 (E_0 m_N)^{-1}
\end{aligned}$$

In addition to the event rate, the average energy deposition in the detector is often of interest. In general, the average energy deposition is given by

$$\langle Q \rangle = \frac{\int Q \frac{dR}{dQ} dQ}{\int \frac{dR}{dQ} dQ} \tag{6.30}$$

Using the exponential expression for the differential rate given in Equation 6.21, Equation 6.30 is easily integrated and the average energy deposition simply becomes

$$\langle Q \rangle_{exp} = \frac{2m_r^2 v_0^2}{m_N} \tag{6.31}$$

However, Equation 6.21 does not include the motion of the sun and earth, and as a result, $\langle Q \rangle_{exp}$ underestimates the true average energy deposition. Numerical integration of Equation 6.30 using the general expression for the differential event rate given in Equation 6.28 indicates that the average energy deposition is approximately given by $1.8\langle Q \rangle_{exp}$ which can be written as

$$\langle Q \rangle \approx 1.9 \frac{m_\delta m_N}{(m_\delta + m_N)^2} \left(\frac{m_\delta}{1\ \mathrm{GeV}}\right) \left(\frac{v_0}{220\ \mathrm{km/s}}\right)^2 \ \mathrm{keV} \tag{6.32}$$

6.2 Expected Sensitivity

Comparing the calculated WIMP interaction rate given by Equation 6.28 with a typical measured background spectrum from a first generation direct detection experiment (such

as that shown in Figure 1.2), it is obvious that in order to achieve the sensitivity required to probe supersymmetric models, a substantial reduction in the measured background is necessary. The electron/nuclear recoil discrimination capability of the detectors discussed in Chapter 2 allows for the identification and subtraction of much of the measured background and the sensitivity of the experiment is determined by the statistical accuracy of this subtraction as described below.

The total number of counts in a detector can be divided into two components, one due to signal events and one due to background events. If the total signal rate is given by S, then the number of counts in the detector due to signal events is given by SMt, where M is the total mass of the detector and t is the counting time. Similarly, if the total background rate is given by B, the number of counts in the detector due to background events is given by BMt. If α is the probability that a signal event is identified as a signal event, and β is the probability that a background event is misidentified as a signal event, then the apparent number of signal events will be given by

$$N_s = (\alpha S + \beta B)Mt \tag{6.33}$$

and the apparent number of background events will be given by

$$N_b = [(1-\alpha)S + (1-\beta)B]Mt \tag{6.34}$$

Combining Equations 6.33 and 6.34, the total signal rate is found to be

$$S = \frac{(1-\beta)N_s - \beta N_b}{(\alpha-\beta)Mt} \tag{6.35}$$

If the signal is much smaller than the background, then Equations 6.33 and 6.34 become

$$N_s = \beta BMt \tag{6.36}$$

$$N_b = (1-\beta)BMt \tag{6.37}$$

and the statistical accuracy of the signal is given by

$$\delta S = \frac{\sqrt{(1-\beta)^2\beta BMt + \beta^2(1-\beta)BMt}}{(\alpha-\beta)Mt} = \frac{\sqrt{\beta(1-\beta)}}{(\alpha-\beta)}\sqrt{\frac{B}{Mt}} \tag{6.38}$$

Thus we see that the sensitivity of the experiment increases as the square root of the mass and the counting time and as one over the square root of the background rate.

As discussed in Chapter 5, background measurements inside the final shield at the Stanford Underground Facility indicate that with the active muon veto, the differential photon background rate at energies below 100 keV is approximately constant and is no more than 7 events/kg/keV/day. Since the WIMP spectrum is approximately exponential, it should be sufficient to integrate the differential background rate out to twice the average energy deposition. Thus, for a 40 GeV WIMP for example, the average energy deposition in germanium is about 18 keV and the total background rate is approximately

$$B = 7 \text{ events/kg/keV/day} \times 36 \text{ keV} = 252 \text{ events/kg/day} \tag{6.39}$$

As discussed in Chapter 2, an electron recoil background rejection efficiency of 99% is expected for the detectors (i.e., $(1-\beta) = 0.99$) and nuclear recoils are identified at least as well (i.e., $\alpha \simeq 1$). Assuming a counting time of 100 days with 1 kg of germanium detectors at the Stanford Underground Facility, the statistical accuracy given by Equation 6.38 is then $\delta S_{er} = 0.16$ events/kg/day. However, the background due to neutrons must also be considered. Simulations of the expected nuclear recoil rate due to muon-induced neutrons lead to recoil event rates of the order of 17 events/kg/day without the muon veto system active. If the muon veto efficiency for neutrons is known, this background can also be subtracted with the statistical accuracy given by Equation 6.38 where B now represents the neutron background rate. Assuming a muon veto efficiency for neutrons of 95%, $\delta S_{nr} = 0.1$ events/kg/day. These two results are combined to give the total statistical accuracy of the background subtraction

$$\delta S = \sqrt{\delta S_{er}^2 + \delta S_{nr}^2} = 0.19 \text{ events/kg/day} \tag{6.40}$$

and a 95% confidence limit is set at a level of $1.64\delta S = 0.3$ events/kg/day. With this level of sensitivity, the CDMS experiment begins to probe models of supersymmetry as illustrated in Figure 6.4.

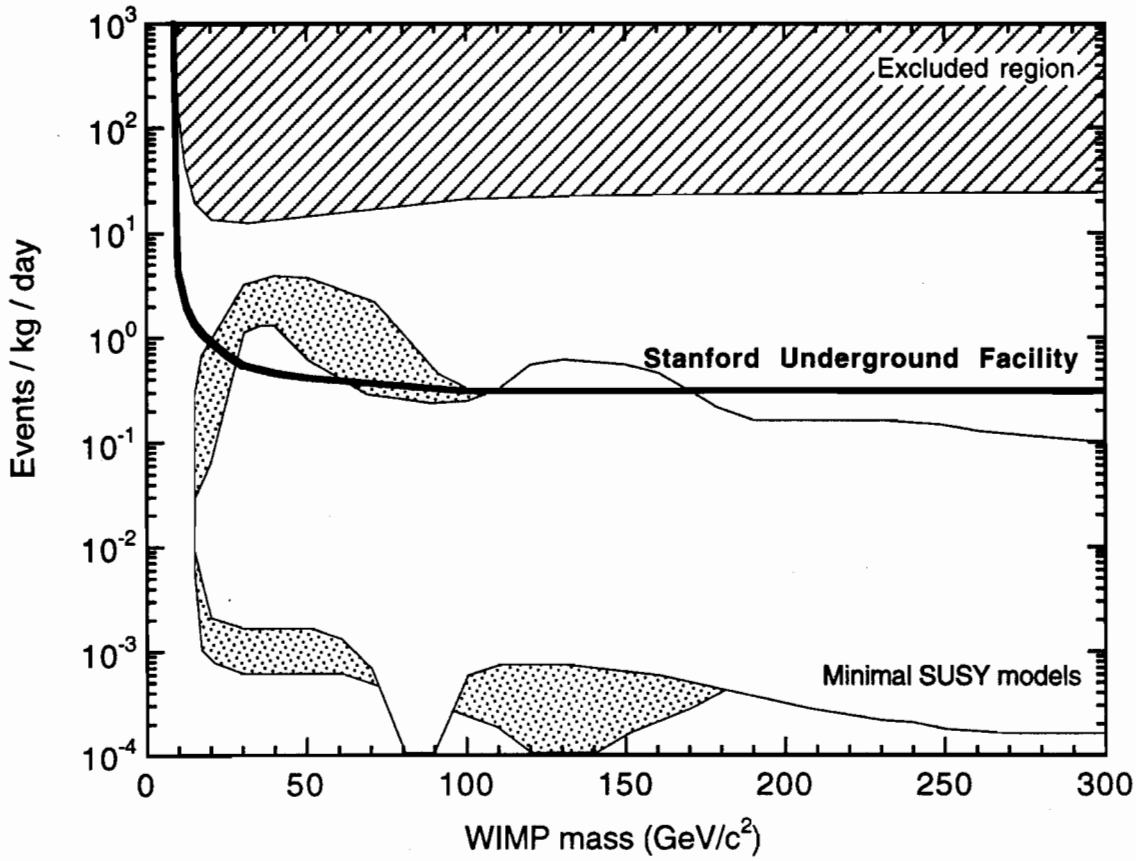

Figure 6.4: Expected sensitivity for the CDMS experiment at the Stanford Underground Facility plotted as the total event rate in germanium as a function of the WIMP mass. The limit shown assumes 100 kg · days of data, with an electron recoil rejection factor of 99% and a muon veto factor for neutrons of 95%. Also shown is the region excluded by the first generation direct detection experiments [54] and the allowed parameter space for various models of the lightest supersymmetric particle [55]. (The light shaded region is for models assuming a Higgs mass of 50 GeV/c^2 with $\tan\beta = 2$. The dotted region is for models assuming a Higgs mass between 80 GeV/c^2 and 90 GeV/c^2 with $\tan\beta$ between 6 and 22).

Chapter 7

Future of the CDMS Experiment

The experiments and calculations described in this thesis have shown that, as in the case of the first generation direct detection experiments, the CDMS experiment will eventually become background-limited due to the shallow depth of the Stanford Underground Facility. This work also demonstrates that to increase the sensitivity of the experiment, it will become necessary to move the experiment to a deep underground site where the muon flux has been substantially reduced. By this time, the level of detector development and the experience gained in operating the experiment at the Stanford Underground Facility will make the experiment at a remote site a viable operation. With the increased sensitivity at a deep site and the use of advanced detectors, the CDMS experiment will have the potential of identifying a WIMP signal.

7.1 Deep Underground Site

The main advantage of a deep underground site are the reductions in the primary cosmic ray muon flux and in the flux of secondary particles, particularly neutrons, which cannot be rejected by the electron/nuclear recoil discrimination capability of the CDMS detectors. For reference, the cosmic ray muon flux as a function of depth is illustrated in Figure 7.1.

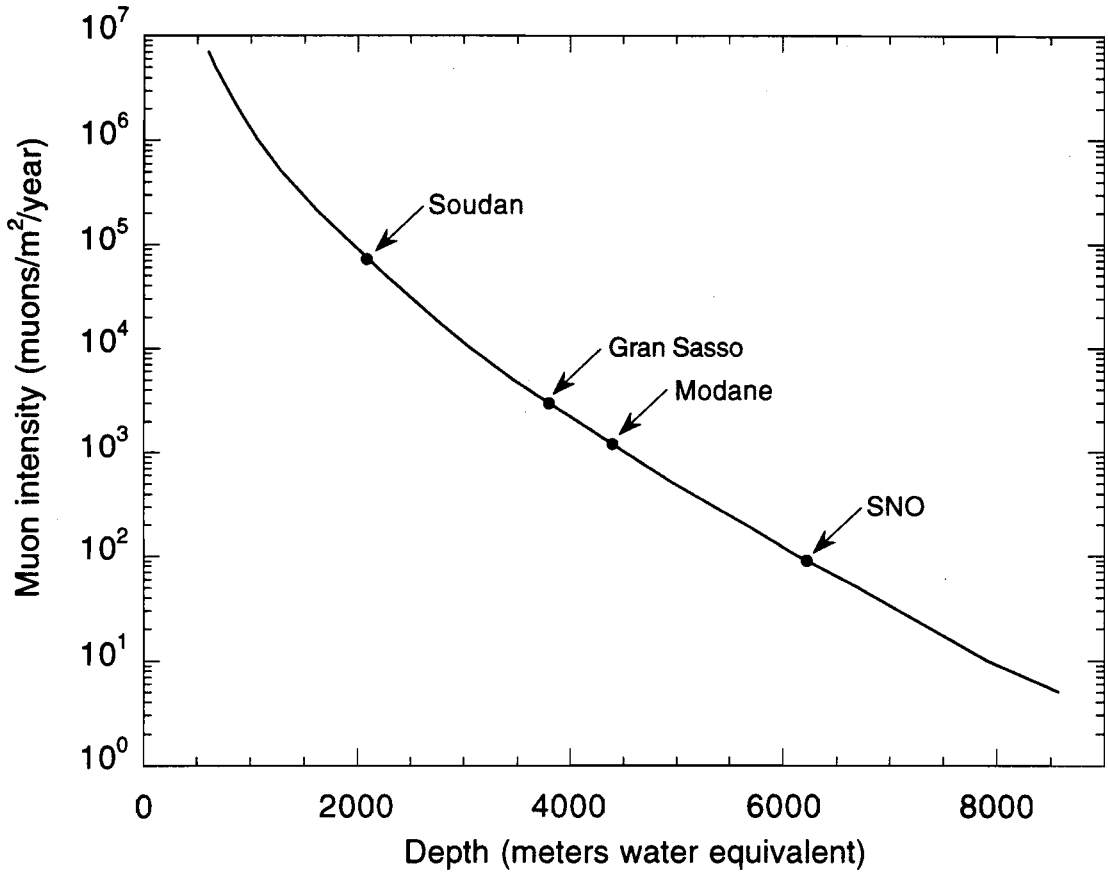

Figure 7.1: Cosmic ray muon flux as a function of depth (adapted from [124]). The depth of four underground laboratories are indicated on the curve. For reference, the cosmic ray muon flux at the Stanford Underground Facility, located at a depth of 16 m.w.e., is 1.4×10^9 muons/m^2/year.

Also shown in this figure are the vertical locations of the four underground laboratories discussed in Section 7.1.2. In moving to a deep underground site, the basic design of the experiment would remain unchanged, however, some modifications would be necessary to make the most of the reduced muon flux.

7.1.1 Changes to the Experiment

In a deep underground site where the cosmic ray muon flux is substantially attenuated, the lead shield surrounding the icebox is no longer the dominant source of neutrons.

In this case, there is no longer a need for the large volume of moderator inside the lead shield. Without this moderator, the lead shield can be made substantially smaller, permitting the use of higher quality lead with lower levels of radioactive contamination. A moderator could then be used outside of the lead to attenuate the neutron flux from natural radioactivity in the surrounding rock which would be the dominant source of background neutrons. Furthermore, should internal photon shielding become necessary inside the icebox, it could be used without introducing an additional source of background neutrons.

Depending on the depth of the site, a muon veto would no longer be absolutely necessary, although one could still be useful. With the reduced muon flux, a much simpler veto shield could be used; it would only be necessary to cover the top of the shield where the muon flux is highest. Since the muon rate at large depths falls quickly with zenith angle and the total muon rate would be relatively small, the top panel could be made considerable larger in area than the shield, effectively covering the side walls, without introducing substantial deadtime. Furthermore, with a low veto rate, the veto time could be made long enough to include delayed events without incurring an excessive increase in deadtime.

Finally, with the reduced muon flux, the neutron moderator inside the icebox would no longer be needed. This would greatly increase the volume of experimental space at base temperature available for active detectors. Without the inner moderator, the icebox is capable of housing seven towers instead of only three. By increasing the diameter of the germanium detectors to 7.6 cm (the largest diameter that can be accommodated in the towers) and only modestly increasing the thickness of the detectors to 1.6 cm, the active mass of germanium could easily be increased to 15 kg with the seven towers.

A fringe benefit of moving to another site is that relocation would provide a perfect opportunity to make improvements to the experiment. Flaws in the design or construction of the icebox, towers or detectors may only be discovered during the course of operation at the Stanford Underground Facility. For instance, the experiment itself may be the

only way to determine whether or not certain materials used in the system contain sufficiently low levels of radioactive contamination. These flaws could then be corrected while installing the experiment at the new deep site.

7.1.2 Potential Locations

A number of possible locations for the next phase of the CDMS experiment have been explored. Each of these locations has a variety of advantages and disadvantages that must be examined. A brief description of each of the four the deep sites being considered for the next phase of the CDMS experiment is outlined below.

The Soudan Underground Laboratory

The Soudan Underground Laboratory is operated by the School of Physics and Astronomy of the University of Minnesota-Twin Cities. The Soudan laboratory site, leased by the University of Minnesota from the State of Minnesota, Department of Natural Resources (DNR), is located in the Soudan Underground Mine State Park, approximately 340 km north of Minneapolis, MN. The Soudan mine, the oldest iron mine in Minnesota, is no longer an operating mine but is maintained by DNR as a tourist attraction.

The laboratory is located on the 27th level of the mine, at a depth of 690 m corresponding to 2090 m.w.e. At this depth, the cosmic ray muon flux is approximately 7×10^4 muons/m^2/year. The laboratory has a permanent staff of technicians who live in the local communities surrounding Soudan. In addition to the experimental space underground, there are a number of machine tools available as well as facilities for maintaining electronics.

The Soudan Underground Laboratory has two major drawbacks, both relating to accessibility. Since it is located in a mine, only vertical access to the laboratory is available. Furthermore, the mine is located in a rather remote region of northern Minnesota, making travel to the laboratory a difficult, time-consuming process. However, experiments have

been successfully operated there [125], and the installation of a long-baseline neutrino oscillation experiment (MINOS) [126] is currently being considered by Fermilab.

Laboratorio Nazionale del Gran Sasso

The Laboratorio Nazionale del Gran Sasso (LNGS) [127], often referred to simply as Gran Sasso, is located beside the 10.4 km long Gran Sasso Tunnel on the highway connecting Rome to L'Aquila and Teramo in southern Italy. The highway tunnel provides convenient horizontal access to the laboratory. Gran Sasso, which consists of three experimental halls and a series of connecting tunnels and service areas, is operated by the Italian Instituto Nazionale di Fisica Nucleare (National Institute of Nuclear Physics). In addition to the underground experimental halls, the laboratory includes a group of external buildings that house the LNGS headquarters and administrative offices, the computer center, the technical and engineering services, the electronic and chemical laboratory, the machine shop, the stockroom and a conference center.

The natural temperature inside the underground laboratory is 6 °C and the relative humidity is near 100%, but an air conditioning system maintains the temperature at 18 °C and the relative humidity at 50%. Each of the three experimental halls is more than 100 m long and approximately 18 m high and 18 m wide providing, in total, more than 10^5 m^3 of experimental space. The laboratory, which is located at 963 m above sea level, has a minimum rock overburden of 1400 m corresponding to 3800 m.w.e. This is sufficient to prevent muons with energies below 2 TeV from reaching the laboratory and to reduce the ambient muon flux to 3000 muons/m^2/year. The neutron flux measured in the laboratory [101] is $(1.08 \pm 0.02) \times 10^{-6}$ neutrons/cm^2/s for thermal neutrons, $(1.98 \pm 0.05) \times 10^{-6}$ neutrons/cm^2/s for epithermal neutrons (i.e., 0.05 eV to 1 keV), and $(0.23 \pm 0.07) \times 10^{-6}$ neutrons/cm^2/s for neutrons above 2.5 MeV. In addition, the Gran Sasso rock is characterized by a low rate of natural radioactivity which results in a relatively low ambient photon background.

Gran Sasso offers a number of advantages. Firstly, access to the laboratory is convenient and unlimited via the highway tunnel. Secondly, the numerous experimental programs currently underway in the laboratory make it a stimulating scientific environment complete with technical support and expertise. Thirdly, despite the large number of experiments already installed, the laboratory still has plenty of space available for an experiment such as CDMS. Finally, Gran Sasso is readily accessible from Rome, making travel to the laboratory relatively easy.

Laboratoire Souterrain de Modane

The Laboratoire Souterrain de Modane (LSM) is a French laboratory jointly operated by the Centre National de la Recherche Scientifique (CNRS) and the Commissariat à l'Energie Atomique (CEA). The laboratory is located in the French Alps, at the midpoint of the Fréjus road tunnel, near the French-Italian border.

The elevation of the laboratory is 1260 m and the rock overburden, which consists essentially of a mica schist, has a thickness of approximately 1700 m corresponding to 4400 m.w.e. This is sufficient to reduce the cosmic ray muon flux to approximately 1200 muons/m^2/year. The flux of neutrons with energies above 2.5 MeV is 0.28×10^{-6} neutrons/cm^2/s [128]. The laboratory is maintained by a small on-site technical staff.

Like Gran Sasso, the main advantage of Modane is its unlimited horizontal access via the highway tunnel. Travel to the laboratory is also relatively easy because of its proximity to Lyon. The main disadvantage of this site is that laboratory space is somewhat limited.

Sudbury Neutrino Observatory

The Sudbury Neutrino Observatory (SNO) [129] is an astronomical neutrino observatory that is being built underground in the deepest section of INCO Limited's Creighton Mine, 25 km west of Sudbury, Ontario. The facility is being built by an international

collaboration of scientists from Canada, the United States and the United Kingdom. The Sudbury Neutrino Observatory Institute has been formed to construct and operate the laboratory.

The central feature of the SNO laboratory is the the large cavity, 33 m high by 22 m in diameter, that will house the heavy water neutrino detector. The laboratory also consists of a control room, assembly room, electronics repair area, utility room, wash station, change rooms and a lunch room, all located 2 km below the surface. At this depth, the muon flux is only 80 muons/m^2/year.

The main advantage of this particular site is its extreme depth. Unfortunately, the Creighton Mine is an active nickel mine, and consequently, the area surrounding the laboratory is very dirty. As a result, a great deal of effort is required to maintain the high level of cleanliness necessary for a low background experiment. Also, being located in a mine, only vertical access to the laboratory is available and this access is limited by mining operations. A further disadvantage of SNO is its location, which makes traveling to the site somewhat difficult and time consuming.

7.1.3 Expected Performance at a Deep Site

Operating the CDMS experiment at a deep site is expected to increase the sensitivity of the experiment substantially. As discussed in Section 6.2, the sensitivity increases as the square root of the counting time and the detector mass. By moving to a deep site, the detector mass can easily be increased to 15 kg as described above. Furthermore, because of the suppressed muon flux at a deep site, muon-induced neutron backgrounds are no longer a limiting factor on sensitivity. Finally, a reduction in the photon background level is expected. The photon background level should become comparable to the level obtained in the first generation of direct detection experiments operated at deep sites (i.e., of the order of 1 event/kg/keV/day).

Under these conditions, with an electron recoil background rejection efficiency of 99%

and a counting time of 1 year with 15 kg of germanium detectors, the statistical accuracy given by Equation 6.38 becomes $\delta S = 0.008$ events/kg/day and a 95% confidence limit is set at a level of $1.64\delta S = 0.01$ events/kg/day. At this level of sensitivity, the CDMS experiment probes deeply into supersymmetry parameter space as illustrated in Figure 7.2.

7.2 A Final Word

With the expected sensitivity of the CDMS experiment operated at a deep site, the idea of actually measuring a WIMP signal is conceivable. The identification of WIMP interactions may be possible if additional information is available for each event. For example, the direction of nuclear recoils resulting from WIMP interactions is expected to be highly asymmetric due to the motion of the earth through the dark matter halo [130]. Measuring such an asymmetry in the direction of the nuclear recoils would be a strong indication that the signal was due to WIMPs rather than terrestrial background events.

An attempt to increase the amount of information available for each event has been the motivation for the development of detectors capable of sensing non-equilibrium phonons. Position resolution in small crystals has already been demonstrated with non-equilibrium phonon sensors [131] and theoretical estimates show [132] that it may be possible to determine the directionality of the events from the phonons in high quality crystals (in particular, crystals with high isotopic purity). In addition, although it has not yet been demonstrated, phonon spectroscopy may provide discrimination between nuclear recoils and electron recoils [133]. If this were proven to be possible, simultaneous ionization measurements would no longer be necessary for electron/nuclear recoil discrimination, allowing for a wider variety of target materials.

The continued development of sensors of non-equilibrium phonons will undoubtedly lead to more sensitive dark matter searches that are capable of probing deeply into the parameter space populated by models of supersymmetry. Improvements such as the abil-

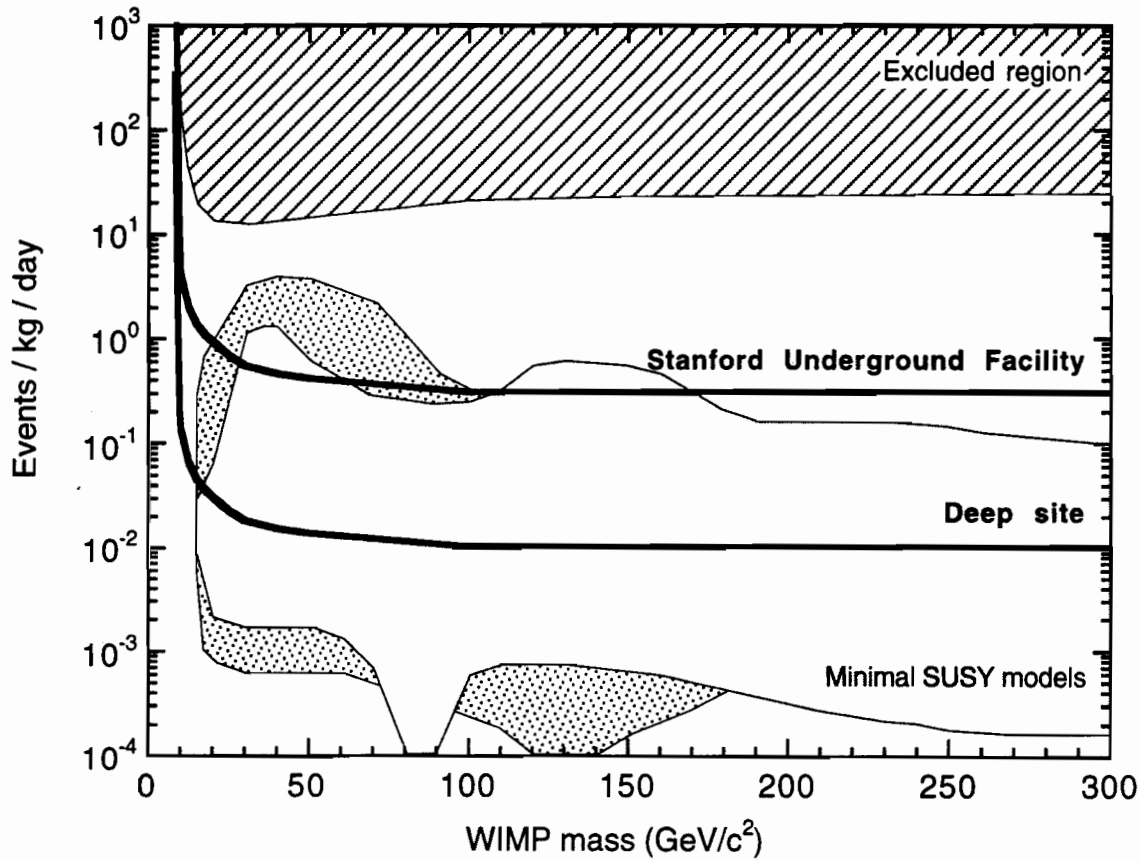

Figure 7.2: Expected sensitivity for the CDMS experiment at a deep site plotted as the total event rate in germanium as a function of WIMP mass. The limit shown assumes 5475 kg · days of data, with an electron recoil rejection factor of 99%. Also shown is the limit expected from the experiment operated at the Stanford Underground Facility with 100 kg · days of data, an electron recoil rejection factor of 99% and a muon veto factor for neutrons of 95%. The hatched region at the top of the figure is the region excluded by the first generation direct detection experiments [54] and the lower shaded regions are the allowed parameter space for various models of the lightest supersymmetric particle [55]. (The light shaded region is for models assuming a Higgs mass of 50 GeV/c^2 with $\tan\beta = 2$. The dotted region is for models assuming a Higgs mass between 80 GeV/c^2 and 90 GeV/c^2 with $\tan\beta$ between 6 and 22).

ity to determine the recoil direction would give the CDMS experiment the potential to measure an unambiguous WIMP signal rather than simply setting a new limit.

Bibliography

[1] See, for example, S. M. Faber and J. S. Gallagher, Ann. Rev. Astron. Astrophys., **17**, 135 (1979); V. Trimble, Ann. Rev. Astron. Astrophys., **25**, 425 (1987); S. Tremaine, Physics Today, **45, no. 2**, 28 (1992).

[2] Fr. W. Bessel, Astronomische Nachrichten, **22**, 145 (1844).
Fr. W. Bessel, Astronomische Nachrichten, **22**, 169 (1844).
Fr. W. Bessel, Astronomische Nachrichten, **22**, 185 (1844).

[3] G. P. Bond, Astronomische Nachrichten, **57**, 131 (1862).

[4] J. M. Schaeberle, Astronomische Nachrichten, **142**, 91 (1896).

[5] "Account of Some Circumstances Historically Connected with the Discovery of the Planet Exterior to Uranus", Mon. Not. R. Astron. Soc., **7**, 121 (1846).

[6] J. G. Galle, Astronomische Nachrichten, **25**, 49 (1846).

[7] J. Oort, Bull. Astron. Inst. Neth., **6**, 249 (1932).

[8] F. Zwicky, Helvetica Physica Acta, **6**, 110 (1933).

[9] V. C. Rubin, W. K. Ford, Jr., N. Thonnard, Astrophys. J., **238**, 471 (1980).

[10] See, for example, A. Bosma, Astron. J., **86**, 1825 (1981).

[11] S. M. Kent, Astron. J., **93**, 816 (1987).

[12] M. R. Merrifield, Astron. J., **103**, 1552 (1992).

[13] See, for example, A. Saha, A. Sandage, L. Labhardt, H. Schwengeler, G. A. Tammann, N. Panagia, F. D. Macchetto, Astrophys. J., **438**, 8 (1995); A. G. Riess, W. H. Press, R. P. Kirshner, Astrophys. J., **438**, L17 (1995); M. J. Pierce, D. L. Welch, R. D. McClure, S. van den Bergh, R. Racine, P. B. Stetson, Nature, **371**, 385 (1994).

[14] V. C. Rubin, Proc. Natl. Acad. Sci. USA, **90**, 4814 (1993).

[15] S. M. Kent, J. E. Gunn, Astron. J., **87**, 945 (1982).

[16] J. P. Hughes, Astrophys. J., **337**, 21 (1989).

[17] J. A. Tyson, F. Valdes, R. A. Wenk, Astrophys. J., **349**, L1 (1990).

[18] N. Kaiser, G. Squires, Astrophys. J., **404**, 441 (1993).

[19] T. J. Broadhurst, A. N. Taylor, J. A. Peacock, Astrophys. J., **438**, 49 (1995).

[20] For further discussions on the FRW cosmological model, see S. Weinberg, *Gravitation and Cosmology*, Wiley, New York, (1972); E. W. Kolb and M. S. Turner, *The Early Universe*, Paperback Edition, Addison-Wesley Publishing Company, Massachusetts, (1990).

[21] G. Efstathiou, R. S. Ellis, B. A. Peterson, Mon. Not. R. Astron. Soc., **232**, 431 (1988).
J. Loveday, B. A. Peterson, G. Efstathiou, S. J. Maddox, Astrophys. J., **390**, 338 (1992).

[22] S. Tremaine, Physics Today, **45, no. 2**, 28 (1992).

[23] M. J. Geller, J. P. Huchra, Science, **246**, 897 (1989).

[24] P. J. E. Peebles, *The Large Scale Structure of the Universe*, Princeton University Press, New Jersey (1980).

[25] A. Dekel, Ann. Rev. Astron. Astrophys., **32**, 371 (1994).

[26] A. Sandage, Physics Today, **23, no. 2**, 34 (1970).

[27] H. U. Norgaard-Nielsen, L. Hansen, H. E. Jorgensen, A. A. Salamanca *et al.*, Nature, **339**, 523 (1989).
A. Goobar, S. Perlmutter, Astrophys. J., **450**, 14 (1995).

[28] L. L. Cowie, Physica Scripta, **36**, 102 (1991).

[29] E. D. Loh, E. J. Spillar, Astrophys. J., **307**, L1 (1986).

[30] See, for example, S. R. Bahcall, S. Tremaine, Astrophys. J., **326**, L1 (1988); D. Caditz, V. Petrosian, Astrophys. J., **337**, L65 (1989); M. Omote, H. Yoshida, Astrophys. J., **361**, 27 (1990).

[31] A. H. Guth, Phys. Rev. D, **23**, 347 (1981).
For reviews of inflation, see R. H. Brandenberger, Rev. Mod. Phys., **57**, 1 (1985); A. Guth, in *Inner Space/Outer Space*, (E. W. Kolb, M. S. Turner, D. Lindley, K. Olive, D. Seckel, eds.), University of Chicago Press, Chicago, p. 287 (1986); W. H. Press, D. N. Spergel, in *Dark Matter in the Universe*, (J. Bahcall, T. Piran, S. Weinberg, eds.), World Scientific, Singapore, p. 197 (1987).

[32] G. Gamow, Phys. Rev., **70**, 527 (1946).
R. A. Alpher, H. Bethe, G. Gamow, Phys. Rev., **73**, 803 (1948).

[33] T. Walker, G. Steigman, D. Schramm, K. Olive, H.-S.Kang, Astrophys. J., **376**, 51 (1991) and references therein.

[34] C. J. Copi, D. N. Schramm, M. S. Turner, Science, **267**, 192 (1995).

[35] J. C. Mather *et al.*, Astrophys. J., **420**, 439 (1994).

[36] J. E. Gunn, B. A. Peterson, Astrophys. J., **142**, 1633 (1965).

[37] K. Griest, Astrophys. J., **366**, 412 (1991).

[38] J. N. Bahcall, C. Flynn, A. Gould, S. Kirhakos, Astrophys. J., **435**, L51 (1994).

[39] C. Alcock *et al.*, (MACHO collaboration), Nature, **365**, 621 (1993).
E. Aubourg *et al.*, (EROS collaboration), Nature, **365**, 623 (1993).
A. Udalski *et al.*, (OGLE collaboration), Acta Astronomica, **43**, 289 (1993).

[40] B. Paczynski, Astrophys. J., **304**, 1 (1986).

[41] C. Alcock *et al.*, Phys. Rev. Lett., **74**, 2867 (1995).

[42] MACHO Project Press Release - AAS Meeting, San Antonio, TX, January 16 (1996).

[43] R. D. Peccei, H. R. Quinn, Phys. Rev. Lett., **38**, 1440 (1977).

[44] S. DePanfilis *et al.*, Phys. Rev. Lett., **59**, 839 (1987).
C. Hagmann *et al.*, AIP Conference Proceedings (no. 194), 366 (1989).

[45] K. VanBibber *et al.*, Intl. J. Mod. Phys. D, **3**, S33 (1994).

[46] B. W. Lee, S. Weinberg, Phys. Rev. Lett., **39**, 165 (1977).

[47] K. Griest, B. Sadoulet, "Model Independence of Constraints on Particle Dark Matter", in Proceedings of the *Second Particle Astrophysics School on Dark Matter*, Erice, Italy, 1988.

[48] See, for example, J. R. Primack, D. Seckel, B. Sadoulet, Ann. Rev. Nucl. Part. Sci., **38**, 751 (1988); P. F. Smith, J. D. Lewin, Physics Reports, **187**, 203 (1990); R. Bernabei, Rivista del Nuovo Cimento, **18, no. 5**, 1 (1995).

[49] M. W. Goodman, E. Witten, Phys. Rev. D, **31**, 3059 (1985).
I. Wasserman, Phys. Rev. D, **33**, 2071 (1986).
A. K. Drukier, K. Freese, D. N. Spergel, Phys. Rev. D, **33**, 3495 (1986).
G. L. Kane, I. Kani, Nucl. Phys. B, Part. Phys., **B277**, 525 (1986).

[50] See, for example, J. Silk, K. Olive, M. Srednicki, Phys. Rev. Lett., **55**, 257 (1985); W. H. Press, D. N. Spergel, Astrophys. J., **296**, 679 (1985); L. M. Krauss, M. Srednicki,F. Wilczek, Phys. Rev. D., **33**, 2097 (1986); J. Silk, M. Srednicki, Phys. Rev. Lett., **53**, 624 (1984).

[51] M. Beck, F. Bensch, J. Bockholt, G. Heusser, H. V. Klapdor-Kleingrothaus, B. Maier, F. Petry, A. Piepke, H. Strecker, M. Völlinger, K. Zuber, A. Balysh, S. T. Belyaev, A. Demehin, A. Gurov, I. Kondratenko, W. I. Lebedev, A. Müller, Phys. Lett. B, **336**, 141 (1994).
D. Reusser, M. Treichel, F. Boehm, C. Broggini, P. Fisher, L. Fluri, K. Gabathuler, H. Henrikson, V. Jörgens, L. W. Mitchell, C. Nussbaum, J.-L. Vuilleumier, Phys. Lett. B, **255**, 143 (1991).
D. O. Caldwell, R. M. Eisberg, D. M. Grumm, M. S. Witherell, B. Sadoulet, F. S. Goulding, A. R. Smith, Phys. Rev. Lett., **61**, 510 (1988).
S. P. Ahlen, F. T. Avignone III, R. L. Brodzinski, A. K. Drukier, G. Gelmini, D. N. Spergel, Phys. Lett. B, **195**, 603 (1987).

[52] D. O. Caldwell, B. Magnusson, M. S. Witherell, A. Da Silva, B. Sadoulet, C. Cork, F. S. Goulding, D. A. Landis, N. W. Madden, R. H. Pehl, A. R. Smith, G. Gerbier, E. Lesquoy, J. Rich, M. Spiro, C. Tao, D. Yvon, S. Zylberajch, Phys. Rev. Lett., **65**, 1305 (1990).

[53] J. Lindhard, V. Nielsen, M. Scharff, P. V. Thomsen, Mat. Fys. Medd. Dan. Vid. Selsk., **33**, 10 (1963).

[54] Exclusion data for this plot was compiled by Peter D. Barnes, Jr., from Beck *et al.*, Reusser *et al.*, and Caldwell *et al.* of Reference [51].

[55] Kim Griest, private communication (1992). Details of the supersymmetric model calculations along with updated results will be published in G. Jungman, M. Kamionkowski, K. Griest, "Supersymmetric Dark Matter," submitted to Physics Reports (1995).

[56] For an overview of recent work in the development of cryogenic detectors for dark matter searches (and other applications), see, for example, the Proceedings of the

Fifth International Workshop on Low Temperature Detectors, University of California, Berkeley, July 29-August 3, 1993, J. Low Temp. Phys., **93, nos. 3/4** (1993); Proceedings of the *Sixth International Workshop on Low Temperature Detectors*, Interlaken, Switzerland, August 28-September 1, 1995, Nucl. Instrum. and Meth., **A370** (1996).

[57] T. Shutt *et al.*, Phys. Rev. Lett., **69**, 3425 (1992).

[58] T. Shutt *et al.*, Phys. Rev. Lett., **69**, 3531 (1992).

[59] E. E. Haller, N. P. Palaio, M. Rodder, W. L. Hansen, E. Kreysa, in *Neutron Transmutation Doping of Semiconductor Materials*, p. 21, (R. D. Larrabee, ed.), Plenum, New York (1984).

[60] A. L. Efros, B. I. Shklovskii, *Electronic Properties of Doped Semiconductors*, Springer-Verlag, New York (1984).

[61] N. Wang, F. C. Wellstood, B. Sadoulet, E. E. Haller, J. Beeman, Phys. Rev. B, **41**, 3761 (1990).

[62] N. Wang, Ph.D. Thesis, Department of Physics, University of California at Berkeley, (1991).

[63] T. A. Shutt, Ph.D. Thesis, Department of Physics, University of California at Berkeley, (1993).

[64] T. Shutt *et al.*, Nucl. Instrum. and Meth., **A370**, 165 (1996).

[65] K. D. Irwin, S. W. Nam, B. Cabrera, B. Chugg, B. A. Young, Rev. Sci. Instrum., **66**, 1 (1995).

[66] R. P. Welty, J. M. Martinis, IEEE Trans. Magn., **MAG-27**, 2924 (1991).

[67] K. D. Irwin, Appl. Phys. Lett., **66**, 1998 (1995).

[68] B. Cabrera, Nucl. Instrum. and Meth., **A370**, 150 (1996).
S. W. Nam *et al.*, Nucl. Instrum. and Meth., **A370**, 187 (1996).
M. J. Penn *et al.*, Nucl. Instrum. and Meth., **A370**, 215 (1996).

[69] B. Cabrera, private communication, 1995.

[70] E. Browne and R. B. Firestone, *Table of Radioactive Isotopes*, (V. S. Shirley, ed.), John Wiley & Sons, Inc., New York, (1986).

[71] Y. Feige, B. G. Oltman and J. Kastner, J. Geophys. Res., **73**, 3135 (1968).

[72] J. A. S. Adams, "Radioactivity of the Lithosphere", in *Nuclear Radiation in Geophysics*, pp. 1-17, (H. Israel and Krebs, eds.), Academic Press, New York (1962) (as cited by Feige[71]).
UNSCEAR Report Supplement 14 A/6314, Radiation from natural sources, Annex A, pp. 18-27, United Nations, New York, (1966) (as cited by Feige[71]).

[73] T. Florkowski, L. Morawska and K. Rozanski, Nucl. Geophys., **2**, 1 (1988).

[74] *Uranium Series Disequilibrium: Applications to Earth, Marine and Environment*, (M. Ivanovich and R. S. Harmon, eds.), Clarendon Press, Oxford (1992) (as cited by Heusser[75]).

[75] G. Heusser, Ann. Rev. Nucl. Part. Sci., **45**, 543 (1995).

[76] D. Lal and B. Peters, "Cosmic Ray Produced Radioactivity on the Earth", in *Handbuchder Physik*, **46/2**, 551-612 (1967).

[77] A. Da Silva, B. Pritychenko, A. Smith, R. E. Lanou, B. Sadoulet, Nucl. Instrum. and Meth., **A364**, 578 (1995).

[78] F. T. Avignone III, R. L. Brodzinski, J. C. Evans, Jr., W. K. Hensley, H. S. Miley, J. H. Reeves, Phys. Rev. C, **34**, 666 (1986).

[79] R. L. Brodzinski, J. H. Reeves, F. T. Avignone III, H. S. Miley, J. Rad. Nucl. Chem., Articles, **124**, 513 (1988).

[80] F. S. Goulding, D. A. Landis, P. N. Luke, N. W. Madden, D. F. Malone, R. H. Pehl, A. R. Smith, IEEE Trans. on Nucl. Sci., **NS-31**, 285 (1984).
F. S. Goulding, C. P. Cork, D. A. Landis, P. N. Luke, N. W. Madden, D. F. Malone, R. H. Pehl, A. R. Smith, D. O. Caldwell, R. M. Eisberg, D. M. Grumm, D. L. Hale, M. S. Witherell, IEEE Trans. on Nucl. Sci., **NS-32**, 463 (1985).

[81] This ultra low activity lead, referred to as Nantes lead, was purchased from Lemer Pax, Protection Anti-X, 3 Rue de l'Europe, Zone Industrielle, 44470 CARQUEFOU, FRANCE. The lead purity was measured by J. L. Reyss, Centre des Faibles Radioactivites, Laboratoire Mixte CNRS-CEA, Avenue de la Terrasse, 91198 GIF sur Yvette CEDEX, FRANCE.

[82] The exact history of the Stanford lead is unknown. The lead bricks were probably purchased in the 1950's or early 1960's, but they were not removed from their original packing crates until they were used into the Stanford Underground Facility.

[83] The Glover lead was purchased from R. P. Enterprises/AMPRO, P.O. Box 14233, Torrance, CA 90503.

[84] GEANT version 3.1416, released November 8, 1990, copyright CERN, Geneva.

[85] E. A. Plassmann and L. M. Langer, Phys. Rev., **96**, 1593 (1954).

[86] S. Miyake, PICRC, **5**, 3638 (1973).

[87] G. Cocconi and V. Cocconi Tongiori, Phys. Rev., **84**, 29 (1951).

[88] P. Singer in *Springer Tracts in Modern Physics*, Vol. 71, 39 (1974).

[89] B. MacDonald, J. A. Diaz, S. N. Kaplan, R. V. Pyle, Phys. Rev., **139**, B1253 (1965).

[90] A. Goned, M. Shalaby, A. M. Salem, M. Roushdy, PICRC, **HE5.4-10**, 192 (1985).

[91] S. Charalambus, Nucl. Phys., **A166**, 145 (1971).

[92] L. B. Bezrukov, V. I. Beresnev, G. T. Zatsepin, O. G. Ryazhskaya, L. N. Stepanets, Sov. J. Nucl. Phys., **17**, 51 (1973).

[93] G. V. Gorshkov, V. A. Zyabkin, Atomnaya Énergiya, **34**, 210 (1973).

[94] B. V. Pritychenko, Center for Particle Astrophysics Internal Report DKM-59, University of California, Berkeley, CA, unpublished (1992).

[95] H. C. Fesefeldt III, Program GHEISHA, version 7.03, released September 28, 1985. For additional information, see *Simulation of hadronic showers*, PITHA report 85-02, F. C. Fesefeldt, RWTH Aachen.

[96] The subroutine used to generate the thermal Boltzmann distribution was written by Steve Yellin, Department of Physics, University of California at Santa Barbara (1992). See Yellin's 7/3/92 notebook entry for the theory behind the method.

[97] J. B. Marion, *Classical Dynamics of Particles and Systems*, 2nd ed., Academic Press, Inc., Orlando, p. 300 (1970).

[98] S. W. Gilbert *et al.*, Internal Report UCRL-17941, University of California, Lawrence Radiation Laboratory, Berkeley, CA (September 1968).

[99] G. F. Knoll, "Radioisotope Neutron Sources," in *Neutron Sources for Basic Physics and Applications*, (S. Cierjacks, ed.), Pergamon Press, Oxford, pp. 10-13, (1983).
A. Lorch, Int. J. of Applied Radiation and Isotopes, **24**, 5851 (1973).
K. W. Geiger and L. Van der Zwan, Health Physics, **21**, 120 (1971).

[100] Ted De Castro, Lawrence Berkeley National Laboratory, private communication.

[101] P. Belli, R. Bernabei, S. D'Angelo, M. P. De Pascale, L. Paoluzi, R. Santonico, N. Taborgna, N. Lucci and G. Villoresi, Il Nuovo Cimento, **101 A**, 959 (1989).

[102] W. U. Schröder, Thesis, Technische Hochschule Darmstadt (1971).
U. Jahnke *et al.*, CERN preprint (as cited by Singer [88]).
W. U. Schröder *et al.*, Darmstadt preprint (May 1973) (as cited by Singer [88]).

[103] G. Tsoumis, *Wood as Raw Material*, Pergamon Press, Oxford, (1968).

[104] J. C. Barton, Proc. 19th ICRC, **8**, 98 (1985).

[105] E. Segrè, *Nuclei and Particles*, 2nd edition, Benjamin and Cummings Publ. Co. Inc., Massachusetts, p. 586 (1977).

[106] R. M. Sundelin, Phys. Rev. C, **7**, 1037 (1973).

[107] M. Chen, V. M. Novikov and B. L. Dougherty, Nucl. Instrum. and Meth., **A336**, 232 (1993).

[108] Measurements were performed by Al Smith, Low Background Counting Facility, Lawrence Berkeley National Laboratory, November, 1991.

[109] H. Gotoh and H. Yagi, Nucl. Instrum. and Meth., **96**, 485 (1971).

[110] J. N. Crookes and B. C. Rastin, Nucl. Phys. B, **58**, 93 (1973).

[111] B. Rossi, Rev. Mod. Phys., **20**, 537 (1948).

[112] Measurements of the radioactivity of materials used in the construction of the shield were performed by Al Smith, Low Background Counting Facility, Lawrence Berkeley National Laboratory.

[113] The Carpenter Hipernom Alloy for magnetic shielding consists mainly of Ni (80%), Fe (14.9%) and Mo (4.2%).

[114] A more detailed description of the cryogenic system, complete with the design procedure, can be found in the Ph.D. thesis of Peter D. Barnes, Jr., Department of Physics, University of California at Berkeley, 1996 (in preparation).

[115] D. S. Akerib, A. Da Silva, B. Pritychenko, B. Sadoulet, A. Smith, "Production of Solder and Flux with Low Radioactivity," to be submitted to Nucl. Instrum. and Meth. (1996).

[116] The striplines were fabricated by Litchfield Precision Components, Inc., 1 Precision Drive, Litchfield, Minnesota 55355.

[117] G. Jungman, M. Kamionkowski, K. Griest, "Supersymmetric Dark Matter," submitted to Physics Reports (1995).

[118] J. Binney, S. Tremaine, *Galactic Dynamics*, Princeton University Press, Princeton, p.226 (1987).

[119] M. Kamionkowski, K. Griest, G. Jungman, B. Sadoulet, CU-TP-653, (1994).

[120] K. Freese, J. Frieman, A. Gould, Phys. Rev. D, **37**, 3388 (1988).

[121] J. Engel, Phys. Lett. B, **264**, 114 (1991).

[122] A. Drukier, K. Freese, D. Spergel, Phys. Rev. D, **33**, 3495 (1986).

[123] K. Griest, Phys. Rev. D, **37**, 2703 (1988).

[124] G. T. Ewan, Nucl. Instrum. and Meth., **A314**, 373 (1992).

[125] See, for example, A. S. Barabash, F. T. Avignone, R. L. Brodzinski, J. I. Collar *et al.*, Nucl. Phys. B, **S28A**, 236 (1992); T. Kafka, Nucl. Phys. B, **S28A**, 377 (1992); E. A. Peterson, "The Soudan Mine Experiment," in *Gauge Theories, Massive Neutrinos and Proton Decay*, (B. Kursunoglu, A. Perlmutter, eds.), Plenum, New York, pp. 301-307 (1981).

[126] P. Litchfield for the MINOS Collaboration, "A Long Baseline Neutrino Oscillation Experiment at Fermilab", Submitted to the PPESP (1995).

[127] The Gran Sasso Project, INFN/AE-82/1 (1982).

[128] Y. Bourlat, J.-C. Millies-Lacroix, D. Abt, Nucl. Instrum. and Meth., **A339**, 309 (1994).

[129] G. T. Ewan *et al.*, "Sudbury Neutrino Observatory Proposal", SNO-87-12 (1987).

[130] D. N. Spergel, Phys. Rev. D, **37**, 1353 (1988).

[131] See, for example, F. Probst, T. Peterreins, F. VonFeilitzsch, H. Kraus, Nucl. Instrum. and Meth., **A288**, 125 (1990); D. J. Goldie, A. M. Swift, N. E. Booth, G. L. Salmon, Nucl. Instrum. and Meth., **A344**, 592 (1994); B. Cabrera, Nucl. Instrum. and Meth., **A370**, 150 (1996).

[132] H. J. Maris, S. Tamura, Phys. Rev. B., **47**, 727 91993).
T. More, H. J. Maris, J. Low Temp. Phys., **93**, 387 (1993).

[133] For a hint of this possibility, see A. T. Lee, B. Cabrera, B. L. Dougherty, M. J. Penn, J. G. Pronko, Phys. Rev. Lett., **71**, 1395 (1993).